THE UNIVERSITY OF CHICAGO

TRANSITION METAL IONS AS OPTICALLY ADDRESSABLE SPIN QUBITS

A DISSERTATION SUBMITTED TO
THE FACULTY OF THE PRITZKER SCHOOL OF MOLECULAR ENGINEERING
IN CANDIDACY FOR THE DEGREE OF
DOCTOR OF PHILOSOPHY

BY
BERK DILER KOVOS

CHICAGO, ILLINOIS
DECEMBER 2021

For my love, Eliana

Table of Contents

List of Figures

List of Tables

List of Publications

This thesis represents the motivations, results, and conclusions from the following works:

[1] Optically addressable molecular spins for quantum information processing.

S. L. Bayliss*, D. W. Laorenza*, P. J. Mintun, **B. D. Kovos**, E. D. Freedman, D. D. Awschalom, *Science* **370**, 6522, 1309-1312 (2020)

[2] Trigonal bipyramidal V^{3+} complex as an optically addressable molecular qubit candidate.

M. S. Fataftah, S. L. Bayliss, D. W. Laorenza, X. Wang, B. T. Phelan, C. B. Wilson, P. J. Mintun, **B. D. Kovos**, M. R. Wasielewski, S. Han, M. S. Sherwin, D. D. Awschalom, D. E. Freedman, *J. Am. Chem. Soc. 142*(48), 20400-20408 (2020)

[3] Vanadium spin qubits as telecom quantum emitters in silicon carbide.

G. Wolfowicz, C. P. Anderson, **B. Diler**, O. G. Poluektov, F. J. Heremans, D. D. Awschalom, *Science Advances* **6**, 18, eaaz1192 (2020)

[4] Coherent control and high-fidelity readout of chromium ions in commercial silicon carbide.

B. Diler, S. J. Whiteley, C. P. Anderson, G. Wolfowicz, M. E. Wesson, E. S. Bielejec, F. J. Heremans, D. D. Awschalom, *npj Quantum Information* **6**, 11 (2020)

[5] Resonant optical spectroscopy and coherent control of Cr^{4+} spin ensembles in SiC and GaN.

W. F. Koehl, **B. Diler**, S. J. Whiteley, A. Bourassa, N. T. Son, E. D. Janzén, D. D. Awschalom, *Phys. Rev. B* **95**, 035207 (2017)

Acknowledgments

First and foremost, I would like to thank my advisor David Awschalom for his guidance and support throughout my graduate career. I am continuously inspired by David's ability to build a group of exceptional researchers and promote a culture of collaboration, resulting in groundbreaking science that is greater than the sum of individual contributions. David is also a leader of the field of quantum sciences. David is always very thoughtful about the future of the field, how to get there, and how we can help to facilitate it. David's vision of the scientific future and the communities he has built widened my perspective of my own research and its applications towards future technologies. David has always supported my extracurricular activities which allowed me to branch out and hone my multidisciplinary skills, from teaching to entrepreneurship. David sets an example as a great scientist, leader and mentor and I feel extremely lucky to have been his student. I would also like to thank other members of my thesis committee: Giulia Galli and Tian Zhong for their time and support.

I did my undergraduate studies at the University of Chicago College, earning a BA in Physics and a BS in Applied Mathematics. During this time, I worked with Juan Collar on dark matter research, and I am very grateful for the exposure to experimental research that he provided me. As the time was approaching for my graduate school applications, Juan encouraged me to consider fields of physics that were closely applicable to industry. Right around the same time, the professor for my statistical mechanics class (a 4th year class in the Physics program), David Biron, advised us to watch David Awschalom's TED talk to learn

about the potential applications of the concepts we were learning in the class - which was my first introduction to applying quantum science to engineering problems. A few weeks later, at the Einstein Bagels coffee shop on campus, I ran into my friend, David Goldfeld, who was helping to design the webpage for the upcoming Institute for Molecular Engineering.[1] He advised me to apply for the inaugural class and shared that David Awschalom would be the first quantum faculty in the department. The rest is history... I am extremely grateful to all these individuals for playing a role in these chains of events that led me to the PME.

I have been at the University of Chicago since 2010, longer than the PME existed (therefore I have ten-year), and witnessed the immense growth of the school, especially in the field of quantum engineering. The Chicago Quantum Exchange (CQE), led by my advisor David, has been a game changer for our field. The events they organize and the educational, industrial, and governmental engagement opportunities they provide have been instrumental in my professional growth. I would like to thank Kate Timmerman and Preeti Chalsani for their amazing work in CQE and for extending opportunities to me. Preeti was also extremely helpful with intellectual property filing for some of the work in this thesis.

Of course, none of this work would have been possible without my other mentors, colleagues, and friends. I would especially like to thank Will Koehl. When I first joined the lab, Will became my mentor and we worked very closely over the years. Will was interested in exploring analogs of NV centers in diamond, and he had just discovered the divacancy center in silicon carbide when I joined the lab. We explored many novel semiconducting and organic systems to find similar optically accessible spins until realizing transition metal ions could be made into such qubits - the main topic of this thesis. I have learned most of the fundamental experimental skills from Will. We spent many days together, talking about fishing, Texas highways, birds, and southern barbeque, and had many lunches in Bergstein Deli on 55th Street, mostly because they had the best iced tea in Hyde Park. I am extremely grateful for Will's mentorship and friendship.

1. Since then IME grew into Pritzker School of Molecular Engineering

The 'Santa Barbara' folk fit right into the University of Chicago culture. I enjoyed listening to David Christle nerd out on various topics from 'optimizing packing based on weight over calorie for hiking in Yosemite National Park' to using artificial intelligence for his research in novel ways. Paul Klimov always thought outside of the box, exemplified by my first experience in a cleanroom shadowing Paul where he used the imaging microscope in an etch-a-sketch manner to expose a pattern on his substrate. I thoroughly enjoyed the debates I had with Paolo Andrich from moral philosophy to climate change to European coffee culture. Andrew Yeats' creative thinking permeated to every aspect of the lab, including hacking the demo espresso unit to froth chocolate milk, and making one regular-sized cup of coffee with ten espresso pods. Besides being a great scientist, Chris Yale set an example of being a great partner, where he and Anna Marie were always together at lunch. Charlie De Las Casas was the embodiment of energy drinks, always pushing forward no matter what research curve balls he got. I was always impressed (and a little intimidated) by Abram Falk's professionalism and immense scientific knowledge, that when I first joined the group, I thought he was a post-postdoc.

Chris Anderson was David's first student from the University of Chicago's Department of Physics. Chris undertook some very exciting projects and pretty much had a hand in everything that our lab was doing, including helping with some of the projects in this thesis. Chris is always willing to listen and help. He is an excellent editor and a great brainstorming partner. Chris shares my passion for science fiction literature and our readings converged over time, forming an 'informal' book club where we discussed many great books including some from Neil Stephenson, the Expanse series and the Three Body Problem.

Gary Wolfowicz, a postdoc in our group (and later a researcher at the Argonne National Labs), and I shared the same lab space for many years and he has been a great friend and a mentor. Gary is one of the most resourceful scientists I have met, where he can kludge together a tool or an electronic part that works better than the commercial solution, for less money, in less time than overnight shipping. Gary, also a member of our book club, has a

wide imagination that has helped him succeed in both life and science. I especially enjoyed our philosophical conversations on interpretations of quantum mechanics over coffee.

Sam Whiteley was another graduate student in my year also trained by Will Koehl. Sam's interests were in material science and device fabrication, while my focus and expertise were on quantum optics experiments and, therefore, we complemented each other. I always knew I could rely on Sam for a substrate, and he always found ingenious ways to prepare them. Although I missed my scientific partner, I was happy to see Sam's research succeed quickly and see Sam graduate. Sam is a great friend and coffee buddy, exemplified by his perfect recreation of Keurig coffee machine sounds.

Sam Bayliss, another postdoc, joined our group in my later years from the UK. Sam's immense knowledge about organic molecules combined with his cheerful, optimistic, and persistent personality led the molecular qubit work to its success. I got to hear many of Sam's adventures about being chased by a mob of elephants to swimming in a snake-infested lake during our car rides to Northwestern University to pick up samples from our collaborators. Although Sam has his tea with milk, he is a great friend and scientific mentor.

Peter Mintun, another student from my year, also worked with Sam Bayliss on the molecular spin qubits project. Peter is probably the most interdisciplinary student with whom I have worked, with immense knowledge about the business world, Disney universe, and a giant repertoire of dad jokes. I know these skills will get him very far in life.

Yeghishe Tsaturyan, a postdoc, joined our group just before the Covid-19 pandemic began and within the small window of normalcy he already suggested many positive changes for the group including replacing some office chairs with Pilates balls and having informal technical meetings to help each other debug experimental challenges. His biggest contribution to the group culture, however, is bringing the tradition of preparing a graduation hat, of which I was the first recipient! During the pandemic, we paired up as laboratory partners, and I got to work with Yeghishe closely and witnessed his scientific prowess firsthand.

Leah Weiss also joined our group as a postdoc right before Covid-19. I got to work

with Leah together for some extracurricular engagement and have witnessed her hard work, embrace of discomfort in pursuit of professional growth and clarity of thought and self-expression. Leah, with her deep understanding of molecular physics combined with her experimental skills, is going to produce amazing science.

Alex Crook another student from my year, and a staple of the group lunch, would always ask the "stupid question" which facilitated some of the most interesting conversations I have had, proving that there are is no such thing as "stupid questions." In addition, Alex's humorous personality has allowed him to persevere and succeed in extremely challenging and long-term projects.

Kevin Miao, another and final student from my year, has been a great resource and partner. Besides taking classes together during our first few quarters, we also TA'd a class together. Kevin co-wrote the Scientific Python Research Environment (SPyRe) which most of the measurements in this thesis used. Kevin was the only other lab member who understood the horrors of cilantro, and that bond will be forever strong between us.

Brian Zhou was the first postdoc hired when the Awschalom group had moved to Chicago. Although Brian and I were working on very different projects, we were both using the 2nd generation custom-built Montana Instruments cryostats which bonded us over all the debugging we had to do together. Brian is currently an Assistant Professor of Physics at Boston College where he continues producing fantastic science and I feel very lucky to have overlapped with his time in the lab.

The next cohort of students joined the lab during the move from our temporary lab space in Jones to our permanent home in ERC and they also overlapped with Santa Barbara folk. Alex Bourassa, the other co-writer of Spyre has an immense expertise in instrumentation and has been a great help. Paul Jerger is very quick witted with a great sense of humor and is very organized, exemplified by being the unofficial group meeting record keeper. Erzsebet Vincent, one of the longest members of the group dating back to her Santa Barbara undergraduate degree, always presents interesting papers at the group meeting with great humor. Masaya

Fukami has a deep appetite for scientific discussion and one can easily discuss the 'meaning of decoherence' for hours in a very rigorous fashion. Yizhi Zhu, a joint student between David and Giulia Galli, possesses one of the most important skills in science: perseverance, and I know this will get her far in life.

The next cohort, who did not know Jones' temporary lab space, are set to be the new leaders of the group. Joseph Blanton with his technical expertise, Grant Smith with his knowledge of random facts and animated personality, Elena Glen, with her hard work and attention to detail, Jonathan Karsch, with his experimental skills and kind heart, and Pratiti Deb with her advocacy and candor, will do a fantastic job carrying the group forward. The members of the young generation of the lab, Benjamin Soloway, Jacob Feder and Cyrus Zeledon, have already proven themselves and I am excited to see their future accomplishments.

The Argonne National Labs crew has also been a great help. F. Joseph Heremans always knows how to navigate the grant agencies, the Argonne organization, and collaborations, and provides great advice and guidance. The group lunches are always more fun when Nazar Delegan and Sean Sullivan are there. Some of our research interests overlap and it is always great talking to and learning from them.

Our collaborators, Majed Fataftah and Daniel Laorenza from Danna Freedman's group at Northwestern University's Department of Chemistry, have been great scientific partners and friends. We spent many hours talking about science in the basement of the Gordon Research Center, waiting for data to come in. These discussions widened my perspective on transition metal *d*-orbitals and their use as a quantum bit platform presented in this thesis.

In Slaughterhouse Five, Kurt Vonnegut writes about a four-dimensional alien civilization called Tralfamadorians that experience time all at once. Because Tralfamadorians can experience the entirety of time, they can see hidden relations to the human condition that are not obvious to us, including that the creation of life requires seven individuals as opposed to only two. Similarly, a PhD requires a lot of nurturing and support besides the immediate academic help. I would like to thank my parents, Zeki and Viki Diler, who raised me with

an inquisitive mind necessary for science and always provided me with the best educational opportunities. All of my teachers in my early education, including Talha Kılıç, İzer Franko and Mert Balın, played a big role in inspiring and helping me to become a scientist. My in-laws, the Butlers, accepted me as their son, and helped my PhD journey with their much needed emotional support.

Most importantly, I would like to thank Eliana, my wife. We got engaged as college sweethearts the day after I graduated from college, and we got married a year later, during the first year of my PhD career. Eliana has gone through this PhD journey with me and has witnessed all the ups and downs and has always been there for me. Her coaching me on professionalism to proper dress attire carried me further in my PhD career than I could have imagined. Eliana is the source of my inspiration and motivation, and this work would not have been possible without her. Eliana, thank you for your everlasting support, friendship, and love. I love our endless discussions and debates about many topics ranging from science and economics to history and culture. I have enjoyed every moment of life with you, and I feel incredibly lucky to be married to you. We've had many adventures together, from hiking in California and skiing in Utah to mastering homemade sourdough and having breakfast picnics by Lake Michigan. I am very excited for the next chapter of our life together.

During the past seven years of my PhD career, I got the chance to meet amazing people, learn from them and become friends with them. My favorite times were lunch and coffee discussions, where I would have the most interesting conversations. These spontaneous encounters and conversations fueled the creative thinking needed for scientific discoveries. I believe this lab culture combined with the amazingly talented people here is the secret sauce of our group and therefore my success. I am grateful to everyone who played a role in it.

Abstract

This thesis investigates transition metal ions (TMIs) as an emerging platform to create quantum bits (qubits). The electronic orbitals of TMIs can be tuned and designed using basic guiding principles to form various structures that contain long lived qubits in the ground state and spin selective optical transitions that form a photonic interface to initialize and readout the quantum states.

This thesis starts with describing the physics behind electron spin qubits and TMI orbitals that host the electrons. We then narrow the focus to a few symmetry configurations based on basic design principles from understanding TMI physics. Through optical spectroscopy we confirm the expected electronic structure that allows for a spin-photon interface of chromium ions within two different semiconducting hosts: silicon carbide (SiC) and gallium nitride (GaN). We observe a striking similarity of the optical and spin structure between the qubits in these different semiconducting hosts. This is a result of the similar local environment of the defects, demonstrating the portability of TMI qubits across various hosts. We then further narrow our focus to TMI qubits within SiC, a technologically mature semiconducting material widely used in industry. We create qubits in this material on demand through ion implantation and annealing, a first step towards scalable quantum devices based on transition metal qubits within solid state. In this system, we show long spin lifetimes for ensembles of chromium ions with high optical initialization and readout fidelities, which demonstrates their viability as spin qubits with optical addressability. We also characterize

vanadium ion defect spins that possess an optical interface within the telecom O-band compatible with single-ion detection, showing promise for using them in long distance quantum communication devices that can utilize the existing low-loss telecommunications fiberoptic infrastructure. Finally, we leverage a new synthetic chemistry approach to atomistically design the local ligand environment of TMIs to generate optically addressable molecular spin qubits and show their coherent control. By changing the ligand environment and/or the core transition metal type, we can keep the physics of the qubit the same while changing both the optical transition over 200 nm and the microwave transitions over 100 GHz, showing the promise of transition metal based molecules as tailor-made qubits for different quantum applications that can range from self-assembled individually addressable spin arrays for quantum computation to highly multiplexed quantum sensors that are a nanometer in size.

The demonstrations of long coherence times with high initialization and readout fidelities, detection of single emitters within the telecom band, and synthetically tunable molecular qubits highlight the promise of TMIs as a flexible, emerging quantum technology platform with potential applications in quantum communication, computation, and sensing.

Chapter 1

Building Quantum Technologies

I often find that within research communities, a researcher's family and friends who are outside of the scientific community have little idea about what the researcher does. I find this sad, because science explains the world in which we live, creates the foundations for the technologies that we use and is awesome. I believe if a particular scientific information explained simply, any person can understand it, find it interesting and enjoy learning it. I was lucky enough to participate in many teaching activities during my PhD career where students' knowledge ranged from high school mathematics and science to PhD students specializing in quantum technologies. During these activities I had to think deeply about the field of quantum information science to cater my explanation for each audience. My goal of this chapter is to take a nontraditional approach and explain quantum information science, its promises, where we are and the current challenges simply and as accessible as possible. This is an exceptionally challenging approach for any PhD student who is accustomed to rigorous scientific writing and it is also a risky one, as there is likely going to be an exception to any general and simplified statement. Nevertheless I believe this is an important task, as I hope any friend, family or interested party can read this chapter to understand the field and the contribution of this thesis to it.

The field of quantum information science is vast, comprised of topics such as: mathemati-

cal foundations of information theory, experimental quantum platforms, support technologies and packaging devices. A whole series of books would still be insufficient to paint a complete picture of the field. Within the limited space and time I have, the perspective I will share here will be filtered through my research focus of using *transition metal ions as optically addressable spin qubits*. My goal is that anyone with some basic science background can read this chapter and understand what *optically addressable spin qubit* means, where quantum information science stands as of 2021 and how this thesis fits into the global effort of building quantum technologies.

1.1 "Classical" Technologies

The late 20th and 21st century experienced a rapid expansion of computational power, most commonly characterized by the phenomenological observation called Moore's Law: roughly every two years, the number of transistors on a microchip double due to the pace of technological advancement. A transistor is an electronic switch and the backbone of all the digital technologies we rely on today, from the laptop on which I am writing these words, to the smart thermostat that controls the air handling system of my home.

Existing technological infrastructure is built on transistors because we are very good at making many of them cheaply and densely. There is, however, nothing magical about transistors. Anything that can 'switch' between two states, like a light switch, can technically be used to build a computer. Transistors are not unique in their capabilities. For example, neurons are also digital switches that either fire or not fire, and a cluster of them can perform computation.

A switch can only have two states: on or off. In the case of transistor *on* means *electrons are flowing* and *off* means *electrons are not flowing*. The state of the transistor encodes the binary information of 0 or 1. This is known as a *classical* bit.[1] By combining many of these

1. Only quantum physicists call this a *classical* bit. *Classical* computer scientists simply refer to it as a bit.

bits, say n-many, we can create 2^n different, unique encoding sequences that can correspond to numbers, text, sound frequency, image and video game logic.

How did we get from a bunch of switches to the interconnected digital world with devices that can augment reality, and store and provide access to all of the information humankind has created? This did not happen overnight. It took a lot of investment from governments, researchers and businesses to build a digital infrastructure. There were a few key components that were essential for these technologies:

- *Processor*: A processor is the part of the computer where it takes one set of binary encoding, and turns it into another set. This is achieved by a 2-bit NAND gate shown below:

Bit 1	Bit 2	NAND
0	0	1
0	1	1
1	0	1
1	1	0

Table 1.1: NAND logic table.

  This gate is universal: any other 2-bit logic can be built by combining various NAND gates. This is a very powerful tool, by simply using a combination of NAND gates, we can convert any binary encoding to any other binary encoding! We have developed computer programming languages to figure out how to do meaningful conversions of the binary code and employ algorithms which is a fancy way of saying "follow a set of predetermined rules" to get the job done. We have built many layers of logic that convert this process into easy to understand human language, but in its essence a computation is conversion of one set of binary into another one and is done within a processor.

- *Memory*: We need to be able to store the sequence of binary bits for later use, reliably. If the data is corrupted before it can be measured or processed, then valuable infor-

mation can get lost. In a sense, a processor is by definition a memory since the binary must be stored to be processed. It is however, costly to use a processor, an architecture that is optimized for rapid gating of bits, simply as memory as the idle information occupies unnecessary resources to be saved. Having some excess memory where information can be stored for a longer time is a more efficient architecture. Ultimately, the cost of material, energy, bandwidth and other parameters determine whether the information is held locally within the processor, temporarily within dedicated processor memory, permanently in a magnetic disc or the cloud (a remote server farm).

- *Interface*: How do you flip the millions of binary switches in our pockets to the right state (0's and 1's) for processing, storing or transmitting information? Suppose you have some data in the memory with a sequence of a million 0's and 1's - how do you make sense out of it? In some science fiction media (e.g. Neo in *The Matrix*), one can look at a sequence of binary on screen and make sense of the data immediately. This, however, is very far from a realistic depiction of how we use computers. We need intuitive ways for us to interact with this digital infrastructure. First, we need a way to input data into a computer, for example with a keyboard (as opposed to memorizing the unique binary encodings for each letter and flipping switches one by one). We also need a way to measure the end result of the computation, for example convert a collection of bits that encode the letter **a**, into a recognisable pattern of pixels that light up on our monitors such that we can visually recognize the encoded letter. A screen and keyboard are just some examples of how one communicates with these switches. There are many other forms of input (e.g.'s camera, microphone, mouse, heart rate monitor) and output (speakers, screens, printers, coffee makers). The point is, an information processing device cannot be a *brain in a jar*, it needs a way to have inputs and outputs to be useful.

- *Modem*: The data that is computed within a processor needs to move around, for exam-

ple to a memory for storage or a different computer for further processing. Although, the native binary encoding of "electrons flowing" vs. "electrons not flowing" can easily move the data within a computer through copper wires, this task becomes more challenging for longer distances. A *modem* solves this problem by converting the binary information encoded within electron flow to other forms of encoding, while retaining the digital information. For example, when one accesses a web-page, their computer generates the necessary query in binary, and an internal modem converts it into 5 gigahertz WiFi signal. A microwave receiver within a router detects the information, and translates the same information in a different microwave signal that is sent into the web through a coaxial cable. At a certain node, this microwave information gets translated into a laser beam (terahertz) through another modem and is sent through a fiber-optic cable. There are many nodes along the way that detect the laser beam, and repeat the signal to counteract natural losses. Sometimes the signal can traverse half way across the Earth! Eventually the light signal reaches a node close to the target server, gets converted into a microwave signal, then deciphered by the server modem. After all these conversions, the server that is halfway across the globe now has the query encoding in its own local memory! The server processes it, prepares a response accordingly and sends the information back into the web where the response binary traverses the same path backwards to the querying computer. All of this happens in less than a tenth of a second! The modem enables the conversion of the binary across multiple encoding architectures and is responsible for what we call the *internet*.

Within the existing digital framework, the information is converted between many forms. Transistors can temporarily store information within a central processor unit (CPU) or a random access memory (RAM), but these elements are not ideal to store information indefinitely as the "on" switches must be powered the entire time. Once the power is gone, the information is deleted forever. This is why a computer needs to boot up after it is powered down, the necessary transistors within the CPU and the RAM need to be turned

on. A more permanent way of storing information is the good old magnetic memory where data is encoded as magnetization on a piece of tape. So far, biological evolution holds the record for the highest density of long term data storage within DNA, where scientists, today, can encode and readout digital information at will [6]. We already discussed how the digital information also needs to be both transformed into and transcribed from electromagnetic waves for the internet to function. The key takeaway for the next part of the discussion is that transistors are not the only binary encoders of information. There are many other forms of binary encoding that is used for data storage and its transportation as well as devices that convert these encoding into each other.

When we discuss quantum technologies at Sec.1.3 we will see very similar ideas to the ones discussed above, but within the quantum context.

1.2 Need for Quantum Technologies

1.2.1 Quantum Computing

We are rapidly approaching the limits of the Moore's Law. As the transistors are shrinking to the size of a few atoms, the quantum effects start kicking in. For example, electrons can tunnel through electronic potential barriers that would be impossible classically, turning an 'off' transistor into an 'on' state and introducing unwanted errors. Given this limit, it is expected that within the next few decades we will hit a wall of doubling the density of transistors every two years. In order to continue increasing the computational power, we will need to employ new strategies that utilize quantum mechanics.

The theory of quantum mechanics explains the universe extremely accurately[2] and has held up to much scrutiny. As far as we know, the universe follows the laws of quantum mechanics, explained in detail at Sec.2.1. In order to accurately describe a quantum mechanical system, one needs to keep track of every possible scenario the system can have. On a macro

2. Except for gravity.

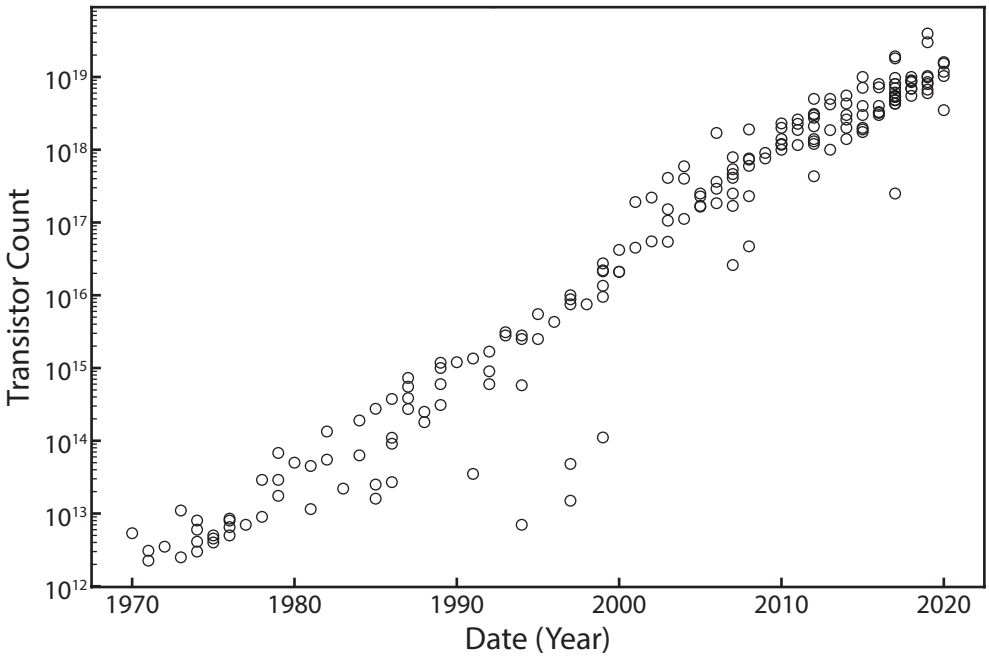

Figure 1.1: Moore's Law: the number of transistors are roughly doubling every two years. Data taken from Wikipedia's Transistor Count page.

scale, this is not necessary and one simply can use the laws of classical mechanics to model large scale objects. For example, when one shoots a cannon ball, one just needs to know the location of the ball and its velocity at some point in time to figure out how it is going to evolve later. However, quantum mechanically, to predict how an electron is moving, one would need to keep track of all possible trajectories since the initiation of the problem from a known state. Furthermore, if one increases the number of possible paths the electron can take, the problem becomes exponentially harder as all of the new combinations in addition to the initial ones must now be considered. As a result it is impossible for a classical system to simulate a large *highly entangled*[3] quantum mechanical system [7]. This has profound implications.

There are many problems that we care about in the fields of chemistry, biology and materials science that all act according to the laws of quantum mechanics and thus cannot be

3. A quantum mechanical property with no classical analogs that describe correlations which transcend space.

accurately simulated by a classical computer[4] using the first principles. A caffeine molecule with 24 atoms requires 10^{48} bits just to encode all of its possible configurations [8]. It is estimated that there are 10^{50} atoms in the world. In order to just store the data of all configurations a single caffeine molecule can have so that we can simulate it quantum mechanically, we need to use 1 out of every 100 atoms on the world! In contrast a 160 quantum bit (qubit) quantum computer can hold the same amount of data in its memory. Nature is able to keep track of all of the possible configurations and compute a cup containing full of this simple molecule that was essential for the work done in this thesis, in picoseconds with no trouble! If nature can do it, we should be able to as well.

I should note that quantum computers are not a golden bullet that will solve *all* mathematical problems; there is a large set of mathematical problems beyond the reach of a quantum computer. Nevertheless, there is hope that a quantum computer can at least help approximate solutions for certain problems faster than the classical ones.

So far we only know of 'quantum mechanical' problems that a quantum computer can solve exponentially faster than a classical computer. There are also some quantum algorithms that can solve non-quantum problems exponentially faster than classical computers. For example, *quantum Fourier transform* can find repeating patterns within data and *Shor's algorithm* can factor prime numbers and therefore can decrypt existing digital encryption systems. It is not yet known whether these are uniquely quantum solutions or if there exists a classical algorithm which works equally well that is not yet discovered. It is however encouraging that there exists at least one element (quantum mechanical problems) in the set of mathematical problems, that only a quantum computer can solve which may indicate that there may be a quantum advantage for solving other problems beyond materials science, chemistry and biology.

4. There are very useful approximation methods that allows modeling these quantum mechanical systems which guide and explain important physics and chemistry. Some of the largest built computers are used to run such such classical approximation algorithms to explore quantum mechanical phenomena.

1.2.2 Quantum Communication

A qubit, very similar to a classical bit, can only be measured as a 0 or 1. Unlike a classical bit, however, a qubit's measurement outcome is not predetermined, but instead most of the time probabilistic. The nature of this probabilistic behavior is described by a wavefunction and its dynamics by quantum mechanics. Once the qubit is measured, however, the probabilistic nature of the qubit ceases to exist (collapses), and it is permanently in the 0 or 1 state until it is placed in a different quantum mechanical state (see Sec.2.1 for more detailed description). It is impossible to decipher the wavefunction of an unknown qubit without repeating a measurement on identically-prepared qubits many times and building statistics. I should emphasize that repeatedly measuring the same qubit will not reveal more information about the original state of the qubit prior to the first measurement, since the initial measurement fundamentally changed the qubit. The fact that the very act of measuring a qubit changes it in a testable way and the measurement outcome probability is determined by the quantum state (wavefunction) is both a resource and a headache.

These quantum mechanical phenomena are a resource: since the measurement physically changes the qubit, a qubit can be used to build a shared secret code between two parties with the confidence that nobody else eavesdropped (measured) into their encryption protocol [9]. The fully secure, shared code (one-time pad), can be used to encrypt sensitive information like medical records or credit card information. Such a network of quantum particles can create encryption, secured by the laws of physics. The protocol that generates the secret codes is called *quantum key distribution*.

On the flip side, the collapse property is a headache, because it means that we cannot use a classical channel to send an unknown quantum wavefunction, since measuring the quantum wavefunction will inherently destroy it. Suppose we have a set of quantum sensors that are separated by long distances that need to communicate to each other, or we would like to send their wavefunction that contains information about the sensed object to a quantum computer for a quantum analysis or two quantum computers need to communicate; how

can these fragile wavefunctions be sent without physically transporting the encoding qubits or measuring them? Quantum mechanics does allow for quantum communication channels through a property called *quantum-entanglement*. A network of quantum entangled particles would enable teleportation of quantum wavefunctions over long spatial distances without collapsing the quantum state [10]. This network of quantum entangled particles can both be used for quantum encryption and wiring of quantum devices together and is called the *quantum internet*.

1.2.3 Quantum Sensing

A major challenge for qubits is preserving their quantum states as they are very sensitive to their local environment. On the flip side, this sensitivity makes them excellent sensors. A joke I've heard many times in the field is: "if you have a bad qubit, you have a good sensor, and if you have a bad sensor, you have a quantum random number generator".

The term, quantum sensor encompasses many different sensing strategies. This umbrella term includes the usage of highly localized and sensitive qubits to sense classical fields to using highly entangled quantum states to beat classical measurement limits [11].

Advanced quantum sensing schemes utilize quantum properties of the sensors and the desired signal gets encoded in the wavefunction of a qubit. This signal cannot be measured with a single experiment due to *collapse* property of qubits discussed earlier. Generally, the sensing scheme followed by a measurement is repeated many times to build statistics to decipher the wavefunction that contains the signal about the sensing target.

A quantum computer can manipulate wavefunctions without collapsing them. Therefore a quantum computer can extract the acquired information within a quantum sensor by employing a quantum algorithm where the sensor and the computer would be wired together by the quantum internet. This hybridization between a quantum sensor and a computer through a quantum channel could improve sensing techniques and also building quantum

databases [12]. Converting the existing classical data to a quantum one takes exponential time scaling and is currently a big bottleneck for quantum computers that require quantum data for the promised speed-ups [13]. Therefore, quantum sensors are essential to realize the full potential of quantum computers, with quantum communication channels wiring them together. All of these components: quantum sensors and processors wired together through a quantum internet need to work together to form the quantum technological landscape.

1.3 Quantum Technologies

Analogous to classical information technology components we have discussed, we will need to pioneer certain quantum technologies.

- *Quantum Memory*: Just like classical memories, we need quantum memories to store quantum wavefunctions. For example, we would need a quantum-database to be able to apply a quantum search algorithm (e.g. Grover's algorithm) which would be square-root times faster than classical database search. We may wish to train a quantum neural network, which would require a quantum data set to be trained on - therefore that database needs to be solidly in memory without corruption. A quantum memory would allow storing quantum states for long enough times for processing.

- *Quantum Interface*: Sadly, we are classical beings - so in order to measure the computational results from a quantum computer, we need to collapse the wavefunction and present it through a classical monitor or other interfaces for us to understand. All of the data we have today, including the results of quantum experiments, are stored in classical databases, and they are generated by classical input devices like a keyboard or a cell phone camera. As quantum technological landscape grows, it is possible to imagine a network, where most parts of the information remain quantum mechanical. We already explored the idea of quantum sensors and quantum computers sharing quantum wavefunctions to improve sensor sensitivity. It may also be possible to in-

sert quantum mechanical wavefunctions into ambient environment for a certain task through quantum actuators. For example Magnetic Resonance Imaging (MRI) polarizes the protons in our blood with very large magnetic fields (which makes the machine large, heavy and expensive) and then measures the polarization decay time to make deductions about the tissues in which they are. This is an example of quantum sensing. A qubit platform called the NV center in diamond can be used as a quantum actuator. Instead of using large magnetic fields for proton polarization, one can use the NV center qubits to insert the polarized quantum states to the ambient protons in water around the qubit without a large magnetic field. This technique can potentially enable miniaturizing MRI technology to make it cheaper and more accessible [14]. As quantum technologies advance, it could be possible to improve measurements through quantum sensors and control chemical and biological processes through injecting wavefunctions computed in a quantum computer by quantum actuators. Such quantum interfaces, inputs from quantum sensors and outputs from quantum actuators will be an essential part of quantum technologies.

- *Quantum Processor*: Just like classical computers, quantum computers' objective is converting one set of binary data into another set of binary data. Unlike classical computers, however, the data in a quantum computer is encoded within qubits and the result of a measurement is not deterministic. A measurement of a quantum system simply samples from all possible configurations that the qubit space can have. The point of a computation is to amplify the probability of all the results that are answers to the questions we are asking while minimizing the probability of measuring incorrect outputs. This wavefunction manipulation must follow certain operations allowed by quantum mechanics called *unitary transformations*. Just like the NAND gate was a universal computation basis for classical computers, it turns out that one two qubit operation (e.g. Controlled-NOT[5]), and a simple set of single qubit operations (e.g. X,

5. This is the quantum analog of the classical *Exclusive Or* (XOR) gate

Y, Z, T[6]) can exponentially accurately approximate any arbitrary two qubit operation in polynomial time [15] and any large unitary transformation can be decomposed into two qubit unitary transformations [16]. These are very powerful results, as they imply that it is possible to construct any quantum mechanical transformation within a quantum processor! A quantum algorithm, in essence, is a unitary transformation made out of single and two qubit gates that result in the desired final wavefunction that maximizes the probability of measuring the correct answer.

- *Quantum Modem*: Just like classical technologies rely on multiple platforms (e.g. telecom light, microwaves, electric current running through a transistor, magnetic domain on a tape etc.) to encode binary information between various physical systems, it is widely believed that quantum technologies will have to employ a similar strategy. This means, we will need to master the technology to transfer a quantum wavefunction (transduct) between multiple physical systems and quantum degrees of freedom that may be useful for various applications from communication to storage to computation. Such transduction technologies would open up the doors to bringing together many different quantum platforms each possessing a different strength for various applications.

1.4 Quantum Platforms

A qubit is a quantum degree of freedom that can be manipulated and measured. Just like a classical bit, where the abstract binary of 0 and 1 is attached to a physical object such as a transistor or a magnetic tape, the qubit is also attached to a physical quantum system. There are many available platforms that we will briefly discuss. Coherence is a figure of merit used to quantify the quality of a qubit and it describes qubit memory: how long the quantum

6. X-Gate is the quantum analog of the classical NOT gate which flips the bit. NOT gate is the only classical single bit operation. Y, Z, T are purely quantum mechanical single qubit gates with no classical analogs and control a qubits additional available degrees of freedoms.

wavefunction can be retained within a qubit. All of quantum platforms obey a fundamental, phenomenological rule: if a qubit is insensitive to the environment and therefore highly coherent, then it is difficult to manipulate it. Conversely, if one can easily manipulate the qubit, then the coherence times will also suffer. We commonly refer to this in the lab as: "nature hardly lets you win". One can intuitively understand it as follows: if a system is easy to interface with, then it is also easy for the environment to interact with it too and as such, the environment can 'take an unwanted measurement' and collapse the wavefunction or do any other undesired operation on the qubit. Therefore, there is not a single quantum platform available that can *rule them all*, yet.

Each qubit platform comes with its own set of advantages and challenges. The consensus in the field is that in order to build various quantum technologies, one needs to use multiple qubit platforms and convert (transduce) quantum information from one platform into another to take advantage of each platforms strengths for a specific application (e.g. photonic qubits for quantum communication). Thus, it is important to interface with a qubit with multiple degrees of control. The platforms I will discuss below at least have either an optical interface and/or a microwave interface, where a single light particle (photon) or a magnetic degree of freedom (spin) can itself be a qubit. Having more than one quantum interface available makes a qubit candidate more appealing for hybrid quantum applications. We will conclude this chapter with the discussion of transition metal ions, the subject matter of this thesis, and an emerging quantum bit platform.

1.4.1 Terahertz Photons

Our current information highways transport classical bits by encoding them within light that propagates through a fiber optic network that connects the entire world. A fiber-optic cable is essentially a piece of glass, most commonly made out of silica, and the light reflects from the walls of the cable, forcing it to propagate within it. During its travel through the fiber-optic cable, light can scatter off of grains within the glass, as silica can have domains with

different refractive indexes and domain mismatches. This is called Rayleigh scattering and is responsible for losses within the fiber optic cables and it is highly wavelength dependent ($\propto 1/\lambda^4$). The higher the wavelength, the lower the loss is and therefore photons that carry information can travel further. On the other end of the spectrum, however, photons can excite the bonds between silicon and oxygen in silica and therefore get absorbed through a process called multiphonon absorption. The closer the energy of the photon to this absorption process, the more likely it will be absorbed. Therefore higher wavelengths (lower energy) also get dissipated within a fiberoptic cable [17]. This leaves a window of maximum transmission around 1550 nanometer (nm) wavelength called C-band and is the current standard for telecommunication network. The probability of sending a single photon qubits through the existing fiberoptic network is maximized for this telecom band. Therefore, most of the fiberoptic related quantum network experiments are done in this wavelength regime.

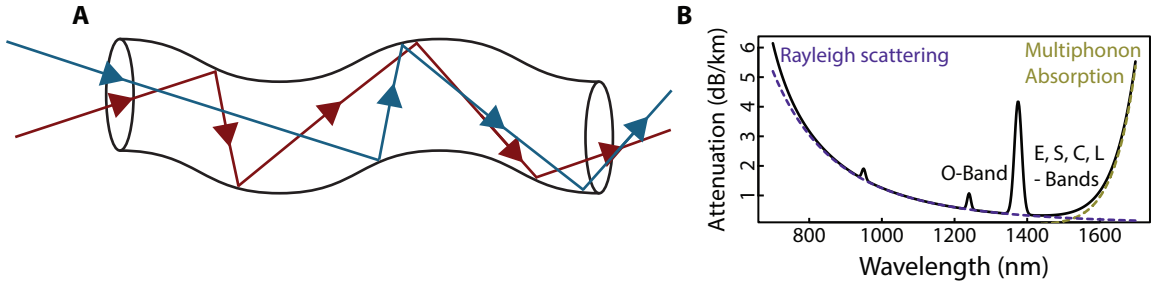

Figure 1.2: Photons within fiberoptic cables. (**A**) Illustration of photons traveling within a fiberoptic cable, contained by reflections from the walls. (**B**) Photon attenuation plot as a function of wavelength. The absorption peaks are due to unintentional OH within silica. Figure is adapted from wikipedia.

A single photon can be used as a qubit in many ways [18]. For example, the existence (1) or non-existence (0) of a single photon can encode a qubit. For long distance communication such encoding can be problematic, since a single photon can be absorbed or scattered within a traveling medium such as a fiberoptic cable or earths atmosphere, turning a 1 into a 0. Photons have a polarization axis which can also encode a qubit and this can be easily controlled with polarization optics, creating single qubit gates. By the same token, a photon's

polarization axis can unintentionally rotate as it is traveling through a material medium and create errors. A more robust qubit encoding is an early (0) vs. late (1) arrival photon, as one can easily detect photon losses. One needs to be careful again with real world long distance quantum communication using an early-late photon qubit as, for example, a fiberoptic cable can stretch or contract with ambient temperatures, or the location error of a moving satellite can introducing errors. It is generally possible to correct for timing errors with feedback from non quantum channels traversing the same photon paths. These three degrees of freedoms can be more or less easily transduced into each other with some simple optics [19].

One of the main reasons we do not have gate-based photonic quantum computers[7] is that it is extremely difficult to build two qubit gates as photons do not interact with each other except for very special circumstances, and when they do, the interaction is extremely weak. On the flip side, this allows for sending a massive amounts of data, multiplexed in photon energy, or other degrees of freedom without having to worry about one photon effecting another [20]. A second issue is that the photon is always moving at the speed of light through a medium, so in order to increase the number of gates, one needs to keep adding more optical elements to the photons path which makes building arbitrarily large circuits challenging. In contrast a stationary qubit is only limited by the coherence time and can be gated many number of times within that time window [21]. Therefore, a good avenue to explore are material qubits that naturally interface with photons. The material qubit can perform the two qubit gate operations, or store the quantum information for a long time, and on demand, that quantum information can be transduced into a photon to be either measured or sent over long distances through the existing telecommunication network.

7. There are other strategies that photonic qubit based architectures use including effects of measurement altering quantum states to perform wavefunction evolution.

1.4.2 Atoms

Just like cows can be approximated as spheres with uniform density in vacuum, atoms can be approximated as positively charged nuclei with negatively charged electrons orbiting around. We will have a more realistic description of electronic orbitals of an atom in Sec.2.4. Unlike planetary systems, in an atomic environment, there are only discrete number of orbitals available. In a nutshell, in quantum mechanics, everything is treated with probability waves, including the location of an electron. The front of the electron's wave must catch its tail after a full rotation around the atomic core. If this is not satisfied, over many rotations, the wave averages to zero - meaning the electrons probability of being measured there is zero. There are, therefore, only a discrete number of non-zero solutions creating the atomic orbitals. This discretization of solutions is generally true for any bound quantum system; it also gives the name to quantum physics, as in *quantization of energy*.

Two electrons cannot occupy the same quantum state, for example be at the same location at the same time, as we will see in Sec.2.3.2. Just like a ball falling down to minimize its potential energy due to gravity, an electron also tries to minimize its energy by being in the lowest energy orbital. However, if that orbital is already occupied, then the electron has be in the next available lowest energy orbital. When every electron is in the lowest allowed state, the system is said to be in the **ground state**. The highest energy electron can be excited to an even higher energy orbital when given energy, for example with a photon. After spending some time in this higher energy, unstable state, the system relaxes back to the ground state, and releases the energy difference in the form of a photon which can be measured. Since each atom (and molecule) has slightly different energetics depending on the nucleus (and bonds), it is possible to uniquely identify them by looking at this emitted or absorbed light through spectroscopy. We use this quantum effect to gather information about chemical composition of many materials including drugs, biological systems, planets and stars!

A single atom can be used as a qubit, where the quantum information is encoded within

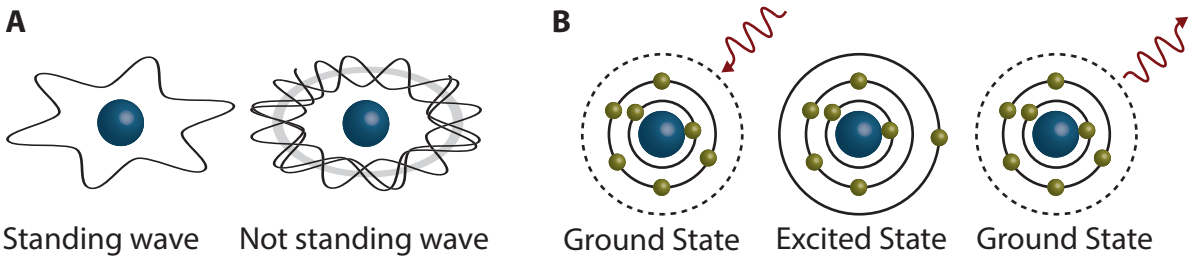

Figure 1.3: Atomic orbitals and electronic excitations. (**A**) If the tail of an electrons probability wave catches the wave front, then there is a stable orbital, otherwise the probability of electrons existence averages to zero. (**B**) Electrons around an atom stack to minimize the total energy called *ground state*. An electron can be excited to a higher energy orbital, for example with a photon and the atom is said to be in an *excited state*. A while later the atom decays back to the ground state and emits the energy difference as a photon. Blue sphere is the atom's core, yellow spheres are electrons and red sinusoidal line is a photon.

the state of the atom (e.g. ground-state: 0, excited-state: 1) controlled with lasers. Of course, one needs to well localize the atom, which can be achieved within an ultra-high vacuum chamber with the aid of electromagnetic forces and/or optical tweezers. The excitation of the atom changes the physical size of the atom since the outermost electron is now in a 'larger' orbital. This change can be felt by other atoms allowing for two qubit gates. However, localizing atoms beyond several hundreds in a scalable way to build large quantum systems is still an open research question [22].

1.4.3 Molecules

Molecules are a cluster of atoms held together with electronic bonds. The field of chemistry is dedicated to understanding and engineering the bonds between various atoms and the resultant material properties. Since the electronic energy levels, determined by the nearby nuclei, are all quantum mechanical, exact calculations of molecular ground and excited states become impossible beyond a couple of atoms using classical computational techniques. This is one of the main motivations behind quantum computers as discussed earlier. Such quantum degrees of freedom within molecules could be used as qubits or quantum simulators.

There are many quantum degrees of freedoms a molecule can have, including electronic

spins [23], nuclear spins [24], rotation [25], electronic excitation [26] just to name a few. The topic of this thesis is spin qubits, and therefore, we will focus on spin degrees of freedom of molecules. Spin is an intrinsic quantum property of subatomic particles including electrons and certain atomic nuclei. One can think of it as a quantum bar magnet attached to the subatomic particle. We will be extensively discussing spin physics in Sec.2.2. Just like bar magnets are influenced by external magnetic fields (e.g. a compass needle that points to magnetic north) spins can be controlled with both fixed and rotating magnetic fields allowing for qubit control. As each spin also creates its own magnetic field, multiple spins can magnetically interact with one another that can create quantum gates between such qubits.

Historically such quantum control and measurements were performed within an ensemble of molecules using electron spin resonance (ESR) or nuclear magnetic resonance (NMR) measurements. These measurement techniques are also the basis of magnetic resonance imaging (MRI). A large magnetic field causes the spins to preferentially point in one direction over another, called polarization. Thermal effects can cause the spins to flip unintentionally, therefore most of the non-biological experiments lower the temperature to increase the polarization rate. A rotating magnetic field, generally in the radio or microwave regime excites the spin to another orientation and as the spin relaxes back to the ground state it re-emits this energy where the emission or the absorption can be inductively detected. As spins within a material interact with each other based on the makeup of ambient magnetic conditions, one can decipher certain structural and chemical information of the system, which makes ESR and NMR a very widely used technique for characterization. The first quantum algorithm was run in such a system using nuclear spins of an ensemble of molecules to factor the number 15 using Shor's algorithm [27]. In order to build a functional quantum computer, one needs to manipulate and detect a single quantum wavefunction. Inductive detection is extremely weak, and detecting a single molecular spin that way is still an open research question with the best sensitivity of 12 electron spins [28] so far.

1.4.4 Solid State Defects

A crystal is a periodic array of atoms. Sometimes within this array, there can be structural defects. Among many types of defects an important subset are the point defects where one or more atoms within the array can be missing and/or an atom could be substituted by another kind. Similar to atom and molecular qubits discussed earlier, these point defects can form well-localized quantum states with discrete energy levels or spin states that electrons can occupy which can encode quantum information and therefore can constitute a qubit [29, 30].

If the host material is conductive, the electrons will flow freely through the crystal and will not form a well-localized qubit that can be individually controlled and measured. Therefore, semiconducting crystals are a good host material for such defects. A certain subset of point defects within semiconductors can be optically active, meaning there are higher energy states the electrons can occupy within the defect. Another subset of point defects can bear a spin, just like molecules, that could be used as a qubit. Defects that are both spin bearing and optically active are particularly interesting [31] as there can be spin-selective optical interfaces, with prototypical system being the negatively charged nitrogen vacancy center in diamond [32]. This optical interface allows for preparation (set) and readout (measurement) of the spin without the need for very high magnetic fields for spin polarization or inductive readout. Optical excitation can be much more efficient than thermal preparation in ESR and easier to access with ever improving laser and optical technologies [33, 34]. There are also easily accessible single photon detectors that enable single spin measurements. Since defect-center based qubits are within a semiconducting host, it is also relatively easy to build devices and control electronics around the defects using standard fabrication techniques [35–40], making solid state defects a scalable platform once some of its challenges are overcome.

A major challenge with solid state defects is material engineering. In an ideal world, we would have single defect centers in a periodic formation with atomic precision and not have any other unwanted damage or defects around. None of the existing processes create single defects reliably, and each defects' local environment can be slightly different due

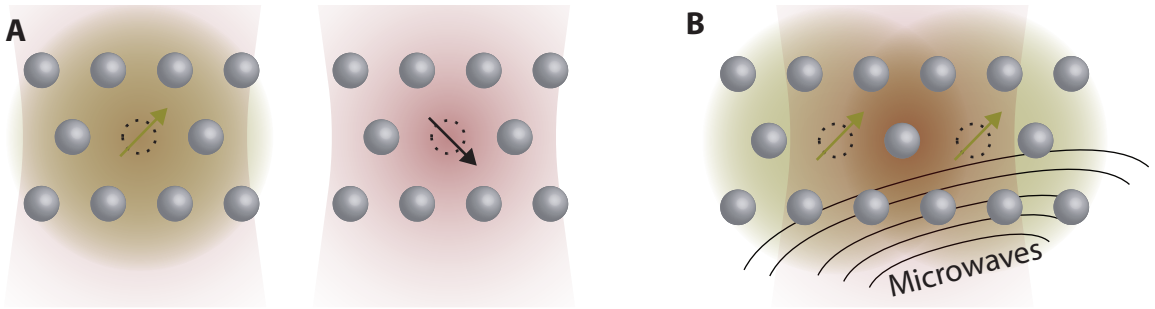

Figure 1.4: Optically active spin defects. (**A**) Defect spin emits light when probed if the spin is oriented up and emits less light if it is oriented in the opposite direction. (**B**) Defects need to be close together for magnetic interaction to realize quantum gates, but identical ones lose their individual addressability because they respond to the same optical probe and microwave color.

to unintentional local differences, slightly altering the quantum properties of defect centers. Another potential issue is the availability of multi-qubit registers for computation or memory. Two defect centers could magnetically interact with each other for gating if they are within a few nanometers of each other. Due to the wave nature of light, an excitation/detection spot size can be only as small as roughly the wavelength, called the diffraction limit. This is around a few hundred nanometers for visible to telecom wavelengths. If all the defects are identical within this spot size, it would not be possible to address or detect a single one of them because the laser cannot spatially differentiate between them. Similarly, if the magnetic properties of the defects are also the same, then one cannot individually manipulate a single defect center. This is potentially even a larger problem, as there are no magnetic monopoles, meaning it is not possible to confine magnetic fields to individually access a single spin in a small volume. There are potential solutions where some of the optical transitions could be shifted with strain gradients [41], and magnetic properties could be shifted with magnetic field gradients [42], or some of the properties can be altered with local electric fields [43]. Another potential solution is using the nearby nuclear, or other, dark impurity spins as extra qubit registers [44]. These 'dark' spin registers can be interfaced with optically accessible spin defects magnetically. These extra registers however are probabilistically distributed within the lattice, and each device would need individual calibration and characterization

to operate, limited by the number of available nearby spins. Overall, the control of the material properties at the nanometer scale remains as the largest issue to be resolved for scalable multi-qubit architectures.

1.4.5 Rare Earth Ions

Lanthanides are a special subset of metals also called rare earth elements. It turns out that the highest energy orbitals, *4f*, are radially closer to the nuclei than some of the lower energy orbitals. When the electrons are filling the orbitals from the lowest energy to the higher ones, there are a few unpaired electrons that remain in the f orbitals shielded by lower energy but radially larger, outer orbitals. This shielding has some important implications. Firstly, the f-f optical transitions of rare earth elements are almost unchanged between various hosts as local environment does not change the energetics of the inner f orbitals. This is especially useful for Erbium 3+ where the transition between the first excited state and the ground state is right in the telecom band regardless of the host material. Therefore, a photon emitted by an Erbium 3+ ion will travel much further than other emitters at other wavelengths through the already existing optical fiber network, relaxing distance requirements for fiberoptic based quantum communication channels. Furthermore rare earth ions can have an unpaired electron within these f-orbitals allowing for a spin qubit that interfaces with the optical transitions, very similar to the defect spins discussed earlier [45].

The two main problems with rare earth ions are excited state lifetimes and again, material preparation. f-f transitions are forbidden, and therefore once a rare earth ion is excited within f-orbitals, it can take up to 10 millisecond for it to decay back [46]. This means that if every single photon could be collected from a system, one could only measure 100 photons per second which is a very low number, especially as there are many inefficiencies involved with capturing single photons. Recently scientists overcame this limitation by building optical cavities, essentially placing an ion between two very good mirrors, to improve the ions interaction with photons which allowed for measurement of single rare earth atoms [47]

and their spin states [48, 49]. The second limitation is that rare earth ions are large compared to atoms that make up mature semiconductors. One can technically incorporate them into common semiconductors like silicon, but the rare earth atoms do not occupy a lattice site due to their size [50]. This technically is not an issue as the ion will continue emitting light if it is in the right charge state. However many optically active ions each with potentially different local symmetry configuration make optically controlling the spins in these hosts challenging [51]. Discovering new material platforms that support rare earths, and developing new host fabrication techniques are pursued aggressively across different groups, and recent demonstration of single spin control of rare earth ions is extremely encouraging. Just like defect centers in the solid state multi-qubit control of closely spaced ions and their individual addressability is still an open question[52].

1.4.6 Other systems

There are a few other qubit systems such as superconducting qubits [53], which rely on a single microwave photon to encode and manipulate quantum information, and quantum dots (also referred as artificial atoms), which use electronic gates to trap single electrons within semiconductors [54]. I will not spend much space discussing these technologies as they are tangential to the rest of the thesis. One thing to note however is that there are companies betting on these technologies such as Intel, Google and IBM. There are even small-scale quantum computers built by Google that demonstrated advantages of quantum computers over classical ones [55] and IBM placed a few similar devices on the cloud, open to anyone to play with as of 2021.

The main advantage of quantum dots and superconducting qubits is that, they are fabricated using the same tools that manufacture our modern electronics. However they also suffer from wiring issues: each qubit requires at least 3 wires which need cooling to dilution fridge temperatures. This could be a limiting factor as the number of qubits reaches the thousands. Material quality is still an active area of research as disorder or strain in

the material caused during growth or fabrication limits reliable qubit manufacturing. Most of the instruments, tools and techniques used in these platforms are shared across other qubit platforms. Generally, technical advances in one of these platforms will advance other platforms as well.

1.4.7 Transition Metal Ions

Transition metal ions are another metal species distinct from the rare-earth ions, with valance electrons filling the d-orbitals. Unlike the f-orbitals of the rare-earth ions, the d-orbitals are not shielded and therefore are highly sensitive to local bond environment (ligands) [56, 57]. These five orbitals have their own unique shapes, and thus their energies are highly dependent on the geometric configuration of the ligand environment with respect to the metal center. This flexibility allows for engineering the energy levels the electrons can occupy, allowing for chemically designing both the spin and optical properties. The tunability of transition metals provide a highly customizable platform where the spin of the electron forms a qubit that can be initialized and read-out optically, very similar to the defect spins we have discussed earlier. As a matter of fact, most of my PhD work investigates these metal centers as defects in semiconductors.

The key difference between transition metal ions and some of the other discussed platforms (defect centers, atoms and rare earth ions) is tunability of both the spin resonance energies of the qubit and its optical interface energy. These parameters for defect spins are determined by the host lattice where they reside. Atoms' and rare earth ions' excitation energies are determined by atomic physics and do not change much. This can be seen as a strength for reliability, or a weakness as an engineering limitation. This trade off is not unique in the engineering world and does not imply one platform is superior over another; these different platforms have different uses. Furthermore, transition metal ions can display the same physics as defects across multiple host crystals [5, 58]. This is generally not the case for other non-rare-earth defects as the host material is responsible for creating the electronic

structure. Furthermore, one technically does not even need a host crystal, as few chemical ligands are sufficient to create a desired electronic structure [1]. Such a system can leverage many of the chemistry and molecular qubit community tools and can overcome qubit initialization and measurement limitations with an engineered optical interface. The tunability of transition metal based molecular qubits can also allow overcoming individual addressability of nearby qubits by engineering different colors for optical and microwave access. All of these properties: portability across multiple hosts, tunability, and atom by atom engineering of electronic structure through chemical synthesis set up transition metal ions as a highly flexible and scalable optically accessible spin qubit platform.

Chapter 2

Quantum Mechanics

In this part, I will assume that the reader has extensive knowledge of linear algebra, complex analysis, differential equations and some familiarity with quantum mechanics. My goal is to build the mathematical machinery that explains the physics of spin qubits and atomic orbitals that will be used to construct the electronic structure of optically addressable spin qubits out of transition metal ions in Chapter 3. This chapter uses many sources including lecture notes, and timeless quantum mechanics textbooks such as Shankar [59] and Sakurai [60].

2.1 Postulates of Quantum Mechanics

The ontology of quantum mechanics is still being debated among physicists and philosophers and the interpretation of the following mathematics is still very much an open question [61]. As far as we know, however, the below description of the universe has held up to many experiments and tests over the last decades and yields accurate predictions. These are the postulates of quantum mechanics, and the physics we will describe are based on these rules:

- *Wavefunction:* The quantum state of a particle is described with a wavefunction called a **ket**, shown with a $|\cdot\rangle$ and labeled with any character in the middle, for example:

$|\psi\rangle$. The wavefunction is a vector in a complex vector space and contains all of the information about the system an observer possibly can obtain. Another way of saying this is, $|\psi\rangle$ is in the space of all possible states a particle can have. By definition this statement already allows for *superposition*, i.e. if $|\psi_1\rangle$, $|\psi_2\rangle$ are two states a particle can have, then $|\psi\rangle = a\,|\psi_1\rangle + b\,|\psi_2\rangle$ where $a, b \in \mathbb{C}$ is also a valid state. Another important note is, the vector space, by definition, has an inner product which maps two vectors in this space to a scalar the following way: $|\phi\rangle \cdot |\psi\rangle = \langle\phi|\psi\rangle = \int \phi^*(x)\psi(x)\mathrm{d}x$ where x is a free parameter indexing over the vectors.

- *Observables:* An observable is a Hermitian operator that maps a ket to another one within the vector space with left multiplication, i.e. $\mathcal{A} : |\psi\rangle \to |\psi'\rangle = \mathcal{A}\,|\psi\rangle$. For every operator, there are special states that do not change except by a scalar, i.e. $\mathcal{A}\,|a_n\rangle = a_n\,|a_n\rangle$ where $a_n \in \mathbb{R}$ and is called an eigenvalue and $|a_n\rangle$ is called an eigenvector. Another property of a Hermitian operator is, the eigenstates are orthogonal to one another and they span the vector space, which means the eigenvectors of an observable form a basis of the vector space.

- *Measurement Results:* The only possible result of a measurement $\mathcal{A}$ is one of its eigenvalues: a_n. This postulate is the basis of quantization of quantum mechanics. For a finite dimensional vector space, there are a finite number of possible eigenvalues, resulting in discrete and quantized measurements.

- *Measurement Probability:* When $\mathcal{A}$ is measured for an arbitrary state $|\psi\rangle$, the probability of measuring a_n is given by $|\,\langle a_n|\psi\rangle\,|^2$ where $|a_n\rangle$ is the eigenvector corresponding to the eigenvalue a_n.

- *Collapse:* When $|\psi\rangle$ is measured to be a_n, the wavefunction $|\psi\rangle$ collapses to $|a_n\rangle$ after the measurement. This is the mathematical description of "measuring alters the quantum state". The probability of measuring $|\psi\rangle$ as a_n was $|\,\langle a_n|\psi\rangle\,|^2$ by the previous postulate, but subsequent measurements of $\mathcal{A}$ will yield a_n with a 100% probability.

- *Time Evolution:* The time evolution of a wavefunction is given by $|\psi(t)\rangle = U(t, t_0)\,|\psi(t_0)\rangle$ where U is a unitary operator: $UU^\dagger = U^\dagger U = 1$. Unitary operators leave the length of a vector unchanged. Say $U\,|\psi\rangle = |\psi'\rangle$, then $|\,\langle\psi'|\psi'\rangle\,|^2 = |\,\langle\psi|\,U^\dagger U\,|\psi'\rangle\,|^2 = |\,\langle\psi|\psi\rangle\,|^2$. Describing time evolution by a unitary operator makes sense, since an observable creates a complete basis set for the vector space, any arbitrary wavefunction can be represented as a superposition of the observable eigenvectors: $|\psi\rangle = \sum c_i\,|a_i\rangle$ where the probability of measuring a_n is $|c_n|^2$. By definition, the measurement probabilities must add up to 1. This means the time evolution should only change the measurement probabilities, leaving the total sum of all possibilities as 1 which is precisely the definition of a unitary operator. Unitary mapping, therefore, can also be interpreted as rotations and we will discuss this more in Sec.2.2.6. Quantum gates are constructed through unitary evolution of a state vector which is a function of time, hence the reason for calibrating quantum gates as time duration.

  One can show that this postulate implies the Schrödinger's Equation:

$$i\hbar\frac{\partial}{\partial t}\,|\psi(t)\rangle = \mathcal{H}\,|\psi(t)\rangle \tag{2.1}$$

  Where $\mathcal{H}$ is called the Hamiltonian and describes the total energy of the system.

2.2 An Example Qubit: Spin

In this part, we will explore a single spin as an example qubit. The step-by-step explanation may seem trivial but I believe it is valuable to carry out for two reasons: firstly, the equations that we will derive here will explain the experimental data later on. Secondly, these dynamics are not unique to spins, and they generally explain any two level quantum system: a qubit.

2.2.1 Energies and Eigenstates

A qubit is a quantum state that lives in a 2 dimensional complex vector space. An arbitrary quantum state, or a wavefunction, can be shown as $|\psi\rangle = \alpha|0\rangle + \beta|1\rangle$, where $\alpha, \beta \in \mathbb{C}$ and $|\alpha|^2 + |\beta|^2 = 1$, with $|0\rangle, |1\rangle$ define a basis for this vector space.

An example two dimensional quantum system is a spin-1/2 particle. Hamiltonian for it under a constant magnetic field in the $\hat{z}$ direction is given by the simple Zeeman interaction Hamiltonian:

$$\mathcal{H} = \mu_B g B_z S_z \tag{2.2}$$

where μ_b is a constant called the Bohr magneton, g is a constant factor that we will discuss in Sec.2.4.2, B_z is the magnitude of the magnetic field applied in the $\hat{z}$ direction, $S_z = \sigma_z/2$, where σ_z is the Pauli matrix and is defined in Sec.A.1. In matrix form:

$$\mathcal{H} = \frac{\mu_B g B_z}{2} \begin{pmatrix} 1 & 0 \\ 0 & -1 \end{pmatrix} \tag{2.3}$$

Per postulates, the only energy we can measure are the eigenvalues of this Hamiltonian. Therefore we need to solve $\mathcal{H}|\psi\rangle = E|\psi\rangle$, where E is a real scalar. This is equivalent to $(\mathcal{H} - \mathcal{I}E)|\psi\rangle = 0$ where $\mathcal{I}$ is the identity matrix for any arbitrary $|\psi\rangle$. This condition is satisfied for an arbitrary $|\psi\rangle$ if $\det(\mathcal{H} - \mathcal{I}E) = 0$. There are two E values that solve this equation $E_\pm = \pm\frac{\mu_B g}{2} B_z$. One can only measure relative energy with respect to some reference point and not absolute values. Therefore a good measurement is the difference between the two energies: $\Delta E = E_+ - E_- = \mu_B g B_z$. A simple unit analysis allows us to define constants in frequency domain as opposed to energy domain with the following definition of $\gamma = g\mu_B/\hbar$, where $\hbar$ is a fundamental constant. Thus we find $\Delta E(B_z) = \gamma B_z \simeq 2.8 B_z$ MHz/Gauss for a free electron which is $g \simeq 2$. This equations shows that for a spin$-1/2$ particle, the energy splitting between two spins increase linearly with magnetic

field. This is a great test of spin measurements as we will see later in this thesis.

For completeness, let's also find the two eigenstates of this Hamiltonian. I will label the eigenstate for E_+ as $|0\rangle$ and E_- as $|1\rangle$. We are solving $\mathcal{H}|0\rangle = E_+|0\rangle$ or, $(\mathcal{H} - \mathcal{I}E)|0\rangle = 0$. Writing this in matrix notation:

$$\left(\begin{pmatrix} E_+ & 0 \\ 0 & E_- \end{pmatrix} - \begin{pmatrix} E_+ & 0 \\ 0 & E_+ \end{pmatrix}\right)\begin{pmatrix} a \\ b \end{pmatrix} = \begin{pmatrix} 0 \\ 0 \end{pmatrix} \tag{2.4}$$

Therefore $-\Delta E b = 0$, so $b = 0$. Knowing the $|0\rangle$ must be normalized, $a = 1$, therefore $|0\rangle = \begin{pmatrix} 1 \\ 0 \end{pmatrix}$. Also knowing that the eigenstates of this Hamiltonian must create a basis for the vector space leaves $|1\rangle = \begin{pmatrix} 0 \\ 1 \end{pmatrix}$.

Putting all of this information together: an arbitrary spin-1/2 wavefunction can only be measured E_- or E_+ and after the measurement, the wavefunction collapses to either $|0\rangle$ or $|1\rangle$ respectively depending on the outcome.

2.2.2 Free Time Evolution

For an eigenstate, there is no time evolution. We can easily observe this from Eq.2.1. For example, assume $|\psi(0)\rangle$ is an eigenstate of an arbitrary $\mathcal{H}$, then $\frac{d}{dt}|\psi(t)\rangle = -i\frac{\mathcal{H}}{\hbar}|\psi(t)\rangle$. Solving this linear equation we get $|\psi(t)\rangle = e^{-i\mathcal{H}t/\hbar}|\psi(0)\rangle$. One can Taylor expand the exponential to get

$$
\begin{aligned}
|\psi(t)\rangle &= \sum_n \left(\frac{-it}{\hbar}\right)^n \mathcal{H}^n |\psi(0)\rangle \\
&= \sum_n \left(\frac{-it}{\hbar}\right)^n E^n |\psi(0)\rangle \\
&= e^{-iEt/\hbar} |\psi(0)\rangle \\
&= e^{-i\gamma B_z t/2} |\psi(0)\rangle = |\psi(0)\rangle
\end{aligned}
\tag{2.5}
$$

In the last step we removed the global phase since it is not measurable. If the initial state is an eigenstate of a Hamiltonian, then the state remains unchanged with time. This statement is tautological, as the physical interpretation of an eigenstate is a stationary one but it is nevertheless a useful demonstration as we will use the same calculation strategy below.

Let's look at what happens if a state is in a superposition instead. Say, our starting state is an equal superposition this time: $|\psi\rangle = (|0\rangle + |1\rangle)/\sqrt{2}$ and we are still working with Hamiltonian Eq.2.3. At $t = 0$ the probability of measuring $E_\pm$ are equal and is $1/2$ per postulates outlined in Sec.2.1. Using the mathematical procedure demonstrated in the previous paragraph, we solve the linear Eq.2.1 and find the time evolution:

$$
\begin{aligned}
|\psi(t)\rangle &= (e^{-iE_+t/\hbar} |0\rangle + e^{-iE_+t/\hbar} |1\rangle)/\sqrt{2} \\
&= (|0\rangle + e^{i\Delta Et/\hbar} |1\rangle)/\sqrt{2} \\
&= (|0\rangle + e^{i\gamma B_z t} |1\rangle)/\sqrt{2}
\end{aligned}
\tag{2.6}
$$

where in the second step we renormalize by a global phase. The probability of measuring $E_\pm$ is unchanged is still $1/2$, but the relative phase between $|0\rangle$ and $|1\rangle$ precesses over time with the frequency γB_z - this is the Larmor precession. We will see that a similar calculation in the *rotating frame* where we change references to follow the Larmor precession,

allows for precise measurements of magnetic field fluctuations in Sec.2.2.4 through Ramsey interferometry.

Next natural question to ask is, how does one actually build the unitary evolution gates? The answer is by driving the system.

2.2.3 Driven Time Evolution

Now along with a main field in the $\hat{z}$ direction, let's also have a rotating magnetic field (e.g. microwaves) with a frequency ω_0. Then our Hamiltonian is:

$$\mathcal{H} = \mu_B g(B_z S_z + B_1(I\cos(\omega_0 t) + Q\sin(\omega_0 t))S_x) \tag{2.7}$$

I and Q are free parameters such that $|I|^2 + |Q|^2 = 1$. They determine the phase of the applied microwave. S_x is the spin matrix defined in Sec.A.2. This appears to be a more complex Hamiltonian since it is time dependent. Some very clever people realized that if we look at this problem in a rotating frame, the time dependence may disappear! Mathematically we use the following assumption: $|\psi\rangle_r = e^{i\omega S_z t}|\psi\rangle_l$ where subscript l denotes the lab frame and r denotes the rotating frame. Plugging this into Eq.2.1 we get:

$$\begin{aligned}
i\hbar\frac{\partial}{\partial t}|\psi\rangle_r &= i\hbar\frac{d}{dt}\left(e^{i\omega S_z t}|\psi\rangle_l\right) \\
&= -\hbar S_z\omega e^{i\omega S_z t}|\psi\rangle_l + e^{i\omega S_z t} i\hbar\frac{d}{dt}|\psi\rangle_l \\
&= -\hbar S_z\omega|\psi\rangle_r + e^{i\omega S_z t}\mathcal{H}|\psi\rangle_l \\
&= -\hbar S_z\omega|\psi\rangle_r + e^{i\omega S_z t}\mathcal{H}e^{-i\omega S_z t}|\psi\rangle_r \\
&= \mathcal{H}_r|\psi\rangle_r
\end{aligned} \tag{2.8}$$

Where:

$$
\begin{aligned}
\mathcal{H}_r &= -\hbar S_z\omega + e^{i\omega S_z t}\mathcal{H}e^{-i\omega S_z t} \\
&= -\hbar\omega S_z + \hbar\gamma e^{i\omega S_z t}\left(B_z S_z + B_1(I\cos(\omega_0 t) + Q\sin(\omega_0 t))S_x\right)e^{-i\omega S_z t} \\
&= -\hbar\omega S_z + \hbar\gamma B_z e^{i\omega S_z t}S_z e^{-i\omega S_z t} + \hbar\gamma B_1(I\cos(\omega_0 t) + Q\sin(\omega_0 t))e^{i\omega S_z t}S_x e^{-i\omega S_z t}
\end{aligned}
\tag{2.9}
$$

In order to solve the above Hamiltonian, we need to solve how S_z and S_x transform under the rotating frame, everything else are just coefficients. To do that we use the relation in Sec.A.2, $e^{i\omega S_z t} = e^{i\omega\sigma_z t/2} = \mathcal{I}\cos(\omega t/2) + i\sigma_z\sin(\omega t/2)$. In matrix form this is:

$$
e^{\pm i\omega S_z t} = \begin{pmatrix} \cos(\omega t/2) \pm i\sin(\omega t/2) & 0 \\ 0 & \cos(\omega t/2) \mp i\sin(\omega t/2) \end{pmatrix} = \begin{pmatrix} e^{\pm i\omega t/2} & 0 \\ 0 & e^{\mp i\omega t/2} \end{pmatrix}
\tag{2.10}
$$

Next, we rewrite the transformation using the matrix representation from Eq. 2.10:

$$
\begin{aligned}
e^{i\omega S_z t}S_z e^{-i\omega S_z t} &= \frac{1}{2}\begin{pmatrix} e^{i\omega t/2} & 0 \\ 0 & e^{-i\omega t/2} \end{pmatrix}\begin{pmatrix} 1 & 0 \\ 0 & -1 \end{pmatrix}\begin{pmatrix} e^{-i\omega t/2} & 0 \\ 0 & e^{i\omega t/2} \end{pmatrix} \\
&= \frac{1}{2}\begin{pmatrix} 1 & 0 \\ 0 & -1 \end{pmatrix} = S_z
\end{aligned}
\tag{2.11}
$$

$$
\begin{aligned}
e^{i\omega S_z t}S_x e^{-i\omega S_z t} &= \frac{1}{2}\begin{pmatrix} e^{i\omega t/2} & 0 \\ 0 & e^{-i\omega t/2} \end{pmatrix}\begin{pmatrix} 0 & 1 \\ 1 & 0 \end{pmatrix}\begin{pmatrix} e^{-i\omega t/2} & 0 \\ 0 & e^{i\omega t/2} \end{pmatrix} \\
&= \frac{1}{2}\begin{pmatrix} 0 & e^{i\omega t} \\ e^{-i\omega t} & 0 \end{pmatrix}
\end{aligned}
\tag{2.12}
$$

We also can rewrite the time varying coefficient in the exponential form:

$$\begin{aligned} I\cos(\omega_0 t) + Q\sin(\omega_0 t) &= I\frac{e^{i\omega_0 t} + e^{-i\omega_0 t}}{2} - iQ\frac{e^{i\omega_0 t} - e^{-i\omega_0 t}}{2} \\ &= e^{i\omega_0 t}\frac{I - iQ}{2} + e^{-i\omega_0 t}\frac{I + iQ}{2} \end{aligned} \tag{2.13}$$

Putting derived Eq. 2.11, 2.12, 2.13, into Eq. 2.9 we get:

$$\begin{aligned} \mathcal{H}_r = \frac{\hbar}{2}\Bigg[& \begin{pmatrix} \gamma B_z - \omega & 0 \\ 0 & -\gamma B_z + \omega \end{pmatrix} \\ & + \gamma B_1 \begin{pmatrix} 0 & e^{i(\omega_0+\omega)t}\frac{I-iQ}{2} + e^{i(\omega-\omega_0)t}\frac{I+iQ}{2} \\ e^{i(\omega_0-\omega)t}\frac{I-iQ}{2} + e^{-i(\omega_0+\omega)t}\frac{I+iQ}{2} & 0 \end{pmatrix} \Bigg] \end{aligned} \tag{2.14}$$

Now, we realize that if we set the rotating frame to be the same as the driving frequency i.e. $\omega = \omega_0$, one of the S_x components time dependence disappears, while a second term emerges that oscillates rapidly with $e^{\pm 2\omega_0 t}$. We will assume that this oscillation is fast and averages to zero in the time scales that we are interested in, hence the name *rotating wave approximation*. After this assumption Eq. 2.14 simplifies to:

$$\begin{aligned} \mathcal{H}_r &= \frac{\hbar}{2}\left[\begin{pmatrix} \gamma B_z - \omega_0 & 0 \\ 0 & -\gamma B_z + \omega_0 \end{pmatrix} + \gamma B_1 \begin{pmatrix} 0 & \frac{I+iQ}{2} \\ \frac{I-iQ}{2} & \end{pmatrix} \right] \\ &= \hbar\left[(\gamma B_z - \omega_0) S_z + \frac{\gamma B_1}{2}\left(I S_x - Q S_y \right) \right] \\ &= \hbar\left[\Delta S_z + A\left(I S_x - Q S_y \right) \right] \end{aligned} \tag{2.15}$$

Where $\Delta = \gamma B_z - \omega_0$ is the detuning from the resonance frequency and $A = \gamma B_1/2$ is the driving strength. As we removed the time dependence from the Hamiltonian in this new

rotating frame, it is easy to solve for the time dependent wavefunction:

$$\begin{aligned} |\psi(t)\rangle_r &= e^{-it[\Delta S_z + A(IS_x - QS_y)]} \, |\psi(0)\rangle_r \\ &= [\mathcal{I}\cos(\Omega t/2) - i(\hat{n}\cdot\vec{\sigma})\sin(\Omega t/2)] \, |\psi(0)\rangle_r \end{aligned} \tag{2.16}$$

Where we once again use the Sec.A.2 with $\Omega = \sqrt{\Delta^2 + A^2(I^2+Q^2)} = \sqrt{\Delta^2 + A^2}$ and $\hat{n} = [\Delta\hat{z} + A(I\hat{x} - Q\hat{y})]/\Omega$. The rotating wave approximation is valid if the Rabi frequency is much slower than the microwave frequency meaning $\Omega << \omega_0$ or more generally $\Delta << \omega_0$ and $A << \omega_0$. We will discuss the geometric interpretation of this time evolution at Sec.2.2.6 after we build the mathematical machinery to understand it.

Now suppose we prepare the state in $|0\rangle_l$ at $t = 0$, and we are interested in seeing what the probability of measuring it in $|1\rangle_l$ as a function of t. Using the postulates:

$$\begin{aligned} P_1(t) &= |_l\langle 1|\psi(t)\rangle_l|^2 \\ &= |_r\langle 1|e^{i\omega_0 t S_z} e^{-i\omega_0 t S_z}|\psi(t)\rangle_r|^2 \\ &= |_r\langle 1|\psi(t)\rangle_r|^2 \\ &= |_r\langle 1|\mathcal{I}\cos(\Omega t/2) - i(\hat{n}\cdot\vec{\sigma})\sin(\Omega t/2)|0\rangle_r|^2 \\ &= \frac{A^2\sin^2(\Omega t/2)}{\Delta^2 + A^2} \end{aligned} \tag{2.17}$$

This function is the crux of the experiments we will talk about later on. Firstly, we observe that when $\Delta = 0$, the probability of measuring $|1\rangle$ oscillates with time $\Omega = A$ which is called a Rabi measurement. Secondly, under continuous driving and measuring conditions $\sin^2(\Omega t/2) \to \varepsilon > 0$ so the probability of measuring $|1\rangle$ is $\propto A^2/(\Delta^2 + A^2)$ which is a Lorentzian function and peaks when $\Delta = 0$ as the driving frequency is swept. This describes a magnetic resonance experiment where the sharpest point of the peak is the resonance frequency precisely because of this mathematical description. We also see that

excess driving power increases the Lorentzian linewidth which is called power broadening.

2.2.4 Ramsey Interferometry

Previously, in the lab frame, we had found that the equal superposition Larmor precessed with frequency γB_z in the lab frame. Let's look at this state in the rotating frame:

$$\begin{aligned}
|\psi(t)\rangle_L &= (|0\rangle_L + e^{i\gamma B_z t}\,|1\rangle_L)/\sqrt{2} \\
|\psi(t)\rangle_R &= (e^{-i\omega_0 t S_z}\,|0\rangle_R + e^{-i\omega_0 t S_z} e^{i\gamma B_z t}\,|1\rangle_R)/\sqrt{2} \\
&= (e^{-i\omega_0 t S_z}\,|0\rangle_R + e^{i\gamma B_z t} e^{-i\omega_0 t S_z}\,|1\rangle_R)/\sqrt{2} \\
&= (e^{-i\omega_0 t/2}\,|0\rangle_R + e^{i\gamma B_z t} e^{i\omega_0 t/2}\,|1\rangle_R)/\sqrt{2} \\
&= (|0\rangle_R + e^{i(\gamma B_z - \omega_0)t}\,|1\rangle_R)/\sqrt{2} \\
&= (|0\rangle_R + e^{i\Delta t}\,|1\rangle_R)/\sqrt{2}
\end{aligned} \tag{2.18}$$

where a global phase is eliminated from step three to four. Looking at the expression above, we observe that if the microwave frequency is resonant with energy splitting ($\Delta = 0$), then the equal superposition is a stationary state. If however, there is a detuning, we expect the time evolution to oscillate with detuning frequency Δ. In its superposition form, this effect cannot be measured, however, it can be measured through interference by mixing the two spin states. This can be achieved with a $\pi/2$ pulse, or a Hadamard gate, H where $H\,|0(1)\rangle_R = (|0\rangle_R \pm |1\rangle_R)/\sqrt{2}$. This is a unitary transformation and can be achieved by turning on the microwave for a specific duration. After this transformation, the new state is

$$|\psi(t)\rangle_R = \left(\frac{1 + e^{i\Delta t}}{2}\,|0\rangle_R\right) + \left(\frac{1 - e^{i\Delta t}}{2}\,|1\rangle_R\right) \tag{2.19}$$

The probability of measuring $|0\rangle$ is:

$$
\begin{aligned}
P_0(t) &= |_L \langle 0|\psi(t)\rangle_L|^2 \\
&= \left|_R \langle 0| e^{i\omega_0 t S_z} e^{-i\omega_0 t S_z} |\psi(t)\rangle_R\right|^2 \\
&= |_R \langle 0|\psi(t)\rangle_R|^2 \\
&= \left(\frac{1+e^{-i\Delta t}}{2}\right)\left(\frac{1+e^{i\Delta t}}{2}\right) \\
&= \frac{1+\cos(\Delta t)}{2}
\end{aligned}
\tag{2.20}
$$

The probability of measuring $|0\rangle$ oscillates with the detuning frequency. This is the crux of many quantum sensing schemes. When an effect changes the energy between the two qubit states, the qubit becomes off resonant with respect to the microwave pulses, which then can be measured as Ramsey oscillations. This can be used to sense both field induced effects (e.g. magnetic fields) as well as time keeping to calibrate the microwave source.

2.2.5 Bloch Sphere

In the previous section, we had talked about a qubit as a state living in a 2-dimensional complex vector space and used a spin-1/2 as an example to show how to calculate eigenvalues (energies) and the eigenstates they correspond to and how to use Schrödinger equation to solve for time evolution of states and measurement probabilities for both under constant magnetic field and time dependent magnetic field. In this section we are going to use the Bloch Sphere representation to geometrically visualize these concepts.

We recall that a qubit is mathematically represented as $|\psi\rangle = \alpha|0\rangle + \beta|1\rangle$, where $\alpha, \beta \in \mathbb{C}$ and $|\alpha|^2 + |\beta|^2 = 1$ per our postulates. We also recall from complex algebra that any complex number $c = a + ib = re^{i\varphi}$ where $a, b, r, \varphi \in \mathbb{R}$. Therefore $|\psi\rangle = r_\alpha e^{i\varphi_\alpha}|0\rangle + r_\beta e^{i\varphi_\beta}|1\rangle$, where $r_\alpha, r_\beta, \varphi_\alpha, \varphi_\beta \in \mathbb{R}$. Since global phases are not measurable quantities, we can rewrite $|\psi\rangle = r_\alpha|0\rangle + r_\beta e^{i\varphi}|1\rangle$, where $\varphi = \varphi_\beta - \varphi_\alpha$. Now let $r_\alpha = z$, $r_\beta e^{i\varphi} = x + iy$, then we have $|\psi\rangle = z|0\rangle + (x+iy)|1\rangle$. Using the normalization, we can further constrain these parameters,

$z^2 + x^2 + y^2 = 1$ - we immediately recognize this is the formula of a spherical surface in 3-dimensions with radius 1! We can use the spherical transformation outlined in Sec.A.1.3:

$$x = \sin\theta' \cos\varphi \qquad y = \sin\theta' \sin\varphi \qquad z = \cos\theta'$$

$$\begin{aligned} |\psi\rangle &= z\,|0\rangle + (x + iy)\,|1\rangle \\ &= \cos\theta'\,|0\rangle + \sin\theta'(\cos\varphi + i\sin\varphi)\,|1\rangle \\ &= \cos\theta'\,|0\rangle + \sin\theta' e^{i\varphi}\,|1\rangle \end{aligned} \tag{2.21}$$

In this formalism, we realize that there is a problem. The spherical coordinates are bound by $0 \leq \theta' < \pi, 0 \leq \varphi < 2\pi$. Let's say $|\psi\rangle = \cos\theta'\,|0\rangle + \sin\theta' e^{i\varphi}\,|1\rangle$ and let $|\psi'\rangle$ be the opposite point at $(\pi - \theta', \varphi + \pi)$, i.e.

$$\begin{aligned} |\psi'\rangle &= \cos\big(\pi - \theta'\big)\,|0\rangle + \sin\big(\pi - \theta'\big) e^{i(\varphi+\pi)}\,|1\rangle \\ &= -\cos\theta'\,|0\rangle + \sin\theta' e^{i\varphi} e^{i\pi}\,|1\rangle \\ &= -\cos\theta'\,|0\rangle - \sin\theta' e^{i\varphi}\,|1\rangle = -\,|\psi\rangle \end{aligned} \tag{2.22}$$

These two states only by a global phase which is not measurable, meaning there is a redundancy between the states mapped to the top hemisphere and the bottom hemisphere. We can overcome this redundancy by $\theta = 2\theta'$. This parameterization allows us to describe any qubit with two real numbers $0 \leq \theta < \pi$ and $0 \leq \varphi < 2\pi$ by

$$|\psi\rangle = \cos\left(\frac{\theta}{2}\right)|0\rangle + e^{i\varphi}\sin\left(\frac{\theta}{2}\right)|1\rangle \tag{2.23}$$

The above form paints a nice geometric picture, where the surface of the Bloch sphere represents the 2-dimensional complex vector space, and an arbitrary $|\psi\rangle$ can be shown as a point on it. There is also a canonical relationship between the Bloch sphere and the Pauli

matrices. An important question to ask is, what is the probability of measuring $|\psi\rangle$ in the direction $|u\rangle$? This is given by $|\langle u|\psi\rangle|^2 = \langle\psi|u\rangle\langle u|\psi\rangle = \langle\psi|\mathcal{P}_u|\psi\rangle$ where $\mathcal{P}_u$ is the projection operator of $|u\rangle$. It returns a vector in the direction $|u\rangle$ with the length of the projection of the vector $|\psi\rangle$ in that direction, i.e. $\langle u|\psi\rangle$. Since $|u\rangle = \cos\left(\frac{\theta}{2}\right)|0\rangle + e^{i\varphi}\sin\left(\frac{\theta}{2}\right)|1\rangle$ for some θ, φ, this projection operator can be written as:

$$
\begin{aligned}
\mathcal{P}_u &= |u\rangle\langle u| \\
&= \begin{pmatrix} \cos\left(\frac{\theta}{2}\right) & e^{-i\varphi}\sin\left(\frac{\theta}{2}\right) \end{pmatrix} \begin{pmatrix} \cos\left(\frac{\theta}{2}\right) \\ e^{i\varphi}\sin\left(\frac{\theta}{2}\right) \end{pmatrix} \\
&= \begin{pmatrix} \cos^2\left(\frac{\theta}{2}\right) & e^{-i\varphi}\sin\left(\frac{\theta}{2}\right)\cos\left(\frac{\theta}{2}\right) \\ e^{i\varphi}\sin\left(\frac{\theta}{2}\right)\cos\left(\frac{\theta}{2}\right) & \sin^2\left(\frac{\theta}{2}\right) \end{pmatrix} \\
&= \begin{pmatrix} 1+\cos\theta & e^{-i\varphi}\sin\theta \\ e^{i\varphi}\sin\theta & 1-\cos\theta \end{pmatrix} \\
&= \frac{1}{2}\begin{pmatrix} 1+\cos\theta & \cos\phi\sin\theta - i\sin\phi\sin\theta \\ \cos\phi\sin\theta + i\sin\phi\sin\theta & 1-\cos\theta \end{pmatrix} \\
&= \frac{1}{2}\left(\mathcal{I} + \sin\theta\cos\phi\sigma_x + \sin\theta\sin\phi\sigma_y + \cos\theta\sigma_z\right) \\
&= \frac{1}{2}\left(\mathcal{I} + \hat{n}\cdot\vec{\sigma}\right)
\end{aligned}
\tag{2.24}
$$

Where $\hat{n} = (\sin\theta\cos\phi, \sin\theta\sin\phi, \cos\theta) = (x, y, z)$, by spherical coordinate transformation. How do we interpret this relation? It means that the probability of measuring any $|\psi\rangle$ in the direction of $|u\rangle$ on the Bloch sphere can be decomposed as separate measurements of $\sigma_x, \sigma_y, \sigma_z$ with weights (x, y, z) normalized. Therefore σ_i can be thought of as the axes that define the Bloch sphere. And the 6 corner points are the eigenvectors of the corresponding σ_i. I will also note that this projection operator has another interpretation called a density matrix, and this formalism allows for ensemble calculations of quantum states, but we will not go into its details of density matrices in this thesis.

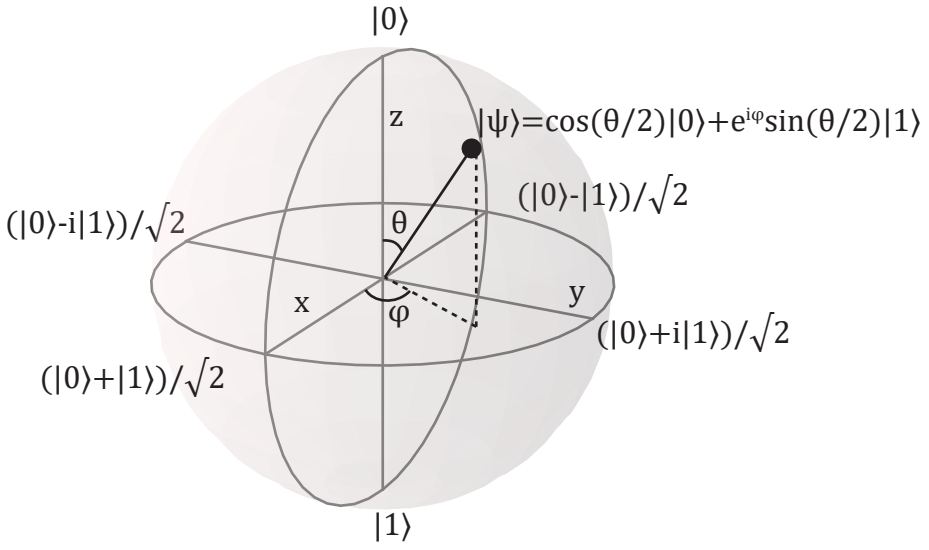

Figure 2.1: Bloch sphere can visually represent a qubit with two independent parameters θ, ϕ where the 3-space x, y, z axes correspond the the projection of the wavefunction on $\sigma_x, \sigma_y, \sigma_z$ operators. Therefore, the six corners are the eigenstates of the Pauli operators.

2.2.6 Rabi driving visualized on a Bloch sphere

We are interested in understanding the time evolution of the driven states where we had derived the Eq.2.16. I claim that this is a rotation about $\hat{n}$ with a frequency Ω. To prove this claim, we need to show three things:

1. The $|\psi(t)\rangle$ is contained on the surface of the Bloch sphere: this is true by the unitary nature of the allowed transformation. We can demonstrate this easily

$$|\langle\psi(t)|\psi(t)\rangle|^2 = |\langle\psi(0)| e^{it(\hat{n}\cdot\vec{\sigma})} e^{-it(\hat{n}\cdot\vec{\sigma})} |\psi(0)\rangle|^2 = |\langle\psi(0)|\psi(0)\rangle|^2 = 1 \tag{2.25}$$

2. Eq.2.16 is a periodic function (a rotation), with frequency Ω, which is also easy to observe as the transformation will be the identity matrix (up to a phase) when $\Omega = 2k\pi/t$ for $k \in \mathrm{N}$.

3. Finally, we had claimed that the rotation is by $\hat{n}$ - this is true only if the projection

of the state $|\psi(t)\rangle$ on $|n\rangle$ (the vector pointing in $\hat{n}$) is always the same for all times t. We are going to prove this by using the derived identity in Eq.2.24:

$$\begin{aligned}
\mathcal{P}_n |\psi(t)\rangle &= \frac{1}{2}(\mathcal{I} + \hat{n}\cdot\vec{\sigma})\left[\mathcal{I}\cos(\Omega t/2) - i(\hat{n}\cdot\vec{\sigma})\sin(\Omega t/2)\right]|\psi(0)\rangle \\
&= \frac{1}{2}\left[\mathcal{I}\cos(\Omega t/2) - i(\hat{n}\cdot\vec{\sigma})\sin(\Omega t/2)\right. \\
&\quad \left. +(\hat{n}\cdot\vec{\sigma})\cos(\Omega t/2) - i(\hat{n}\cdot\vec{\sigma})^2\sin(\Omega t/2)\right]|\psi(0)\rangle \\
&= \frac{1}{2}\left[\mathcal{I}e^{-i\Omega t/2} + (\hat{n}\cdot\vec{\sigma})e^{-i\Omega t/2}\right]|\psi(0)\rangle \\
&= \frac{e^{-i\Omega t/2}}{2}\left[\mathcal{I} + (\hat{n}\cdot\vec{\sigma})\right]|\psi(0)\rangle \\
&= e^{-i\Omega t/2}\mathcal{P}_n|\psi(0)\rangle = \mathcal{P}_n|\psi(0)\rangle
\end{aligned} \tag{2.26}$$

Where we used $(\hat{n}\cdot\vec{\sigma})^2 = 1$ identity from the second line to the third, and in the last equality we removed a global phase. This precisely says that any time dependent evolution of $|\psi(t)\rangle$ projects to $|n\rangle$ the same way $|\psi(0)\rangle$ projects on $|n\rangle$. The mathematical interpretation of this result is a circle whose center point is on the line in the direction of $\hat{n}$.

Putting the above three points together, helps use visualize what is happening to the spin vector on the Bloch sphere during Rabi driving. We understand Eq.2.16 as a time dependent rotation about an axis $\hat{n} = \Delta\hat{z} + A(I\hat{x} - Q\hat{y})$ with an angle Ωt, where $\Omega = \sqrt{A^2 + \Delta^2}$ is the rotation frequency. When the driving frequency ω_0 matches the γB_z (resonance), or $\Delta = 0$ then the spin only precesses by the $\hat{x}(\hat{y})$ axis if $Q(I) = 0$ with frequency A, linearly depending on the magnetic driving field strength. Therefore the I, Q control of the microwaves allow rotation axis control of the spin while, detuning both shrinks the angle at which we are rotating by and adds a $\hat{z}$ component to it. This 3-axis control around the Bloch sphere combined with the microwave duration knob, t, allows us to evolve the spin wavefunction anywhere around the Bloch sphere, giving a full qubit control. These knobs span the Bloch sphere which building any unitary gate such as H used in Sec.2.2.4.

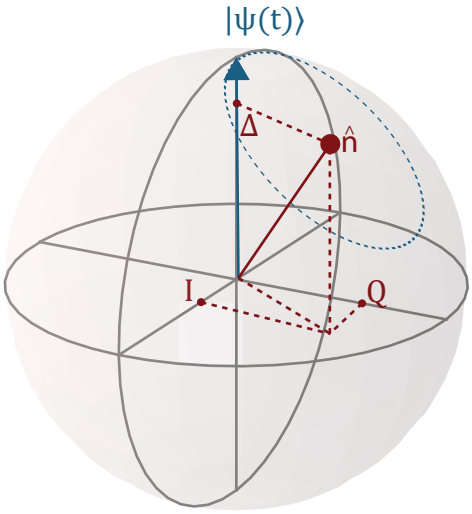

Figure 2.2: Rabi driving visualized on Bloch sphere. A wavefunction starting at $|0\rangle$ under driving rotates around a circle on the Bloch sphere (blue dotted trace) whose center is $\hat{n} = \Delta\hat{z} + A(I\hat{x} - Q\hat{y})$ (red dot). The rotation frequency (not shown) is $= \sqrt{A^2 + \Delta^2}$ where A is the driving power.

2.3 Multiple Qubits

So far we have only investigated a single qubit. In nature, however, there are many quantum systems and they interact with each other, so we need to be able to describe them mathematically. This formalism is also useful in the context of computation as we need to describe multi-qubit architectures mathematically to build useful quantum devices.

The mathematics of describing multiple qubits is straightforward. If there are two quantum states $|\psi_1\rangle \in \mathscr{H}_1$ and $|\psi_2\rangle \in \mathscr{H}_2$, where $\mathscr{H}_{1,2}$ are square integrable complex vector (Hilbert) spaces that host quantum states, then the composite quantum state vector $|\psi_1\rangle \otimes |\psi_2\rangle \in \mathscr{H}_1 \otimes \mathscr{H}_2$ where $\mathscr{H}_1 \otimes \mathscr{H}_2$ is also a Hilbert space. Sometimes, as a short hand notation $|\psi_1\rangle \otimes |\psi_2\rangle$ can be written as $|\psi_1\psi_2\rangle$. If operators $U_{1,2}$ act on $|\psi_{1,2}\rangle$, then the operator $U_1 \otimes U_2$ acts on $|\psi_1\rangle \otimes |\psi_2\rangle$ as $(U_1 \otimes U_2)(|\psi_1\rangle \otimes |\psi_2\rangle) = U_1 |\psi_1\rangle \otimes U_2 |\psi_2\rangle$.

The measurements also work analogous to the single quantum system. If only $|\psi_1\rangle$ is measured for observable A_1 out of the composite state $|\psi_1\psi_2\rangle$, to be a_{1i}, the new system

after the measurement is the renormalized projection on $|a_{1i}\rangle$ - the eigenvector corresponding to the measured energy of A_1. For example let:

$$\left|\Phi^+\right\rangle = \frac{1}{\sqrt{2}}\left(|00\rangle + |11\rangle\right) \tag{2.27}$$

The probability of measuring 0 for the first particle is calculated by looking at the projection of the system in that eigenvector:

$$\begin{aligned} P_1(0) &= \left\langle\Phi^+\right| \left(|0\rangle\langle 0| \otimes \mathcal{I}\right) \left|\Phi^+\right\rangle \\ &= \frac{1}{2}\left(\langle 0|0\rangle\langle 0|0\rangle \otimes \langle 0|0\rangle\langle 0|0\rangle + \langle 1|0\rangle\langle 0|1\rangle \otimes \langle 1|1\rangle\langle 1|1\rangle\right) = \frac{1}{2} \end{aligned} \tag{2.28}$$

So the probability of measuring the first quantum particle in 0 is 1/2. One can carry a very similar calculation to see that the probability of measuring $|\psi_2\rangle$ as 0 is also 1/2. After measuring the first particle as 0, however, the wavefunction collapses to the renormalized projection:

$$\begin{aligned} \left|\psi'\right\rangle &= \frac{\left(|0\rangle\langle 0| \otimes \mathcal{I}\right)\left|\Phi^+\right\rangle}{\sqrt{\left\langle\Phi^+\right| \left(|0\rangle\langle 0| \otimes \mathcal{I}\right) \left|\Phi^+\right\rangle}} \\ &= \frac{1/\sqrt{2}(\langle 0|0\rangle\,|0\rangle \otimes |0\rangle + \langle 0|1\rangle \otimes |1\rangle)}{1/\sqrt{2}} = |00\rangle \end{aligned} \tag{2.29}$$

In this case, we find that the probability of measuring the second quantum state after measuring the first one as 0 as also 0 all the time; the measurement of the first quantum state collapsed the wavefunction of the second one! This is one of the non intuitive results of quantum mechanics. We got this result, for this particular wavefunction, because it describes an *entangled* quantum state. Famously Einstein described entanglement as *spooky action at a distance*, measuring one particle immediately effects another one regardless of how far apart they are. This effect is non-intuitive because we are used to thinking that

the physical properties of particles must be where the particles are, i.e. locality. Quantum mechanics allows for distributing properties over many particles. In a sense, the idea that the measurement is only on the first quantum particle is misleading which causes the confusion and the awe about quantum entanglement. The reality is that the measurement is on the system and the system is made out of these two particles transcending locality, therefore the second particle is also affected.

Entanglement is the cause of many complexities in nature and also a resource for technology. When modeling nature, looking at individual particles is not sufficient, as one needs to model the entire isolated system. This makes a problem exponentially harder - hence the need for a quantum computer for accurate description of quantum mechanical systems like chemistry. One way to understand *decoherence* is - nature can get entangled with a qubit and then collapse it through measurement. This ties back to the discussion in Sec.1.4. Entanglement can also be a resource for encryption, since measurement can effect multiple qubits at different locations, one can measure the existence/absence of eavesdroppers to create secret shared keys. This non-local property of quantum systems also raise philosophical questions about the nature of information, and what it means to do a computation on an aggregate system made out possibly of many entangled computers all across the globe and potentially the space.

Now that we know how to mathematically describe larger dimensional Hilbert spaces out of smaller ones, we will investigate how to describe multi-electron systems that will form the basis of the spin qubits.

2.3.1 Two Identical Particles

Let $|ab\rangle$ be a quantum state for two particles where the first particle is state a and the second one is state b for a measurement basis, say $S_{z1,2}$. If the particles are distinguishable, then the state $|ba\rangle$ is a different state than $|ab\rangle$. In the first measurement we can definitively measure particle-1(2) as a(b) and in the second scenario as b(a). If however these two particles are

indistinguishable, it is not possible to measure a difference under their exchange. In the indistinguishable scenario, the two wavefunctions can at most differ by an immeasurable global phase: $|ab\rangle = e^{i\phi}|ba\rangle$.

We still can measure a sum however $S_{z1} + S_{z2}$. There are two eigenvectors with the same eigenvalue $|ab\rangle$ and $|ba\rangle$. So a good question to ask is, what is the state vector of $S_{z1} + S_{z2}$ basis? It must be composed of a linear combination of $|ab\rangle$ and $|ba\rangle$. Without loss of generality, we can label this eigenstate as $|\psi(a,b)\rangle$. We can see what happens under the exchange to this state vector:

$$\begin{aligned} |\psi(a,b)\rangle &= \alpha|ab\rangle + \beta|ba\rangle \\ &= e^{i\phi}(\alpha|ba\rangle + \beta|ab\rangle) \\ &= e^{i\phi}|\psi(b,a)\rangle \end{aligned} \tag{2.30}$$

So we find $\alpha = e^{i\phi}\beta$ and $\beta = e^{i\phi}\alpha$. Which means $\alpha = e^{2i\phi}\alpha$ and therefore $\phi = \pi, 2\pi$. Just from this simple argument we find that the state vector for two indistinguishable particles either need to be symmetric: $|\psi(a,b), S\rangle = (|ab\rangle + |ba\rangle)/\sqrt{2}$ or antisymmetric: $|\psi(a,b), A\rangle = (|ab\rangle - |ba\rangle)/\sqrt{2}$.

A given species of particles must either be once and for all symmetric or antisymmetric. If this was not true, then one could build a $|\psi(a,b)\rangle = \alpha|ab, S\rangle + \beta|ab, A\rangle$ which is neither symmetric or antisymmetric and contradicts the above calculation. Therefore a composite Hilbert space $\mathscr{H} = \mathscr{H}_S \oplus \mathscr{H}_A$ can be decomposed into linearly independent symmetric and antisymmetric Hilbert subspaces, where $\oplus$ denotes the direct sum of vector spaces. The particles that occupy the symmetric subspace are called Bosons (e.g. photons) and the ones that occupy the antisymmetric subspace are called Fermions (e.g. electrons). In this thesis we will be dealing with the properties of electrons mostly, therefore I will not discuss Bosons and their properties any further.

2.3.2 Pauli Exclusion Principle

Let's look at what happens if $a = b$ for a Fermionic wavefunction $|\psi(ab, A)\rangle = |\psi(aa, A)\rangle = |aa\rangle - |aa\rangle = 0$. This means two identical Fermions cannot occupy the same quantum state! This is also known as the Pauli exclusion principle and the explains why there are at most 2 electrons allowed in each atomic orbital (one spin up and one spin down), extended structures made out of atoms such as tables and humans and their chemistry.

2.3.3 Multi Electron Spins

Finally, let's investigate a specific case as an example. Suppose we have two electrons (identical Fermions) and two spatial quantum states they can occupy (e.g. an atomic orbital). Therefore in this system, each particle has two quantum degrees of freedom, the orbital $\omega_{1,2}$ and spin state $s_{1,2}$. The wavefunction of this system must be antisymmetric due to Fermionic nature of electrons and is

$$|\omega_1 s_1, \omega_2 s_2, A\rangle = (|\omega_1 s_1, \omega_2 s_2\rangle - |\omega_2 s_2, \omega_1 s_1\rangle)/\sqrt{2} \tag{2.31}$$

This wavefunction is allowed only when either the spin or the orbital components are antisymmetric. If they are both antisymmetric, each component picks up a minus sign under the exchange, making the whole wavefunction symmetric which is not allowed for Fermions. For this particular example, there are 6 such states. Assuming 'orbital' wavefunctions are independent of the 'spin' wavefunctions[1] we can write the allowed state as:

1. This is the low spin-orbit regime. The new eigenstates must be diagonalized if the spin and orbital degrees of freedom are mixed

$$|\omega_1 s_1, \omega_2 s_2, A\rangle = \begin{cases} |\omega_1\omega_2, A\rangle \otimes |s_1 s_2, S\rangle & = |\omega_1\omega_2, A\rangle \otimes \begin{cases} |+1/2, +1/2\rangle \\ (|+1/2, -1/2\rangle + |-1/2, +1/2\rangle)/\sqrt{2} \\ |-1/2, -1/2\rangle \end{cases} \\ |\omega_1\omega_2, S\rangle \otimes |s_1 s_2, A\rangle & = \begin{cases} |\omega_1\omega_1\rangle \\ (|\omega_1\omega_2\rangle + |\omega_2\omega_1\rangle)/\sqrt{2} \\ |\omega_2\omega_2\rangle \end{cases} \otimes |s_1 s_2, A\rangle \end{cases} \tag{2.32}$$

The antisymmetric orbital with symmetric spin has three possible spin values of $S_z = S_{z_1} + S_{z_2}$, which are $m_s = 1, 0, -1$. This is a total spin-1 system and is called a triplet. Conversely, the symmetric orbital with anti-symmetric spin part of the wavefunction only has one S_z outcome and it is $m_s = 0$, therefore it is a total spin-0 system and is called a singlet. This is the electronic structure we use to construct optically addressable spin qubits out of transition metal ions. Specifically the spin-1 manifold is the spin qubit ground state and the spin-0 states are the higher excited states that that allow for the optical access of the spin qubit.

2.4 Spatial Hamiltonian

Now that we have mastered the electron spin, we would like to explore how we can localize it to use it as a resource for quantum technologies. In the previous section we just assumed the existence of two orbitals which allowed us to build a spin triplet and a bunch of spin singlet systems. As we will see later the spin triplet part will be our spin qubit and its transition to spin singlet manifolds will enable the optical control of the spin. The question we want to answer here is, how does one actually get these orbitals, and what do they look like? This discussion will be crucial for our effort of using valance electrons of transition metal ions to

engineer electronic structures that can be used as an optically addressable qubit.

Atoms are made out of positively charged nuclei and some electrons 'orbiting' around. The nuclear positive charge at the core is uniform. There is not an inherent orientation to an atom in a vacuum or another way of saying this is, the system is rotationally symmetric. Therefore the electronic wavefunction must be rotationally symmetric as well. As we will see later when we discuss ligand fields, the existence of nearby charges can introduce new symmetries which further constrain the electronic wavefunction. These point charges, their symmetry, electric field strength (or bond strength) will allow the engineering of electronic structures. To understand all of this physics (or chemistry), we need to first study rotational invariance and what these orbitals look like.

2.4.1 Rotational Symmetry

The purpose of this section is two-fold: (i) demonstrate an example of how the symmetry of a system translates into a symmetry of the wavefunction and (ii) get a qualitative sense to what atomic orbitals look like which will help us build intuition about electronic configuration engineering. To start, we will discuss a hydrogen like atom.

We want to solve the Schrödinger's equation for a radially symmetric system. The total energy of the system is the kinetic energy given by $P^2/2m$, where P is momentum operator and m is mass and a potential energy $V(r)$ that is radially symmetric and therefore only depends on radius r. We will see that there are a few quantized numbers/labels that define the solutions to $H\psi = E\psi$ for this problem. One strategy we will employ is finding states that are simultaneous eigenstates of both H and some measurable quantity. As we see in Sec.A.2 if two operators commute, they share eigenvectors, and therefore it is sufficient to find eigenvectors of only one of the operators. We will employ this technique to construct the wavefunctions of the Hamiltonian. This is a commonly used strategy in quantum mechanics and we will revisit it when we discuss other point symmetries later on. For the radially symmetric wavefunction, one symmetry preserving measurable quantity that also commutes

with the Hamiltonian is angular momentum, therefore finding its eigenvectors should help us solve what happens in radially symmetric problem. For that we need to find angular momentum operators.

The position operator is $X = \vec{x}$ and the momentum operator in space is $P = -i\hbar$. As a sanity check, we can confirm the definitions of these operators by observing how they act on a plane wave particle with the wavefunction: $\psi = \exp(i(\vec{x}\cdot\vec{p} - Et)/\hbar)$ where $\vec{x}$ and $\vec{p}$ are the position and momentum vectors, E is the energy and t is the time evolution. By definition, this free particle wavefunction is normalized, it is in a wave-like form and the units work out in a physical and expected way. The position operator $X = \vec{x}$ acts in the obvious way: $X\psi = \vec{x}\psi$ - and hence $\vec{x}$ is the eigenvalue and therefore the measurement outcome. After some algebra, we find the eigenvalue of the momentum operator $P\psi = -i\hbar\nabla\exp(i(\vec{x}\cdot\vec{p} - Et)/\hbar) = \vec{p}\exp(i(\vec{x}\cdot\vec{p} - Et)/\hbar) = \vec{p}\psi$ - to be $\vec{p}$ and therefore confirming that P indeed measures the momentum. We will now use these operators to build angular momentum operator L.

We recall from classical mechanics that angular momentum $\tau = \vec{x}\times\vec{p}$. Similarly we can build the observable

$$L_z = XP_y - YP_x = -i\hbar\left(x\frac{\partial}{\partial y} - y\frac{\partial}{\partial x}\right) = -i\hbar\frac{\partial}{\partial\phi} \tag{2.33}$$

after a spherical coordinate transformation (Sec.A.1.3). There exists an eigenvalue l_z for an eigenvector $|l_z\rangle$ of this operator such that $L_z|l_z\rangle = l_z|l_z\rangle$. To find it, let's write the wavefunction in spherical coordinates:

$$-i\hbar\frac{\partial\psi_{l_z}(\rho,\theta,\phi)}{\partial\phi} = l_z\psi_{l_z}(\rho,\theta,\phi) \qquad \rightarrow \qquad \psi_{l_z}(\rho,\theta,\phi) = \Phi(\rho,\theta)e^{il_z\phi/\hbar} \tag{2.34}$$

We can further constrain this problem. Because of the rotational symmetry, we must have $\psi_{l_z}(\rho,\theta,0) = \psi_{l_z}(\rho,\theta,2\pi)$ this means that $e^{i2\pi l_z/\hbar} = 1$ or $l_z = m\hbar$ where $m = 0, \pm1, \pm2, ...$

$$\psi_{l_z}(\rho, \theta, \phi) = \Phi(\rho, \theta) e^{im\phi} \tag{2.35}$$

m is the magnetic quantum number of the system. It is very cumbersome to write everything in coordinate form when the problem we are dealing with is radially symmetric. Therefore by finding these quantum numbers, we can form a wavefunction that is an eigenvalue of the physical description of the system. We just found one such operator L_z and its eigenvalue $m\hbar$. One can easily show that $L_{x,y,z}$ do not commute with each other, which means they cannot be diagonalised simultaneously, which means we cannot use l_x, l_y as a quantum number if we are using l_z.

L_z in itself is not sufficient to talk about the total angular momentum - it is just a projection of the total angular momentum in the $\hat{z}$ direction. Even though we cannot simultaneously diagonalize the individual components, we can look at the total angular momentum. It is customary to talk about $L^2 = L_x^2 + L_y^2 + L_z^2$ as opposed to just L. With some algebra one can show that L^2 commutes with spherically invariant wavefunction and L_z. Therefore, there must exist a simultaneous eigenvector for both L_z and L^2 that we can label as $|\lambda m\rangle$ such that $L^2 |\lambda m\rangle = \lambda\hbar^2 |\lambda m\rangle$, $L_z |\lambda m\rangle = m\hbar |\lambda m\rangle$, then we find the following relation:

$$\begin{aligned} \langle \lambda m | L^2 - L_z^2 | \lambda m \rangle &= \langle \lambda m | L_x^2 + L_y^2 | \lambda m \rangle \geq 0 \\ &= \hbar^2 (\lambda - m^2) \end{aligned} \tag{2.36}$$

the inequality follows from $L_x^2 + L_y^2$ being positive definite. This means that $\lambda \geq m^2$ and this relation makes sense since the total angular momentum must be greater than its projection to a single axis. To find the exact relationship between the two quantum numbers, we define raising and lowering operators $L_\pm = L_x \pm iL_y$. Since L^2 commutes with each one of the $L_{x,y,z}$, and $[L_i, L_j] = i\hbar\varepsilon_{ijk}L_k$, where $i, j, k \in \{x, y, z\}$ - with a little bit of algebra one can show that:

$$
\begin{aligned}
[L^2, L_\pm] &= 0 \\
[L_z, L_\pm] &= \pm\hbar L_\pm
\end{aligned}
\tag{2.37}
$$

We see two interesting things with these operators:

$$
\begin{aligned}
L^2 L_\pm |\lambda m\rangle &= L_\pm L^2 |\lambda m\rangle = \lambda L_\pm |\lambda m\rangle \\
L_z L_\pm |\lambda m\rangle &= (L_\pm L_z \pm \hbar L_\pm) |\lambda m\rangle = \hbar(m \pm 1) L_\pm |\lambda m\rangle
\end{aligned}
\tag{2.38}
$$

The first relation says that the $L_\pm$ operator leaves L^2 virtually unchanged, while the L_z eigenvalue for $L_\pm |\lambda m\rangle$ is $\hbar(m \pm 1)$, which is the same eigenvalue for $|\lambda(m \pm 1)\rangle$ - meaning $L_\pm$ raised (lowered) the L_z's quantum number by $m\hbar$, hence the operators name. Finally, since we know that there is an upper limit to how much m can be raised, for a $m^2 \leq \lambda$ let k be the smallest possible integer such that, $L_+^k |\lambda m\rangle = 0$. Then we have:

$$
\begin{aligned}
0 &= L_- L_+^{k+1} |\lambda m\rangle = L_- L_+ L_+^k |\lambda m\rangle \\
&= \left(L_x - iL_y\right)\left(L_x + iL_y\right) |\lambda(m+k)\rangle \\
&= L_x^2 + L_y^2 + iL_xL_y - iL_yL_x |\lambda(m+k)\rangle \\
&= L^2 - L_z^2 + i[L_x, L_y] |\lambda(m+k)\rangle \\
&= L^2 - L_z^2 - L_z |\lambda(m+k)\rangle = \hbar^2 \left[\lambda - (m+k)^2 - (m+k)\right]
\end{aligned}
\tag{2.39}
$$

This yields a direct relation between the quantum numbers λ, m. Let $l = m + k$, then $\lambda = l(l+1)$ - since it is easier to keep track of l as opposed to λ, the conventional quantum number used for angular momentum is l, and states can be labeled as $|lm\rangle$ instead where $L^2 = \hbar^2 l(l+1) |lm\rangle$. This also means that $-l \leq m \leq l$, where the lower bound comes from a very similar argument as above in the opposite direction.

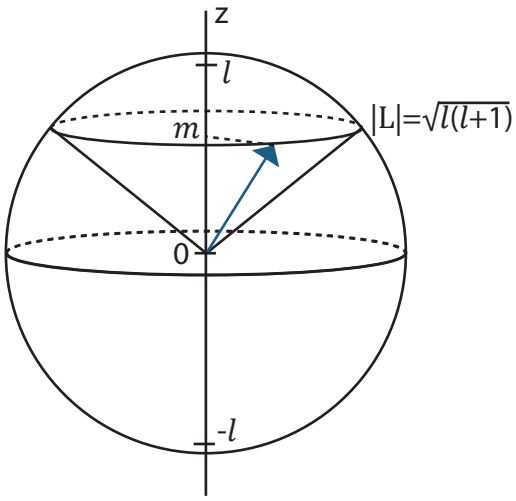

Figure 2.3: Representation of angular momentum of $|lm\rangle$. The total angular momentum L can be interpreted as the surface of a sphere, and the z-projection of the angular momentum vector (blue arrow) is m. Because l_x, l_y cannot be diagonalized simultaneously with l_z their projections are unknown, therefore $|lm\rangle$ has a circular representation.

For each angular momentum l, there are $2l+1$ magnetic numbers m. By Pauli's exclusion principle discussed in Sec.2.3.2, each electron can have two spin states, so there are $2m$ possible states for each l state of an electron. These l numbers are the electronic orbitals that are generally taught in basic chemistry with orbital notations such as s, p, d and f. For example the s orbital is $l = 0$ configuration and therefore $m = 0$, so it can only hold 2 electrons, p is $l = 1$ configuration, has 3 possible magnetic numbers and therefore can hold 6 electrons so on and so forth.

Next question we ask is, what do these $|lm\rangle$ states actually look like. Following a similar strategy to Eq.2.33, we can construct the differential forms for L_x, L_y and put it all together to find L^2:

$$
\begin{aligned}
L_x &= YP_z - ZP_y = i\hbar\left(\sin\phi\frac{\partial}{\partial\theta} + \cot\theta\phi\frac{\partial}{\partial\phi}\right) \\
L_y &= ZP_x - XP_z = i\hbar\left(-\cos\phi\frac{\partial}{\partial\theta} + \cot\theta\sin\phi\frac{\partial}{\partial\phi}\right) \\
L^2 &= -\hbar^2\left[\frac{1}{\sin\theta}\frac{\partial}{\partial\theta}\left(\sin\theta\frac{\partial}{\partial\theta}\right) + \frac{1}{\sin^2\theta}\frac{\partial^2}{\partial\phi^2}\right]
\end{aligned}
\tag{2.40}
$$

We recognize this form as the solution to Laplace's equation in a spherical coordinates (which is not that surprising given that the kinetic energy term in the Hamiltonian is a Laplacian). Eigenvectors of this equation are called spherical harmonics and one can solve it with separation of variables. They are notated by Y_l^m for the two quantum quantum numbers l, m, which are the same as $|lm\rangle$ quantum numbers from the above discussion. The mathematical expression is:

$$
Y_l^m(\theta,\phi) = (-1)^m\left[\frac{2l+1}{4\pi}\frac{(l-m)!}{(l+m)!}\right]^{1/2} P_l^m(\cos\theta)e^{im\phi} \tag{2.41}
$$

where $P_l^m(\cos\theta)$ is the associated Legendre polynomial. One can check that this indeed satisfies the eigenvalues we have derived (which is not that surprising because we got this expression by solving for the eigenvalue problem).

It turns out that $Y_l^m(\theta,\phi)$ creates a new basis. By design they are normalized, i.e.

$$
|\langle lm|lm\rangle|^2 = \int Y_l^{m*}(\Omega)Y_l^m(\Omega)\mathrm{d}\Omega = 1 \tag{2.42}
$$

And furthermore for different quantum numbers l, m, the functions are orthogonal to each other:

$$
|\langle l'm'|lm\rangle|^2 = \int Y_{l'}^{m'*}(\Omega)Y_l^m(\Omega)\mathrm{d}\Omega = \delta_{l',l}, \delta_{m',m} \tag{2.43}
$$

Y_l^m only describe the angular part of the electronic orbital. There also is a radial component which is shown with R_{nl}. Where n is the principle quantum number and constrain

$(n-1) \geq l \geq 0$. The radial part of the wavefunction can be solved for a free atom, but in the ligand field picture, these solutions do not translate easily. Therefore we will limit our discussion to only to the angular part. The model system explored in this thesis is group-3 transition metal ions and their d-orbitals, meaning $n = 3, l = 2$. The m quantum number provides 5 degrees of freedom, or orbitals that electrons can occupy. Understanding how these orbitals are energetically ordered as a function of the ligand environment determines the electronic structure and creates the basis of optically addressable spin qubits.

2.4.2 Spin-Orbit Effects

So far we have constructed and discussed two different magnetic components of electrons. The spin S describes the intrinsic angular momentum of electrons, and L describes the orbital momentum of them due to spatial containment around an atomic charge. If these two degrees of freedom do not interact, then the relevant electron Hamiltonian can be described as:

$$\mathcal{H}_Z = \mu_B \vec{B} \cdot (\vec{L} + g_e \vec{S}) \tag{2.44}$$

These two angular momentum vectors can interact which is called 'spin-orbit interaction', described with the following additional Hamiltonian:

$$\mathcal{H}_{SO} = \lambda \vec{L} \cdot \vec{S} = \lambda \left[L_x \cdot S_x + L_y \cdot S_y + L_z \cdot S_z \right] \tag{2.45}$$

When evaluating the energies of this mixed Hamiltonian, we need to keep track of both the spatial and the spin quantum numbers. As we will see in the next chapter (Chapter 3), in a ligand environment (or any system where some electrostatic potential removes degeneracies of the orbitals), the orbitals, Y_l^m, get mixed. To make our lives simpler, we will concatenate both angular momentum quantum numbers to G and use orthogonality principles. To evaluate the new energies of the system, we will use perturbation theory. We will focus on the non-degenerate orbitals for this calculation for the reasons that will be

clear soon. Specifically, the Zeeman effect is much smaller compared to orbital energies, and therefore the entire Zeeman Hamiltonian below can be treated as a correction to the orbital Hamiltonian that we will discuss in Chapter 3. The zeroth order energies are the orbital energies. To the first order, the corrections are the diagonal elements of $\mathcal{H} = \mathcal{H}_Z + \mathcal{H}_{SO}$:

$$U_G^{(1)} = \langle Gs|g_e\mu_B B_z S_z|Gs\rangle + \langle Gs|(\mu_B B_z + \lambda S_z)L_z|Gs\rangle \tag{2.46}$$

The first term is the 'spin-only' electron Zeeman energy, previously discussed in Eq.2.2. The second term can be decomposed into its individual spin and orbital components and be rewritten as:

$$\langle s|\mu_B B_z + \lambda S_z|s\rangle \ \langle G|L_z|G\rangle \tag{2.47}$$

As we will see in the next chapter, under a ligand environment, the orbitals become real (the imaginary components cancel out) for example for transition metal d-orbitals under ligand field. If the evaluated state is non-degenerate (i.e d^2 ground state), then the expectation value of $\langle G|L_z|G\rangle = \langle L_z\rangle = 0$. Thus to the the first order, there is no spin-orbit correction and the energy splitting is just given by the Zeeman Hamiltonian. This is not the case for degenerate orbitals, and this first term must also be considered, as is the case for V^{4+} in SiC which makes spin-orbit effects larger. Since the remaining calculation is illustrative of some of the spin-orbit effects, we will not consider the first order terms for the degenerate case. The second order correction is given below:

$$\mathcal{H}_{ss'} = -\sum_{n\neq G} \frac{\left|\left\langle Gs\right|(\mu_B\vec{B} + \lambda\vec{S})\cdot\vec{L} + g_e\mu_B\vec{B}\cdot\vec{S}\left|ns'\right\rangle\right|^2}{U_n^0 - U_G^{(0)}} \tag{2.48}$$

This sum runs over all possible orbital states n. The matrix elements for $g_e\mu_B\vec{B}\cdot\vec{S}$ are all zero since $\langle G|n\rangle = \delta_{Gn}$ by orthogonality of the orbitals. Thus we are left with:

$$\begin{aligned}\mathcal{H}_{ss'} &= -\sum_{n\neq G}\frac{\Big[\big\langle s\big|(\mu_B\vec{B}+\lambda\vec{S})\big|s'\big\rangle\ \langle G|\vec{L}|n\rangle\Big]\Big[\langle n|\vec{L}|G\rangle\ \big\langle s'\big|(\mu_B\vec{B}+\lambda\vec{S})\big|s\big\rangle\Big]}{U_n^0-U_G^{(0)}} \\ &= -\Big(\big\langle s\big|(\mu_B\vec{B}+\lambda\vec{S})\big|s'\big\rangle\Big)\left[\sum_{n\neq G}\frac{\langle G|L|n\rangle\ \langle n|L|G\rangle}{U_n^0-U_G^{(0)}}\right]\Big(\big\langle s'\big|(\mu_B\vec{B}+\lambda\vec{S})\big|s\big\rangle\Big)\end{aligned} \tag{2.49}$$

At this point it is beneficial to define Λ:

$$\Lambda = -\sum_{n\neq G}\frac{\langle G|L|n\rangle\ \langle n|L|G\rangle}{U_n^0-U_G^{(0)}} \tag{2.50}$$

which is a 3×3 symmetric matrix ($i,j=x,y,z$) whose matrix elements are:

$$\Lambda_{ij} = -\sum_{n\neq G}\frac{\langle G|L_i|n\rangle\ \langle n|L_j|G\rangle}{U_n^0-U_G^{(0)}} \tag{2.51}$$

Using this definition in Eq.2.50 we get:

$$\mathcal{H}_{ss'} = \big\langle s'\big|\mu_B^2\vec{B}\cdot\Lambda\cdot\vec{B}+2\lambda\mu_B\vec{B}\cdot\Lambda\cdot\vec{S}+\lambda^2\vec{S}\cdot\Lambda\cdot\vec{S}\big|s\big\rangle \tag{2.52}$$

The first term only shifts the diagonal energy levels by a constant and has no spectroscopic value - therefore we ignore it. The second and the third terms in the matrix constitute a Hamiltonian that only operates on the spin levels when combined with the Zeeman term from Eq.2.44, we get:

$$\begin{aligned}\mathcal{H} &= \mu_B\vec{B}\cdot(g_e+2\lambda\Lambda)\cdot\vec{S}+\lambda^2\vec{S}\cdot\Lambda\cdot\vec{S} \\ &= \mu_B\vec{B}\cdot g\cdot\vec{S}+\vec{S}\cdot D\cdot\vec{S}\end{aligned} \tag{2.53}$$

Where

$$\begin{aligned} g &= g_e + 2\lambda\Lambda \\ D &= \lambda^2\Lambda \end{aligned} \tag{2.54}$$

where the D term is only valid for systems with total spin $S \geq 1$. We have just shown two effects of spin-orbit interactions. First, although, we may be investigating an isolated electron, the spin-orbit effects can cause the observed g-factor to deviate from that of a free electron, and furthermore, can cause anisotropy depending on the Λ matrix. Secondly, the spin-orbit effects can induce zero-field splitting D. When speaking of D, one also needs to consider the dipole interaction (where both electron spins prefer to be oriented one way over another depending on their spatial distribution). Although the non-degenerate ground state orbitals generally have total angular momentum of zero, as shown in the above calculation, they can mix with higher energy orbitals with non-zero angular momentum which results in spin-orbit effects.

Now that we have all the necessary machinery, we will discuss the spin and angular momentum properties of electrons in transition metal ions within a ligand environment.

Chapter 3

Transition Metal $d-$ Orbitals

In this part, we will start putting together some of the mathematical machinery we have thus far built to explain orbital and spin dynamics of transition metal ions. Even though the example we will follow will be about the main subject of this thesis, a transition metal ion under a tetrahedral ligand symmetry, the same analysis can be carried for various symmetries (and charge configurations) to engineer different electronic structures to construct optically accessible spin qubits. This will not be a complete mathematical description either as it would take a few textbooks to fully account for all of the effects, for example [56, 57].

The purpose of this chapter is to build a qualitative description and intuition on how transition metal electronic structures form under symmetry, understanding Tanabe-Sugano diagrams, and thinking about the electronic structures for optically addressable spin qubits.

3.1 Crystal Field Theory

We will start with a toy model: a transition metal ion surrounded by point charges. Under this scenario, besides the radial potential exerted by the central ion, there are also the electric potentials that are present from the neighboring ligands that need to be summed:

$$\vec{V} = \sum_i \vec{v}(i, x, y, z) = \sum_i ez_i/r_{ij} \tag{3.1}$$

where e is the coulomb constant, z_i is the charge at the ith locations and r_{ij} is the distance from the ith charge to the point (x, y, z). To solve the relative energies of these orbitals, we will use perturbation theory. We will see that that, under the crystal field, the Y_m^l orbitals are no longer the eigenstates of the system, but the real orbitals shown in Sec.B.2 are. As an exercise we will explore the tetrahedral ligand field, and show how the orbitals split into two sets.

A shorthand way of thinking about the real orbitals however is looking at how much they overlap with the charges in the crystal environment. Qualitatively we know from Coulomb's law that two electrons will repel each other inversely proportional to the distance between them, captured by Eq.3.1. Therefore the existence of a crystal field does two things: firstly it creates a preferred axis for the d-orbitals by forming a frame of reference, and secondly changes the relative energies of the orbitals. Specifically, the more a real orbital overlaps with the charges around, the more energy an electron will need to occupy that orbital. Therefore we can qualitatively realize that in a tetrahedral ligand environment shown in Fig.3.1**A**, $d_{z^2}, d_{x^2-y^2}$ orbitals will be lower energy than d_{xy}, d_{yz}, d_{xz} as they are further away from the neighboring atoms shown in Fig.3.1**B**.

3.1.1 A toy model

For intuition building, I will carry out the example calculation of this toy model. Even though this toy model is far from an accurate description, it demonstrates how the existence of the ligand environment changes the orbitals to real ones (superposition of orbitals with no imaginary components), how the ligand symmetry determines splitting of the d-orbitals and the ligand strength can change this splitting. The transition metal ions investigated in this thesis are in tetrahedral-like like symmetry environment, therefore we will use this configu-

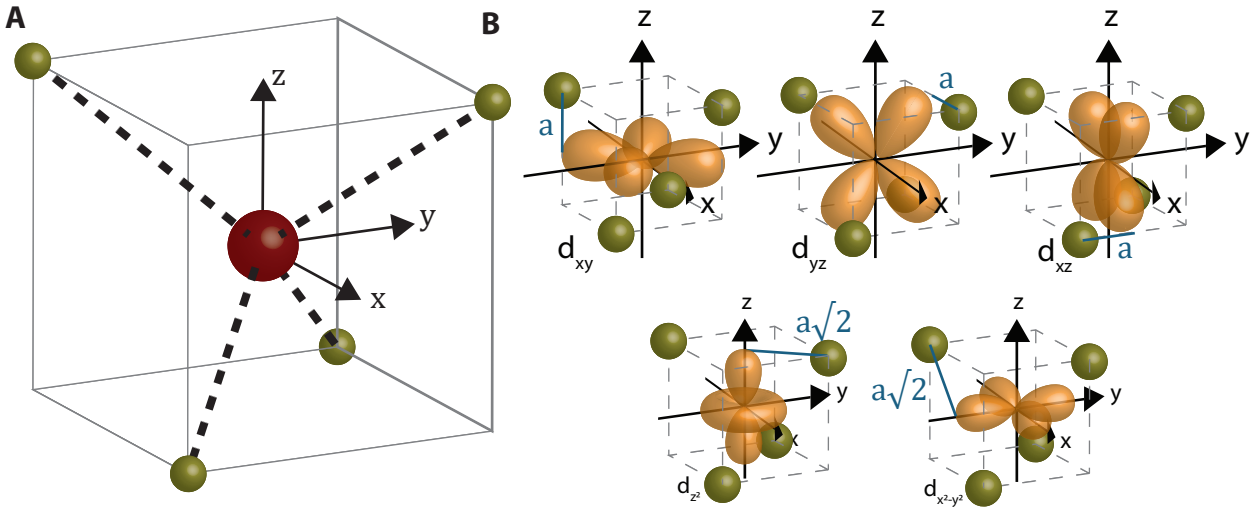

Figure 3.1: (**A**)Transition metal within a tetrahedral symmetry and (**B**) d-orbital distance from the nearest atom. The cube that contains the tetrahedral symmetry has a side length of $2a$ for illustrative purposes. Orbitals contained in the d_t manifold are a away from the nearest atom while the orbitals within the d_e manifold are further away with a distance of $a\sqrt{2}$ and therefore has lower energy.

ration for our example. A free atom's d-orbital ($l = 2$) has the following time independent equation:

$$H_0 \left|n, l = 2, m\right\rangle = E \left|n, l = 2, m\right\rangle \tag{3.2}$$

for some fixed radial quantum number n (e.g. $n = 3$ for $3d$ orbitals) and magnetic number m. The energy eigenvalue is the same for all m, hence we will use degenerate perturbation theory. Under the perturbative crystal field, the equation is now modified to

$$(H_0 + H_1) \left|\psi_i\right\rangle = E_i' \left|\psi_i\right\rangle \tag{3.3}$$

where H_1 is the perturbative Hamiltonian from the ligands, E_i' are the new energy eigenvalues and $|\psi_i\rangle$ are the new eigenstates that can be written as a superposition of the eigenvectors of the free ion Hamiltonian:

$$\left|\psi_i\right\rangle = \sum_{m=-2}^{2} c_{mi} \left|n, l = 2, m\right\rangle \tag{3.4}$$

with c_{mi} normalized complex scalars. To find the energy perturbation, we want to find $\det(H_1 - E) = 0$, where matrix elements are

$$\langle n, l = 2, m | H_1 | n, l = 2, m' \rangle = e \int R^*_{n,2} Y_2^{m*} \vec{V}(x, y, z) R_{n,2} Y_2^{m\prime} \mathrm{d}\tau \tag{3.5}$$

We see that by expanding $\vec{V}$ in spherical harmonic functions, we can use the orthonormality principles to simplify this equation to construct the matrix. r_{ij} represents the distance from point i to point j. The expansion for

$$\frac{1}{r_{ij}} = \sum_{n=0}^{\infty} \sum_{m=-n}^{n} \frac{4\pi}{2n+1} \frac{r^n}{\alpha^{n+1}} Y_{n_j}^m Y_{n_i}^{m*} \tag{3.6}$$

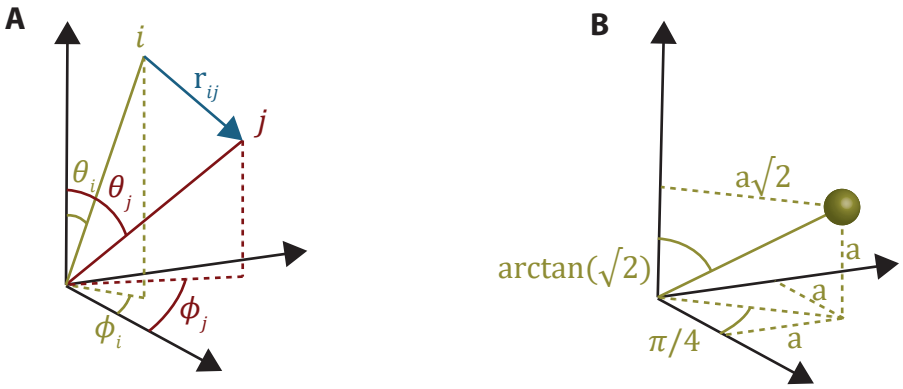

Figure 3.2: (**A**) Geometric illustration of two points in 3-space and (**B**) angular calculation of tetrahedral charge $i = q_1$.

where the index i labels the location of the neighboring atom, $\alpha = a\sqrt{3}$ is the ligand length to that atom, and r is the radial distance from the central ion and j is some free index that spans the 3-space. In the tetrahedral symmetry, there are 4 ligands with the angles below:

	Point	θ_i	ϕ_i
q_1	(a,a,a)	$\arctan(\sqrt{2})$	$\pi/4$
q_2	(-a-,a,a)	$\arctan(\sqrt{2})$	$5\pi/4$
q_3	(a,-a,-a)	$-\arctan(\sqrt{2})$	$7\pi/4$
q_4	(-a,a,-a)	$-\arctan(\sqrt{2})$	$3\pi/4$

Because the odd n will integrate to zeros for the matrix elements we do not need to consider them. We will see that most of the other matrix elements will also add up to zeros because of the symmetry. We will expand Eq.3.1 term by term according to Eq.3.6 for even n to then later compute the perturbation matrix:

n=0

$$\frac{4\pi ze}{\alpha} Y_{0\,i}^{0} Y_{0\,j}^{0} = \frac{4\pi ze}{\alpha}\left(\frac{1}{2\sqrt{\pi}}\right)\left(Y_{0_j}^{0}\right) = \frac{ze}{\alpha} \tag{3.7}$$

Thus the total contribution from all 4 ligands will be $4ze/a$.

n=2, m=0

$$\mathbf{V}_{2,0} = ze\sum_{i=1}^{4}\frac{4\pi}{5\alpha^3} r^2 Y_2^0(\theta_i,\phi_i) Y_2^0(\theta_j,\phi_j) = zeY_2^0(\theta_j,\phi_j)\frac{4\pi}{5\alpha^3} r^2 \sum_{i=1}^{4} Y_2^0(\theta_i,\phi_i) \tag{3.8}$$

So it is sufficient to look at the sum of Y_2^0 for the angles we have. Looking at the Eq.B.1 we get:

$$\frac{1}{4}\sqrt{\frac{5}{\pi}}\left[2\left(3\cos^2(\arctan\sqrt{2})-1\right)+2\left(3\cos^2(\arctan\left(-\sqrt{2}\right))-1\right)\right]=0$$

Therefore the contribution from the $\mathbf{V}_{2,0}=0$. I will be summing over only the spherical contributions of the i component going forward.

n=2, m=±1,±2

Similar to the above analysis we have $\mathbf{V}_{2,\pm m} \propto \sum_{i=1}^{4} Y_2^{\pm m*}(\theta_i, \phi_i)$. We also know that $Y_l^{\pm m*} = Y_l^{\mp m}$ therefore it is sufficient to look at only positive m.

Point	$Y_2^1/\sqrt{15/(8\pi)}$	$Y_2^2/\sqrt{15/(32\pi)}$
q_1	$-(1+i)/3$	$2i/3$
q_2	$(1+i)/3$	$2i/3$
q_3	$(1-i)/3$	$-2i/3$
q_4	$-(1-i)/3$	$-2i/3$
$+$	0	0

Thus all the contributions for the expansion of $l = 2$ add up to 0.

n=4, m=0

We continue with the expansion:

$$\begin{aligned}
\mathbf{V}_{4,0} &= ze \sum_{i=1}^{4} \frac{4\pi}{9\alpha^5} r^4 Y_4^0(\theta_i, \phi_i) Y_4^0(\theta_j, \phi_j) \\
&= ze \frac{4\pi}{9\alpha^5} r^4 Y_4^0(\theta_j, \phi_j) \sum_{i=1}^{4} Y_4^0(\theta_i, \phi_i) \\
&= ze \frac{4\pi}{9\alpha^5} r^4 Y_4^0(\theta_j, \phi_j) \left(4\left(\frac{-7}{12\sqrt{\pi}}\right)\right) \\
&= -ze \frac{28\sqrt{\pi}}{27} \frac{r^4}{\alpha^5} Y_4^0(\theta_j, \phi_j)
\end{aligned} \tag{3.9}$$

There actually is a contribution from this term!

n=4, m=±1,±2,±3,±4

Similar to the above analysis we create a table

Point	$Y_4^1/\sqrt{45/(64\pi)}$	$Y_4^2/\sqrt{45/(128\pi)}$	$Y_4^3/\sqrt{315/(64\pi)}$	$Y_4^4/\sqrt{315/(512\pi)}$
q_1	$2(1+i)/9$	$8i/9$	$2(1-i)/9$	$-4/9$
q_2	$-2(1+i)/9$	$8i/9$	$-2(1-i)/9$	$-4/9$
q_3	$-2(1-i)/9$	$-8i/9$	$-2(1+i)/9$	$-4/9$
q_4	$2(1-i)/9$	$-8i/9$	$2(1+i)/9$	$-4/9$
$+$	0	0	0	-16/9

All the contributions for the expansion of $l = 4, m = 1, 2, 3$ add up to 0. But $l = 4, m = \pm 4$ does have a contribution:

$$\begin{aligned} \mathbf{V}_{4,\pm 4} &= ze\frac{4\pi}{9\alpha^5} r^4 Y_4^{\mp 4}(\theta_j, \phi_j) \left(4\left(\frac{-1}{12}\sqrt{\frac{35}{2\pi}}\right)\right) \\ &= -ze\frac{2\sqrt{70\pi}}{27}\frac{r^4}{\alpha^5} Y_4^{\mp 4}(\theta_j, \phi_j) \end{aligned} \tag{3.10}$$

We need not expand this any further, because

$$\int_\Omega Y_l^{m^*} Y_{l'}^{m'} Y_l^m \mathrm{d}\Omega = 0, \qquad l' > 2l$$

Thus putting together Eq. 3.7, 3.9, 3.10 we find the pertubrative potential to be

$$\begin{aligned} \vec{V} &= \mathbf{V}_{0,0} + \mathbf{V}_{4,0} + \mathbf{V}_{4,4} + \mathbf{V}_{4,-4} \\ &= 4\frac{ze}{\alpha} - ze\frac{28\sqrt{\pi}}{27}\frac{r^4}{\alpha^5}\left[Y_4^0(\theta_j, \phi_j) + \sqrt{\frac{5}{14}}(Y_4^4(\theta_j, \phi_j) + Y_4^{-4}(\theta_j, \phi_j))\right] \end{aligned} \tag{3.11}$$

The first term can be dropped as it is a constant. Matrix element $\int Y_2^{m*} \frac{4ze}{a} Y_2^{m'} d\Omega = \frac{4ze}{a}\delta_{m,m'}$ shifts all of the orbital energies the same. We are interested in their differences, therefore this term is not important and will be discarded going forward. I will label the new potential energy V_{tet} that doesn't have the constant term. Next, we can integrate the r component. The radial distribution is not that important, so we will assume some functional

form $R_{n,2}$ for the d-orbitals within the crystal and integrate out the radial component:

$$\int_0^\infty R_{n,2}^* r^4 R_{n,2} r^2 \mathrm{d}r = \overline{r^4} \tag{3.12}$$

where one can interpret $\overline{r^4}$ as the fourth-power mean of the electron's location by the central metal atom. Thus now we can calculate the matrix in Eq.3.4:

$$\begin{aligned}\left\langle n, l=2, m \middle| V_{tet} \middle| n, l=2, m' \right\rangle = &- ze^2 \frac{28\sqrt{\pi}}{27} \frac{\overline{r^4}}{\alpha^5} \int \Big[Y_2^{m*} Y_4^0 Y_2^{m'} \\ &+ \sqrt{\frac{5}{14}} \left(Y_2^{m*} Y_4^4 Y_2^{m'} + Y_2^{m*} Y_4^{-4} Y_2^{m'} \right) \Big] \mathrm{d}\Omega \end{aligned} \tag{3.13}$$

where the n dependence no longer matters as it is accounted for in Eq.3.12. A property of the spherical harmonics is that, for a given integral:

$$\int_0^{2\pi} Y_{l_1}^{m_1} Y_{l_2}^{m_2} Y_{l_3}^{m_3} \mathrm{d}\phi = \begin{cases} 2\pi & m_1 + m_2 + m_3 = 0 \\ 0 & \text{otherwise} \end{cases} \tag{3.14}$$

For the first term of the integral where $m_2 = 0$, $-m_1 = m_3$, but since $Y_l^{\pm m*} = Y_l^{\mp m}$ it means that $m = m'$ which are all the diagonal terms. For $m_2 = \pm 4$, $m_1 = \mp 4 - m_3$, which means that $m' = \pm 2, m = \mp 2$ which are the outermost off-diagonal terms.

The integral of all non-zero terms are:

$$\int_0^{2\pi} \int_0^{\pi} Y_2^{m*} Y_4^0 Y_2^m \sin\theta \mathrm{d}\theta \mathrm{d}\phi = \begin{cases} \frac{3}{7\sqrt{\pi}} & m = 0 \\ \frac{-2}{7\sqrt{\pi}} & m = \pm 1 \\ \frac{1}{14\sqrt{\pi}} & m = \pm 2 \end{cases} \tag{3.15}$$

$$\int_0^{2\pi} \int_0^{\pi} Y_2^{\pm 2*} Y_4^{\pm 4} Y_2^{\mp 4} \sin\theta \mathrm{d}\theta \mathrm{d}\phi = \sqrt{\frac{5}{14\pi}} \tag{3.16}$$

To easily collect the terms together, we define $\Delta = \frac{2ze^2\overline{r^4}}{27\alpha^5}$ and plugging Eq. 3.15, 3.16

into Eq. 3.14, get the perturbation matrix in the Y_2^m basis:

$$V_{tet} = \begin{array}{c} \\ Y_2^{-2} \\ Y_2^{-1} \\ Y_2^0 \\ Y_2^1 \\ Y_2^2 \end{array} \begin{array}{c} \begin{array}{ccccc} Y_2^{-2} & Y_2^{-1} & Y_2^0 & Y_2^1 & Y_2^2 \end{array} \\ \begin{pmatrix} -\Delta & 0 & 0 & 0 & 5\Delta \\ 0 & 4\Delta & 0 & 0 & 0 \\ 0 & 0 & -6\Delta & 0 & 0 \\ 0 & 0 & 0 & 4\Delta & 0 \\ 5\Delta & 0 & 0 & 0 & -\Delta \end{pmatrix} \end{array} \tag{3.17}$$

To find the energy corrections, we calculate the secular determinant $\det(V_{tet} - E) = 0$. The diagonal terms are easy, and there are three of them, $Y_2^{\pm 1}$ has $E_{\pm 1} = 4\Delta$ and $Y_2^0 = d_{z^2}$ has $E_0 = -6\Delta$. Calculating the secular determinant of the submatrix of V_{tet}, we find:

$$\det(V_{tet\text{sub}} - E) = \begin{array}{c} \\ Y_2^{-2} \\ Y_2^2 \end{array} \begin{array}{c} \begin{array}{cc} Y_2^{-2} & Y_2^2 \end{array} \\ \begin{vmatrix} -\Delta - E & 5\Delta \\ 5\Delta & -\Delta - E \end{vmatrix} \end{array} = 0 \tag{3.18}$$

We find two energy values by solving $(\Delta + E)^2 = 25\Delta^2$ and get eigenenergies of $E = -6\Delta, 4\Delta$ with eigenfunctions $(Y_2^2 - Y_2^{-2})/i\sqrt{2} = d_{xy}$ and $(Y_2^2 + Y_2^{-2})/\sqrt{2} = d_{x^2-y^2}$ respectively.

This calculation mathematically showed what was already qualitatively argued in Sec.3.1 but it provides more insights. The existence of the ligand environment split the d-orbitals into two sets, $d_e = \{d_{z^2}, d_{x^2-y^2}\}$ and $d_t = \{d_{xy}, d_{xz}, d_{yz}\}$ with mathematical forms given in Sec.B.2.[1] The orbitals within the sets have degenerate energies, and under the tetrahedral symmetry, $E_e < E_t$, therefore the orbitals in d_e will form the ground state. Furthermore, the energy splitting between these two sets are proportional to $\Delta \sim 1/\alpha^5$ - therefore the closer the neighboring atoms (higher the ligand field) the larger the energy separation between

1. A, B refer to orbital singlet configuration, E refers to two degenerate orbitals and T refers to three degenerate orbitals.

d_e and d_t will be. Since the energies of the orbitals are degenerate within each set, any superposition of them is also a valid orbital.

As mentioned earlier, this is a toy model. The treatment of the neighboring atoms as point charges is far from a realistic description. A more accurate description looks at the $d-$orbital interactions with the chemical bonds to the metal center. The main reason this toy model could capture the physics of this system actually comes from the symmetry of the ligand environment.

We will not discuss ligand field theory any further, as the subject itself is vast, and beyond the scope of this thesis. We will however use some of the main principles we have learned in this consideration:

- The symmetry of the ligand environment determines how and which $d-$orbitals will split.
- Qualitatively one can determine the trend by looking at how much the real orbitals overlap with the neighboring atoms.
- The strength of the ligand will determine the energy magnitude of the splitting.

Based on there qualitative principles, we can see that under an octahedral symmetry (e.g. Corundum (Al_2O_3)), the energy of the set of orbitals will be swapped, that is, the lower energy orbitals will be $d_t = \{d_{xy}, d_{xz}, d_{yz}\}$ and higher energy orbitals will be $d_e = \{d_{z^2}, d_{x^2-y^2}\}$. This is the level structure for Cr doped corundum, also known as ruby. The Cr^{3+} has three valance electrons occupying the three ground state orbitals and therefore displays some very similar physics to Cr^{4+} in tetrahedral environment.

So far we have discussed the orbital energies. Next we will discuss what happens when we load electrons into these orbitals to create the quantum bit out of their spins and optical paths for initialization and readout.

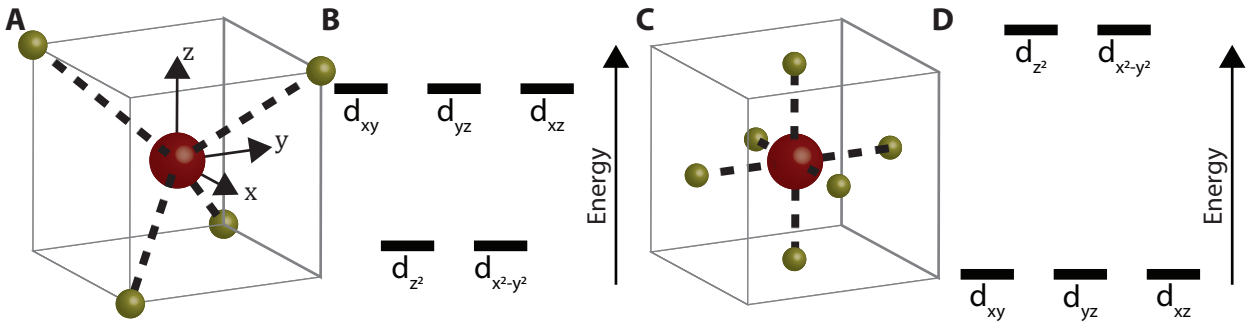

Figure 3.3: d-orbital energies under different symmetries. (**A**)Transition metal within a tetrahedral symmetry and (**B**) the energies of d-orbitals. (**C**) Transition metal within a octahedral symmetry (**D**) has the orbital energies flipped.

3.2 $d-$Orbital Configurations

The $d-$orbital electronic structures that emerge in well known symmetries such as octahedral and tetrahedral are well understood and are plotted in Tanabe-Sugano diagrams. In this section we will discuss how to make sense out of these graphs and understand how they are derived. These graphs plot the energies of electronic orbitals that arise from different electron configurations and how they evolve as a function of the ligand field strength. Not all of the diagrams are relevant. For example, if an atom has no d orbital electron (d^0) or all of the d orbitals are filled (d^{10}), then we cannot talk about electron energies of d orbitals. If there is only one electron d^1 or nine electrons d^9, then the resultant electronic structure closely follows the orbitals under the ligand field strength, which is already discussed in Sec.3.1.1. In this case, one does not need to think about configurations that arise from multiple electrons, and therefore the problem is simple, so there aren't any diagrams. Tanabe-Sugano diagrams only exist for 2 to 8 electron configurations.

In this thesis, we are discussing tetrahedral symmetry but as mentioned earlier the octahedral symmetry results in very similar orbital energetics, but just inverted. In the single particle picture, one can convince themselves that an electron moving from d_e to d_t manifold in tetrahedral symmetry is the same as a hole (absence of electron) moving from d_e to d_t to octahedral symmetry. Therefore Tanabe-Sugano diagrams are the same for $d^n_{\text{oct}} = d^{10-n}_{\text{tet}}$.

We will be using the ${}^{n}X_{m}$ notation, where n is the total number of spin configurations (1 for spin-0, 2 for spin-1/2, 3 for spin-1, etc.), $m = 1, 2$ for symmetric or antisymmetric wavefunction relative to a rotation axis and X is the symmetry label where A, B are non degenerate single states symmetric or antisymmetric wavefunction relative to a principal axis, E and T are labels for doubly and triply degenerate orbitals, defined in Chapter C in detail. Finally, one will see in Tanabe-Sugano diagrams different orbital manifolds, labeled with S, P, D, F, G indicating a total *character of* angular momentum of $L = 0, 1, 2, 3, 4$ respectively.

3.2.1 d^1 configuration

A free transition metal ion with a single electron in the $d-$orbital will have 10 possible magnetic configurations, 5 of $-2 \leq m_l \leq 2$ angular momentum levels and 2 of $m_s = \pm 1/2$ spin levels. Therefore, the system will be described as ${}^{2}D$. As derived, under a tetrahedral ligand field, for example V^{4+} in silicon carbide discussed in Chapter 6, the degeneracy of the d orbitals will be lifted and the system will end up with two ground states that is composed of the d_e manifold and three excited states composed of the d_t manifold. The two orbitals in the d_e manifold and the three excited state orbitals d_t are degenerate under perfect symmetry and without an electron and therefore are labeled as ${}^{2}E$ and ${}^{2}T$ respectively.

When there is an electron present, however, the system tries to minimize the energy by rearranging the ligand lengths which results in breaking of the degeneracies. This is called Jahn-Teller distortion. In the d^1 configuration, this results in two close ground states. The composition of the ground states depend on how the system relaxes and requires careful calculations and modeling beyond the scope of this thesis. We will generically call them GS1 and GS2 when we discuss V^{4+}. Spin orbit effects or second nearest neighbors within the host can also introduce further splittings both in the ground and the excited state resulting in different energy splittings between various SiC lattice sites for V^{4+}.

3.2.2 d^2 configuration

In the d^2 configuration, the physics get more complicated as we have to both consider the energies of the orbitals that electrons occupy as well as electron-electron interactions. A good strategy to understand what happens to a system is looking at it at two extreme limits and extrapolating the intermediate states with a continuous functional. In this spirit we will investigate the d^2 configuration without any ligands and very strong tetrahedral ligand field. Although the weak ligand field regime is not relevant to the experimental results of this thesis, it is important to understand them to understand Tanabe-Sugano diagrams. In this spirit, we will start the discussion with a transition metal ion in vacuum with five degenerate orbitals and two electrons.

Both of the valance electrons occupy the d orbitals with the total angular momentum of $L = L_1 + L_2 = 2 \times (\sqrt{2(2+1)})$. The l_z of each electron can take a value anywhere between $-2, ..., 2$ where the total $L_z = L_{z1} + L_{z2}$ will range $-4, ..., 4$ with multiple degeneracies. As we have seen in Sec.2.3.3 where two spin-1/2 electrons can form spin-1 and spin-0 manifolds ($\mathscr{H}_{1/2} \otimes \mathscr{H}_{1/2} = \mathscr{H}_1 \oplus \mathscr{H}_0$), a similar treatment of angular momentum yields a total angular momentum of $L = 4, 3, 2, 1, 0$ labeled with G, F, D, P, S respectively ($d \otimes d = G \oplus F \oplus D \oplus P \oplus S$). Each one of the these macro states will have a macro-magnetic number shown with capital letter $M_L = m_{l1} + m_{l2}$ where $-L \leq M_L \leq L$. Since each electron also has a spin, the macrostates will either be spin-1 or spin-0 that needs identifying. In order to find the macrostates, we will count various electron occupation combinations of the microstates below.

To start with, the two electrons occupying the 5 orbitals have $\binom{10}{2} = 45$ different possible electronic configurations. There are $\binom{5}{2} = 10$ each possible configurations where spins are symmetric (electrons must be in separate orbitals where order does not matter, given by *5 choose 2*), creating the triply degenerate spin-1 manifold and the remaining 15 configurations where spins are anti-symmetric (5 of them where electrons are on the same orbitals, and the remaining 10 where they are anti-symmetric on separate orbitals) creates the non degenerate

spin-0 manifold. Next, we calculate how many L levels there are. We realize that if the two electrons are in two different orbitals, then they span a 4-dimensional spin configuration space ($\mathscr{H}_1 \oplus \mathscr{H}_0$), where basis elements can be given with $\{|\uparrow,\uparrow\rangle, |\uparrow,\downarrow\rangle, |\downarrow,\uparrow\rangle, |\downarrow,\downarrow\rangle\}$. If the two electrons occupy the same orbital, then they must be anti-aligned due to Pauli exclusion principal discussed in Sec.2.3.2 and therefore must belong to the spin-0 manifold ($\mathscr{H}_0$).

We will talk about only the positive total M_l, since negative part is the same with a minus sign. The below discussion is pictorially demonstrated in Fig.3.4 below. There is only 1 configuration for $M_l = +4$ where both electrons occupy the $m_l = +2$ orbital and therefore $L = 4$ must be spin-0, creating the character ${}^1G$.

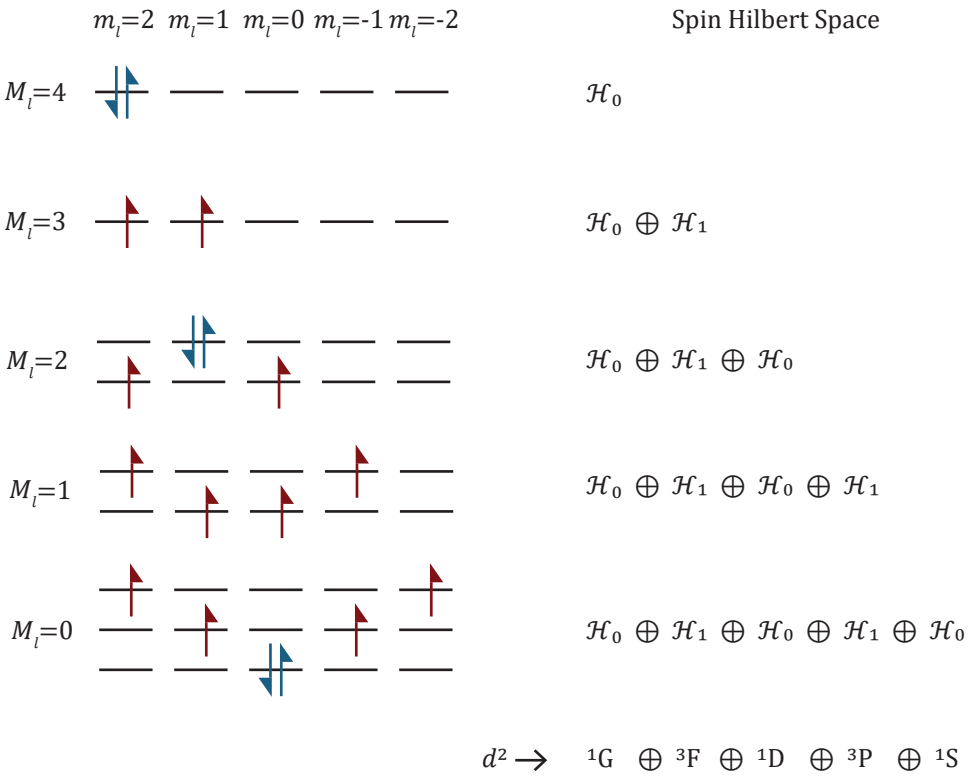

Figure 3.4: Total angular momentum character of d^2 configuration with no ligands. The total angular momentum M_l is the sum of both electrons occupation of m_l of the d orbitals. Different possible combinations of getting M_l are indicated by multiple rows for each value. Blue spins indicate only a spin-0 Hilbert space while the red arrows indicate a spin-0 plus a spin-1 Hilbert space.

There are 4 configurations for total $M_l = +3$ where one electron is in the $m_l = +2$ and

the other one is in $m_l = +1$ orbital. One of the $m_s = 0$ configurations must belong to the spin-0 space that contains $|L = 4, M_l = +3\rangle$. Therefore the remaining $|L = 3, M_l\rangle$ must be spin-1 creating the character ${}^3F$.

There are 5 configurations for $M_l = +2$, four where the electrons are on different orbitals, one $m_l = +2$ and the other at $m_l = 0$ forming a spin-0 and a spin-1 space and an additional single configuration where both electrons are at $m_l = +1$ which forms a spin-0 state. One of the spin-0 states must belong to $|L = 4, M_l = +2\rangle$ and the spin-1 state must belong to $|L = 3, M_l = +2\rangle$ which leaves only the remaining spin-0 Hilbert space for $|L = 2, M_l\rangle$ forming the character of ${}^1D$.

There are 8 configurations for $M_l = +1$, where both electrons are on different orbitals of ($m_l = +2$ and $m_l = -1$) and ($m_l = +1$ and $m_l = 0$), creating two spin-0 and two spin-1 Hilbert spaces. The spin-0 spaces must belong to $|L = 4, M_l = +1\rangle$ and $|L = 2, M_l = +1\rangle$, while one of the spin-1 space must belong to $|L = 3, M_l = +1\rangle$ which leaves $|L = 1, M_l\rangle$ with the other spin-1 Hilbert space creating the character of ${}^3P$.

Finally there are 9 remaining configurations for total $M_l = 0$ four configurations for each electron are in $m_l = \pm 2, \pm 1$ orbitals and an additional one where both electrons are anti parallel in $m_l = 0$ orbital which in total forms 2 spin-1 Hilbert spaces and 3 spin-0 Hilbert spaces. The spin-1 Hilbert spaces must belong to $|L = 3, M_l = 0\rangle$ and $|L = 1, M_l = 0\rangle$ while two spin-0 Hilbert spaces must belong to $|L = 4, M_l = 0\rangle$ and $|L = 2, M_l = 0\rangle$, leaving the $|L = 0, M_l\rangle$ with the final spin-0 Hilbert space and therefore forming the character ${}^1S$.

We therefore find that in the absence of any ligands, the d^2 can be broken down as:

$$d^2 \rightarrow {}^1S + {}^3P + {}^1D + {}^3F + {}^1G \tag{3.19}$$

The relative energies of these subspaces are well understood and is a result of electron-electron repulsion between different orbital occupation configurations that can be calculated using Racah parameters [62]. This creates the left axis of a Tanabe-Sugano diagram where the ground state is ${}^3F$ and with increasing energies for (${}^1D$,${}^3P$),${}^1G$,${}^1S$ respectively.

If one is curious, the single particle wavefunctions of the no-ligand regime can be found by using ladder operators introduced in Sec.2.4.1. For example, the ^1G states highest $M_l = 4$ value can only be composed of when both electrons occupy the $m_l = 2$ orbital: $|L = 4, M_L = 4\rangle = |2, m_l = 2\rangle \otimes |2, m_l = 2\rangle$. Knowing that a lowering operator acting on an arbitrary state will yield $L_- |l, m\rangle = \sqrt{l(l+1) - m(m-1)}\, |l, m-1\rangle$ one can find:

$$L_- |L = 4, M_L = 4\rangle = L_- |l = 2, m_l = 2\rangle \otimes |l = 2, m_l = 2\rangle + |l = 2, m_l = 2\rangle \otimes L_- |l = 2, m_l = 2\rangle \quad (3.20)$$

$$2\sqrt{2}\, |L = 4, M_L = 3\rangle = 2\, |l = 2, m_l = 1\rangle \otimes |l = 2, m_l = 2\rangle + |l = 2, m_l = 2\rangle \otimes 2\, |l = 2, m_l = 1\rangle \quad (3.21)$$

$$|L = 4, M_L = 3\rangle = \tfrac{1}{\sqrt{2}} \left(|l = 2, m_l = 1\rangle \otimes |l = 2, m_l = 2\rangle + |l = 2, m_l = 2\rangle \otimes |l = 2, m_l = 1\rangle \right) \quad (3.22)$$

Firstly we realize that this is indeed the expected expression for a spin-0 system for $M_l = 3$ as the spatial wavefunction is symmetric. Secondly, carrying out similar calculations to the above one, one can construct all 45 microstates. Once a ligand field is introduced however, these states will mix once more as a function of the ligand symmetry and its strength. Although the splittings are generally plotted as each total angular momentum space is splitting shown in Fig.3.5A, the mixed states within a ligand field need not be contained within a total angular momentum character space. The microstates for the weak ligand field regime where electron repulsion can be treated as a simple perturbation, can be found by constructing a secular determinant, a very similar exercise to Sec.3.1.1, where the matrix elements are given by $\langle M_l | \mathbf{V}_{\text{tet}} | M_{l'} \rangle$, where the eigenvalues of this secular determinant show how the orbitals split and evolve as a function of crystal field strength, and the eigenvectors yield the wavefunctions that can be degenerate. The symmetry labels and their energetic evolutions are plotted within a Tanabe-Sugano diagram. An example of d^2 evolution under ligand field is shown in Fig.3.5B.

Now we discuss the very strong ligand field case, shown all the way on the right side of the diagrams in more concrete terms. Under the very strong ligand field strength, we would

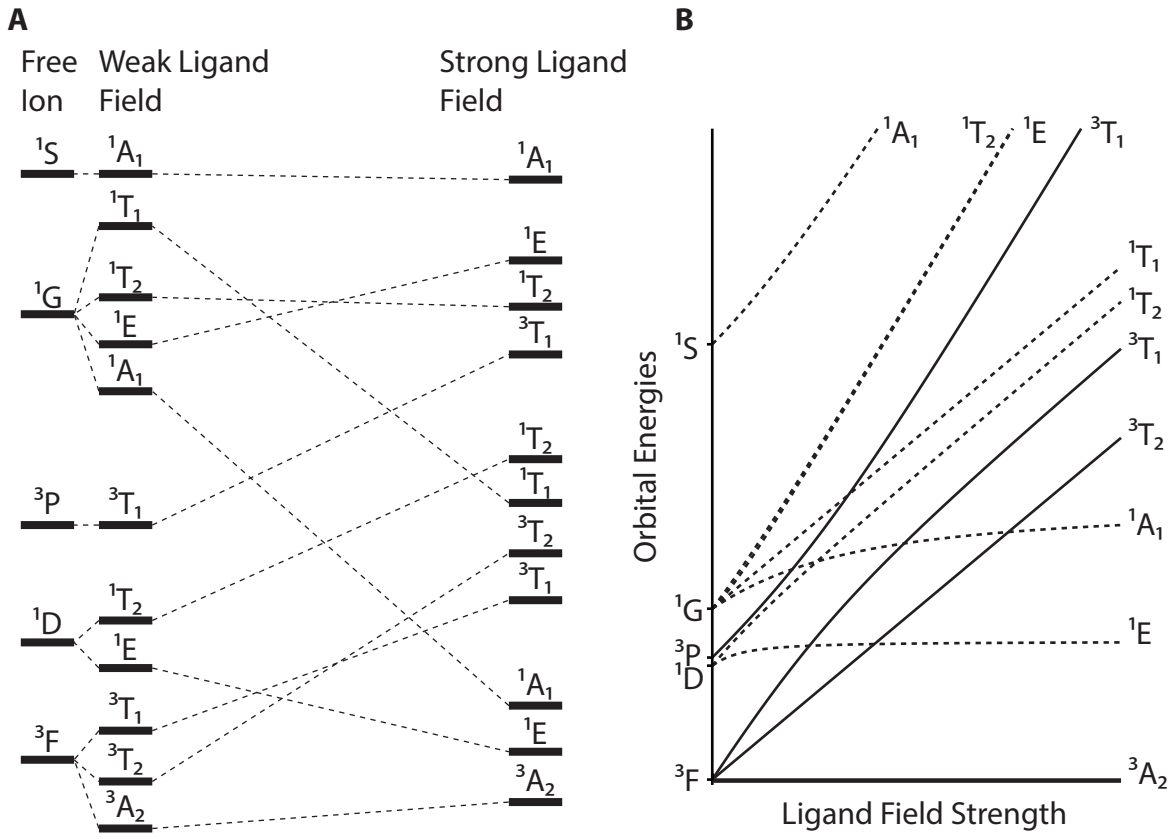

Figure 3.5: (**A**) Configuration and Tanabe-Sugano (**B**) diagrams for d^2 under tetrahedral ligand symmetry. The configuration diagram energies are not to scale, it illustrates how the atomic orbitals split and evolve under increasing ligand strength. Tanabe-Sugano diagram summarizes these results, the dashed lines indicate S=0 orbitals and solid lines show S=1 orbitals. Figure **B** is adapted from wikipedia.

expect the energy splitting between d_e ground state orbitals and d_t excited state orbitals to be very large, therefore the electrons occupying the d_e manifold will be the ground state. Due to electron repulsion interaction, the configuration where each electron is in one orbital will be lower energy as opposed to two electrons occupying the same orbital. Since this is the anti-symmetric orbital configuration, per the discussion in Sec.2.3.1, the spin will be in the symmetric configuration of $S = 1$ and the spatial wavefunction will be anti-symmetric. There is only one such configuration available, and therefore the ground state will be $^3A_2$. Next, the spin-paired electrons will form the anti-symmetric portion of the total wavefunction, while the orbitals will form the symmetric part. As we have seen in Sec.2.3.3, there are three

basis elements, two where both electrons are in one orbital and one entangled state between the two orbitals all of which are $S = 0$. This three dimensional spin-singlet orbital space will a doubly degenerate first excited state ${}^1E$ a higher energy second excited state of ${}^1A_1$. These constitute the 6 total possible configurations two electrons can have in two orbitals. Notice that the electrons in these levels do not jump to a different orbital but stay within the d_e manifold. Even if there is an external electric field, strain or another effect that can shift the absolute energy of the d_e manifold, the relative energies between ${}^1A_1$, ${}^1E$ and ${}^3A_2$ will remain unchanged as they will be mostly moving all together. One can immediately see this from the Tanabe-Sugano diagrams, as the energy difference between ${}^3A_2$, ${}^1E$ and ${}^1A_1$ are roughly flat, independent of the ligand field strength. This is an extremely important property that will allow for narrow transitions and high Debye-Waller factor of d^2 electronic structure under strong tetrahedral symmetry which enables the optical spin interface.

At this point, the next higher energy state is given by transferring an electron from d_e manifold to the d_t manifold. There are 3 orbitally degenerate options and 2 ground states to chose from and each configuration will result in a lower energy $S = 1$ configuration followed by a higher energy $S = 0$ manifold creating the next set of ${}^3T$ and ${}^1T$ structure. In these excited states, since one of the electrons are in the d_t set, the energy splittings between ${}^3A_2$ and T states will be highly ligand field strength dependent, resulting in a broad absorption spectrum. One can carry this analysis out until all possible 45 micro-states are calculated.

3.2.3 d^7 configuration

We will not spend much time here but it is good to mention that this the level structure of Ruby which is Cr^{3+} doped Al_2O_3. This crystal has a octahedral symmetry, and therefore has a d_t ground state and a d_e excited state , as it was discussed at the end of Sec.3.1.1 with 3 valance electrons. Following a similar discussion to d^2 structure, at the high ligand field strength, we expect to see a single spin-3/2 ground state composed of 3 valance electrons occupying the three different ground state orbitals forming the ${}^4A_2$ ground state, and eight

different spin pairing of the 2 electrons ($^2E + ^2T_1 + ^2T_2$) within the same d_t manifold, forming the spin-1/2 excited states. These excited states are also insensitive to ligand field strength (and therefore its fluctuations), which is captured in Tanabe-Sugano diagrams again. This results in similar to d^2 transitions between the excited states and the ground states that are narrow and relatively strain insensitive.

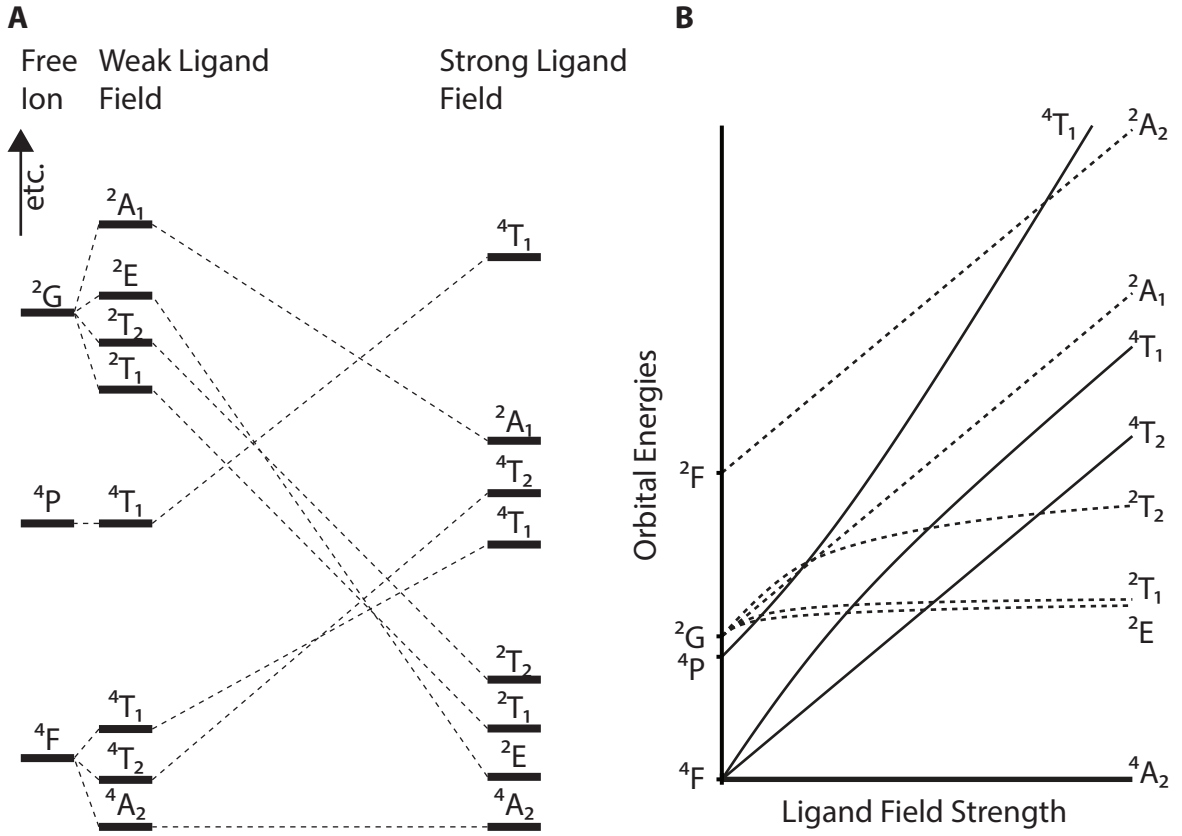

Figure 3.6: (**A**) Configuration and Tanabe-Sugano (**B**) diagrams for $d^3(d^7)$ under octahedral (tetrahedral) ligand symmetry. The configuration diagram energies are not to scale, it illustrates how the atomic orbitals split and evolve under increasing ligand strength. Tanabe-Sugano diagram summarizes these results, the dashed lines indicate S=1/2 orbitals and solid lines show S=3/2 orbitals. Figure **B** is adapted from wikipedia.

3.3 A brief group theory discussion

To summarize what we have done so far, we found the wavefunctions that form the d-orbitals Y_2^m, we characterized how these orbitals shift as a function of ligand field which depends on

the symmetry of the ligands, explored multi electron systems to construct composite wavefunctions, and followed a similar analysis to see how these multi electron systems form the electronic structure. All of these considerations arise from looking at the Slater determinant of the ligand environment ($\det(H_1 - E) = 0$) which highly depends on the symmetry of the system.

Specifically, say, there is a symmetry operation R that leaves the ligand environment unchanged (e.g. $\phi \to \phi + \pi$ rotation for a tetrahedral system) and therefore $[H_1, R] = 0$. Say $|\psi\rangle$ is a normalized eigenvector of H_1, such that $H_1 |\psi\rangle = E_\psi |\psi\rangle$, then $H_1 R |\psi\rangle = E_\psi R |\psi\rangle$. This means that $R |\psi\rangle = \pm |\psi\rangle$ where the sign determines whether the wavefunction is symmetric or antisymmetric under this symmetry operation. Just like the our analysis in Sec.2.4.1, one can also use the eigenvectors of the symmetry operators in the $(Y_l^m)^{\otimes n}$ basis to find the wavefunctions that mimic the symmetry of the system, therefore the electronic structure under the ligand field.

The group theory treatment of orbitals are very well understood and commonly used within chemistry. We will not go into any further discussions in this thesis, as building the necessary mathematics, notation and intuition is not critical to the experimental demonstrations. These techniques, however allow for analysing how the orbitals split under various ligand symmetries, as briefly discussed in the previous section and how they evolve as the symmetry is reduced through *correlation tables*. An example for how the symmetry terms of T_d further split with reduced symmetry are shown below in Table 3.1. The meanings of symmetry elements and labels are discussed in Appendix C.

T_d	D_{2d}	C_{3V}	S_4	D_2	C_{2v}	C_3	C_2	C_s
A_1	A_1	A_1	A	A	A_1	A	A	A'
A_2	B_1	A_2	B	A	A_2	A	A	A''
E	A_1+B_1	E	$A+B$	$2A$	A_1+A_2	E	$2A$	$A'+A''$
T_1	A_2+E	A_2+E	$A+E$	$B_1+B_2+B_3$	$A_2+B_1+B_2$	$A+E$	$A+2B$	$A'+2A''$
T_2	B_2+E	A_1+E	$B+E$	$B_1+B_2+B_3$	$A_1+B_1+B_2$	$A+E$	$A+2B$	$2A'+A''$

Table 3.1: Correlation table for the T_d symmetry. It shows how the orbital characters (rows) further split into new characters, when the symmetry is reduced (columns).

So far we've discussed how the d-orbitals split under the ligand field, how ligand symmetry determines the orbital configurations and that one can use group theory to deduce a lot of the basic characteristics. These considerations demonstrate the flexibility of transition metal ions d-orbitals as a platform to engineer various electronic structures that can be used as spin qubits. To couple the spin degree of freedom with optical degree of freedom we need to discuss transitions between the electronic states.

3.3.1 Transitions

For any operator represented with $\hat{A}$, to be allowed, one needs to satisfy

$$\langle \psi_i | \hat{A} | \psi_f \rangle = \int \psi_i \hat{A} \psi_f \mathrm{d}\tau \neq 0 \tag{3.23}$$

where ψ_i is the initial state and ψ_f is the final state wavefunctions. Since the result of this integral is a scalar value, and the volume element $\mathrm{d}\tau$ is also a scalar quantity, they must

remain unchanged under any symmetry operation. This means $\psi_i \hat{A} \psi_f$ must also remain unchanged under any symmetry operation. Furthermore, if the integrand changes sign, the result must be zero as the positive part would cancel the negative. Therefore, the integral is non zero if and only if the symmetry of the products $\Gamma_i \otimes \Gamma_A \otimes \Gamma_f$ spans the totally symmetric representation A_1, where Γ is the symmetry representation of the state or the operator.

In the T_d symmetry, electric dipole moment $\mathbf{p} = q\mathbf{r}$ transforms as the T_2 symmetry element, so one needs to look at $\Gamma_i \otimes T_2 \otimes \Gamma_f$ to see which electric dipole transitions are allowed shown in Table 3.2.

$\otimes T_2 \otimes$	A_1	A_2	E	T_1	T_2
A_1	T_2	T_1	T_1+T_2	$A_2+E+T_1+T_2$	$A_1+E+T_1+T_2$
A_2	T_1	T_2	T_1+T_2	$A_1+E+T_1+T_2$	$A_2+E+T_1+T_2$
E	T_1+T_2	T_1+T_2	$2T_1+2T_2$	A_1+A_2+2E $+2T_1+2T_2$	A_1+A_2+2E $+2T_1+2T_2$
T_1	$A_2+E+T_1+T_2$	$A_1+E+T_1+T_2$	A_1+A_2+2E $+2T_1+2T_2$	A_1+A_2+2E $+3T_1+4T_2$	A_1+A_2+2E $+4T_1+3T_2$
T_2	$A_1+E+T_1+T_2$	$A_2+E+T_1+T_2$	A_1+A_2+2E $+2T_1+2T_2$	A_1+A_2+2E $+4T_1+3T_2$	A_1+A_2+2E $+3T_1+4T_2$

Table 3.2: Dipole transition products for the T_d symmetry. Green cells contain the totally symmetric representation A_1 and therefore allow a dipole transition while red cells do not.

In the d^1 case for the tetrahedral symmetry, the ground state has an E character and the excited state has a T character. We can read from the table that the transitions between the two are dipole allowed![2] This is also a spin preserving transition, therefore the electronic

2. The spin-orbit effects cause $T \rightarrow E + A$ which can forbid the optical transitions in the perfect T_d symmetry. The dipole transition between A and E states are allowed however in C_{3v}

structures in this configuration will have a fast and therefore bright optical cycle. For example the excited state lifetimes for SiC:V^{4+} [3] and SiC:Mo^{5+}[63] are $\sim 100ns$.

In the d^2 case, under the strong ligand field, the dipole transition between the ground state $^3A_2$ and the first excited state ^1E are not allowed. Furthermore this is a spin flip transition further forbidding the transition. Despite these effects, it is possible to observe emission from this configuration albeit with a long life time of order $\sim$ 100 μs for defects embedded in crystals (e.g. SiC [4, 5] and GaN [64]) and $\sim$ 1 μs for d^2 molecules [1]. There are a few possible explanations for breaking this both dipole and spin forbidden transition [65]. As the T_d symmetry is reduced, shown in Table 3.1, the degeneracy of the first excited state E is lifted, taking A and/or B character. For certain, now reduced symmetries (e.g. S_4 symmetry of Cr^{4+} molecule in Sec.7.1.3), a dipole transition can be allowed between the spin-1 $^3A_2$ ground state and spin-0 excited state. Another possibility is that, depending on the ligand field strength, the E state can be energetically close to the T states, which can result in some mixing between the two, giving the first excited state a spin-1 like character which then could weakly allow for a transition through spin-orbit effects. It is also possible for higher orbitals (e.g. p) to mix with the d-orbitals [66], relaxing some of the selection rules.

Finally when there is centrosymmetric configuration like in the case of O_h (octahedral) symmetry, there is an additional symmetry subscript g or u (Sec.C) which identifies if the the system is symmetric by an inversion center. Inversion symmetry is not applicable to T_d so we did not discuss it previously. I will note though, all of the d-orbitals have g character in O_h symmetry and the dipole transition has character T_{1u}. This means $g \times u \times g = u$ cannot contain the totally symmetric representation of A_{1g} therefore any d to d transition is forbidden under O_h symmetry. Some of the potential mechanisms discussed in the previous paragraph can play a role to relax this consideration, but this additional restriction further pushes the spin pairing decay rate especially in Ruby Al_2O_3:Cr^{3+} to millisecond regimes [67].

The electric dipole transition considerations discussed here can also be applied to other transitions such as magnetic dipole transitions, quadrupole transitions, vibrational spectra or other such effects[3]. The character tables for symmetry groups, their similarity tables and product tables are all well documented and one can easily access them to figure out electronic structure evolution under reduced symmetry and various transitions between electronic levels [68]. This is what we mean, when we say *d*-orbitals can be used to engineer electronic structures for optically active spin qubits. We now know how to localize electrons within the *d*-orbitals, and engineer its electronic structure through ligand design. The final question we should answer is: what properties do we want an ideal optically active spin qubit to have?

3.3.2 Optically Addressable Spin Qubits

To have an optically addressable spin qubit, we must have two properties:

- **Spin**: The spin degree of freedom constitutes the *qubit* part of the transition metal ions. Ideally, the ground state spin should be used as the qubit, otherwise, an excited state spin qubit will be limited by the optical lifetime. Therefore ions with fully occupied orbitals with no valence electrons to form a spin will not be good candidates for spin-qubits. This eliminates d^0 and d^{10} configurations as well as the d^4 configuration in the strong field regime, as the d_e set of orbitals can be filled with 4 electrons, each set made of two anti-parallel electrons with no total spin labeled with ${}^1A_1$.

- **Optical Interface**: An optical-spin interface describes an excited state that is ideally only coupled with one of the ground spin sublevels. This results in spin selective optical emission; that is *bright* spin state emits photons when probed and a different *dark* spin state emits preferably no photons when probed. The motivation for an optical spin interface were discussed in Chapter 1 at great lengths. As we have seen, there are some basic dipole selection rules one may follow to see which transitions are symmetry

3. Magnetic dipole is much weaker than electric dipole since $E = cB$ where c is the speed of light

allowed in Sec.3.3.1, but there are also many non-trivial effects such as spin-orbit, orbital mixing, distortions and/or vibronic couplings. Therefore a lot more theoretical considerations must be used to understand and predict optical spin interfaces. This being said, one of the most direct approaches is using the spin flip transition as a way to couple the ground state with an excited state to form a Λ-like system. This is the strategy we employ for most of the qubits we will discuss that have d^2 configuration.

In the last chapter, Sec.8.2, we will discuss some other important characteristics that optically active spin qubits to have to build the technologies discussed in Chapter 1. There is, however, another important criteria when picking an electronic level structure, which is long spin lifetimes characterized by T_1 and T_2. T_2 time depends mostly on the host material, and is not a function of the ligand engineering aspect. T_1 time, characterizing the spin flip error rate, depends on spin-lattice relaxation where the magnetization of the system can be flipped because of either phonons or nearby other magnetic impurities. There are many possible phonon mediated processes that we will discuss in more detail in Sec.5.3.1 for Cr^{4+} in 4H-SiC. One main mechanism for T_1 decay, called Orbach process, is caused by a close second ground state that the spin can easily be excited to with little phonon energy. This is a limiting factor for many defects with closely spaced ground states such as V^{4+} in 6H- and 4H-SiC that we will discuss in Sec.6.5.1 as well as group-IV in the -1 charge state defects in diamond [69, 70]. Mo^{5+} in 4H-SiC also has doubly degenerate ground state orbital structure, however due to spin-orbit effects, $g_\perp = 0, g_\parallel \simeq 1.6$ and therefore the electron spin is shielded against magnetic flip-flops both with nearby nuclear spins and other paramagnetic defects with $g = 2$ resulting in long T_1 times [63]. On the flip side[4], the high spin-orbit effect resulting in $g_\perp = 0$ limits the magnetic driving of the ground state, inhibiting its control; a great example of the *nature hardly lets you win* principle.

One can limit Orbach processes by selecting a symmetry and charge state to produce a level structure that have spin bearing orbitally non-degenerate ground state to get long

4. Pun intended.

T_1 times. For transition metal based qubits, these are d^2 (Sec.3.2.2) and d^7(Sec.3.2.3) configurations as well as d^5 in weak ligand field regime in tetrahedral symmetry. This criteria already constrains the configuration space to investigate. The strain insensitive spin-flip optical transitions of the d^2 symmetry allows us to resolve individual spin sublevels optically and hence form an optical spin interface which satisfies the second criteria. In order for this optical interface to exist, however, the transition metal must be under the strong ligand field regime, which SiC and GaN provides, as well as the deliberately picked aryl ligands for the molecular spin qubits. As we will see in Chapter 6, the T_1 time of V^{4+} in SiC indeed suffers due to closely spaced ground states and the the optical spin interface is still under investigation. Nevertheless this is an exciting qubit system to study because the optical transition is both bright and lies within the telecom O-band. Although V^{4+} lacks high fidelity optical spin initialization and readout, we still can optically characterize both 4H- and 6H-SiC:V^{4+} spins since any imbalance in population due to selective excitation will result in contrast. Therefore, d^2 level structure produced by Chromium 4+ in SiC, GaN (Chapters 4 and 5) as well as organometallic compounds (Chapter 7), and Vanadium 4+ in SiC (Chapter 6) are great candidates to demonstrate the power and flexibility of transition metal ions as optically addressable spin qubits.

Chapter 4

Identification and characterization of as grown Cr^{4+} in 4H-SiC and GaN

In this chapter we are going to discuss the identification and characterization of chromium 4+ photoluminescence and ground state spin properties through spectroscopy in as-grown samples. This is the first necessary step to start exploring the d^2 electronic configuration in strong tetrahedral ligand field of transition metal ions as optically accessible spin qubits. The figures and some of the language in this chapter are reprinted with permission from [5].

4.1 Background

Chromium 4+ in SiC and GaN are observed to substitute the silicon [71, 72] and gallium [64, 73, 74] sites respectively illustrated in Fig.4.1**A,B**. Within the 4H-SiC, there are two distinct silicon sites, quasi-cubic and quasi-hexagonal, whereas within GaN there is only one: the hexagonal site. Previous studies investigating chromium doped 4H-SiC during growth observed two distinct, sharp, optical emission lines at 1.1583 and 1.1898 eV under above bandgap, ultraviolet excitation at cryogenic (T = 6 K) conditions. These emissions are attributed to the zero phonon lines (ZPL) of SiC:Cr_A(quasi-cubic) and SiC:Cr_C(quasi-

hexagonal) sites. These sharp emissions split into 3, or 6 transitions under large, multi-Tesla magnetic fields, depending on the field orientation where the set of 3 transitions split as $g \sim 2$ Zeeman relation shown in Fig.4.1**C**. The additional peak replicas arise from the excited splitting with low g-factors due to spin-orbit effects (Sec.2.4.2) at high fields [71]. These transitions point at the expected and extensively discussed electronics structure of d^2 configuration under strong tetrahedral symmetry in Sec.3.2.2, namely between the $^3A_2$ ground state and ^1E excited state. Furthermore, these observed transitions have weak phonon sidebands and long lifetimes which is consistent with these assignments.

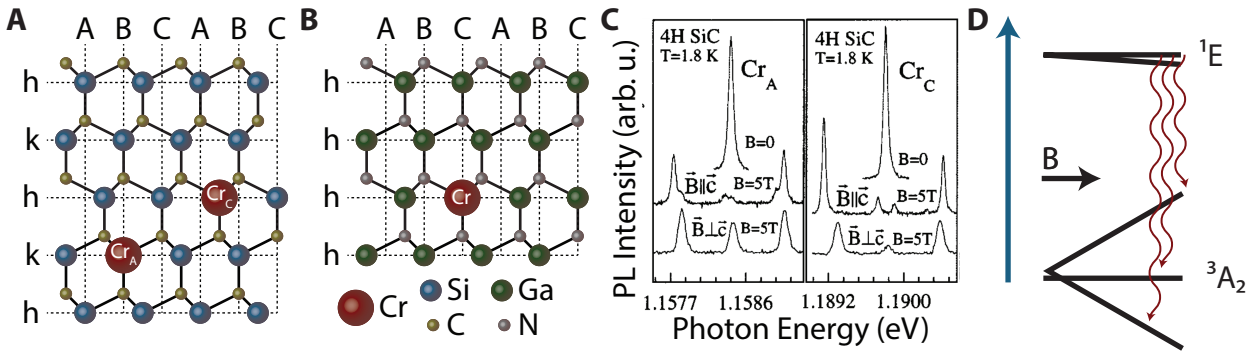

Figure 4.1: Structure of chromium 4+ defects in SiC and GaN and its optical identification. An illustration of substitutional Cr^{4+} ions in (**A**) silicon sites of a 4H-SiC lattice and (**B**) of gallium site of GaN. (**C**) is reprinted from [71], with the permission of AIP Publishing and shows two sharp optical transitions visible under above band gap excitation attributed to SiC:Cr_A(k-site) and SiC:Cr_C(h-site) at 1.1583 eV and 1.1898 eV respectively split according to the expected level structure under high fields illustrated at (**D**)

It is a common practice to compensation dope GaN with Fe^{3+} to pin the Fermi level midgap. During this doping process, unintentional Cr^{4+} is also introduced to the crystal. Within GaN similar measurements reveal a sharp ZPL at 1.193 eV, with weak sideband emission, consistent, again, with the d^2 configuration of Cr^{4+}.

4.2 Samples

The samples under study include a $\sim 5 \times 8$ mm piece of chromium doped 4H-SiC grown epitaxially on an off-axis, n-type 4H-SiC substrate, as well as a 1.0 cm^2 freestanding bulk

semi-insulating GaN substrate shown in Fig.4.2. The 4H-SiC:Cr^{4+} epilayer was grown via high-temperature chemical vapor deposition (HTCVD) at 2100°C to a thickness of 60 μm with a chromium density of $10^{15} - 10^{16}$ cm^3. The GaN sample is 468 μm thick and was grown via hydride vapor phase epitaxy (HVPE) as a commercial substrate by Kyma, Inc. (part no. GB.SE.010.DSP.D). Other GaN samples purchased from Kyma with nominally identical specifications exhibit varying amounts of Cr^{4+} luminescence, depending on the growth batch.

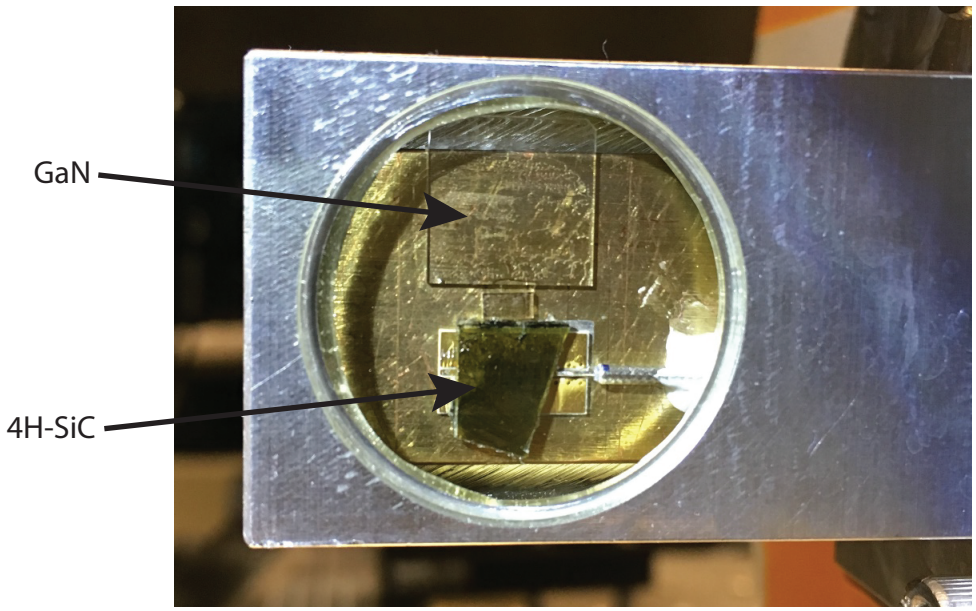

Figure 4.2: GaN and SiC samples grown with chromium dopants. The samples are pictured within the flow cryostat setup where the SiC sample is mounted on a coplanar waveguide antenna for microwave excitation.

The SiC sample looks dark and opaque, likely due to low sample quality. It is possible to visually observe qualitative crystal imperfections with valleys, crevasses and domains indicating a high strain profile across the sample.

4.2.1 Photoluminescence Characterization

To confirm the existence of the Cr^{4+} defects, we use a confocal microscopy setup, similar to the one described in Sec.D.1. The samples are loaded in a Janis flow cryostat set to T = 30

K, and they are off-resonantly excited with a Ti:sapphire laser tuned to an energy far above the 1st excited state (710 nm/1.74 eV). The laser is focused and the emission is collimated with a lens (f = 20 mm) giving a spot size of 30 μm. Cr ions are excited off-resonantly from the $^3A_2$ ground state to ^3T excited state which then rapidly decays nonradiatively to the ^1E state and photoluminescences as it decays back to the $^3A_2$ ground state (Fig.4.3**A**). This emissions is collected with a spectrometer and a liquid nitrogen cooled InGaAs Princeton Instruments OMA-V near infrared pixel array. The observed spectra shown in Fig.4.3**B** matches with the reported Cr^{4+} emission in the literature [64, 71].

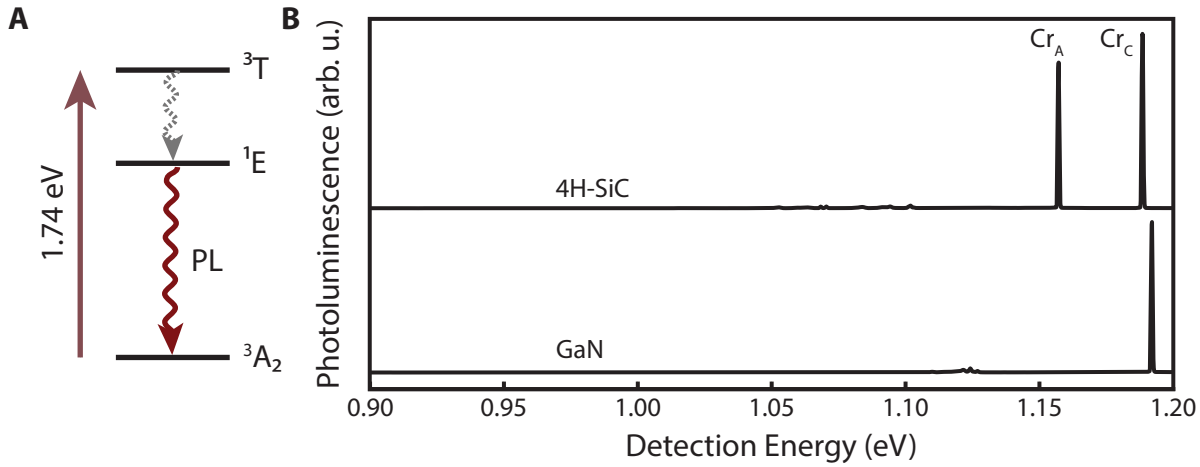

Figure 4.3: Photoluminescence of GaN and SiC samples grown with chromium dopants. (**A**) Illustration of off-resonant excitation of Cr^{4+} to ^3T excited state which then rapidly decays nonradiatively to the ^1E state and photoluminescences as it decays back to the $^3A_2$ ground state. (**B**) The photoluminescence spectra of Cr^{4+} in 4H-SiC and GaN under 1.74 eV (710 nm) excitation at T = 30 K.

An important figure of merit is called the Debye-Waller (DW) factor, which is the ratio of light emitted from the ZPL over the entire spectral range. Remote defect spin entanglement experiments rely on interfering two indistinguishable photons to erase the information of the defect origin [75]. If the photons are distinguishable for example due to energy differences, then this scheme will not work. Therefore, it is important to have a large DW factor where most of the emitted light comes from the indistinguishable ZPL portion of the spectrum. In order to carefully calibrate the DW factor we accounted for all of the possible wavelength

dependent absorptions within the optical path with a precalibrated white light source.

We integrate the calibrated photoluminescence data across two regions: light emitted within the ZPLs only (blue shaded regions), and all light emitted by the chromium impurities (both the red and blue shaded regions together). Because there are two Cr^{4+} impurity sites in 4H-SiC with overlapping emission energies, it is difficult to evaluate them separately. Therefore, we make the assumption that they possess relatively similar radiative efficiencies and consider them together as a whole. We find that the fraction of light emitted in the ZPLs is 75%. Evaluation of GaN:Cr luminescence is complicated by the fact that it is situated on top of the low-energy tail of Fe^{3+} luminescence. We compensate for this by approximating this tail as a straight line, and determine the slope of this line by assuming that the base of the Cr^{4+} ZPL feature should normally lie at the dotted blue line. With this approximation, we determine the ZPL contains 73% of the overall impurity luminescence, which is similar in magnitude to our result in 4H-SiC.

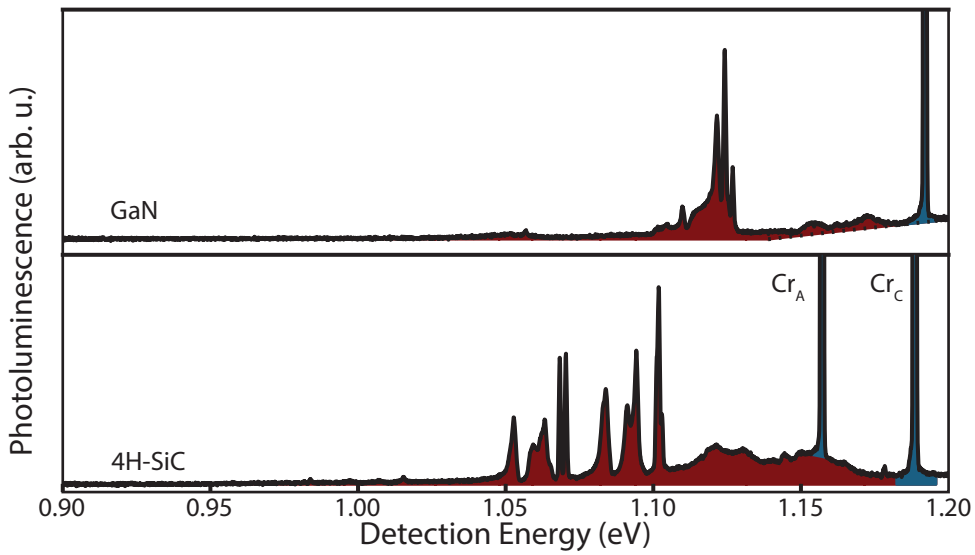

Figure 4.4: Debye-Waller factor measurement of GaN:Cr^{4+} and SiC:Cr^{4+}. The close up photoluminescence data shows the phonon-sideband structure. Blue shaded regions mark the zero-phonon line emissions while the red shaded region marks the remaining luminescence in the phonon sideband.

4.3 Photoluminescence Excitation

To characterize the optical properties only between the ^1E first excited state $^3A_2$ ground state (Fig.4.5**A**) we switch to the continuously tunable, narrow line laser with a dichroic mirror at 1090 nm that reflects the sideband emission to the detector. Sweeping the laser tone over the tunable window of 1035-1075 nm and picking up 1% of the excitation light for precise wavelength calibration with a wavemeter, we observe sharp increases at 1.1584 and 1.1898 eV for 4H-SiC (Fig.4.5**B**), and 1.193 eV for GaN (Fig.4.5**C**) that match the ZPL energies observed in PL measurements of the same samples, demonstrating that we are able to resonantly excite all three forms of chromium ions with the narrow-linewidth, tunable laser.

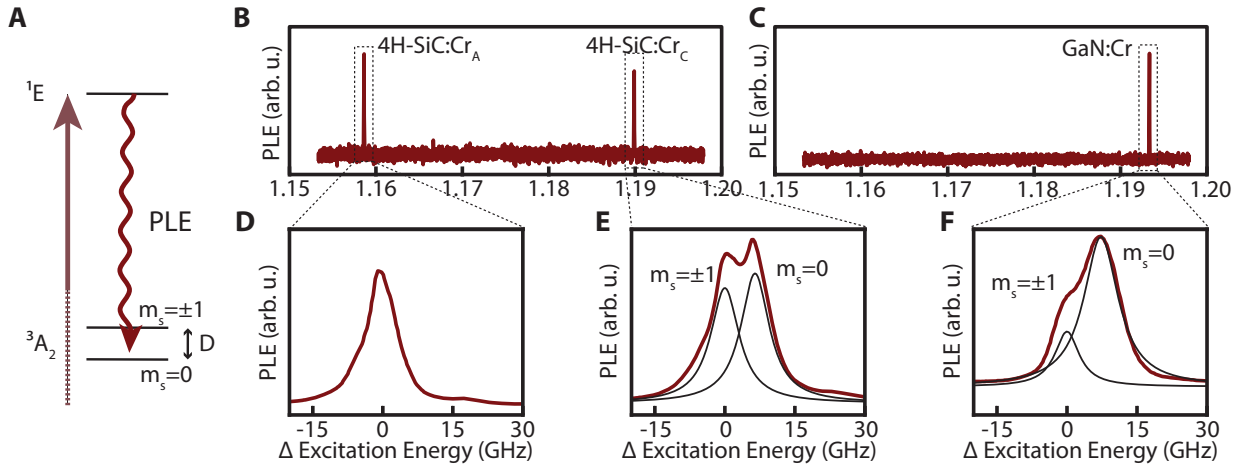

Figure 4.5: Photoluminescence excitation of GaN:Cr^{4+} and SiC:Cr^{4+}. The narrow line laser is scanned over the Cr ZPL energies (**A**) while the sideband is collected at T = 30 K. There are two sharp peaks at 1.1584 eV and 1.198 eV within the 4H-SiC sample (**B**) for SiC:Cr_A and SiC:Cr_C respectively and one sharp peak within the GaN sample (**C**). Fine scans for (**D**) SiC:Cr_A, (**E**) SiC:Cr_C and (**F**) GaN:Cr with fits to the data for the latter two panels are shown, where spin sublevels of the electronic ground state can be resolved optically at zero magnetic field.

Fine frequency scans reveal further details. While only a single maximum is resolved in the PLE signal for 4H-SiC:Cr_A ions (Fig.4.5**D**), two maxima are clearly observed for both the 4H-SiC:Cr_C (Fig.4.5**E**) and GaN:Cr (Fig.4.5**F**) impurities. In these two latter cases, we

fit the data to the sum of two Lorentzians, where this functional form was derived at Sec.2.17 for a two level transition (in the context of spin):

$$\mathrm{PLE}(f) = \frac{A}{\pi}\left(\frac{\Gamma/2}{(f-f_0)^2+(\Gamma/2)^2}\right) + \frac{B}{\pi}\left(\frac{\Gamma/2}{(f-f_1)^2+(\Gamma/2)^2}\right) + C \tag{4.1}$$

where f_0 and f_1 (A and B) are the central frequencies (amplitudes) of the two Lorentzians, Γ is the full-width at half-maximum (FWHM) linewidth of both Lorentzians, and C is a constant to account for nonzero background offset in the signal. For the 4H-SiC:$\mathrm{Cr_C}$ defect, we find that the linewidth of these features is $\Gamma = 7.42(7)$ GHz at 30 K and 0 G, with an energy splitting between the two maxima of $f_0 - f_1 = 6.46(5)$ GHz. For the GaN:$\mathrm{Cr^{4+}}$ ions, these values are $\Gamma = 8.28(14)$ GHz and $f_0 - f_1 = 6.91(5)$ GHz. Note that in the case of 4H-SiC:$\mathrm{Cr_C}$, the energy splitting between the two peaks is roughly similar to the previously reported values of 6.70 GHz [72] and 6.0 GHz [71] given for the ground state zero-field spin splitting. This suggests that these two peaks correspond to the $m_s = 0$ and $m_s = \pm 1$ spin sublevels of the ion's purported $S = 1$ ground state, and we tentatively label them as such for ease of description in the measurements that confirm this identification detailed below.

4.3.1 Spin sublevel identification

To confirm that the two peaks observed within the SiC:$\mathrm{Cr_C}$and GaN:CrZPLs and a potential hidden structure within SiC:$\mathrm{Cr_A}$, we first study the effect of magnetic field when it is applied along the c-axis of the crystal at 30 K for all $\mathrm{Cr^{4+}}$ sites. We see that the PLE line shape indeed changes as the magnetic field is increased from 13–2500 G (Fig.4.6**A**, **B**, **C**), although the exact nature of this evolution is somewhat obscured by the inhomogeneous broadening of the optical transitions. By converting the data into a differential measurement in which the data at B = 13 G is subtracted from each PLE scan Fig.4.6 **D**, **E** and **F**, we see more clearly what occurs. As the magnetic field is applied, a dip forms that is flanked symmetrically on either side by two small peaks. This dips are centered at the same frequency as the feature

labeled $m_s = \pm 1$ in Fig.4.5**D**, **E** and **F** respectively, and grow in magnitude as the field is increased. Similarly, the two peaks on either side for each site grow and appear to move slowly outward away from the dip. This is the expected behavior for an optical transition between an excited state spin singlet and a ground state spin triplet; under the application of a magnetic field, the degenerate optical transitions connecting the $m_s = \pm 1$ sublevels of the ground state to the singlet excited state will begin to split apart in energy according to the Zeeman effect discussed in Sec.2.2.1. Note that no signal related to the $m_s = 0$ sublevel is observed in the differential data since its energy remains unchanged by the magnetic field.

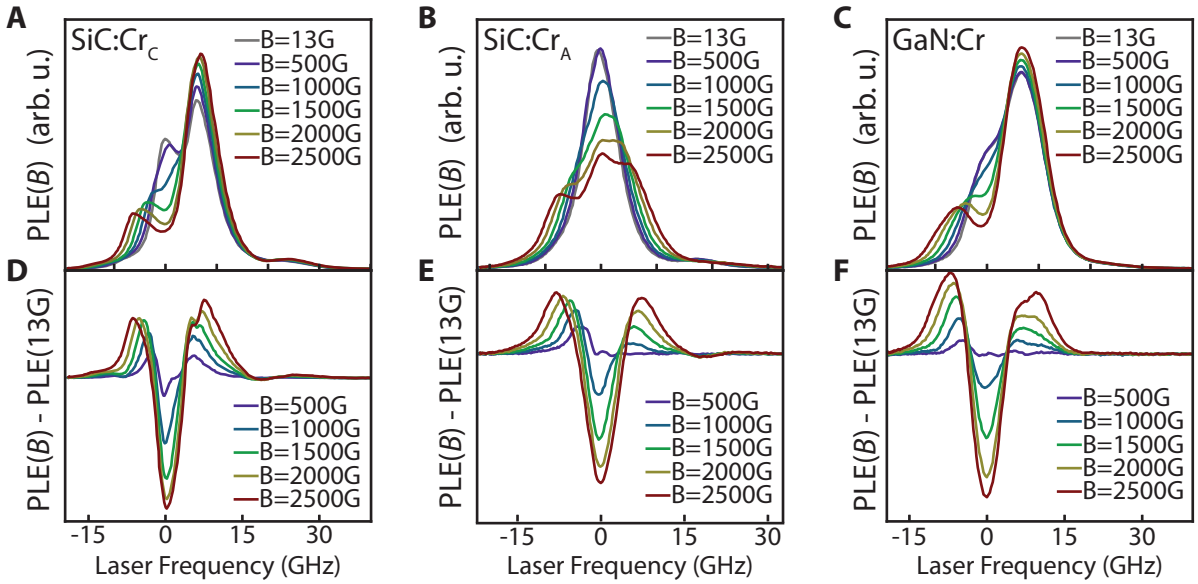

Figure 4.6: SiC:Cr^{4+} (**A**, **B**) and GaN:Cr^{4+}(**C**) PLE spectrum as a function of c-axis magnetic field at T = 30 K. The effect of the magnetic field on the SiC:Cr_C(**D**), SiC:Cr_A(**E**) and GaN:Cr(**f**) PLE spectrum is clarified by subtracting their respective B = 13 G data from the spectra taken at higher fields. With increasing magnetic field, a single dip forms at the energy corresponding to the $m_s = \pm 1$ transitions. Simultaneously, two peaks emerge on either side while moving symmetrically outward. This is the behavior expected from the proposed spin singlet to spin triplet optical transition.

4.3.2 Spin polarization

We can characterize the magnetic field dependent behavior more precisely at lower temperatures using optical spin polarization. According to the level structure discussed in Sec.3.2.2

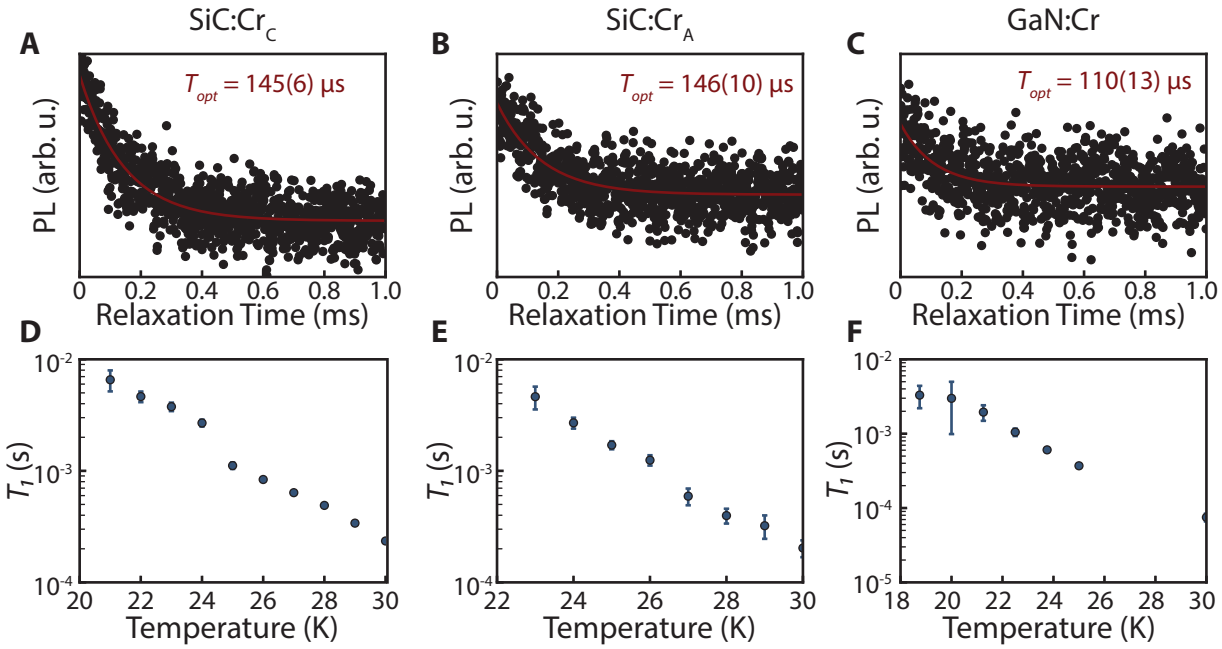

Figure 4.7: SiC:Cr^{4+} and GaN:Cr^{4+}optical and spin lifetime. (**A**-**C**) Ions are excited non-resonantly with 710 nm light at T = 20 K and a monochromator in the collection path is used to collect only the ZPL emission. A fit to the data reveals an optical decay time for SiC:Cr_C(**A**) 145(6) μs, SiC:Cr_A(**B**) 146(10) μs and GaN:Cr(**C**) 110(13) μs. T_1 time of of (**D**) SiC:Cr_C, (**E**) SiC:$Cr_A$and (**F**) GaN:Crspins as a function of temperature. Note that T_1 is $\sim 45\times$ longer than T_{opt} near 20 K for SiC:Cr_C. Error bars are 95% confidence intervals. All the data is taken at B = 0 G.

and Fig.4.5**A**, selective optical excitation of one ground state spin sublevel with a narrow-linewidth laser will pump the system into another sublevel via resonant excitation followed by spontaneous emission. A polarized ion will then remain dark and inaccessible to the laser until a spin-flip occurs. As shown in Fig.4.7**D**-**F**, this phenomenon allows us to measure the spin-lattice relaxation time T_1 as a function of temperature. To measure this parameter, the ensemble is first pumped into the $m_s = \pm 1$ sublevels, using a 500 μs long resonant laser pulse. After waiting for a predetermined time τ, the degree of remaining spin polarization is measured optically using a second 500 μs long laser pulse. The spins are then allowed to relax fully for 25 ms before the pulse sequence is repeated. At each value of τ, the pulse sequence is repeated for several seconds while PLE emission is collected. After each exposure, the same experiment is repeated with no delay between the laser pulses (a continuous

1 ms laser pulse). This control data is then subtracted to reveal the effect of the delay τ. The duty cycle of the laser is kept constant throughout the entire T_1 measurement. This all optical measurement puts a lower bound on the spin-relaxation time, as there may be other, for example charge related spin-reset mechanisms. Nevertheless, we observe a T_1 time of at least 1 ms at for all Cr species below T = 23 K.

These measurements can be compared to the optical relaxation time T_{opt} of the ions measured at T = 20 K shown in Fig.4.7**A**-**C**. The optical relaxation time is measured by exciting the ensemble with the off resonant laser pulse and then monitoring the PL that follows as a function of time. This measurement is repeated for several seconds to build up sufficient signal. The optical signal of SiC:$Cr_A$and SiC:$Cr_C$are differentiated with a spectrometer by only detecting from their ZPL's. At temperatures below $\sim$ 20 K, the spin-lattice relaxation time T_1 of all Cr ions becomes much longer than the optical relaxation time $T_{\text{opt}} = 145$ μs and $T_{\text{opt}} = 110$ μs for 4H-SiC:$Cr^{4+}$and GaN:Cr^{4+}respectively.

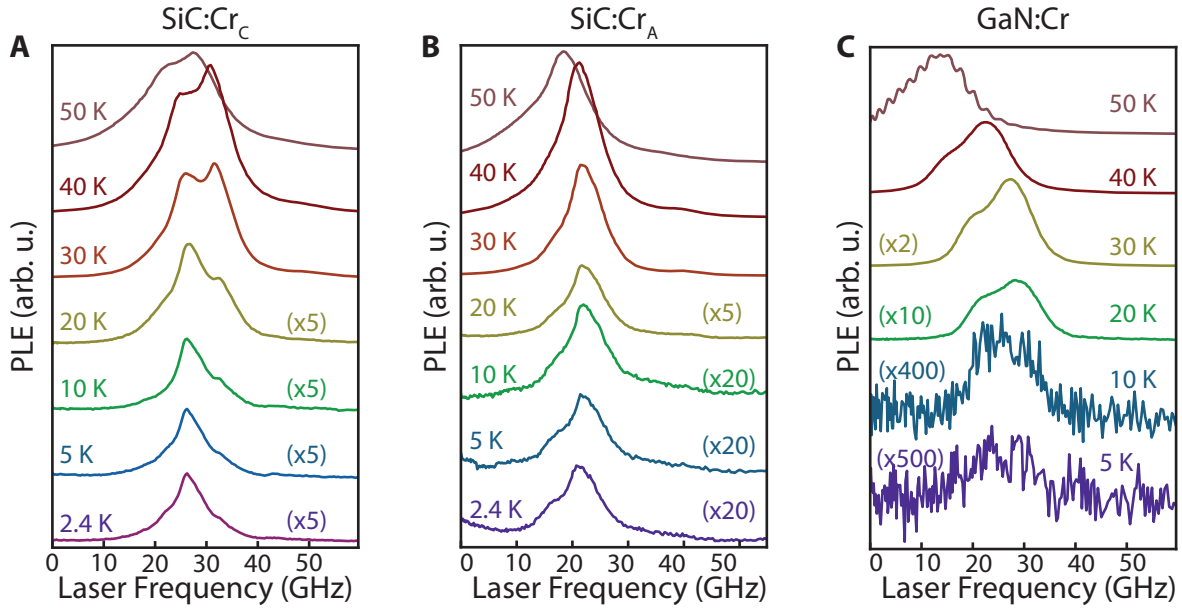

Figure 4.8: PLE spectra of SiC:Cr^{4+} and as a function of temperature. Spectra taken at T = 20 K and below multiplied by a factor for clarity.

As a result, the PLE signal is substantially reduced at lower temperatures due to the long-lived optical spin polarization within the subensemble of ions excited by the laser (Fig.4.8).

4.3.3 Optical PLE Recovery

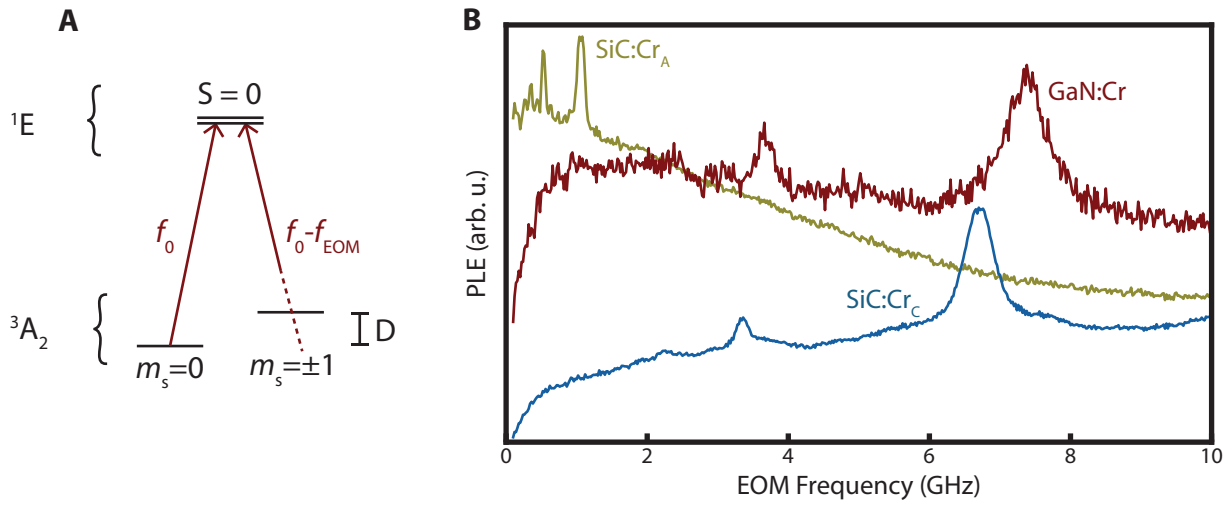

Figure 4.9: Optical home recovery of SiC:Cr^{4+} and GaN:Cr^{4+} at T = 15 K and B = 0 G. (**A**) Experimental illustration of hole recovery. Cr spins are polarized into dark $m_s = \pm 1$ sublevels via resonant optical excitation of $m_s = 0$ sublevel. Recovery of the PLE signal is observed when a second laser tone is at $f_{\mathrm{EOM}} = D$. (**B**) D is measured 6.711(1), 1.064(4) and 7.252(3) GHz for SiC:Cr_{C}, SiC:$Cr_{\mathrm{A}}$and GaN:Crrespectively.

A recovery of luminescence should be observed if both spin sublevels are excited simultaneously. To test this assumption, we perform two-color experiments on the defect ensemble at T = 15 K and $B = 0$ G. We set the laser frequency f_0 to the frequency of the $m_s = 0$ peaks for all Cr species. We then add optical sidebands to the laser emission at $f_s = f_0 + f_{\mathrm{EOM}}$ by modulating the EOM with a microwave signal in the range of 0–10 GHz (Fig.4.9**A**). If we are indeed polarizing the impurity spins through resonant optical excitation at f_0, then an increase in PLE should be observed when $f_{\mathrm{EOM}} = D$, the zero-field spin splitting of the ground state. As shown in Fig.4.9**B**, this is, in fact, what we observe. Fits to the data reveal the D value of 6.711(1), 1.064(4) and 7.252(3) GHz for SiC:Cr_{C}, SiC:$Cr_{\mathrm{A}}$and GaN:Crrespectively, which are consistent with the splitting measured between the two PLE maxima of Fig.4.3**E**,**F**, for SiC:$Cr_{\mathrm{C}}$and GaN:Cras well as with the reported values given in Refs. [71, 72]. The D value of SiC:$Cr_{\mathrm{A}}$is also consistent with the apparent single PLE peak at low magnetic fields, as the inhomogeneous PLE linewidths are much larger than the D

value which prevents resolving the multi-peaked structure. Additional features observed at D/n GHz for integer n are measurement artifacts resulting from the n^{th} order sideband harmonics generated by the EOM.

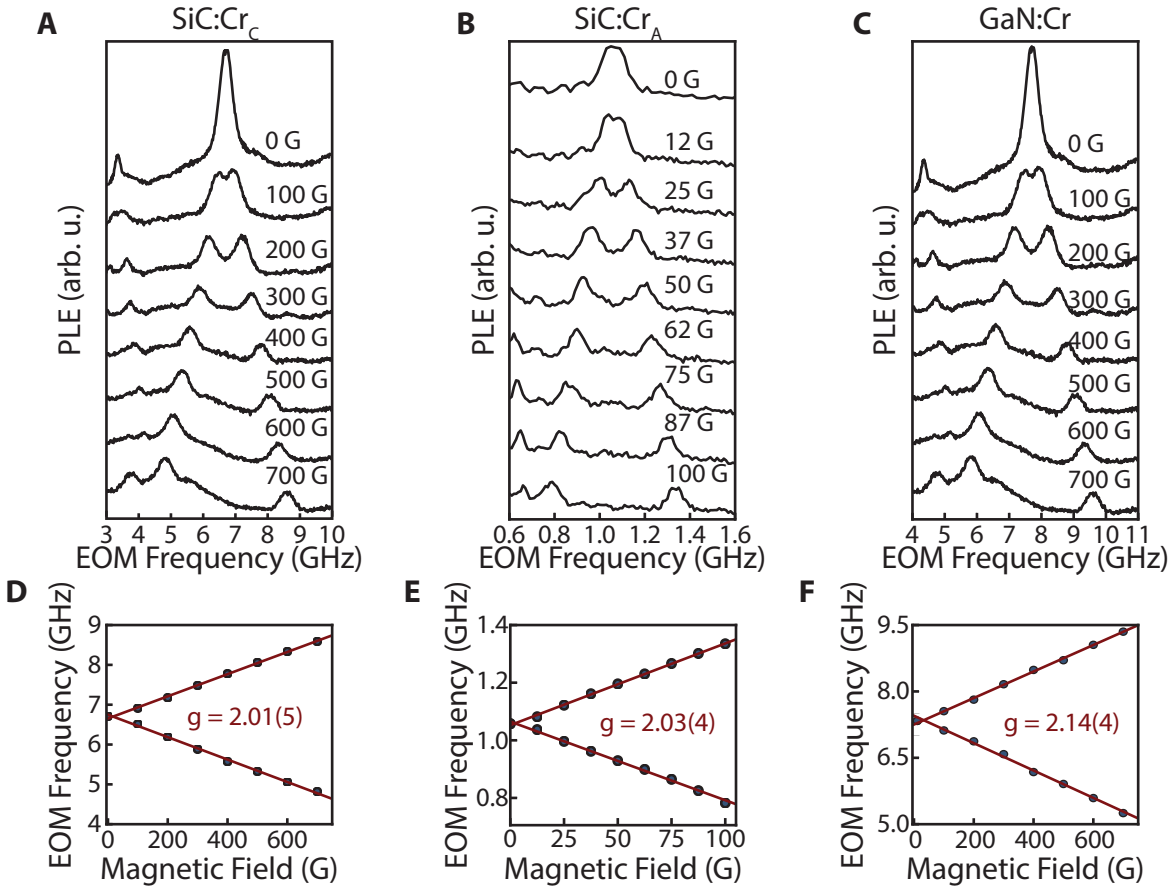

Figure 4.10: Optically measuring ground state Zeeman splitting of SiC:Cr^{4+} and GaN:Cr^{4+}at T = 15 K and B = 0 G. (**A**-**C**) Two-color excitation experiment as a function of magnetic field applied along the crystal c-axis. The single feature at Fig.4.9**B** splits in two as expected for the electronic structure shown in Fig.4.9**A**. (**D**-**F**) Fits to the peaks in (**A**-**C**) reveal a clear Zeeman relationship with g of 2.01(5), 2.03(4), 2.14(4) for SiC:Cr_C, SiC:$Cr_A$and GaN:Crrespectively . Error bars are 95% confidence intervals, which are $\sim$ 2 MHz and smaller than the point size. Additional features at lower frequencies are artifacts due to higher order optical sidebands generated by the EOM.

Importantly, the linewidth of the hole-recovery peak at the corresponding D values are much narrower (489(5), 128(4), 773(8) MHz for SiC:Cr_C, SiC:$Cr_A$and GaN:Crrespectively)

than the PLE linewidths observed in single-color experiments at 30 K in Fig.4.5. This is because we probe only a subpopulation of the impurity ensemble in these two-color measurements so that the resulting linewidth is set by factors such as the laser linewidth, laser stability, and ion spectral diffusion [76]. This narrow linewidth allows us to very clearly observe the Zeeman splitting, as a magnetic field is once again applied along the crystal c-axis. Using fits to this data, we plot the evolution of this splitting as a function of magnetic field strength. A Zeeman relationship consistent with an S = 1 system is clearly apparent, with a linear fit revealing a g-factor of 2.01(5), 2.03(4), 2.14(4) for SiC:Cr_C, SiC:$Cr_A$and GaN:Crrespectively.

4.3.4 Optically Detected Magnetic Resonance

An increase in the PLE signal at low temperatures will also occur if we apply microwave radiation resonant with the ground state spin splitting energy. This enables optically detected magnetic resonance (ODMR) of the optically polarized spin ensemble. In Fig.4.11, we excite the sample at T = 15 K with a single optical frequency tuned to the center of the $m_s = 0$ optical transition. We then apply continuous microwave excitation to the sample while scanning the microwave frequency between 0–10 GHz. At zero magnetic field, a single resonance is observed at $6.707, 1.063$ GHz for SiC:$Cr_C$and SiC:Cr_Arespectively, consistent with the data in Fig.4.9. The ODMR data for the GaN:Crspins exhibits a 'dead spot' at ~ 7.2 GHz where the signal drops to zero. This is an experimental artifact due to low microwave transmission to the sample in this frequency range. In the plots, the PLE contrast is defined as $\Delta\text{PLE} = (I_{ON} - I_{OFF})/I_{OFF}$, where $I_{ON(IOFF)}$ is the integrated intensity of the phonon sideband emission when the microwave driving field is on (off). Therefore, the intensity of the phonon sideband roughly doubles at B = 0 G under these driving conditions. The observed contrast is a function of many competing rates including spin T_1 time, spectral overlap of various transitions and the microwave driving strengths. The hole recovery process, and the relevant rates and therefore the contrast will be discussed at great length

in the next chapter (Chapter 4).

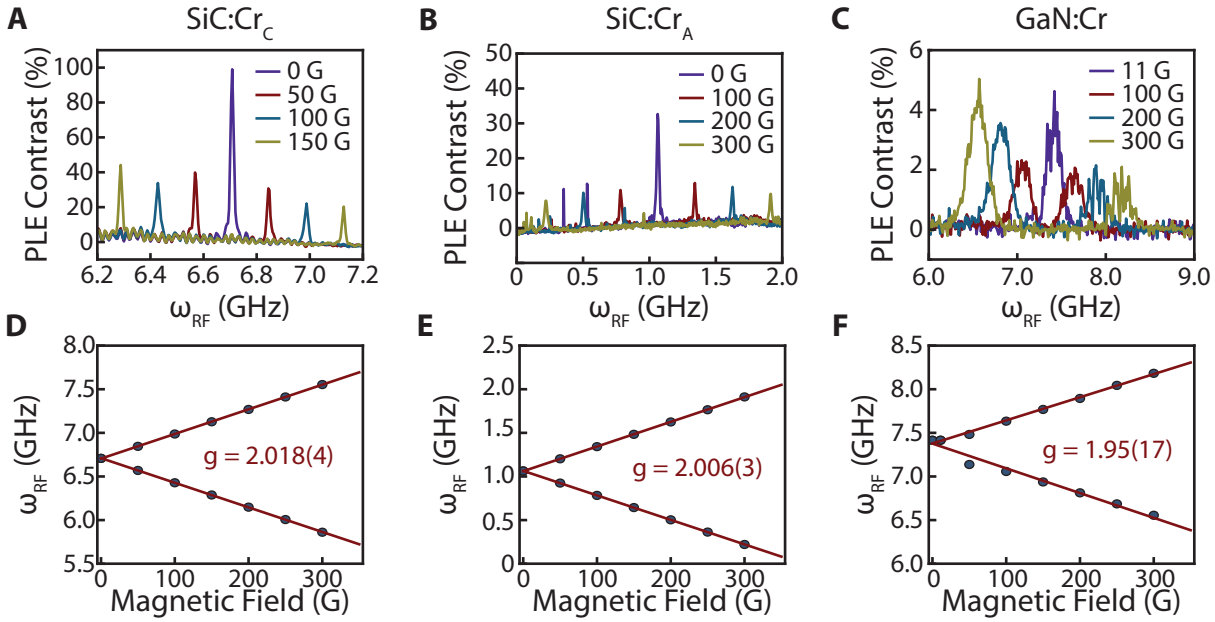

Figure 4.11: ODMR of SiC:Cr^{4+} (**A**, **B**) and GaN:Cr^{4+}(**C**) at T = 15 K as a function of c-axis magnetic field. Spins are polarized into the $m_s = \pm 1$ sublevels via resonant excitation of $m_s = 0$ optical transition. When ω_{RF} is resonant with the spin splitting energy, the PLE signal increases. Small oscillations seen at the base of the signal are artifacts due to imperfect transmission in the microwave driving lines. Fits to ODMR peaks as a function of magnetic field reveal a clear Zeeman relationship consistent with an S = 1 spin system with a g of 2.018(4) (**D**), 2.006(3) (**E**) and 1.95(17) (**F**) for SiC:Cr_{C}, SiC:$Cr_{\mathrm{A}}$and GaN:Crrespectively. Error bars are 95% confidence intervals, which are $\sim$ 0.1 MHz and smaller than the point size.

As a magnetic field is applied, the resonance splits into two roughly equal peaks, as expected for an S = 1 Zeeman system, with a fit yielding a g-factor of 2.018(4), 2.006(3) and 1.95(17) for SiC:Cr_{C}, SiC:$Cr_{\mathrm{A}}$and GaN:Crrespectively. These observations are identical to those measured using two-color optical excitations in Fig.4.10 and further confirm that we have been probing the ground state spin of this system. A fit to data taken at lower microwave power to reduce power broadening and higher magnetic fields to clearly resolve a transition, reveals linewidths of $8.6(5), 11.95(2), 231(14)$ MHz for SiC:Cr_{C}, SiC:$Cr_{\mathrm{A}}$and GaN:Crrespectively. This corresponds to an inhomogeneous spin coherence time of $T_2^* = 1/(\pi\Gamma) = 37, 26, 1$ ns in the same order. We note, however, that the 4H-SiC sample under

study likely has high variation of local strain and is likely contaminated with other paramagnetic impurities that may limit the coherence times during the doped growth. As we will see in Chapter 4 improvements in materials quality will lead to increases in observed coherence times. The measured $\sim 27\times$ larger ODMR linewidth for GaN:Cris expected due to interactions with the surrounding nuclear spin bath within GaN.

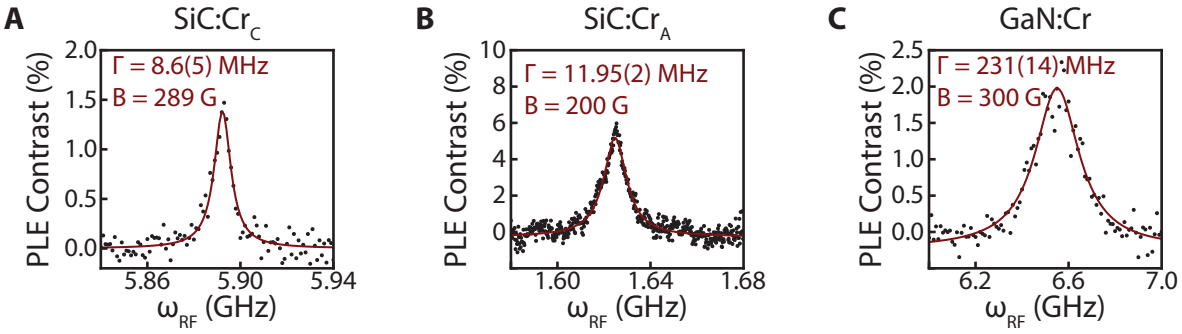

Figure 4.12: Low power ODMR at T = 15 K of (**A**) SiC:Cr_Cat B = 289 G, (**B**) SiC:Cr_Aat B = 200 G and (**C**) GaN:Cr^{4+}at B = 300 G all in c-axis magnetic field. The non power broadened linewidth yield 8.6(5), 11.95(2), 231(14) MHz for SiC:Cr_C, SiC:$Cr_A$and GaN:Cr, which correspond to a T_2^* of 37(2), 26(0), 1.4(1) ns respectively.

4.4 Summary

In this chapter, we have shown that Cr^{4+} ion spins in 4H-SiC and GaN can be directly manipulated with a narrow-linewidth laser tuned to resonance with the first excited state ZPL optical transition. The ensemble optical linewidths we observe are similar in magnitude to the zero-field spin splitting of the electronic ground state, which enables ensemble optical spin polarization and measurement at liquid helium temperatures and low magnetic fields. This capability was used to precisely determine the g-factor and zero-field spin splitting D of all three spin species. Careful optical characterization shows that SiC:Cr^{4+}has more than 75% of the emitted luminescence from the first excited state within the narrow ZPL optical transitions, which form a very simple lambda structure with no competing intermediate transitions other than those of the weakly coupled phonon sideband. The ions, therefore,

exhibit quite atomlike optical properties, while also being embedded within semiconductor hosts amenable to advanced optoelectronic device design. This suggests their use as quantum emitters that couple efficiently to chip-scale, integrated photonic control structures—an effort that depends critically on limiting both intrinsic and extrinsic sources of optical and nonradiative loss [77].

The low coherence times combined with limited microwave power within this set of experiments does not allow for resonant Rabi driving of Cr spins. We overcome this problem in the next chapter, through creation of high quality SiC:Cr^{4+}sample by ion implantation.

Chapter 5

Creation and coherent control of Cr^{4+} in commercial 4H-SiC

In this section we are going to discuss creation of Cr spin ensembles in commercial 4H-SiC through ion implantation and annealing and coherent characterization of the created Cr spin ensembles.

5.1 Creation of Cr in commercial SiC

Creation and activation of SiC:Cr^{4+}in commercial SiC is a critical step for devices with integrated defect qubits. To this end we introduce isotopically pure, nuclear spin-free ^{52}Cr atoms into commercially purchased (from Norstel AB) high purity semi-insulating 4H-SiC substrates through implantation at elevated temperatures up to 600 ^{o}C.

The samples were co-implanted with ^{52}Cr at 190 keV energy with a dose of 5×10^{11} cm^2, and ^{12}C at 100 keV energy with a dose of 5×10^{11} cm^2 by CuttingEdge Ions, LLC. Both ions were implanted with a 7 ^{o} tilt. Chromium atoms are calculated to have an average depth of 110 nm and a 30 nm straggle using the program Stopping Range of Ions in Matter (SRIM). All samples were subsequently cleaned with organic solvents. A photoresist layer (AZ1518) is spun ~ 2 μm thick, baked at 95 ^{o}C for 1 minute then 350 ^{o}C for 30 minutes, as a

protective surface coating by forming a graphite cap during the high temperature annealing. The samples are annealed in a tube furnace with high purity argon gas at 800–1400 ^{o}C for 15 minutes with ramp rates of 100 ^{o}C per hour. The annealing of the samples at 1500–1800 ^{o}C was performed by Fraunhofer IISB in an Ar environment for 15 minutes with ramp rates of 900 ^{o}C.

We believe that the implanted chromium atoms sit mainly in interstitial sites of the SiC lattice and do not photoluminescence with the characteristic 4H-SiC:Cr^{4+}signature. During the subsequent annealing, Cr atoms move to the silicon (Si) site and form bonds with the surrounding carbon atoms and get activated. This generates the d^2 level structure extensively discussed in Sec.3.2.2. To investigate the electrical activation of the defect ensembles, we anneal different samples from the same implanted substrate between 800 and 1800 ^{o}C and then measure the ZPL intensities of SiC:$Cr_A$and SiC:Cr_CFig.5.1. Cr^{4+} activation, not observable when the samples are not annealed, increases monotonically as a function of annealing temperature until 1600 ^{o}C where it saturates.

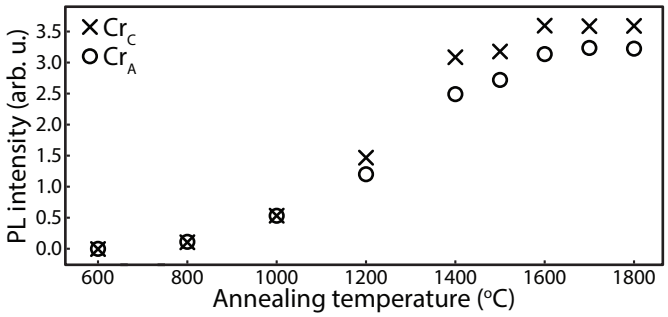

Figure 5.1: SiC:Cr^{4+} activation as a function of annealing temperature is measured by integrating the zero-phonon lines (ZPLs) intensity of the photoluminescence under off-resonant (730 nm) excitation at T = 30 K.

5.1.1 Parasitic background luminescence

These aforementioned SiC substrates have native, intrinsic vacancy and divacancy defects. During the implantation process likely more form as well. These optically active defects

have fast excited state lifetimes 4 orders of magnitude shorter than 4H-SiC:Cr^{4+}resulting in bright backgrounds even though their densities may be low.

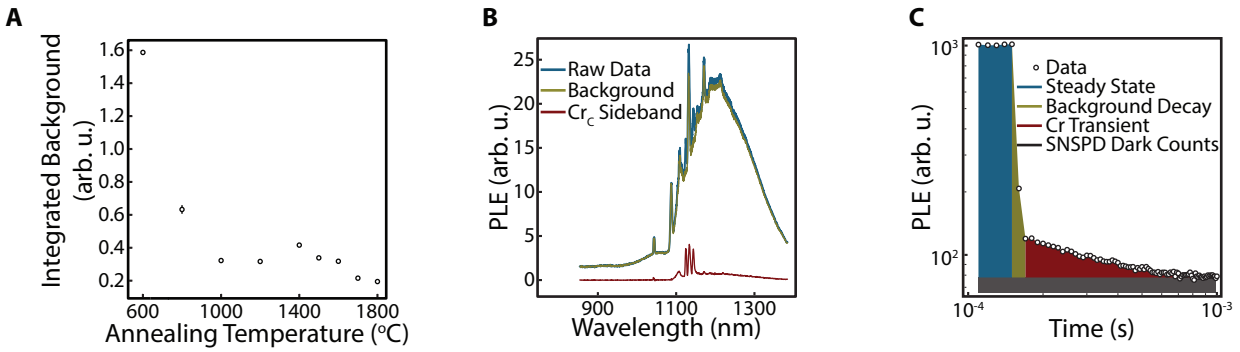

Figure 5.2: Background analysis of SiC:Cr^{4+} at T = 30 K. (**A**) Integrated background spectrum under the SiC:Cr^{4+}zero-phonon lines under 730 nm excitation. (**B**) SiC:Cr_Csideband of the 1800°C sample under resonant and detuned excitation. The signal is dominated by the background PL that is insensitive to the detuning. The difference between resonant and detuned excitation yields the SiC:Cr_Csideband which makes 4% of the all emitted PL signal. (**C**) Time resolved SiC:Cr_CPLE under pulsed resonant excitation. The shaded colors correspond to the PLE spectra shown on **C**. The background decays rapidly while the SiC:Cr_Ctransient persists for the 155 μs lifetime.

Fig.5.2**A** shows the integrated background photoluminescence at T = 30 K under 730 nm excitation. The data is extracted from the same experiment shown in Fig.5.1. As the annealing temperature increases, the background PL diminishes. This may be due to the background defects' charge states or structures changing with annealing.

The background PL becomes a significant problem under resonant excitation for these substrates, where only a sub-population of SiC:Cr^{4+}ions are probed and also the resonant laser excites the ions weakly. To analyze the background, we measure the SiC:Cr_Cspectrum with the narrow line laser in Fig.5.2**B**. When the laser is resonant with SiC:$Cr_C$of the 1800 °C sample at T = 30 K, we measure the blue trace. When the laser is detuned outside of the resonance, the SiC:Cr_Crelated sideband disappears however the background PL from other defects persist. The difference between the two traces is the signal of interest: the SiC:Cr_Csideband. It makes less then 4% of the entire PL spectrum in intensity. This sideband signal further diminishes as the temperature decreases to T = 15 K since the

optical hole linewidth narrows and the accessible sub-ensemble further shrinks in size.

Since the bright PL background decays rapidly, we can reject it temporally by gating the PLE signal. In order to time resolve this trend (T = 30 K), we pulse the resonant laser and collect the sideband PLE in 5 μs wide windows. When the counting time bins overlap with the laser excitation, we measure the steady state of SiC:Cr_CPLE which is comprised of the background and the SiC:Cr_Csignal combined. Right after the laser is off, the background PL rapidly decays followed by the SiC:Cr_CPLE decay with its characteristic 155 μs lifetime. Note that the silicon-vacancy and divacancy (other native optically active spin defects) in 4H-SiC have optical lifetimes of $\sim$ 5-20 ns [78, 79], and the background decay time is AOM fall-time limited. For all of the experiments in this chapter, unless stated otherwise, we integrate the Cr transient for 155 μs, after waiting 2 μs for the background to decay.

5.1.2 Box profile implanted sample

Every photon is valuable. Now that we have a recipe to create Cr ensembles in commercial SiC, we prepare a new sample to increase the number of ions being probed without increasing the defect density. Here is our strategy: a single energy of Cr implantation results in a narrow layer of atoms. The objective, however, excites and collects from a Gaussian depth profile. In order to place more Cr ions into the laser spot, we implant the Cr atoms with varying energies. We use a commercially purchased 4H-SiC wafer with an epitaxial, undoped (intrinsic), 20 μm thick 4H-SiC layer that was grown on a 4° off axis semi-insulating 4H-SiC crystal. Both the substrate and the epilayer growth was provided by Norstel AB. The epitaxial layer is very clean, and has a low defect density before implantation. We implant isotopically purified ^{52}Cr at four different energies to keep the Cr-Cr distance and damage densities low. The doses are in Table 5.1.2

Energy (MeV)	Dose (10^{12} cm^{-2})
1	1.5
2	2
5	3
10	3

Table 5.1: Implantation parameters

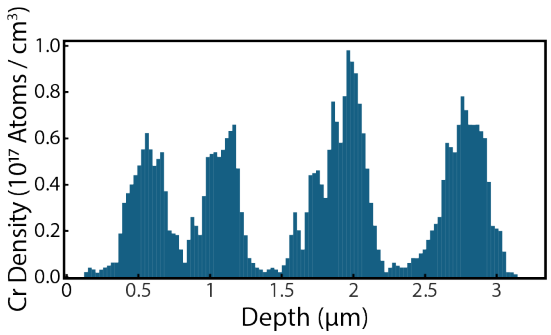

Figure 5.3: SRIM calculated ^{52}Cr density after the implantation parameters given in the table

The implantation was performed at Sandia National Laboratories at 690°C sample temperature. After ^{52}Cr implantation the sample was cleaned, photoresist capped, and annealed at 1800°C for 15 minutes using the same procedures detailed above. SRIM calculates the estimated implantation density profile shown in Fig.5.1.2. The average density of ions is $3(2) \times 10^{16}$ atoms/cm^3. Assuming all of the ions are activated after the annealing, we find the distance between two Cr^{4+} to be 23 - 40 nm. Assuming the creation efficiency of SiC:$Cr_A$and SiC:$Cr_C$are equal, the distance between each set of species is 30 - 50 nm.

To confirm the creation of Cr ions in this sample, we perform off resonant spectrally resolved PL measurements. We image the sample within a confocal microscopy setup discussed in Sec.D.1. A close cycle Montana Instruments nanoscale workstation (7 -300) K holds the sample while a room temperature kept compartment within the radiation shield houses a 50× Olympus NIR-objective that allows imaging. A Thorlabs 730 nm, 50 mW TO can laser off-resonantly excites the SiC:$Cr^{4+}$and a spectrometer and a Princeton Instruments OMA-V InGaAs NIR pixel resolves the resultant PL, confirming the creation of the ions shown in Fig.5.4.

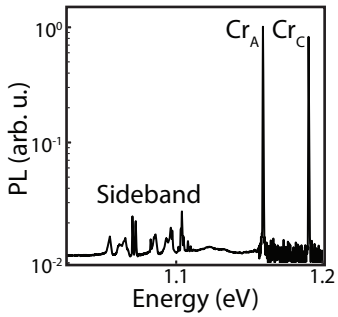

Figure 5.4: Photoluminescence spectrum of SiC:Cr^{4+} within the box profile implanted sample at T = 30 K under 730 nm off-resonant illumination. SiC:$Cr_A$and SiC:Cr_C, ZPL's and their sidebands can be observed.

5.2 Steady state resonant characterization

In order to take advantage of the optical spin interface of the electronic structure, we switch to the resonant excitation scheme. A Newfocus Velocity 6700 tunable (1035-1075 nm), fiber-coupled, external-cavity diode laser resonantly excites to polarize and probe the SiC:Cr^{4+}ensembles while an electro-optical modulator (EOM) with 12 GHz bandwidth can generate sidebands around the primary laser frequency for optical probe and second color excitation. The resonant laser itself is turned on/off with an Aa Opto-Electronic fiber coupled 20 ns rise time acousto-optical modulator for transient background rejection explained in Sec.5.1.1. A Semrock 1090 nm long pass dichroic beam-splitter placed at an angle of 75° separates the sideband from the excitation. After further filtering the SiC:Cr^{4+}sideband with two 1100 nm Thorlabs long-pass filters we collimate it into a 50 μm core multimode fiber. An experimental Quantum Opus multimode superconducting nanowire single photon detector (SNSPD) with a 6-9 kilo counts per second (kcps) dark-counts measure the photons. Two microwave switches gate the counts from the detector, one to only measure the transient signal, and the other one to rapidly switch between two different counters for differential (lock-in style) measurements. We use a vector signal generator (Stanford Research Instruments SG396) with a 30W 0.6–2.7 GHz amplifier (Minicircuits) for microwave excitation. It is fed to a shorted coplanar wave guide patterned on a custom-made printed

circuit board situated behind the sample within the cryostat. An arbitrary waveform generator (Swabian Instruments) synchronizes the time of the laser excitation, probe generation, microwave excitation with IQ control, collection, and counter gating.

5.2.1 Photoluminescence Excitation

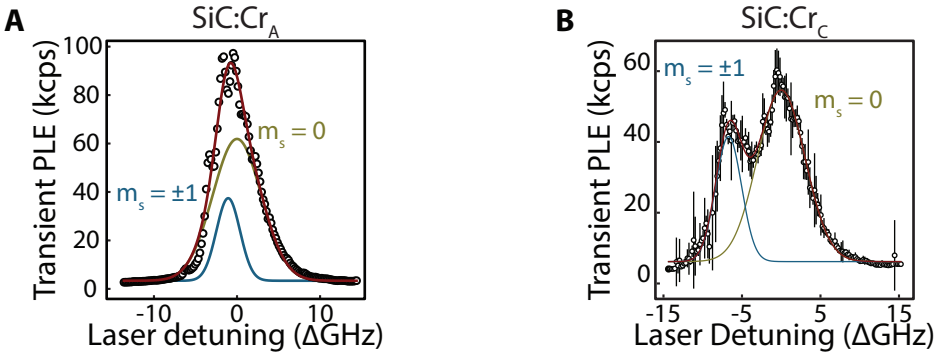

Figure 5.5: Photoluminescence excitation spectrum of SiC:Cr^{4+} of box profile implanted sample at T = 30 K and B = 0 G measured by sweeping the resonant laser and recording the transient sideband signal in counts per second (cps). Both figures are fit to two Gaussians with their known D from Chapter 4, (**A**) SiC:Cr_Afit with $D = 1063$ MHz splitting reveals the full width at half maxima at 6.87(27) GHz for $m_s = 0$ and 3.34(39) GHz for $m_s = \pm 1$ peak. The one sigma errors of the data are smaller than the point size and are not displayed. (**B**) SiC:Cr_Cfit with $D = 6707$ MHz splitting reveals the full width half maxima at 7.14(16) GHz for $m_s = 0$ and 3.88(13) GHz for $m_s = \pm 1$ peak.

We measure the photoluminescence excitation (PLE) spectrum by resonantly exciting SiC:Cr^{4+}ZPL and collecting the transient phonon sideband (Fig.5.5) at 30 K. A fit to two Gaussian functions for the $m_s = 0$ and $m_s = \pm 1$ sublevels with a known ground state crystal field splitting (D) for SiC:Cr_A(1063 MHz) and SiC:Cr_C(6.707 GHz) yields an average PLE linewidth of 5.1(4) GHz with the $m_s = 0$ linewidth roughly two times larger than the $m_s = \pm 1$ linewidth. This trend is more obvious for SiC:Cr_Cas the individual PLE lines are more resolved due to a larger D. The origin of this behavior is unknown and may be a result of mass related shift due to ^{13}C, ^{29}Si, and ^{30}Si isotopes [3, 80, 81] that we observe for vanadium in SiC (Sec.6.3.1), however, the same functional form does not replicate the red-shifted PLE linewidth, possibly due to more complicated electronic level structure discussed in Sec.3.2.2.

The overall sharper inhomogeneous linewidth of the implanted sample compared to the as-grown sample discussed in Chapter 4 allows for better spin sublevel resolution and is likely due to an improved spatial strain profile.

5.2.2 Hole recovery

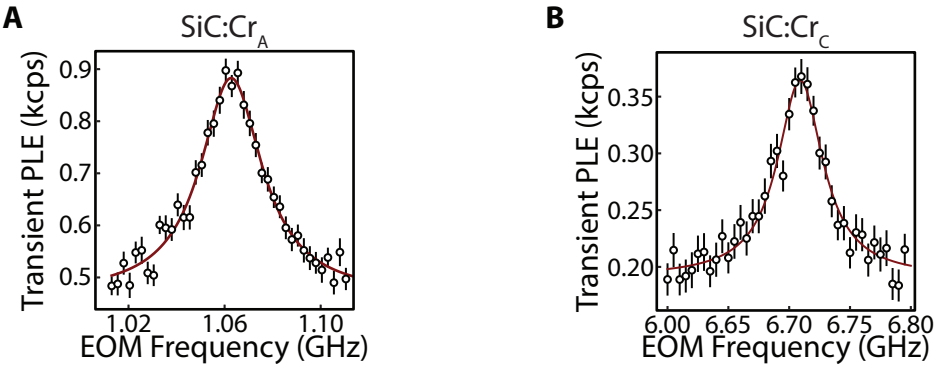

Figure 5.6: Optical hole recovery of SiC:Cr^{4+} of box profile implanted sample at T = 15 K and B = 0 G measured by sweeping a second laser tone while the primary one is parked at the PLE maximum and recording the transient sideband signal in counts per second (cps). Lorentzian fit to the data reveals (**A**) for SiC:Cr_A D = 1062.7(4) MHz with a full width at half maximum of 31(2) MHz and (**B**) for SiC:Cr_C D = 6709.0(4) MHz with a full width at half maximum of 45(2) MHz. The laser power is reduced to prevent optical power broadening.

To characterize the ground state spins of SiC:Cr^{4+}through resonant hole burning and hole recovery, we reduce the sample temperature to 15 K where the spin T_1 is longer than the optical lifetime. The population of a spin sub-ensemble excited by the narrow line resonant laser will be redistributed among the other ground state spin sublevels after spontaneous emission, leading to hole burning and spin polarization. Since the polarized sub-population is off-resonant relative to the probe laser, the defect goes dark resulting in a spin selective optical contrast as we have previously seen in Chapter 4. We can recover the hole by reintroducing the polarized population into the optical cycle in two ways, either by using a second laser color to probe the polarized sublevels or by driving ground state spins with microwaves. A second laser tone generated by a phase modulator recovers the SiC:$Cr_A$and SiC:Cr_Choles at a D of 1062.7(4) MHz and 6.7090(4) GHz (Fig.5.6) respectively, consistent

with previous observations. A Lorentzian fit to the data, extracts a 31(2) and 45(2) MHz ensemble hole linewidths for the SiC:Cr^{4+}sites, which is more than an order of magnitude narrower than the as grown sample discussed in Chapter 4, demonstrating the superior material quality of the implanted and annealed sample.

The sharp hole linewidth is also two orders of magnitude narrower than the inhomogeneous optical linewidth, indicating only 1% of the created SiC:Cr^{4+}defects are accessed under resonant excitation. One could increase the net ensemble polarization by further reducing the inhomogeneous linewidth through material improvements.

The hole can also be recovered by microwave mixing of the ground state spin sublevels, enabling optical detection of magnetic resonance (ODMR) (Fig.5.7). Stray magnetic fields Zeeman split the $m_s = \pm 1$ ODMR by ~ 5 MHz centered around D for both of the SiC:Cr^{4+}species.

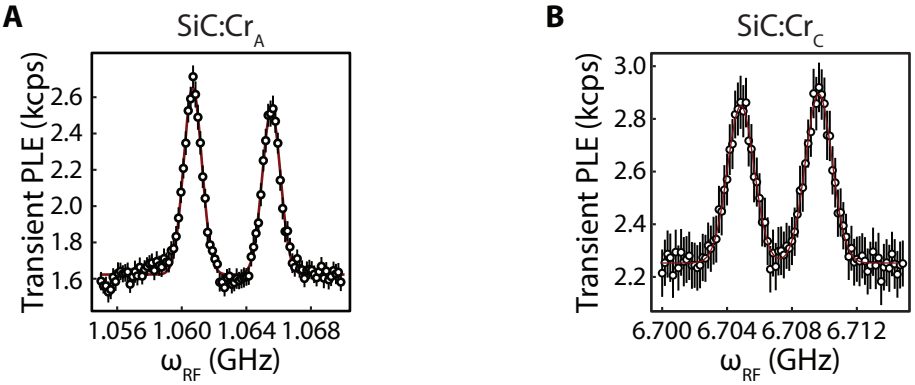

Figure 5.7: ODMR of SiC:Cr^{4+} of box profile implanted sample at T = 15 K and B = 0 G measured by sweeping the frequency of a microwave field while the resonant laser is parked at the PLE maximum and recording the transient sideband signal in counts per second (cps). PLE is recovered when the microwave mixes the ground state spins. There is a ~ 1.7 G stray magnetic field that splits the $m_s = \pm 1$ sublevels. A double Lorentzian fit to the data reveals (**A**) for SiC:Cr_A $D = 1063.11(1)$ MHz with a full width at half maximum of 1.32(2) MHz and (**B**) for SiC:Cr_C $D = 6707.0(0)$ MHz with a full width at half maximum of 1.93(4) MHz.

A Lorentzian fit to the non-power broadened ODMR reveals a linewidth of 1.32(2) and 1.93(4) MHz for SiC:$Cr_A$and SiC:Cr_Crespectively. Because the 31 MHz optical hole linewidth is not confined by the ODMR linewidth, the optical coherence is likely excited-state limited.

The four orders of magnitude difference between the measured and lifetime limited hole linewidth (∼2 kHz) may be a result of decoherence induced by the degenerate excited state orbital doublet structure that can be lifted by applying high magnetic fields [71] or spectral diffusion due to charge fluctuations that can be addressed by creating charge depletion zones [38] the exact mechanism and its solution would require further investigation.

As our microwave power amplifiers range is limited, moving forward we will only be investigating the SiC:Cr_A, however the techniques and characterizations that we will discuss should be readily translated to other d^2 configurations including SiC:Cr_C.

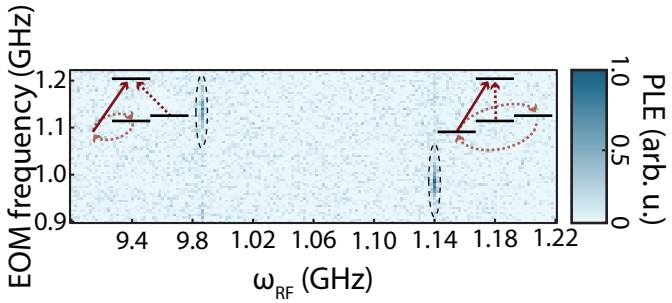

Figure 5.8: Hole recovery of SiC:Cr_A of box profile implanted sample at T = 15 K and B = 26 G measured by sweeping the frequency of a second laser tone and a microwave field at the same time and recording the transient sideband signal in counts per second (cps) while the resonant laser is parked at the PLE maximum. Contrast is achieved when all three ground state sublevels are probed simultaneously with the high contrast area highlighted within dashed ellipses.

A c-axis magnetic field lifts the optical degeneracy of the $m_s = \pm 1$ sublevels by Zeeman splitting while the $S = 0$ excited state remains unaffected. It is worth noting that the population can become trapped in the unprobed third level after using either the optical sideband probe or the microwave mixing, as these techniques can only address one sub-level at a time[1]. By applying both an optical sideband probe and a microwave tone together, all states can be addressed simultaneously resulting in hole recovery (Fig.5.8). Using a second laser to trap the population into the third sublevel provides a path for efficient spin

1. This is not a big concern if there exists a competing reset mechanism like short T_1 (e.g. in Chapter 4) or a broad optical excitation that addresses all spin sublevels (e.g. Chapter 7)

polarization under a magnetic field.

5.3 Transition Rates

To characterize the ground state spin dynamics, we need three ingredients: optical initialization (polarize), microwave manipulation and optical readout (probe + transient readout) shown below in Fig.5.9. We characterize each one of these rates to maximize the signal to noise. This is a chicken-and-egg problem, and finding the right rates is an iterative process. For the discussion below, we assume to have already calibrated a π-pulse.

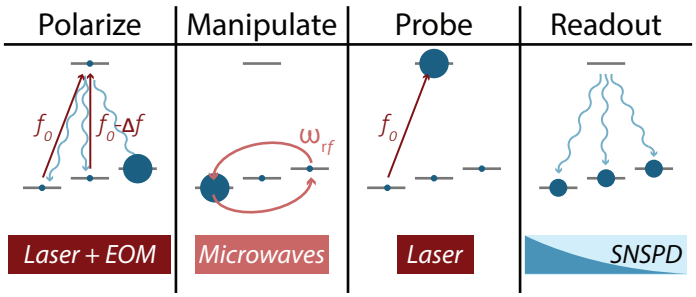

Figure 5.9: Cr^{4+} coherent control pulse sequence.

5.3.1 Spin T_1

The first question to answer is: can the control sequence shown above in Fig.5.9 fit within a spin T_1 time. To answer this question and understand the main T_1 mechanism, we measure the spin T_1 time at B = 0 G by population inversion relaxation using a microwave π-pulse. Locking in to the π-pulse allows for eliminating any potential other spin-reset mechanisms that may be optically induced. By repeating this measurement for temperatures between 15 and 30 K and fitting each data set to an exponential decay function, we extract T_1 times and use this data set to distinguish between Orbach and Raman processes [82] (Fig.5.10). For the Orbach process, we use $T_1^{-1} = A \exp(-E/k_b T)$ as our fit function where A and E, the energy difference to a low-lying excited state, are fit parameters. For the Raman process we

use $T_1^{-1} = A\,(T - \Delta T)^n$ where A and ΔT, a constant temperature offset of the sample, are fit parameters for various fixed odd integers n. The Orbach model fits the data poorly and returns an energy gap of E = 20(1) meV which is a factor of 50 lower from the first excited state energy and a factor of 4 lower than the closest phonon line energy, [71] indicating that Orbach process is not the likely explanation for T_1 decay mechanism.

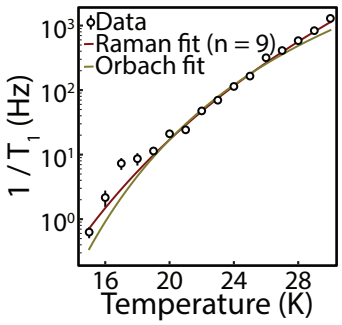

Figure 5.10: Ground state spin T_1 time of SiC:Cr_Aas a function of temperature. After polarization, the contrast between a microwave π-pulse and a 2π-pulse is measured at various temperatures. The resulting time-dependences are fit to an exponential decay, where the displayed error bars are the standard errors of the fits. The extracted T_1 times are fit to both an exponential (Orbach) and a power (Raman) model. The exponential fit (green line) reveals an E = 20(1) meV with a reduced $\chi^2 = 4.18$. The 9th power Raman fit (red line) reveals a constant temperature miscalibration of $\Delta T = 3.2(5)$ K with a reduced $\chi^2 = 1.91$.

Out of the Raman processes, here are 3 n powers available [82] for a two phonon process. These are $n = 7, 9, 13$. Separately there is a single phonon process where $n = 1$, however the fits do not converge and this model does not explain the data shape, therefore we rule out a single phonon process as the main T_1 decay time contributor. Out of the two-phonon processes:

n = 7 arises from anisotropic Zeeman interaction with the $1/T_1 \propto B^2T^7$ relation. Given that SiC:$Cr_A$and SiC:Cr_Cboth have rather isotropic g-factors as seen in Chapter 4 and [71] and we conduct the T_1 measurements at B = 0 G, this mechanism is extremely unlikely. If we do assume it, however, the $1/T_1 = A(T - \Delta T)^7$, reveals a reduced $\chi^2 = 2.54$ with a $\Delta T = 7K$ sample temperature miscalibration. Given the physical interpretation, weak fit confidence and unreasonably high temperature miscalibration we rule out the n = 7 process.

n = 9 term arises from spin flipping due to spin orbit interaction. The fit to $1/T_1 = A(T - \Delta T)^9$ returns a reduced $\chi^2 = 1.91$ and the sample is $\Delta T = 3.16$ K warmer than the internal sensor, which is highly possible. Another interesting thing to point out is that the spin orbit energy shift $\beta \propto Z^4$. Given that the ^{52}Cr has a defect-mass much greater than it's vacancy related counterparts, the spin-orbit effects in SiC:Cr^{4+}should be more pronounced.

n = 13 term arises mostly from sample deformation potentials, sound velocities, etc. and is a weak process. The fit to $1/T_1 = A(T - \Delta T)^{13}$ returns a reduced $\chi^2 = 1.92$ with the sample $\Delta T = -5.0$ K miscalibration, i.e. 5 K colder than the internal sensor. Even though the model confidence is high, the fit value is physically not possible, hence we rule out this process as well.

We, therefore, conclude that the most likely explanation is the $n = 9$ Raman process, indicating that the T_1 is spin-orbit interaction limited. The longest measured spin T_1 time is 1.6(3) s long at T = 15 K, long enough to not limit the spin dephasing times and to offer a very long window for high fidelity spin initialization.

5.3.2 Readout rates

There are two relevant rates for the readout: the probe duration and excited state lifetime after the probe. If we underestimate these rates, then we sacrifice valuable signal, and if we overestimate them then, we waste duty cycle. In order to maximize the signal we will be using the rise and fall times of these exponential dynamics.

We measure the excited state lifetime (T_{opt}) under resonant excitation at 30 K by histogramming the transient PLE and find $T_{\text{opt}} = 156.3(5)$ μs (Fig 5.11**A**). We, therefore, set the transient readout time to be 155 μs. This value is in agreement with the off-resonant excited state lifetime for the same sample, but slightly longer than the as grown sample discussed in Chapter 4. Again, this discrepancy may be attributed to the increased material quality inhibiting various dark decay pathways.

We continue the measurements at 30 K to prevent hole burning under resonant excitation.

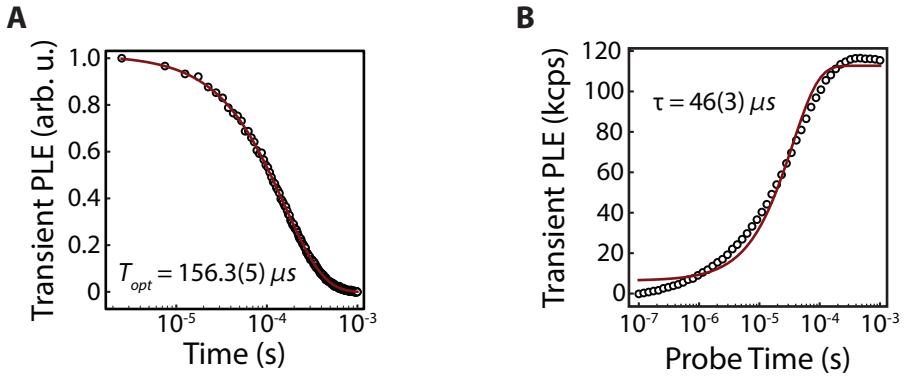

Figure 5.11: Readout rate calibration data for Cr^{4+} coherent control at T = 30 K to prevent hole burning. (**A**) A 300 μs PLE excitation saturates the defect and 5 μs bin with varying start time counts the photons. Normalized PLE decay time for SiC:Cr_Ayields a T_{opt} = 156.3(5) μs. (**B**) The resonant probe time is increased for a fixed 150 μs transient photon collection window. The fit to the model in Eq.5.1 reveals a pump rate of 46(3) μs.

We vary the laser excitation time to measure the defect saturation. Assuming basic pump and sink model with two classical levels, where the pump is the laser and the sink is the optical lifetime T_{opt}, we can derive the following model:

$$A = \left(1 - \exp\left(-t\left(\frac{1}{T_{\text{opt}}} + \frac{1}{T_{\text{Laser}}}\right)\right)\right) \tag{5.1}$$

where we already have measured $T_{\text{opt}} = 155$ μs. The fit to the data (Fig.5.11**B**) returns a laser time of $T_{\text{Laser}} = 46(3)$ μs and therefore we set the probe time to 50 μs.

There may be several reasons why the fit does not match the data in the tail that well. This is an ensemble measurement, and the optical line widths are rather wide at the elevated temperature, hence there will be some detuned excitations. Also, the laser spot is in a Gaussian profile, resulting in a distribution of powers as opposed to a single rise time. But an average $T_{\text{Laser}} = 46(3)$ μs gives a reasonable agreement with the data.

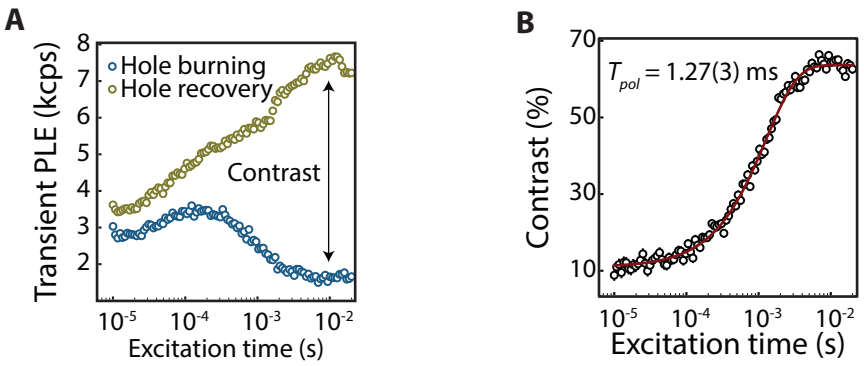

Figure 5.12: Initialization rate calibration data for Cr^{4+} at T = 15 K and B = 158 G. (**A**) $m_s = 0$ state is probed as a function of polarization pulse length. In the absence of a π-pulse (blue trace) the depletion of the $m_s = 0$ state is measured. When a π-pulse is applied, the accumulation of the polarized population in the $m_s = +1$ is measured by coherently transferring the population to $m_s = 0$ (green trace). (**D**) The contrast is the difference between the two traces in **C**. An exponential fit to the contrast shown in red yields a polarization time of 1.27(3) ms with a maximum contrast of 64(2)% for a 50 μs probe time. The error bars in are smaller than the mark size and are not shown.

5.3.3 Initialization rates

We time resolve the polarization dynamics of SiC:Cr_Aat T = 15 K and B = 158 G, same condition we use for coherent control experiments, to optimize for the defect initialization. We sweep the resonant excitation time in panel 1 of Fig.5.9 using the already discussed readout rates and previously calibrated π-pulse. After each sequence a $\pi/2$ pulse redistributes the population among the ground states as a spin reset. When no microwave rotations are applied in panel 2 of Fig.5.9, we measure the depletion of the $m_s = 0$ sub-population. When the resonant excitation time of the $m_s = 0$ is less than the optical lifetime of 155 μs, the population in the excited state transferred from the $m_s = 0$ increases, which is manifested as an increase in signal. Past that point in time, the $m_s = 0$ population depletes as the sub-ensemble polarizes into the $m_s = +1$ (Fig.5.12**A** - blue trace). Using a π-pulse to coherently swap the populations between the $m_s = 0$ and the $m_s = +1$ states, we measure the polarized population within the $m_s = +1$ sublevel which increases monotonically with the laser excitation time (Fig.5.12**A** - green trace). The difference of the two traces is

the optical contrast shown in Fig.5.12**B**. An exponential fit to the data yields a rise time of 1.27(3) ms, corresponding to polarization within ∼10 optical lifetimes with maximum contrast at 64(2)%. In order to maximize the contrast, we polarize the defect for 5 ms.

5.4 Coherent spin control

Now that we have established a 5 ms initialization time, 50 μs probe time and 155 μs transient readout time combined with the confidence that we can squeeze in this pulse sequence within a spin T_1 time with plenty more to spare, we characterize the ground state spin properties.

Once the subpopulation is polarized into $m_s = +1$ and is dark, we coherently control the subpopulation using resonant microwave rotations within the $m_s = 0, +1$ manifold and read out through the $m_s = 0$ population. We measure Rabi rotations discussed in Sec.2.16 at B = 158 G by varying the microwave excitation length and obtain a contrast of 63(1)% with an envelope decay time of 4.76(7) μs at max amplifier power of 46 dBm.[2]

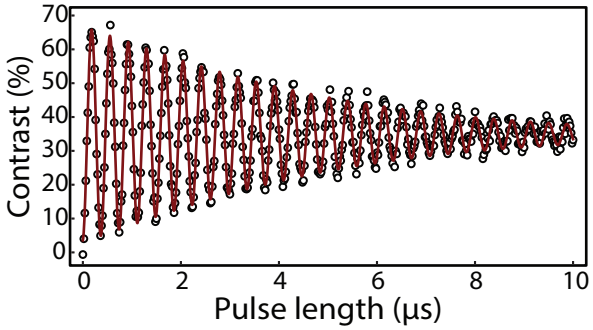

Figure 5.13: Coherent control of SiC:Cr_A at T = 15 K and B = 158 G within $m_s = 0$ and $m_s = +1$ manifold. Resonantly driven Rabi oscillations of the ground state spin measured with a 63(1)% contrast and a decay time of 4.76(7) μs.

By varying the driving power (Fig.5.14), as expected, we measure decreased oscillation frequencies that linearly depend on the square root of the driving power where this relation is derived in Sec.2.16.

2. This is just the output from the amplifier and there are likely losses through the cables, connectors and the microwave stripline. These losses are constant however within the dB scale

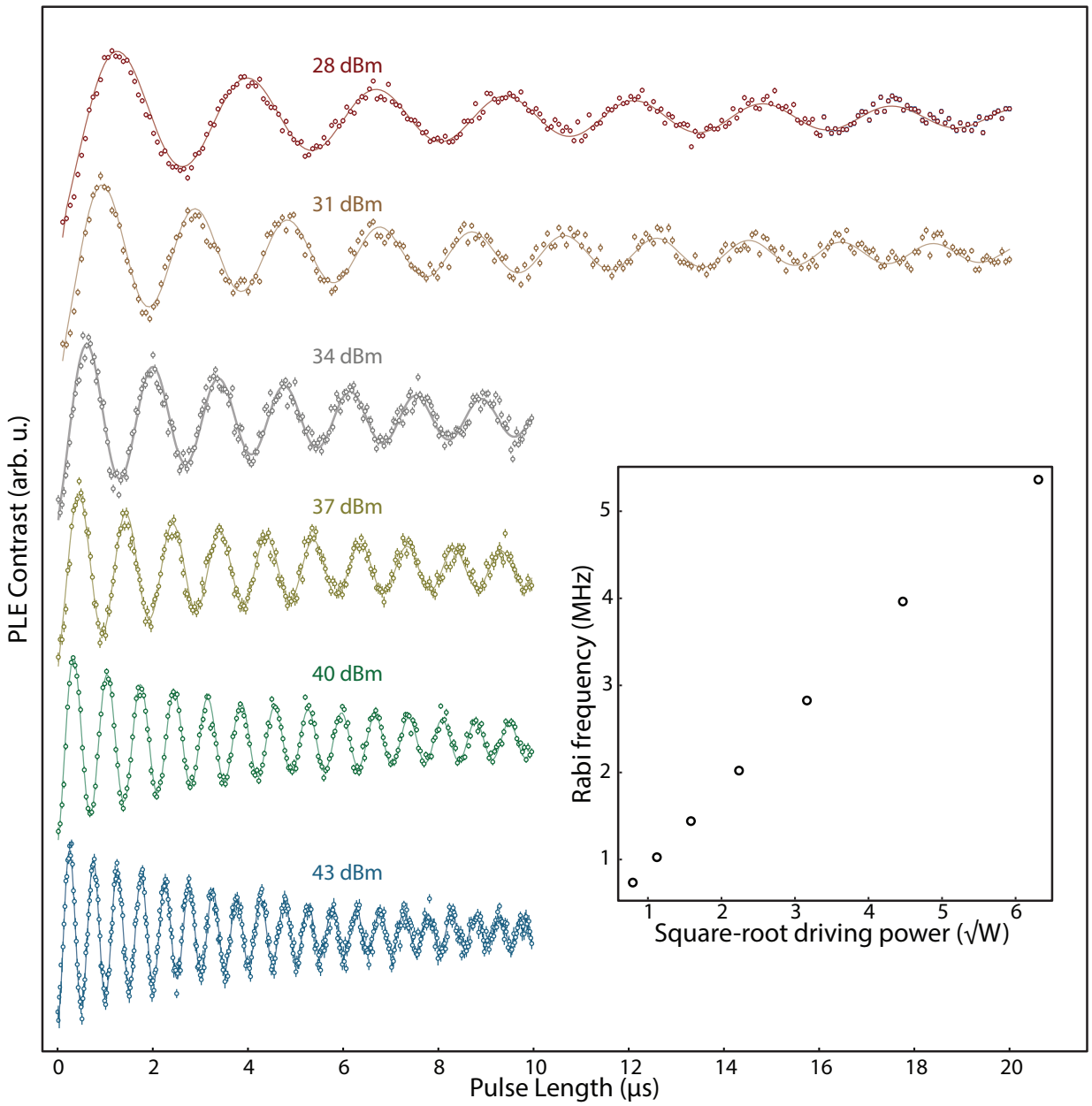

Figure 5.14: Power dependence of SiC:Cr_ARabi driving at T = 15 K, B = 158 G same conditions for Fig.5.13. The contrast for each sequence is around 60-40 % depending on the driving power. (Inset) As expected, the Rabi frequency linearly increases as a function of $\sqrt{W}$ where, W is the resonant microwave driving power. The highest data point with 46 dBm driving power is from Fig.5.13

To characterize the ground state spin coherence times, we perform Ramsey interferometry and Hahn echo measurements. For the Ramsey measurement, we detune the resonant

microwave frequency by 5 MHz to account for any unintentional small detunings that can appear as slow oscillations within the expected exponential decay and then scan the delay between two $\pi_x/2$ pulses. The characteristic oscillations at the detuning frequency derived in Sec.2.2.4 have an envelope with a decay time of $T_2^* = 307(17)$ns (Fig.5.15**A**), in agreement with the ODMR linewidth measurements in Fig.5.7**A**.

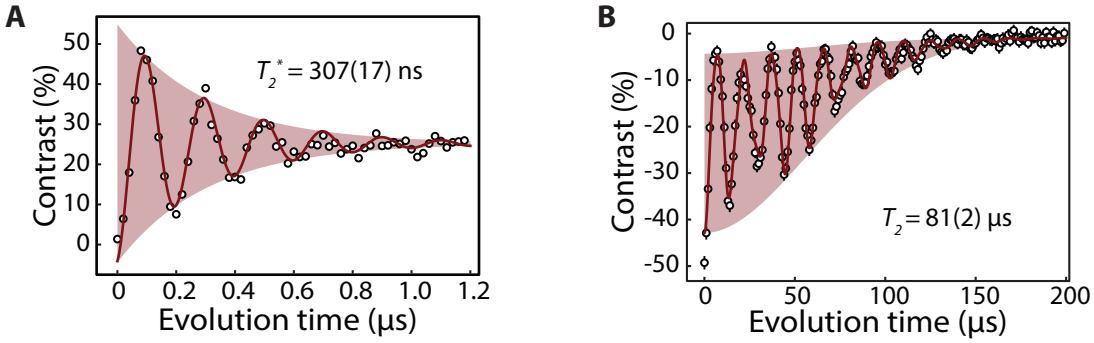

Figure 5.15: Spin coherence characterization of SiC:Cr_A at T = 15 K and B = 158 G. (**A**) A fit to a 5 MHz detuned Ramsey interferometry measurement returns the expected 5 MHz oscillation frequency and $T_2^* = 307(17)$ ns decay envelope. (**B**) A Hahn echo measurement reveals a $T_2 = 81(2)$ μs with characteristic oscillations of ^{13}C (87.5(3) kHz) and ^{29}Si (68.0(1) kHz) Larmor precession frequencies at the field.

We measure the T_2 coherence time by $(\pm\pi_x/2 - \tau_{\text{free}}/2 - \pi_y - \tau_{\text{free}}/2 - \pi_x/2)$ echo-pulse sequence. We fit the data to an electron spin echo envelope modulation function where nuclear Larmor precessions are enveloped by a decay function of

$$\text{PLE}(\tau) = \exp\left(-(\tau/T_2)^n\right) \prod_{\alpha} \left(1 - K_\alpha \sin^2\left(\pi\omega_\alpha \tau\right)\right) \tag{5.2}$$

with the precession amplitudes (K_α), frequencies (ω_α) and decay power (n) and time (T_2) as free fit parameters [83]. We recover the characteristic oscillations at the current B field for ^{13}C (87.5(3) kHz) and ^{29}Si (68.0(1) kHz) as well as $T_2 = 81(2)$ μs with a decay power dependence of n = 1.9(1) (Fig.5.15**B**). The average defect density in our sample is roughly 3×10^{16} atoms/cm^3 as discussed in Sec.5.1 and the measured T_2 time is in line with similarly dense divacancy ensembles in SiC[84]. This indicates that the observed coherence times are likely limited by electron spin–spin interactions between defects, and further reduction of

the Cr^{4+} and background defect densities could result in millisecond long coherence times [79].

5.5 High fidelity readout

When we sacrifice overall signal and reduce the probe time from 50 to 1 μs, the Rabi contrast increases to 79 (2)% contrast (Fig.5.16). This places a lower bound on the ensemble polarization of at least 77%.

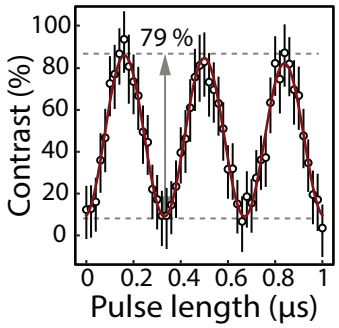

Figure 5.16: High contrast Rabi oscillations of SiC:Cr_Aat T = 15 K and B = 158 G are measured when the probe time is reduced to 1 μs. The total signal is reduced but the contrast is increased to 79(2)%. Error bars are the one sigma of the data.

This contrast, however, is lower than our estimates about to be discussed and we believe a spin-reset mechanism induced by the probe itself could be responsible, therefore, further exploration of this effect could increase the readout fidelity.

5.6 Modeling rates

In order to understand the discrepancy between the measured rates and observed contrast, we model the population dynamics using Python QuTIP simulation. The simulated system is in a 5 dimensional Hilbert space, 2 for the excited state, and 3 for the ground state. The Hamiltonian, without loss of generality, assumes a coherent drive between the upper branch of the excited state and = 0 ground state. The simulation uses a Lindblad master equation

with collapse operators to take the following decoherence mechanisms into consideration: optical T_1 and T_2, ground state T_1 and excited state orbital T_1.

We already measured these governing parameters. For example we discussed the optical lifetime (optical T_1) in Sec.5.11. Based on the optical hole linewidth of 30 MHz at $T = 15$ K, we can assign an upper bound on the optical T_2^*. We also measure a $T_1 = 1.6$ s at $T = 15$. The laser power has a rise time of 46 μs based on Fig.5.11. The purpose of these simulations is to see the population dynamics, hence we will omit the spin T_2 of the ground state since it is irrelevant.

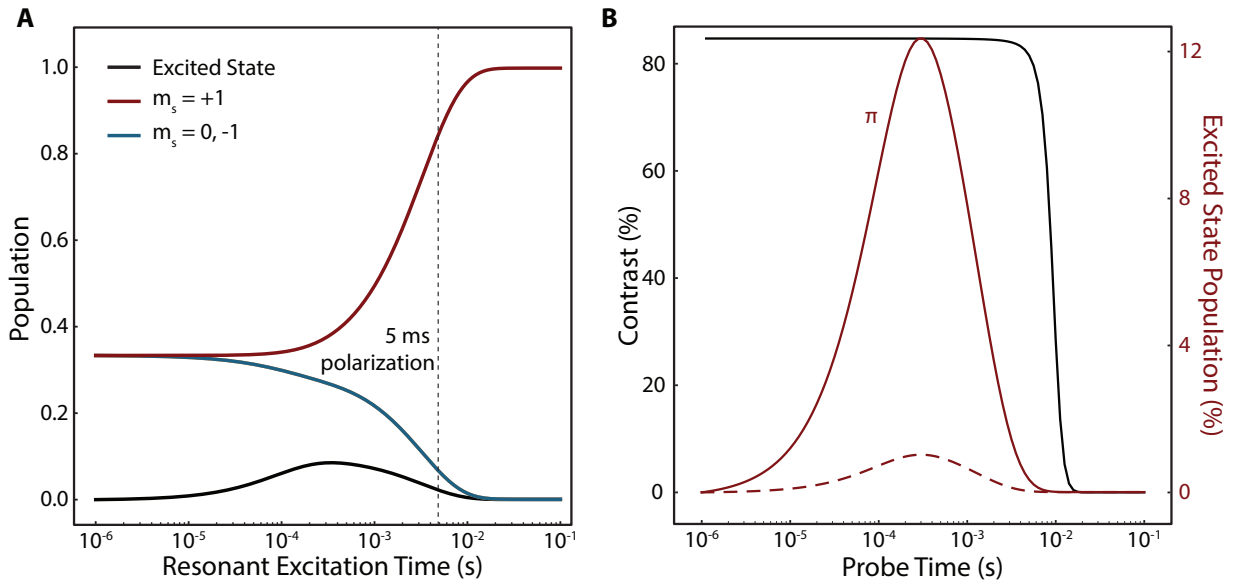

Figure 5.17: QuTIP simulation of Cr^{4+} dynamics assuming $1/2T_1^{\text{Excited}} = 1/T_2^{*\text{opt}} = 30$ MHz, $T_1^{\text{opt}} = 155$ μs, $T_1^{\text{spin}} = 1.6$ s, $T_{\text{Laser}} = 46$ μs. (**A**) Population of states under resonant excitation. The 5 ms excitation used in the main manuscript results in 86% polarization after the excited state decay. (**B**) Probe time of the polarized defect. The black curve is the contrast: $C = 100 \times (\text{PL}_\pi - \text{PL}) / (\text{PL}_\pi + \text{PL})$ where PL $\propto$ Excited state population. The red curve is the population in the excited state as a function of probe time which is the amount of signal extracted.

Fig.5.17**A** shows the population in the each sublevel. The 5 ms excitation time polarizes the defect at most 85% but a 20 ms excitation time should achieve more than 99% polarization under no laser induced resetting mechanism. Fig.5.17**A** is related to the Fig.5.12**A** in the following way: the depletion of the $m_s = 0$ is a convolution of the black and the

blue curve, while the population gain in the $= +1$ is given by the convolution of the black and the red curve. Their difference, the contrast, should keep increasing until it hits 99%, where a 50 μs probe should saturate the readout contrast at that value. However, within our experiments, the contrast saturates at 64% where likely a reset mechanism induced by the laser is responsible for the measured lower polarization and the contrast saturation values.

Fig.5.17**B** shows how much contrast and signal can be extracted from the system as a function of probe time. The black curve is the contrast after a 5 ms polarization as a function of probe laser time. The contrast is defined the same way as in the main text, i.e. $C = 100 \times (\mathrm{PL}_\pi - \mathrm{PL}) \,/\, (\mathrm{PL}_\pi + \mathrm{PL})$ where PL $\propto$ excited state population, shown in red in Fig.5.17**B**. The subscript π indicates, a microwave π pulse to swap the populations of $= +1$ and $= 0$. We can immediately observe that the contrast, in ideal conditions, stays constant until efficient hole burning exposure times in the ms regime. The maximum extractable signal is around ~ 300 μs ($2T_{\mathrm{opt}}$), and it corresponds to placing roughly 1/8 of the population into the excited state. Greater laser powers in an ideal case should increase this ratio. Even though the measured reduced signal with the reduced probe time is consistent with our model, the change in the contrast is not, since it should have been probe length independent (Fig.5.16). A laser induced reset mechanism, however, could explain this observed phenomena as speculated earlier.

5.7 Quantum efficiency

Another important figure of merit is the quantum efficiency of an emitter that is defined as the ratio of radiative decay rate over all possible decay rates. The closer the number to 1, the higher quality the emitter is, since otherwise the emitter needs to be probed many times to get a signal where each probing event can flip the spin and cause an error. We can place a lower number to this figure by comparing the measured signal to the expected signal.

The Olympus LCPLN50XIR objective has an NA of 0.65. For the 1070 nm excitation,

the Gaussian waist size of the beam profile is 1.6 μm. The defects are distributed within a 3 μm layer based on Fig.5.1.2. A cylindrical approximation to the waist combined with defect distribution depth, reveals a 6×10^{-12}cm^3 probe volume. Hence, assuming 100% creation efficiency we probe $1.8(1.2) \times 10^5$ defects at most. Assuming half of the defects will be SiC:$Cr_A$and the other half SiC:Cr_C, the number of SiC:Cr_Adefects within the spot will be $9(6) \times 10^4$. We measure an EOM linewidth of 67 MHz under the full laser power (same conditions for the coherent spin measurements). Since this linewidth is a factor of ~ 75 narrower than the inhomogeneous linewidth, we probe at most $400 - 2000$ SiC:Cr_Adefects for the ensemble hole burning and spin coherence measurements.

We can place a lower bound to quantum efficiency of SiC:Cr_Ausing this estimation. Assuming the upper bound of 2000 defects, 25% PL in the sideband with a 6.45 kHz optical cycle rate, 0.8 quantum efficiency of the detector and no other losses in the collection path and finally a 4% of the photons getting out of the SiC substrate due to the internal reflections ($NA_{4H\text{-}SiC}(1070\text{ nm}) \simeq 2.63$)[85], we expect to collect 103200 photons/s. In our coherent Rabi measurements, the detected count rate exceeds 10000 photons/s after a π pulse which corresponds to the 63% contrast reported. If a we assume that a 50 μs laser probe, excites every single probed SiC:Cr_A, a lower bound of at least 10% quantum efficiency can be set for SiC:Cr_A. Any relaxation in these assumptions would yield much higher quantum efficiencies.

5.8 Summary

In this chapter, we have demonstrated successful creation and activation of SiC:Cr^{4+}ions with exceptional optical and spin properties in commercial semi-insulating SiC substrates. We will be using the same method in the coming chapter to introduce another transition metal ion, vanadium, into SiC. The reported defect creation technique can also be extended to three-dimensional localization of single transition metal ions in SiC for device integration through nanoimplantation [86, 87] which is a critical step for a scalable quantum device

manufacturing.

The careful rate characterization allowed for ground state spin initialized and read out with a high fidelity of at least 79%. Furthermore, the measured ensemble spin coherence time T_2 of 81 μs is spin–spin limited, with spin T_1 times exceeding 1 s at moderately cryogenic (15 K) environments, showing the potential of an isolated SiC:Cr^{4+}as an optically addressable spin qubit [79].

Chapter 6

d_1 spin qubits: vanadium in silicon carbide

Vanadium 4+ (V^{4+}) in SiC has a bright optical emission within the O-band of the telecommunication spectrum which also allows for measuring a single emitter. The importance of the telecom light was previously discussed in Chapter 1 in the context of quantum communication. Having a single spin qubit that can be interface through this optical band within a mature semiconducting host such as SiC can enable remote quantum technologies within the solid state, wired together through the existing fiberoptic network. In this context, we will explore the optical and spin properties of d^1 electronic structure of 4H-SiC:$V^{4+}$and 6H-SiC:V^{4+}.

6.1 Experimental details

We purchased V-doped semi-insulating commercial wafers of 4H-SiC and 6H-SiC from II-VI materials for ensemble measurements. For single defect experiments, a semi-insulating 20 μm epitaxial layer on an n-type 4H-SiC wafer from Norstel AB is implanted with ^{51}V is hot implanted (500°C) with a 10^8 cm^{-2} dose at 190 keV. This places the implanted V atoms roughly 100 nm below the surface according to SRIM simulations. The sample is

subsequently annealed at 1400°C for 30 minutes in argon to activate the V centers and with a carbon cap (later removed) to prevent Si evaporation, similar to the recipe discussed in Sec.5.1. We were unable to obtain 6H-SiC wafers without background V for single-defect measurements.

We use the same confocal microscopy setup principles discussed in Sec.D.1. The Montana Instruments closed cycle cryostat used for these experiments can go down to 3.3 K. To address the vanadium defects resonantly, we use two tunable narrow line laser: EXFO T100S-HP (1260-1360 nm) and Newfocus Velocity TLB6700 (1385-1465 nm). A 10:90 beam splitter separates the excitation and collection paths, while filters within the collection path eliminates the laser back reflection and allows for the sideband collection. We also use a 365 nm light emitting diode ($\sim \mu$W at sample) as an off resonant excitation source and charge stabilisation for the 4H-SiC sample. We detect the PL/E either with a photodiode (FEMTO OE-200-IN1), spectrometer and InGaAs camera previously described in Chapter 4, or with a telecom optimized SNSPD from Quantum Opus. All of the outputs and timings are directly detected with 100 MHz data acquisition card. Unlike other experiments, here we use two home made PCBs for microwave driving: one under the sample generating a field perpendicular to the c-axis and a second one on the sample that generates a driving field parallel to the c-axis within a window that also allows for imaging the sample.

To only resolve the ground state spin parameters we also perform ESR experiment in X-band (9.7 GHz) using an ELEXSYS E580 Bruker spectrometer (Bruker Biospin) equipped with a dielectric ring resonator (Bruker EN 4118X-MD4). A quartz tube suspended in the center of the resonator holds the sample, and a flow cryostat (Oxford Instruments CF935) with pumped liquid helium (3.3 K) holds and cools the assembly.

6.2 V in SiC

Similar to Cr in SiC, V also substitutes the Si site within SiC (Fig.6.1**A**). V^{4+} has only one electron (spin-1/2) in its d-shell. As extensively discussed in Sec.3.2.1, under the tetrahedral symmetry, the ^2D orbitals split into ^2T excited state and ^2E ground state. Due to spin-orbit interactions, the ^2T excited state further splits into a higher energy ^2A and a lower energy ^2E orbital configuration shown in Fig.6.1**B**. 4H-SiC has two inequivalent sites, one quasi-cubic (k) and one quasi-hexagonal (h), according to the nearest-neighbor atomic configuration. 6H-SiC has two quasi-cubic sites (k_1 and k_2) and one quasi-hexagonal site (h). Because the local site symmetry is neither exactly cubic nor hexagonal exact assignment of the V sites is difficult and sometimes contradictory in literature [88–90]. For generality, we use the unassigned site names of α and β in 4H-SiC and α, β, and γ in 6H-SiC. Similarly, the ground and excited states separated by the crystal field are labeled GS1 and GS2 and ES1, ES2, and ES3 for generality.

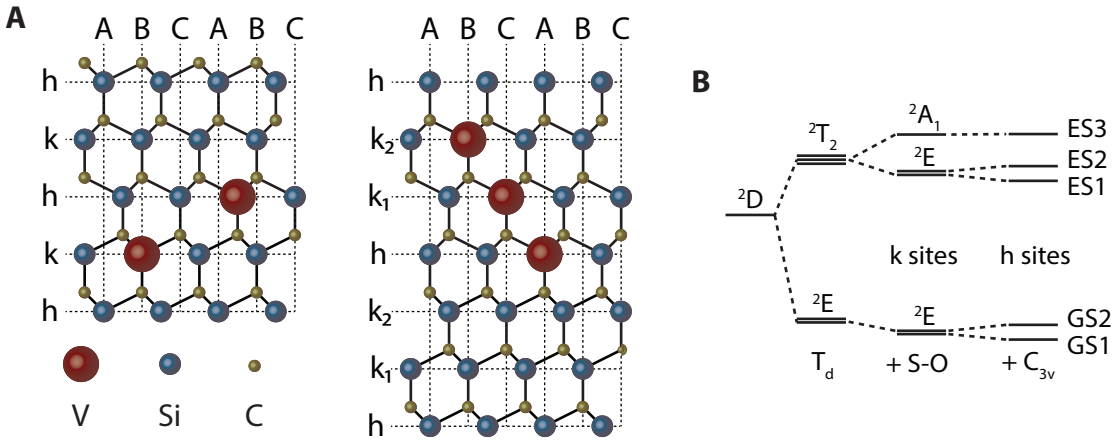

Figure 6.1: SiC:V^{4+} configuration and electronic structure illustrations. (**A**) SiC lattices and their inequivalent sites for the V impurities. (**B**) Expected energy diagram of the orbital d^1 states from crystal field theory and spin-orbit (S-O) coupling according to [89, 91]. The quasi-cubic (k) sites mainly have a tetrahedral (T_d) symmetry, and the quasi-hexagonal (h) sites mainly have a C_{3v} symmetry due to additional trigonal distortion.

6.3 Photoluminescence excitation characterization

We sweep the resonant laser wavelength over the ZPLs of the 5 different V^{4+} sites in both samples and collect the sideband emission (Fig.6.2). We first observe the similarity between the α sites of 4H-SiC and 6H-SiC by comparing their resonant spectra (and other properties in Table 6.1). This similarity is likely related to the quasi-identical crystal configuration of the h sites in both polytypes (Fig.6.1). The splitting between GS1 and GS2 is largest in the α sites ($\sim$ 500 GHz), resulting in substantial thermal polarization at 3.3 K compared to 15 K in Fig.6.2. For the 4H-SiC β and 6H-SiC γ sites, only two transitions are resolved with small ground-state splittings of about 10 to 40 GHz, making it challenging to assign these to specific states. We later solve this issue by looking at the ODMR signal from these transitions (see Sec.6.5) and find that the smallest ground-state splitting (16 GHz) belongs to the 6H-SiC γ site, consistent with the most cubic site k_2. Lastly, only the 6H-SiC β site has six distinct optical transitions that enable the identification of all five orbital states (see Table 6.1).

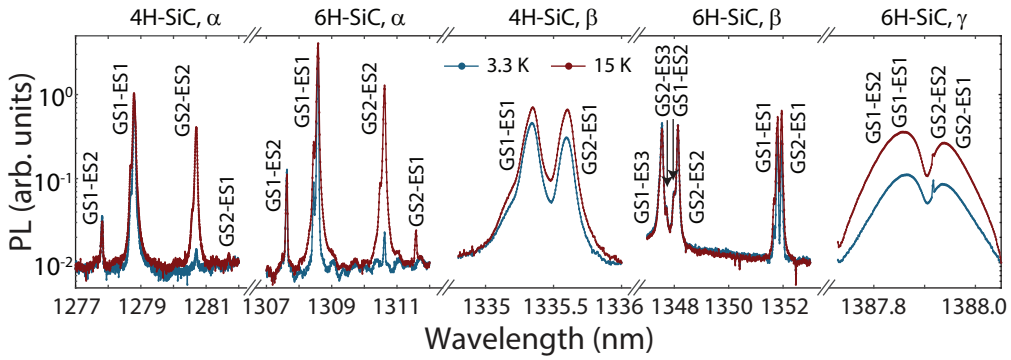

Figure 6.2: PLE spectroscopy of all (6)4H-SiC:V^{4+} sites at 3.3 K (blue) and 15 K (red). The different transitions are partially identified from the difference in thermal population of the orbital states. The weak sharp peak at the center of the 6H-SiC γ site spectrum is an artifact from weak transient laser side modes at this exact wavelength.

6.3.1 Sensing single isotopes

For all inequivalent sites, there are consistent features in the optical spectra that were previously unresolved with off-resonant excitation [89, 91]. The resonant peaks are asymmetric with a longer tail toward higher energies (lower wavelengths) and are also duplicated at higher energies as shown in Fig.6.4 for the 6H-SiC β site where this is the most visible. These duplicates cannot be from additional orbital states, which are already fully accounted for in some of the sites. The single-mode behavior of the tunable laser was confirmed with a Fabry-Perot to discard the possibility of an experimental effect. Following previous studies of donor-bound excitons in natural and isotopically purified silicon [92, 93], we attribute this asymmetry and duplicates to the presence of the minority isotopes of silicon (4.685% of ^{29}Si and 3.092% of ^{30}Si) and carbon (1.07% of ^{13}C) in the nearest-neighbor sites to the vanadium impurity. When a neighbor has a minority isotope, there is a variation in the local mass from the dominant ^{28}Si and ^{12}C that shifts the optical transitions, possibly due to an effective local strain or change in the bandgap. For example, a single ^{30}Si results in twice the shift from a single ^{29}Si. Because there are 4 and 12 equivalent sites for carbon and silicon, respectively, even low abundance of minority isotopes results in significant probability of occurrence for a configuration different from only ^{28}Si and ^{12}C. The shape of the optical peaks is attributed to silicon isotopes, while the duplicate (larger shift) is from the carbon isotopes with larger mass shift ratio than silicon and closer distance to the vanadium.

We model the lineshape of the optical transitions by the presence of minority isotopes within the two nearest neighbor shells of the vanadium impurity as illustrated in Fig.6.3. Starting from a pure lattice of ^{28}Si and ^{12}C, any local change to ^{29}Si, ^{30}Si or ^{13}C leads to a mass and observed linewidth shift. We assume the following:

1. The samples have natural abundance of silicon and carbon atoms.

2. Only the first carbon and silicon shells have a significant influence on the electronic wavefunction.

3. Each Si and C sites are equivalent. This simplifies the model, but it is likely that the c-axis bonds may be different from the basal bonds.

4. One ^{30}Si corresponds to two unit of mass shifts, or equivalently two ^{29}Si.

5. The mass shifts add linearly with each additional local change in isotope.

This leads to the following probability of obtaining a given configuration (and therefore PL intensity):

$$P(N_{^{29}Si}, N_{^{30}Si}, N_{^{13}C}) = \frac{N_{Si}!\left(1 - f_{^{29}Si} - f_{^{30}Si}\right)^{N_{Si}-N_{^{29}Si}-N_{^{30}Si}} f_{^{29}Si}^{N_{^{29}Si}} f_{^{30}Si}^{N_{^{30}Si}}}{\left(N_Si - N_{^{29}Si} - N_{^{30}Si}\right)!N_{^{29}Si}!N_{^{30}Si}!} \times \frac{N_C!\left(1 - f_{^{14}C}\right)^{N_C-N_{^{13}C}} f_{^{13}C}^{N_{^{13}C}}}{\left(N_C - N_{^{13}C}\right)!N_{^{13}C}!} \tag{6.1}$$

where $N_{^{29}Si} = 0, ..., N_{Si}$, $N_{^{30}Si} = 0, ..., N_{Si}$ and $N_{^{13}C} = 0, ..., N_C$ are the number of nearest neighbors ^{29}Si, ^{30}Si and ^{13}C respectively, with $N_{Si} = 12$ and $N_C = 4$ the number of silicon and carbon inequivalent sites. $f_{^{29}Si} = 0.04685$, $f_{^{30}Si} = 0.03092$ and $f_{^{13}C} = 0.0107$ are the natural abundance fractions of the isotopes indicated by their labels. This model provides the relative intensity between each configuration. In order to fit the spectral lineshape in Fig.6.4, we also use a fixed pseudo-Voigt lineshape (mostly Gaussian) for the sub-peak from a single configuration.

With only the intrinsic line shape of the subpeaks and frequency (wavelength) shift per change in atomic mass as free parameters, we are fully able to reproduce the spectra in Fig.6.4. We find an average shift for all sites of the optical transition frequency by 22(3) GHz u^1 or 10^4 u^1 for carbon and by 2.0(5) GHz u^1 or 10^5 u^1 for silicon. The fit also provides an intrinsic inhomogeneous linewidth of about 2 GHz that may be further reduced considering that it includes multiple transitions between the electron and nuclear spin states of ground and excited orbital states. The observed isotope effect suggests that isotopically purified SiC materials may considerably narrow the lines and allow the spin

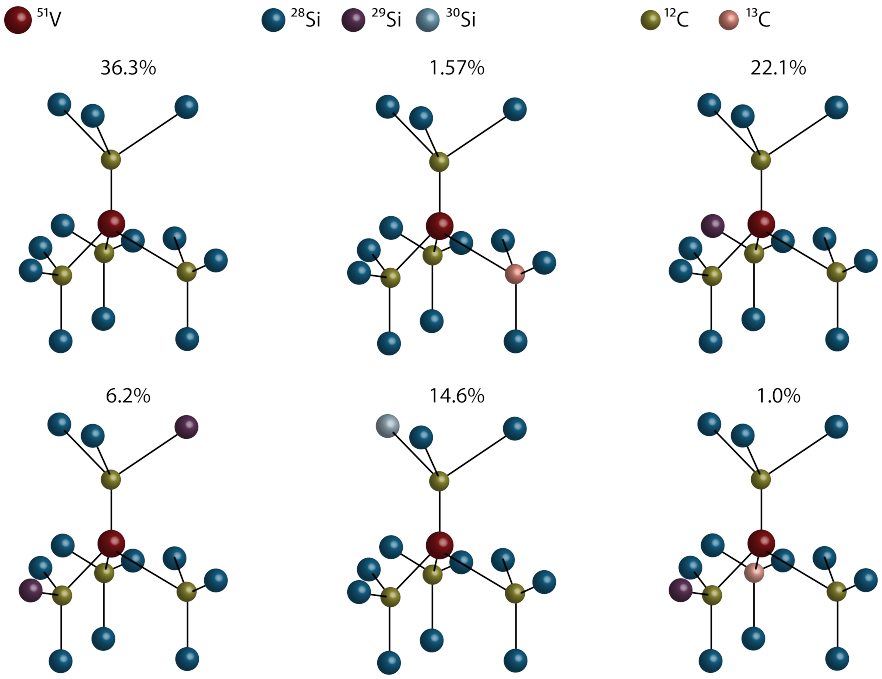

Figure 6.3: Examples of multinomially distributed isotopes within SiC lattice

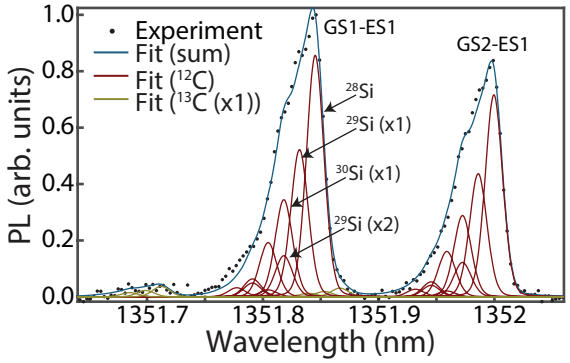

Figure 6.4: Optical energy shift due to nearby isotopes. PLE spectroscopy of the 6H-SiC β site at 3.3 K fitted according to an isotope model for the mass shift from neighbor ^{28}Si, ^{29}Si, ^{30}Si, ^{12}C, and ^{13}C.

states to be optically resolved. By contrast, quantum registers including both the vanadium nuclear spin and a nearest-neighbor carbon or silicon nuclear spin could be directly resolved optically, providing a competitive system for quantum algorithms such as error correction or entanglement distillation. Last, these shifts hint that the wave function of the impurity extends through the first few nearest-neighbor shells and that the optical transitions may be susceptible to static strain.

6.3.2 Optical properties

The excited-state lifetime is an important parameter to estimate the brightness of a defect. Although previous measurements exist for V^{4+} [88], the resonant excitation here excludes possible decay pathways allowed by off-resonant light or possible mixtures of lifetimes from the multiple orbital states. In Fig.6.5**A**, we characterize the ensemble excited-state lifetime by measuring the PLE decay after a pulsed-laser excitation between GS1 and ES1. While the α sites have slower decays (108 and 167 ns) than the β and γ sites (11, 31, and 45 ns), the α sites appear brighter. This may be attributed to the α sites being more favorable during the material creation process and therefore more numerous[1] or to higher quantum efficiency in these sites as suggested by density functional calculations in 4H-SiC [88]. Overall, the lifetimes are much closer to that of vacancy-related defects in diamond and SiC (<20 ns [79, 94]) than that of erbium dopants (∼ms), providing sufficient brightness to observe single V^{4+} emitters without photonic enhancement. Lastly, the DW factor, is resolved for each site with resonant excitation as shown in Fig.6.5**B**, with high values ranging between 25 and 50 % (Table 6.1), confirming the viability of vanadium as a telecom emitter of indistinguishable photons.

6.4 Single V emitter

Although optical cavities are ultimately necessary for any quantum emitter used for efficient quantum communication, the ability to directly measure single defects using only free-space optics has provided alternative applications (e.g., quantum sensing) and ease of characterization in other systems such as the nitrogen-vacancy center in diamond [95]. More generally, the stability and reproducibility of single emitters are key challenges to address, notably, the requirement of low spectral diffusion of the optical transitions for entanglement applications [38, 96].

1. as seems to be the case with Mo dopants in the hexagonal site of 4H- and 6H-SiC [63]

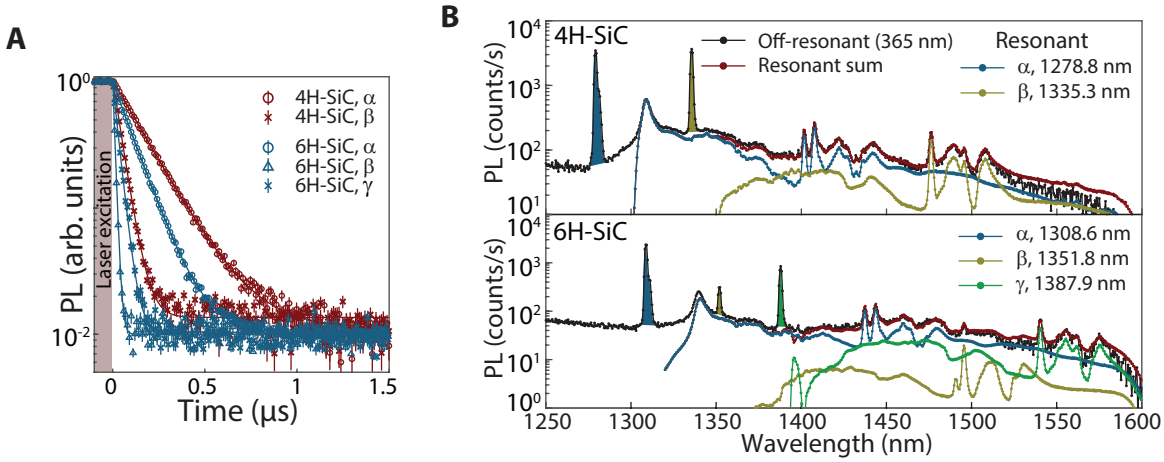

Figure 6.5: Optical properties of (6)4H-SiC:V^{4+} sites at T = 3.3 K. (**A**) Optical lifetimes after laser excitation of the GS1-ES1 transition for each available site. (**B**) Optical spectra for each site is collected two ways: off resonantly with a above bandgap 365 nm light (black) and resonantly for each of the GS1-ES1 transition with background subtraction from slightly detuned excitation. The curve in red provides the sum of the resonant contributions with weights fitted to match the off-resonant excitation. The colored area under the various zero phonon lines and the resonant spectra are integrated to calculate the Debye-Waller factor. The error in this factor from the missing spectra at longer wavelength is estimated to be less than 10 % by Gaussian extrapolation.

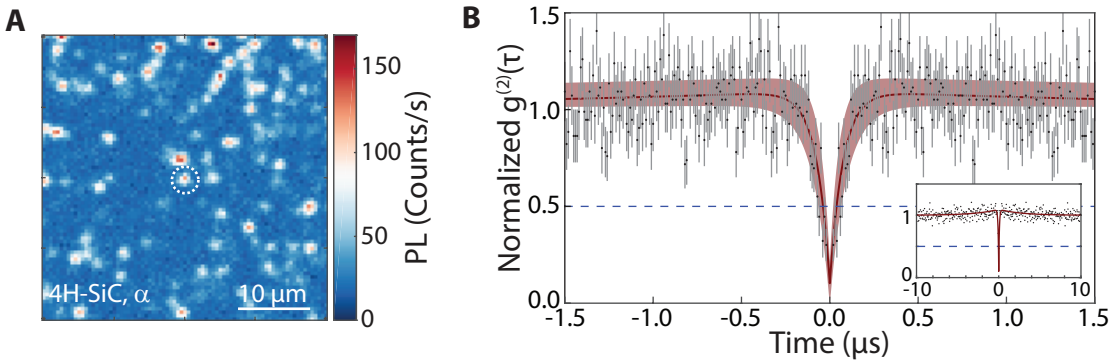

Figure 6.6: Detection of a single 4H-SiC:V^{4+} at T = 3.3 K and B = 700 G under weak 465 nm continuous illumination for charge stability. (**A**) Spatial (near-surface) PLE mapping of single and few V defects by resonant excitation at 1278.8 nm. (**B**) $g^{(2)}$ autocorrelation measurement at the marked area in **A** obtained with a single detector with 20-ns dead time and 10 ns resolution. The autocorrelation signal is normalized using its value at long delay time, and the dark count contribution is calculated and subtracted (3% of total). The red line is the fit [$g^{(2)}(0) = 0.1(1)$], and the red shadowed area is the 95% confidence interval. In the inset, the autocorrelation intensity is shown for longer times.

In Fig.6.6**A**, we scan the surface of the sample while exciting the GS1-ES1 transition of the α site. Isolated bright spots corresponding to single or few V^{4+} defects are observed, with PLE intensity around 100 to 150 counts/s. The combination of low-power resonant excitation and longer-wavelength emission (long-pass filter at 1300 nm) provides a very low background signal limited by the dark counts of the detector ($\sim$20 counts/s). We confirm the single characteristic of one of the spots by autocorrelation $g^{(2)}(\tau)$ measurement (Fig. 6.6**B**), which shows a clear dip below 0.5 near-zero delay ($\tau = 0$). The intensity was obtained using a single-photon counter instead of a Hanbury Brown and Twiss configuration and cannot resolve below 20 ns delay; however, we obtain a $g^{(2)}(0) = 0.1(1)$ from fit using the relation $g^{(2)}(\tau) = 1 - ae^{\tau/\tau_1} + be^{\tau/\tau_2}$, where a and b are amplitude parameters and $\tau_{1,2}$ are the short and long decay times, respectively. The short decay time τ_1 at 0.07(2) μs is reduced from the 0.17 μs optical lifetime (identical to ensemble) by optical Rabi driving. The autocorrelation also rises slightly above 1 (bunching) farther from $\tau = 0$ and is attributed to a shelving state during optical pumping (with shelving time $\tau_2 \simeq 2$ μs) [97]. The measured single-defect photon count rate, combined with the lifetime, DW factor, and optical collection efficiency, provides a lower-bound estimation on the quantum efficiency of the 4H-SiC α site at about 2%. This value may reach about 20% according to theoretical calculations [88] and could be further improved by Purcell enhancement in a photonic cavity.

We then characterize the spectral properties of the confirmed single V emitter. The implanted defects are relatively close to the surface with a calculated mean depth of $\sim$100 nm, a configuration often necessary for photonic integration yet known to cause strong optical spectral diffusion (linewidth broadening) and blinking (PL intensity fluctuations) for other emitters [98]. In Fig.6.7, we repeatedly measure the optical spectrum (GS1-ES1 transition) over the course of 15 hours. The spectrum does not shift, jump, broaden, or lose intensity during that time and has a linewidth of 750 MHz at full width at half maximum. The absence of spectral jumps over long time scales near surfaces may indicate that V^{4+} does not have a strong electric field response. While the linewidth is orders of magnitude larger

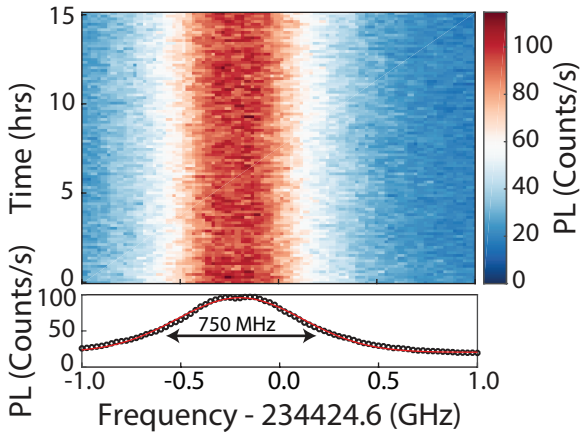

Figure 6.7: Photostability of a single 4H-SiC:V^{4+} at T = 3.3 K and B = 700 G under weak 465 nm continuous illumination for charge stability. The same defect imaged at Fig.6.6**B** is resonantly probed over a 100 times for a total duration of 15 hours, with averaged intensity shown in the bottom. The spectrum shows two maxima from the slightly resolved electron spin states.

than the lifetime limit, it is likely broadened by the many unresolved electron and nuclear spin states in addition to the more typical inhomogeneous strain and spectral diffusion over short time scales.

The optical stability is also consistent across various defects with linewidth varying by about ±100 MHz, as seen in Fig.6.8. The distribution of peak positions follows the measured inhomogeneous linewidth in ensembles (Fig.6.2). Overall, the optical properties of shallow, implanted single V^{4+} impurities in 4H-SiC appear to be mostly unperturbed compared to ensemble measurements, a crucial result for using these defects in photonic and other monolithic devices. The single-defect linewidth remains too broad to resolve the individual spin sublevels, although this may be enabled at higher magnetic fields.

6.5 Spin properties

^{51}V is 100% abundant in nature and has a nuclear spin $I = 7/2$. The single electron of SiC:$V^{4+}$is coupled to the nuclear spin if ^{51}V through hyperfine interaction and the total Hamiltonian of this system is described below:

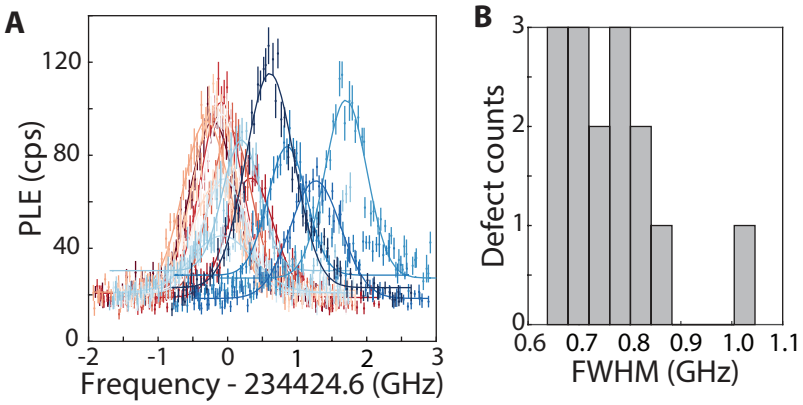

Figure 6.8: Photo variance of potential single 4H-SiC:V^{4+} defects measured at T = 3.3 K and B = 700 G under weak 465 nm continuous illumination for charge stability. (**A**) Resonant spectrum taken for a variety of likely single emitters [not confirmed with $g^{(2)}$]. (**B**) Their fitted linewidths remain consistent at about 750 MHz full width at half maximum. Error bars are 1 standard deviation from experimental acquisition.

$$H = \mu_B \vec{B}_0 \cdot \vec{g} \cdot \vec{S} - \mu_N g_N \vec{B}_0 \cdot \vec{I} + \vec{S} \cdot \vec{A} \cdot \vec{I} \tag{6.2}$$

where $\vec{S}$ and $\vec{I}$ are electron ($S = 1/2$) and nuclear ($I = 7/2$) spin operators defined in Sec.A.2, μ_B, μ_N are the Bohr and nuclear magneton, $\vec{g}, g_N$ are the electron and nuclear g-factors ($\mu_N g_N = 11.213$ MHz/T), $\vec{B}_0$ is the static magnetic field, and $\vec{A}$ is the hyperfine tensor between the electron and nuclear spin. Each of the orbital states therefore split into 16 additional spin states under nonzero magnetic field, as illustrated in Fig.6.9**A**. The spin properties of the V^{4+} ground state (GS1) in some sites of 4H-SiC and 6H-SiC were previously studied using electron spin resonance (ESR) and magnetic circular dichroism [90, 99]; however, they were realized at high magnetic field where it becomes challenging to correctly identify anisotropic hyperfine tensors.

We characterize the spin parameters of each site in V^{4+} defect ensembles using a combination of ESR, ODMR, and optical pump-probe methods. As previously discussed in Chapter 1, ESR is an inductive detection method that measures resonant microwave absorption by spin ensembles; it does not require optical excitation and is sensitive only to the thermally populated ground states. This means that at 3.3 K (where the rest of the measurements

performed), only GS1 can be measured for the α sites, while both GS1 and GS2 may be visible for the γ and β sites. Although, there is not a clear Λ like system to effectively spin polarize the ground state, any imbalance in population due to the optical excitation can give rise to ODMR as long as the population trapped population in a shelving state is reintroduced into the optical path through magnetic driving. As ODMR requires optical excitation, it is sensitive to all orbital states with a preference for ground states when the excited states' lifetimes are short.

Similarly one can detect the shelving state optically through a second color, as previously discussed in Sec.4.3.3. This technique is more sensitive to the orbital excited states and more complex depending on the type of pumping scheme [63]. Namely there are four pumping schemes: $\mathbf{\Lambda}$ for transitions between two ground state levels and one excited state level sensitive to the ground-state spin properties (for example used for SiC:Cr^{4+}), $\vec{V}$ for transitions between one ground state level and two excited state levels sensitive to the excited-state spin properties, and $\vec{X}$ and $\mathbf{\Pi}$ for transitions between two ground state and two excited state levels sensitive to both ground- and excited-state spin properties. When the spin states cannot be optically resolved, all pumping schemes occur simultaneously, and assigning the observed resonances can be challenging.

We use the 4H-SiC β site to discuss the spin measurements as it is the most complete and resolved one. The data for other sites are shown below in Sec.6.6 and their fit parameters in Table 6.1. Selective excitation of the GS1 or GS2 resonantly allows for observing the ODMR from either orbital independently shown in Fig.6.9**B**,**C**. Sweeping the magnetic field allows for identifying the relevant spin parameters. At low magnetic fields, we observe competition between the hyperfine and Zeeman interactions, enabling precise fitting of the hyperfine tensor diagonal components in their principal axis. The two ground states GS1 and GS2 can mostly be excited in the parallel configuration, allowed by mixing between the electron and nuclear spins, but only weakly in the orthogonal configuration indicating an orthogonal g-factor $g_{xx,yy}$ close to zero. The hyperfine interactions for GS1 have $A_{xx} = A_{yy} \neq A_{zz}$

[axial symmetry, d_{z^2} - like orbital if dipolar [100]] for the α sites and $A_{xx} \neq A_{yy} \simeq A_{zz}$ (rhombic symmetry, $d_{xz,yz}$-like orbital if dipolar) for the β and γ sites assuming that equal components have the same sign (not resolved here). These hyperfine aspect ratios may be related to the local symmetry (and corresponding wave function distortion), where the Si-C layers stacking is aligned with the c-axis for the h sites and tilted for the k sites. The GS2 hyperfine tensor was only obtained for the β and γ sites (as thermally populated) and shows a nonzero zz component with a principal axis tilted by about 50° to 52° from the c-axis. This angle matches the 52° tilt off the c-axis between two nearest-neighbor silicon sites in separate layers of the SiC lattice.

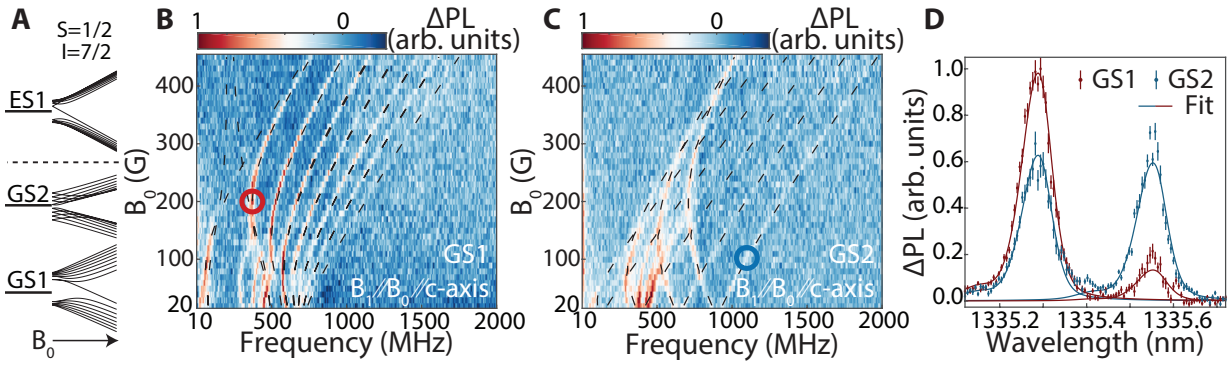

Figure 6.9: Ground state ODMR of 4H-SiC:V^{4+} $\beta-$site at T = 3.3 K (**A**) Energy level structure including the electron spin (S) and nuclear spin (I) for the GS1, GS2, and ES1 levels. The static magnetic field (B_0) dependence is simulated using fitted spin parameters from (**B**) ODMR of the lowest ground-state GS1 as a function of B0 and microwave drive frequency. Both B_0 and the microwave drive (B_1) are applied parallel to the c-axis. The dashed lines in black are modeled from fitting the spin Hamiltonian in Eq.6.2. The lines at low magnetic fields around 400 MHz are attributed to ES1. At high magnetic field under parallel excitation, the spin transitions become forbidden, and the ODMR contrast disappears. (**C**) ODMR of GS2 under similar conditions to **B**. (**D**) ODMR as a function of the laser wavelength to correlate ground states and optical transitions. The red and blue curves are measured, respectively, at the red and blue circles in **B** and **C**. The curves are fitted (using the isotope model line shape) to extract the individual transitions.

It should be noted that the assignment of the ODMR signal to an orbital state is not always straightforward, as shown in Fig.6.9**D**. Spin resonance ascribed to GS2 (blue line) appears when optically exciting either the GS1-ES1 transition or the GS2-ES1 transition. This indicates that spin polarization is transferred between the two ground states likely

from thermal relaxation. The ODMR assignment is resolved in this case by looking at the spin resonance in GS1 (red line) and comparing the hyperfine tensors of the various sites. The ODMR-resolved resonant spectroscopy in Fig.6.9**D** is also a powerful tool to distinguish close transitions and allows us to separate the GS1, GS2, ES1, and ES2 orbital states for the 6H-SiC γ site (see Fig.6.17).

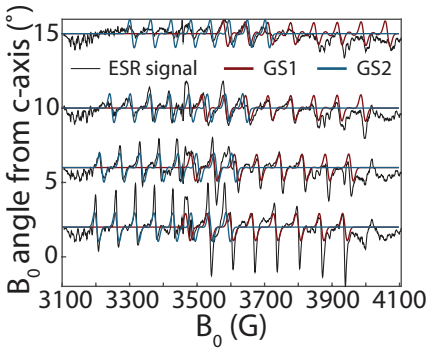

Figure 6.10: ESR of 4H-SiC:V^{4+} $\beta-$site at T = 3.3 K within X-band as a function of B_0 and angles from the c-axis. The blue and red lines are simulated from the spin parameters obtained by ODMR in Fig.6.9 and are shown to compare derivative peak center positions.

For consistency, we compare the ODMR signal with ESR experiments in Fig.6.10. Two sets of peaks are observed and assigned to GS1 and GS2 of the 4H-SiC β site only. Similarly, ESR in 6H-SiC presents (Fig. 6.10) two sets of peaks assigned to GS1 and GS2 of the γ site only. The lack of substantial ESR signal from all other sites results from their lower orthogonal g-factor, forbidding microwave transitions at high magnetic fields ($|g\mu_B B_0| >> |A|$). In general, we find large discrepancies for some of the fitted hyperfine values compared to previous ESR and magnetic circular dichroism experiments [90]. This is explained by the limited influence of A_{xx} and A_{yy} on the spin resonance frequencies in the high field limit where these previous studies occurred.

We lastly characterize in Fig.6.11 the spin properties of the ES1 excited state using both ODMR and two color measurements. The two color optical signal is negative and shows no change when exciting either the GS1-ES1 transition or the GS2-ES1 transition, suggesting that the pump-probe is a $\vec{V}$ scheme and mainly sensitive to the spin levels of the ES1 orbital

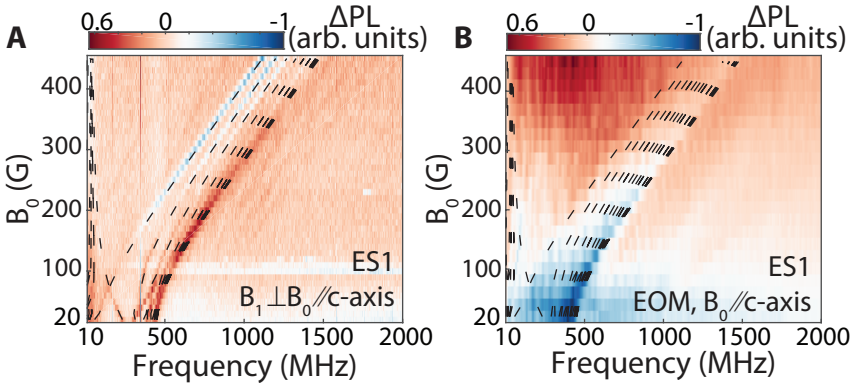

Figure 6.11: Excited state spectroscopy of 4H-SiC:V^{4+} $\beta-$site at T = 3.3 K. (**A**)ODMR of the excited state ES1 with B_1 orthogonal to B_0. Nonfitted signals in the background are attributed to GS1/2 and are much weaker owing to low $g_\perp$ values. (**B**) Optical hole burning recovery using pump-probe excitations between GS1 and ES1 and detuned by the microwave frequency using an EOM. The transitions are modeled (black dashed lines) using the parameters obtained in **A**.

state. The inhomogeneous broadening in these all-optical measurements is quite large (hole linewidth about 100 MHz) and limits precise fitting of the spin parameters. The 4H-SiC β site is unique, however, as it shows a clear ODMR contrast under orthogonal B_1 drive that matches the two color experiment, enabling more sensitive measurement of the ES1 hyperfine parameters.

6.5.1 Spin T_1

We expect that the V^{4+} system undergoes rapid spin relaxation due to phonon processes and the small splitting between the GS1 and GS2 states, similar to silicon vacancies in diamond [101] as discussed in Sec.3.2.1. At 3.3 K, we characterize this population relaxation (T_1) using all optical hole burning recovery experiment, as previously discussed in Sec.4.3.2 and shown in Fig.6.5.1 (A and B). A resonant laser pulse excites the GS1-ES1 transition during which the emitted PL intensity decays because of hole burning. The PL signal requires some delay to regain full intensity after a second laser pulse, corresponding to the thermal relaxation between GS1 and GS2, or to the spin relaxation in GS1, both limiting factors for coherent experiments. The 6H-SiC β site has a short relaxation time of 0.2 μs, and

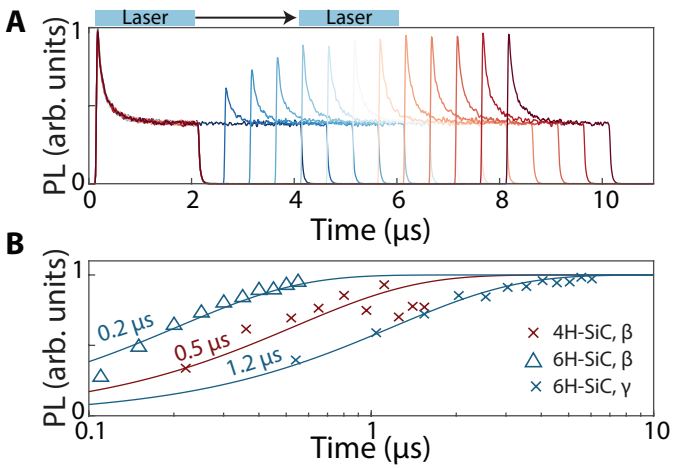

Figure 6.12: Ground state T_1 of 6H-SiC:V^{4+} $\gamma-$site at T = 3.3 K. (**A**)Transient detection of hole burning and recovery in the 6H-SiC γ site. The transition GS1-ES1 is pumped (0 to 2 μs), followed by a moving delay before a second pump measures the intensity of the peak signal. (**B**) Optical decays obtained from the sequence in **A** where the amplitude is the hole depth [differential between maximum and steady-state amplitudes in **A**]. For 6H-SiC, the error bars are within the data point size. For 4H-SiC, the decay has some additional fluctuations that are not modeled here.

the γ site is longest at 1.2 μs, although we are unable to measure the α sites due to weak hole burning. As demonstrated in silicon vacancies in diamond [101], these relatively short lifetimes are not necessarily prohibitive as they are expected to considerably increase at millikelvin temperatures.

6.5.2 Coherent spin driving

Last, we demonstrate in Fig.6.13 coherent driving between two spin states ($\approx 0.74\,|1/2,-7/2\rangle + 0.65\,|-1/2,5/2\rangle$ and $-0.6\,|1/2,-7/2\rangle + 0.74\,|-1/2,5/2\rangle$ in $|m_s,m_I\rangle$ notations) in the GS1 orbital of the 6H-SiC β site. Despite the short lifetime of this site, the corresponding continuous-wave ODMR had a sufficiently narrow inhomogeneous linewidth (about 8 MHz) for coherent driving, possibly due to lower strain sensitivity. We fit the time dependence by a damped Rabi oscillation formula derived in Sec.2.2.3 with an additional dissipation term Γ to account for population loss:

$$P(t) = \frac{A^2 e^{-\Gamma/t}}{\Delta^2 + A^2 + \Gamma^2} \sin^2\left(\frac{t}{2}\sqrt{(\Delta+\Gamma)^2 + A^2}\right) \tag{6.3}$$

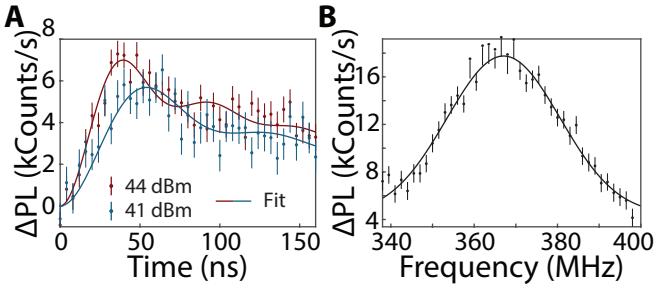

Figure 6.13: Coherent driving oscillations of ground state of 6H-SiC:V^{4+} $\gamma-$site at T = 3.3 K and B - 200 G. (**A**)Coherent Rabi oscillations for two different microwave drive powers. (**B**) Pulsed-ODMR spectrum using an inversion pulse calibrated from **A**. All error bars are 1 SD from experimental acquisition.

Pulsed-ODMR spectrum after calibrating the π-pulse duration from the Rabi oscillations confirm the source of the contrast from the spin transition. Over the course of many acquisitions, we observe some decay of the pulsed-ODMR contrast, suggestive of a slow nuclear hyperpolarization within the full electron-nuclear spin system.

6.6 Characterization of all sites

Below are the ODMR, two-color pump-probe data (if exists) for all sites and a table that summarizes all of the extracted spin Hamiltonian and optical parameters:

6.7 Summary

SiC:V^{4+} offers O-band telecom optical emission with fast lifetimes which allowed for detection of a single emitter without the need for any photonic structure, demonstrating V^{4+}s viability as a single quantum emitter for fiber based long distance quantum architectures. Creation of V^{4+} in commercial SiC through implantation and annealing further displays the feasibility of a scalable device manufacturing scheme. The stable optical properties, despite

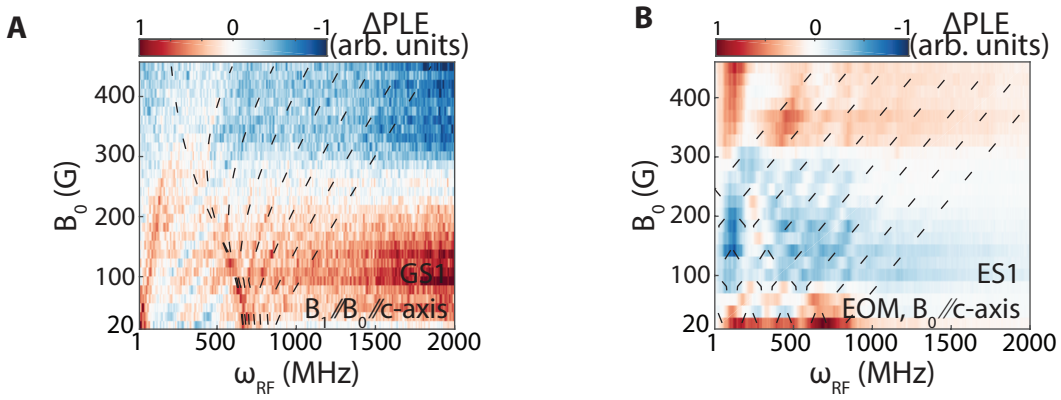

Figure 6.14: Spin properties of 4H-SiC α site at 3.4 K. (**A**) ODMR of GS1. (**B**) Pump-probe (hole recovery) experiment. The dashed lines in black are simulated from the fitted spin model. The ODMR signal in (**A**) also shows contribution from ES1 (blue lines at low frequencies and magnetic fields) which helps fit the spin parameters.

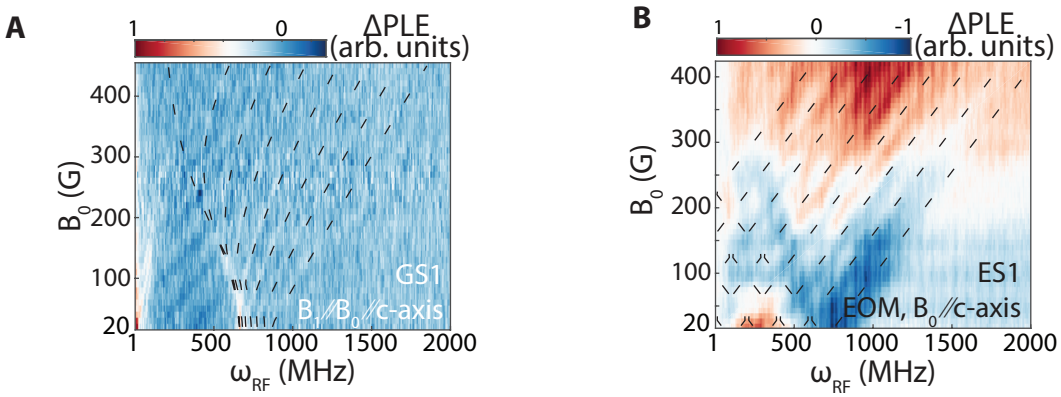

Figure 6.15: Spin properties of 6H-SiC α site at 3.4 K. (**A**) ODMR of GS1. (**B**) Pump-probe (hole recovery) experiment. The dashed lines in black are simulated from the fitted spin model. The ODMR signal in (**A**) also shows contribution from ES1 (blue lines at low frequencies and magnetic fields) which helps fit the spin parameters.

the defect being only a ∼100 nm away from the surface is very promising for integration within quantum opto-electronic devices. The defect comes with a spin-1/2 electronic spin and spin-7/2 nuclear spin creating a 14 dimensional Hilbert space that could be used for various quantum algorithms. Since the optical transitions are sensitive to a nearest neighbor isotope changes, it is also possible to optically identify V^{4+} defects with nearby nuclear spins to further expand the computational Hilbert space for more advanced algorithms (e.g. error correction). High-fidelity coherent control will require lower temperatures, single spins for

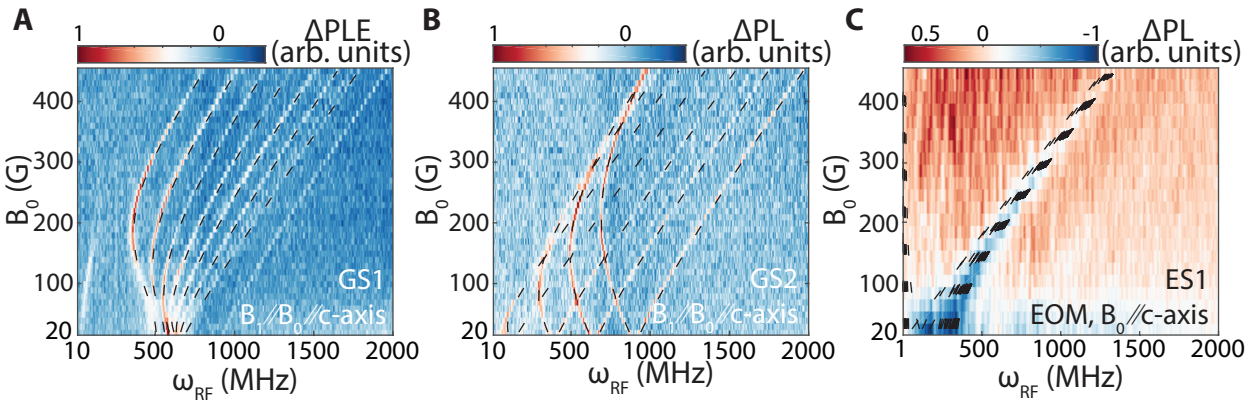

Figure 6.16: Spin properties of 6H-SiC β site at 3.4 K. (**A**) ODMR of GS1. (**b**) ODMR of GS2. (**c**) Pump-probe (hole recovery) experiment. The dashed lines in black are simulated from the fitted spin model.

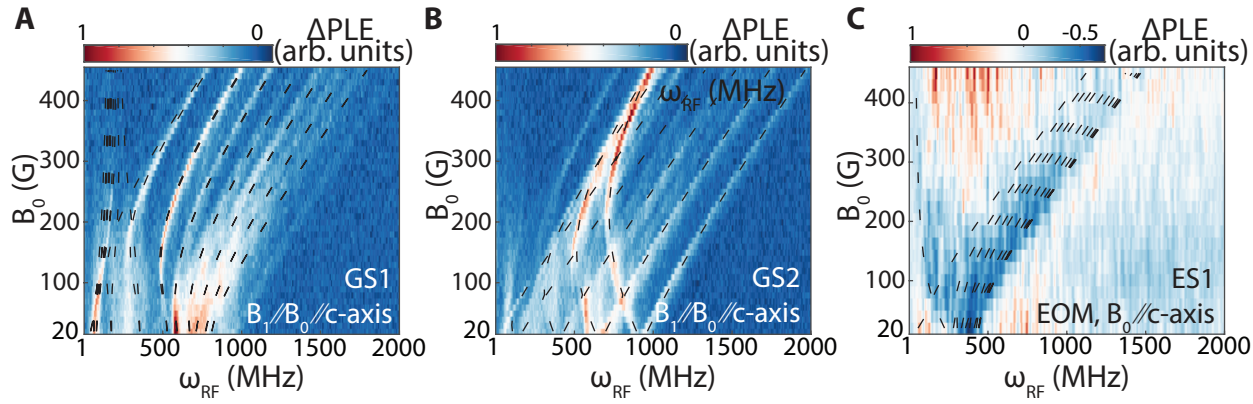

Figure 6.17: Spin properties of 6H-SiC β site at 3.4 K. (**A**) ODMR of GS1. (**b**) ODMR of GS2. (**c**) Pump-probe (hole recovery) experiment. The dashed lines in black are simulated from the fitted spin model.

low detuning and drive inhomogeneity, and efficient spin polarization. Eventually, the ability to reset the V defect to a specific electron and nuclear spin state will be crucial for practical applications and could be achieved either optically or by magnetic resonance [102]. Nevertheless, the identified spin parameters through ODMR and two-color pump probe schemes in this chapter, provided all the necessary components for understanding and controlling the V^{4+} defects both optically and magnetically, setting them up as a prime candidate as telecom emitters for quantum applications.

	4H-SiC		6H-SiC		
	α	β	α	β	γ
Site assignment	*h*	*k*	*h*	k_1	k_2
ES1 – GS1 (nm)	1278.808(6)	1335.331(6)	1308.592(6)	1351.845(6)	1387.806(6)
GS2-GS1 (GHz)	529(1)	43(1)	524(1)	25(1)	16(1)
ES2-ES1 (GHz)	181(1)	-	167(1)	628(1)	6(1)
ES3-ES2 (GHz)	-	-	-	72(1)	-
DW (~%)	25	50	45	50	40
τ (ns)	167(1)	45(1)	108(1)	11(1)	31(1)
GS1 $g_{xx,yy}$, g_{zz}	0, 1.748*	0<g<1, 1.870(5)	0, 1.749*	-, 1.95(2)	0<g<1, 1.933(5)
GS1 A_{xx} ,A_{yy}, A_{zz} (MHz)	165,165,232(5)	103,188,174(5)	165,165,232(5)	114,166,171(5)	45,215,175(10)
GS2 $g_{xx,yy}$, g_{zz}	-	$0 < g < 1$,2.035(5)	-	-,2.00(2)	$0 < g < 1$,1.972(5)
GS2 $A_{xx,yy}$, A_{zz} (MHz)	-	0,257(5)	-	0,258(5)	0,265(5)
GS2 θ_{xx} , θ_{yy}, θ_{zz} (°)	-	0, 52(2), 0	-	0, 50(2), 0	0, 51(2), 0
ES1 $g_{xx,yy}$, g_{zz}	-,2.24†	-,2.03(2)	-,2.24*	-,2.0(1)	-,2.03(2)
ES2 $A_{xx,yy}$, A_{zz} (MHz)	20,220(20)	112,52(5)	20,200(20)	80,20(20)	110,50(20)†

Table 6.1: Optical and spin properties of V^{4+} defects in 4H-SiC and 6H-SiC around 3.3 K. The k_1 site is assigned to the 6H-SiC β site on the basis of having the closest crystal configuration and properties to the 4H-SiC β site. k_2 is the most cubic-like site and therefore assigned to γ with the smallest GS1-GS2 splitting. The Debye-Waller (DW) factor is a coarse estimation as long-wavelength contributions cannot be observed (see Fig.6.5). τ is the optical lifetime. The spin parameters (absolute values for the diagonal components xx, yy, and zz) are given in their principal axis with g being the g-factor and A being the hyperfine interaction. xx and yy components are interchangeable, we cannot distinguish g_{xx} from g_{yy}, and a good fit is obtained when A_{xx} and A_{yy} are equal for GS2 and ES1. xx, θyy, and θ_{zz} are the angles between the principal and the c-axis basis. "-" indicates unresolved parameters. *Parameters taken from literature ([89, 90]). † Partially resolved parameters obtained by comparison with other sites.

Chapter 7

Transition metal centered molecular spin qubits

Thus far the experimental demonstrations of transition metal ions as optically addressable spin qubits have been limited to a solid state host. As discussed in Chapter 3, the electronic structure and therefore the optical and spin properties of transition metal ions are determined by the ligand field and therefore it is possible to build optically addressable molecular spin qubits out of them. As discussed earlier in Chapter 1, chemical synthesis of molecular spin systems affords bottom-up qubit design [103, 104]. A chemical approach offers tunability through atomistic control over the qubit; scalability through chemical assembly of extended structures; and portability across different environments (e.g., solution, surface, solid-state), because the qubit is not confined to a specific host. These capabilities provide substantial control over the intrinsic and extrinsic environment of molecular qubits and can solve many of the problems faced by the defect spins community.

To engineer an optically addressable spin qubit, in this chapter, we target the d^2 configuration under strong tetrahedral ligand field, extensively discussed in Sec.3.2.2 and experimentally demonstrated in Chapter 4 and Chapter 5.

7.1 Cr^{4+} based molecules

7.1.1 Experimental Details

To demonstrate the power of tunability of transition metal based optically addressable molecular spin qubits, we synthesize three different $Cr^{4+}R_4$[R = *o*-tolyl, 2,3-dimethylphenyl, 2,4-dimethylphenyl] molecules (Fig.7.1**A**). An individual molecule is $\sim$ 1 nm in size, therefore we diluted each compound in their S = 0, isostructural tin analogs to reduce interactions between Cr^{4+} centers. We then form molecular crystals (**1**, **2**, **3**) out of this mixture (Fig. 7.1**B**) to make sure all of the spins are oriented in the same direction for ensemble measurements. The metal-center symmetry in these crystals varies from relatively high, S_4 for **1**, to low, C_1 for **3**, directly affecting the ground-state spin structure.

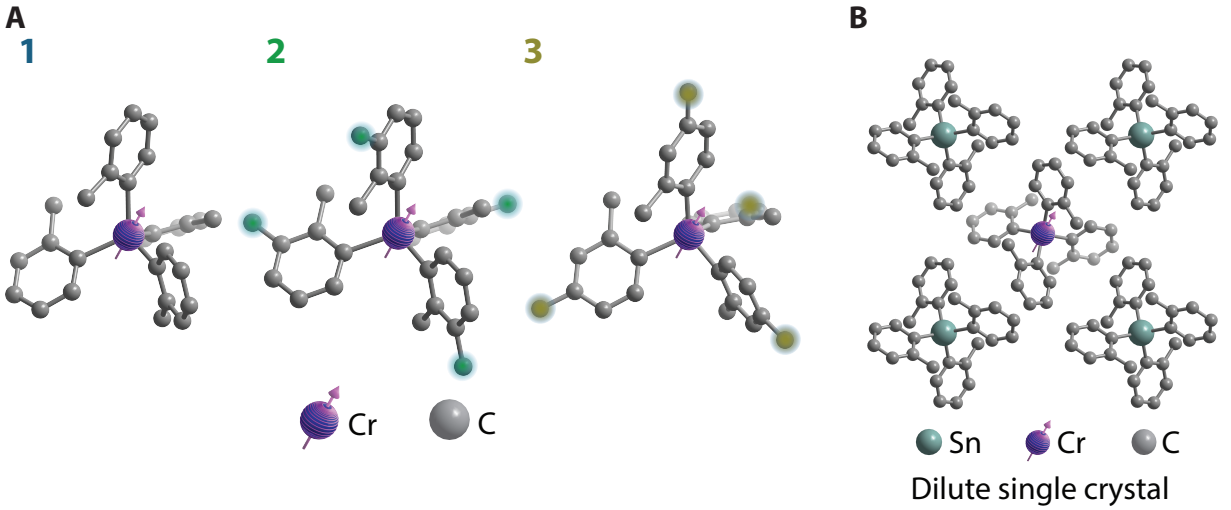

Figure 7.1: Chromium centered organometallic molecules illustration. (**A**)Molecular structures for **1**–**3** determined by single-crystal x-ray diffraction. Hydrogen atoms are omitted for clarity. Ligand modifications for **2** and **3** are highlighted in green and yellow. Chromium and carbon atoms are shown in purple and gray, respectively. (**B**) An illustration of each Cr^{4+} compound diluted in a single crystal (purple) of the isostructural S = 0 tin (Sn) analog.

The dilute crystals, with linear dimensions $\sim 0.1 - 1$mm, are mounted on a coplanar waveguide (CPW) for microwave excitation and encapsulated with a thin layer of epoxy (Illumabond, UV curing epoxy, 60-7180RCL13) to prevent air exposure while sample loading.

This assembly is cooled down with a closed cycle Montana Instruments cryostat and imaged through a confocal microscopy setup with general guidelines discussed in Sec.D.1. A Thorlabs 785 nm laser diode off-resonantly excites the sample, while a narrow-line tunable Sacher, LION laser resonantly excites it. A broadband 50:50 beam splitter separates the excitation and collection paths while corresponding long and short pass filters clean the laser and PL signal. An Olympus LCPLN100XIR objective both focuses the excitation light and collimates the PL signal. We estimate there are 10^7 Cr^{4+} emitters within the laser spot. The signal can either be detected with a Princeton Instruments spectrometer InGaAs camera (Pylon-IR), a fiber coupled Femto OE-200-IN1 photodetector or an SNSPD. A Swawbian Instruments Time Tagger 20 counted the photon arrival times for lifetime measurements.

For high field optical measurements, we custom built a fiber coupled sample mounting rod for a Quantum Design Physical Property Measurement System (PPMS) which can generate single axis magnetic field between -9 and 9 Tesla with design details described in Sec.D.2.

For ESR measurements, the bulk dilute crystals are grounded to form microcrystalline powders. Samples were loaded into 4 mm outer diameter quartz ESR tubes under a dinitrogen atmosphere, restrained with eicosane and flame sealed under vacuum. Prior to measurements, samples were primarily stored in the dark to prevent potential degradation [105]. Continuous-wave (cw) ESR spectra were collected at the California Institute of Technology facility using a Bruker EMX X-band spectrometer and a liquid nitrogen immersion dewar. All measurements were performed at 77 K. Spectra were acquired with the Bruker Win-ESR software suite.

7.1.2 Optical and spin characterization

This molecular system, analog to SiC:Cr^{4+}discussed in Chapter 4, exhibits the same electronic and spin physics. Under the off resonant excitation, ground-state population is promoted to the first S = 1 excited state, undergoes fast intersystem crossing to the S = 0 state, and decays to the S = 1 ground state, emitting near-infrared PL. For **1**–**3**, this emission

comprises sharp zero-phonon lines (ZPLs) ranging from 1009 to 1025 nm (Fig.7.2**A**), along with longer wavelength phonon sidebands. The minor ligand modifications in **1**–**3** also result in distinctive ground-state spin structures, as observed in ground-state electron spin resonance (ESR) measurements (Fig.7.2), with extracted values of D and E lying in the readily addressable regime of < 5 GHz for each compound.[1]

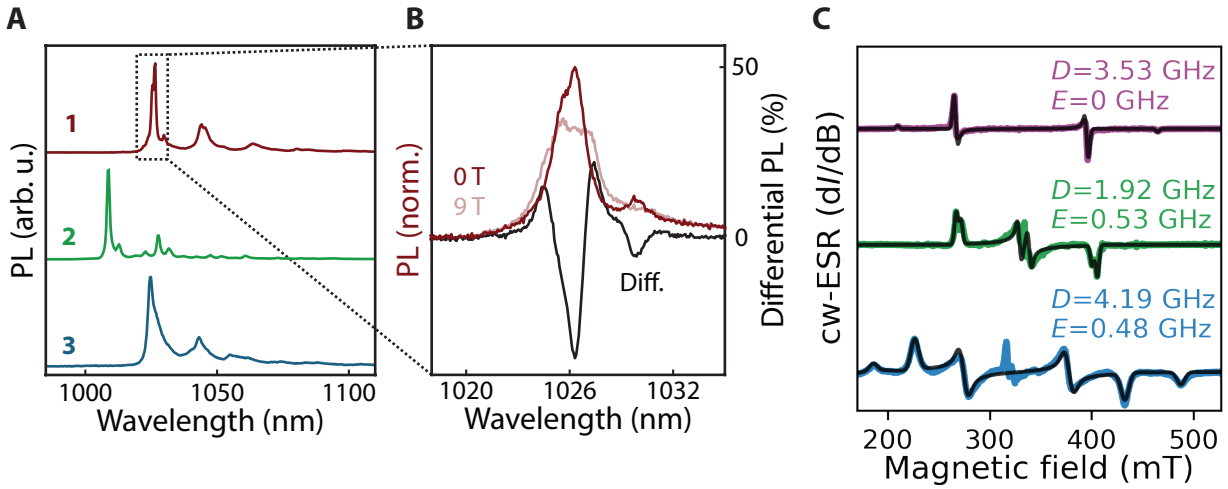

Figure 7.2: Optical and spin properties of molecular spin qubits. (**A**)PL spectra for **1**–**3** at T = 4 K using off-resonant (785 nm) excitation. (**B**) Zeeman splitting of the zero-phonon line of **1** at 9 T. (**C**) X-band continuous-wave electron spin resonance (cw-ESR) spectra for **1**–**3** collected at 77 K. Simulations are shown in black, along with extracted D and E parameters. The central resonances at $g \approx 2 - 2.1$.

To further confirm the d^2 electronic structure under strong tetrahedral ligand environment discussed in Sec.3.2.2, we measure the emission of **1** under a high magnetic field using off-resonant excitation (Fig.7.2**B**), same measurement as in Fig.4.1. Owing to the S = 0 excited state, the Zeeman splitting of the ground state manifests directly as a shift in the optical emission energies. This effect is clearly shown by taking the difference in PL spectra at 9 and 0 T: Optical emission into the $m_s = \pm 1$ spin sublevels shift to lower and higher energies, giving characteristic peaks on either side of the zero-field ZPL in the differential

1. because the signs of D and E are not determined and only their magnitudes influence our experiments, we take $D, E > 0$ for clarity

spectrum, along with a central dip[2].

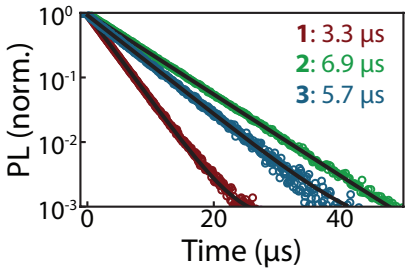

Figure 7.3: Optical lifetimes of molecular spin qubits for **1**–**3** are measured using resonant excitation at the zero-phonon line at T = 4 K.

To effectively hole burn and spin polarize this level structure, the optical lifetime must be shorter than the spin T_1. We measure the excited state lifetime under off resonant excitation to be 3.3 μs, 6.9 μs and 5.7 μs for compounds **1**, **2** and **3** respectively (Fig.7.3).

7.1.3 Optical-spin interface

To demonstrate an optical-spin interface in these systems, we focus on **1** as an illustrative example before discussing **2** and **3**. Using a narrow-line laser, we resonantly excite the S = 1 ground state to the S = 0 excited state and collect emission into the phonon sideband to remove excitation laser scatter. First, we characterize the emission as a function of the excitation wavelength (Fig.7.4**A**), and measure a PLE peak with a linewidth of $\sim$ 150 GHz. For the rest of the experiments the narrow line laser is parked at the maximal signal point of the PLE peak shown with the dashed line.

When we rotate the polarization of the incoming light with respect to the crystal orientation, we observe a clear dipole transition between the ground and the excited states. Although in a T_d symmetry a dipole transition between the ^1E excited state and $^3A_2$ ground state are forbidden, as discussed in Sec.3.3.1, within the reduced S_4 symmetry of the compound **1**, the ^1E splits into ^1A and ^1B, the ground state $^3A_2$ turns into a ^3B. In this

2. the feature at 1030 nm arises from the vibrational sideband

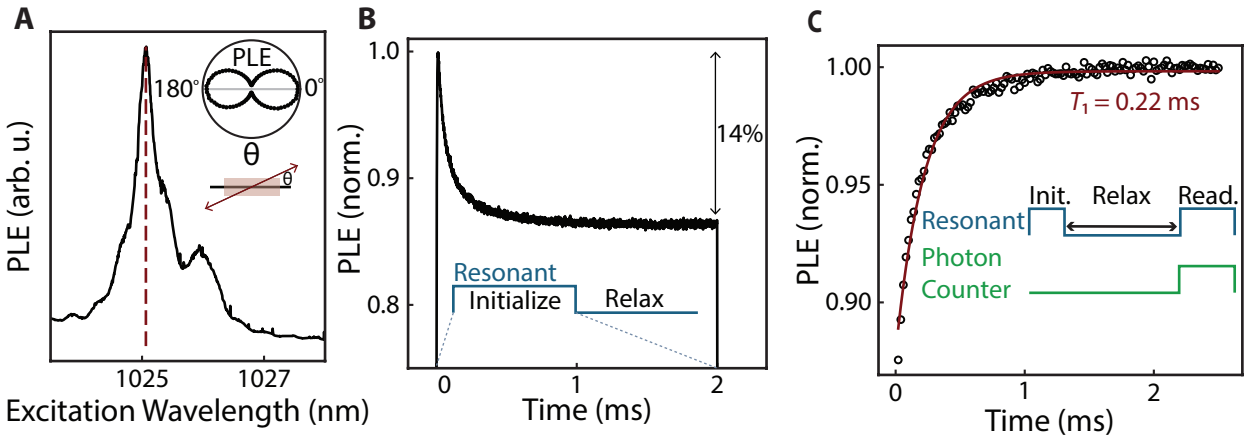

Figure 7.4: All-optical ground-state spin initialization and readout of **1**. (**A**) Photoluminescence excitation (PLE) spectrum obtained by sweeping a narrow-line laser over the zero-phonon line. The dashed line shows the excitation wavelength used for all following experiments. (Inset) Dependence of the PLE on laser polarization, defined by the angle θ from the crystal long axis. (**B**) Time-resolved optical spin initialization. (**C**) All-optical measurement of the spin-lattice relaxation time T_1.

configuration, the electric dipole operator for light polarized in the S_4 symmetry axis has a B character, while the perpendicular component has has an E character. Going through the product table in Sec.C.1, we see that the only allowed transition is between ${}^3B \leftrightarrow {}^1A$ in the crystal axis direction, consistent with the data. Therefore, these electric dipole selection rules explain the observation of Fig.7.4**A** inset that PLE is maximized for polarization along the long axis of the crystal. This may also explain two orders of magnitude faster excited state lifetimes[3] of molecule based transition metal ions compared to more symmetric analogs within the solid state host such as SiC or GaN. To further maximize emission, we align the excitation polarization with the optical dipole transition, which is colinear with the long axis of the needle-like crystal.

Although, the inhomogeneous linewidth is broadened by static energy-level variations, likely caused by strain, the subensemble linewidth is limited only by dynamical processes like electron phonon coupling. Therefore, as long as the spectral hole linewidth is similar

3. This may also be a result of increased non radiative decays from the excited state due to vibronic structure of the molecules

or smaller than the spin splitting energies, it is still possible to spin-selectively excite a subpopulation.

We demonstrate this hypothesis by measuring an all-optical initialization and readout of the ground-state spin using hole burning and recovery. To initialize the spin, we apply the pulse sequence outlined in Fig.7.4**B**, consisting of a long optical pulse (2 ms) followed by a wait time (2 ms) to equilibrate ground-state spin populations before the next pulse. The emission during the optical pulse shows the characteristic behavior of optical spin polarization: a gradual drop in emission as population is pumped from the probed ground-state spin sublevel (the "bright" state) and into the other ("dark") spin sublevels. The optical contrast between the start and the end of the pulse places a lower bound on the spin polarization of 14%.

Using this spin initialization, we all optically measure (same experiments as Sec.4.3.2 and Sec.6.5.1) the ground-state spin-lattice relaxation time, T_1, by performing the two-pulse experiment outlined in Fig.7.4**C**. This sequence consists of an initialization pulse (300 μs), a variable relaxation time, and a readout pulse (20 μs). The initialization pulse transfers population to the "dark" spin sublevels. As ground-state spin population relaxes back to the "bright" sublevel, the emission increases. Measuring this emission at variable relaxation times yields $T_1 = 0.22(1)$ ms. That T_1 is much longer than the optical lifetime ($T_{\text{opt}} = 3.3$ μs, Fig.7.3) confirms that many optical cycles can be used to accumulate ground-state spin polarization.

7.1.4 Spin initialization and readout dynamics

Since the optical hole linewidth is similar to the zero field splitting, it is not possible to resolve a hole recovery all optically. Instead, knowing the polarization contrast, optical lifetime, spin T_1 and D we can estimate crucial parameters such as spin polarization and optical hole linewidth.

We consider a kinetic scheme consisting of spin-dependent optical pumping and excited-

state decay, and spin-lattice relaxation. We neglect coherences between the different levels. Denoting the populations of the triplet spin sublevels as n_0, n_{+1}, and n_{-1}; and the population of the singlet excited state as n_e, the kinetic equations are:

$$\dot{n}_0 = -g_0 n_0 + \frac{\gamma_{\text{opt}}}{3} n_e + \frac{\gamma_{T_1}}{2}\left(n_{+1} + n_{-1} - 2n_0\right) \tag{7.1}$$

$$\dot{n}_{+1} = -g_{+1} n_{+1} + \frac{\gamma_{\text{opt}}}{3} n_e - \frac{\gamma_{T_1}}{2}\left(n_{+1} - n_0\right) \tag{7.2}$$

$$\dot{n}_{-1} = -g_{-1} n_{-1} + \frac{\gamma_{\text{opt}}}{3} n_e - \frac{\gamma_{T_1}}{2}\left(n_{-1} - n_0\right) \tag{7.3}$$

$$\dot{n}_e = g_0 n_0 + g_{+1} n_{+1} + g_{-1} n_{-1} - \gamma_{\text{opt}} n_e \tag{7.4}$$

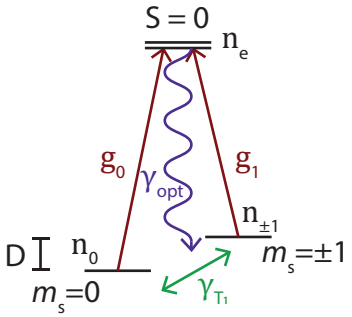

Figure 7.5: Λ structure transition rates. n_x indicates the amount of population in $x = \{0, 1, e\}$ for $m_s = 0$, $_s = \pm 1$ and ES respectively. g_i are spin dependent pumping rates of the ground state m_i sublevels assuming $g_{+1} = g_{-1} := g_1$, $\gamma_{\text{opt}} = T_{\text{opt}}^{-1}$ and $\gamma_{T_1} = T_1^{-1}$.

where g_i are spin dependent pumping rates of the ground state m_i sublevels, $\gamma_{\text{opt}} = T_{\text{opt}}^{-1}$ and $\gamma_{T_1} = T_1^{-1}$. We assume equal decay rates to the three spin sublevels and also assume $g_{+1} = g_{-1} := g_1$ (Fig.7.5).

Hole Burning

To model the hole-burning dynamics in Fig.7.4**B**, we fit Eq.7.1 to the experimental data. We use the separately measured optical lifetime and spin-lattice relaxation time, leaving g_0 and g_1 as the only free parameters. The resulting fit is shown in Fig.7.6, from which we

extract $g_0 = 10^4 \mathrm{s}^{-1}$ and $g_0/g_1 = 3.8$. As discussed below, the observed optical contrast of 14% between the start and end of the pulse provides a lower bound on the spin polarization since the excitation is not perfectly selective i.e. $g_1, g_0 > 0$.

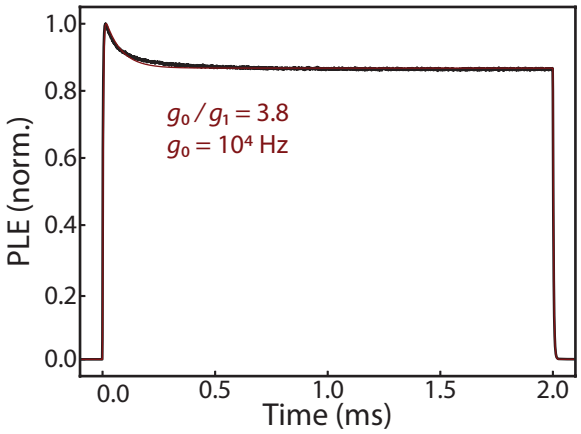

Figure 7.6: Hole-burning dynamics used to extract the spin-selective pumping rates g_0 and g_1.

Estimating optical hole linewidth

Using the extracted ratio g_0/g_1 outlined in the previous section, we can estimate the subensemble optical linewidth Γ_{sub} as follows: we assume that the subensemble broadening takes a Lorentzian form, so that the pumping rate for a transition at center frequency f_0 is

$$g_{\mathrm{sub}} = G\left[\frac{1}{1+\left(\frac{f-f_0}{\Gamma_{\mathrm{sub}}}\right)^2}\right] \tag{7.5}$$

Without loss of generality, we assume the laser frequency f matches the excitation of the $m_s = 0$ sublevel, and therefore the excitation of $m_s = \pm 1$ is detuned by $f - f_0 \simeq D$ - the zero field splitting parameter. Diving g_0 by g_1 based on the Eq.7.5 we get:

$$\frac{g_0}{g_1} = 1 + \frac{D^2}{\Gamma_{\mathrm{sub}}^2} \tag{7.6}$$

Inserting $D = 3.6$ GHz extracted from EPR and ODMR measurements that we are about

describe, and $g_0/g_1 = 3.8$ from the fit we find $\Gamma_{\text{sub}} \simeq 2$ GHz.

Spin polarization

Solving the equations Eq.7.1 in the steady state, optically induced spin polarization is given by:

$$P = \frac{n_1 - n_0}{n_1 + n_1} = \frac{g_0 - g_1}{g_0 + g_1 + 3\gamma_{T_1}} \tag{7.7}$$

Knowing all these parameters from the above discussion, we find $P = 28\%$.

Spin dependent optical contrast

PL is given by the population in the excited state, and the time it takes for it to decay, i.e. PL$= \gamma_{\text{rad}} n_e$. To examine the spin dependence, we find the steady state solution twice: first where $m_s = 0$ and $m_s = \pm 1$ are only mixed because of the spin T_1 process and second where they are fully mixed because of the microwaves (equivalent to $T_1 \to 0$ i.e. $\gamma_{T_1} \to \infty$). Then the optical contrast for ODMR is given by:

$$C = \frac{\text{PL}(\gamma_{T_1} \to \infty) - \text{PL}(\gamma_{T_1})}{\text{PL}(\gamma_{T_1})} = \frac{2(g_0 - g_1)^2 \gamma_{\text{opt}}}{3(3\gamma_{\text{opt}} + g_0 + 2g_1)(g_1\gamma_{T_1} + g_0(g_1 + \gamma_{T_1}/2)} \tag{7.8}$$

Substituting our extracted values for g_0 and g_1, along with the experimental γ_{opt} and γ_{T_1} , we find $C \simeq 19\%$, close to the observed optical contrast of 14% in Fig.7.4**B**.

7.1.5 Optically detected magnetic resonance and coherent driving

We next optically probe the ground-state spin of **1** through hole burning and recovery by microwave driving that we are familiar with from previous chapters. First, using continuous-wave (cw) optical excitation, we place a subensemble of spins in the "dark" state and monitor changes in emission (ΔPL) as we sweep the microwave frequency. When this microwave

frequency matches the spin sublevel splitting, the "dark" and "bright" sublevels are mixed, resulting in increased PL. Fig.7.7 shows this optically detected magnetic resonance (ODMR) as a function of both the microwave frequency and an external magnetic field applied along the long axis of the crystal. The zero-field cw-ODMR spectrum provides $D = 3.63$ GHz, and the Zeeman splitting yields a g-factor of 2.0, in agreement with the ESR measurements.

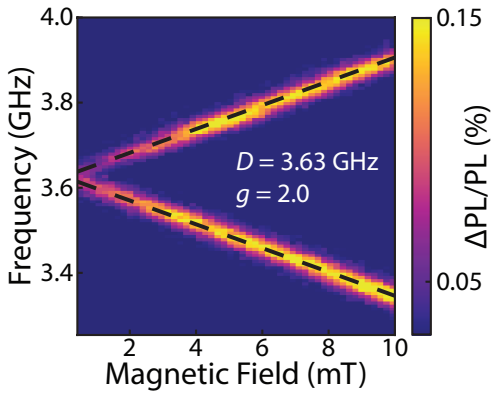

Figure 7.7: Optically detected magnetic resonance (ODMR) of the ground state of **1** as a function of magnetic field and microwave frequency using continuous-wave optical excitation. Dashed lines are a simulation with the stated g and D values.

We measure cw-ODMR linewidths (full width at half maximum) down to $\Delta f = 42$ MHz. We can use this linewidth to estimate the inhomogeneous spin coherence time $T_2^* = 1/(\pi\Delta f) = 8$ ns. We note that the observed linewidths may be due to strain inhomogeneities, possibly induced by the encapsulating epoxy upon cooling the sample, as well as from hyperfine coupling to nuclear spins. Future synthetic and materials control provides opportunities to address both these mechanisms to enhance T_2^*.

To demonstrate coherent control over the ground-state spin, we drive Rabi oscillations as a function of microwave driving power (Fig.7.8 using the following control sequence: an optical initialization pulse, a wait time, a variable length microwave pulse, and an optical readout pulse. We show the expected square-root dependence of the Rabi frequency on the applied microwave power derived in Sec.2.2.3.

Next, using a π-pulse calibrated from Fig.7.8**A**, we perform pulsed ODMR at a fixed

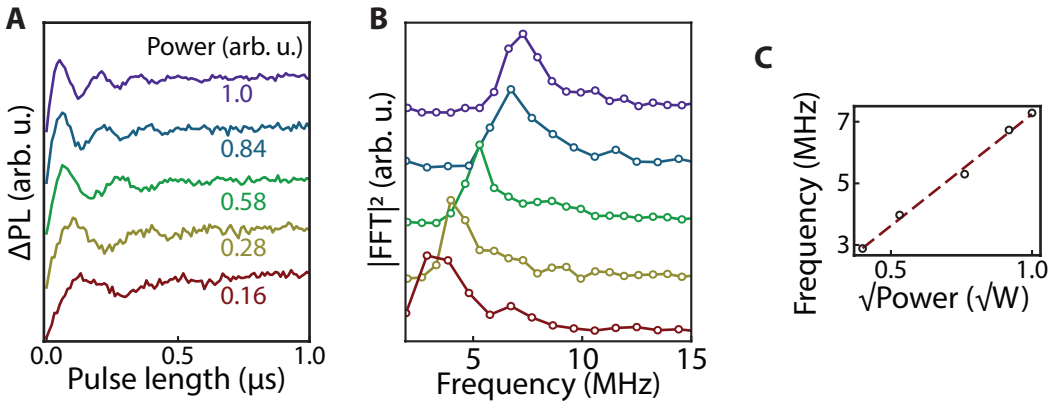

Figure 7.8: Optically detected coherent spin manipulation of the ground state of **1**. (**A**) Rabi oscillations between the $m_s = -1$ and $m_s = 0$ spin sublevels at $B_0 = 10$ mT as a function of driving power and (**B**) their Fourier transform. (**C**) Microwave-power dependence of the Rabi oscillation frequency.

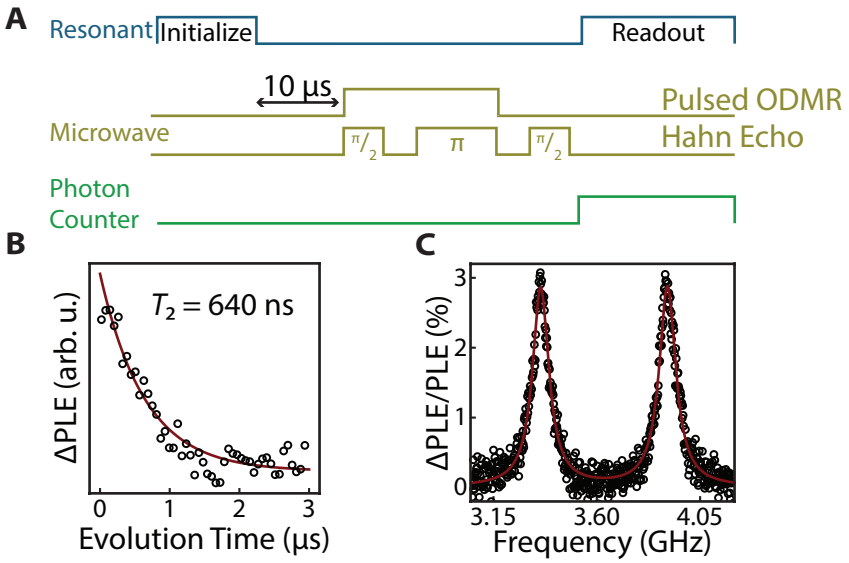

Figure 7.9: Optically detected coherent spin characterization of the ground state of **1**. (**A**) Pulsed ODMR and Hahn echo pulse sequences. (**B**) Pulsed ODMR spectrum ($B_0 = 10$ mT) and double Lorentzian fit (black) confirms the source of the contrast to be the ground state spins in Fig.7.8. (**C**) Optically detected ground-state spin coherence (B0 = 2 mT) with exponential fit (black).

magnetic field, $B_0 = 10mT$, while varying the microwave frequency confirming that the optical contrast is indeed coming from the spin transitions (Fig.7.9**B**). Finally, by replacing the single microwave pulse with a Hahn echo sequence, we measure the spin coherence time

T_2 = 640(60) ns at B_0 = 2 mT (Fig.7.9**C**). In these pulsed ODMR experiments, the wait time (10 μs $\sim 3T_{opt}$) between initialization and microwave manipulation ensures population is in the ground state prior to coherent control. This wait time, along with the above agreement between the ODMR and ESR spin parameters, shows that we coherently control the ground-state spin. Furthermore, the measured T_2, likely limited by the surrounding hydrogen nuclear spins, is comparable to other transition-metal–based molecular qubits in nuclear spin-rich environments [106, 107], and we expect that ligand deuteration should greatly enhance T_2 [107, 108].

7.1.6 Other compounds

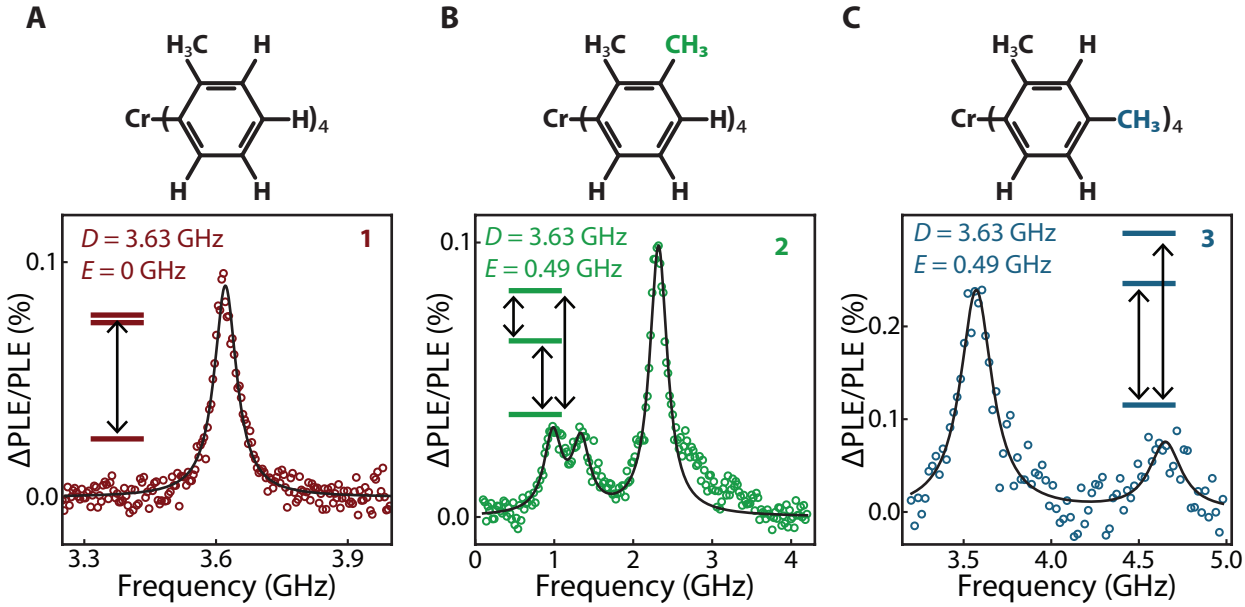

Figure 7.10: Optical spin addressability with synthetic tunability. (**A**-**C**) cw-ODMR spectra and simulations (black) for **1**-**3**, with microwave transitions and ligand modifications depicted.

Having demonstrated an optical-spin interface and coherent spin control for **1**, we highlight how this functionality is not specific to a single compound. In Fig.7.10, we show optical initialization, microwave spin manipulation, and optical readout of **2** and **3** through cw- ODMR. As captured by the simulations, the variable peak intensities arise from ESR se-

lection rules (23). Notably, the additional ligand methyl groups in **2** and **3** lead to substantial E by lowering the crystal symmetry.

7.1.7 Quantum efficiency

Quantum efficiency of an emitter is the ratio of radiative decay from the excited state over all other decay mechanisms and is an important figure of merit for optically accessible qubits. We can estimate it by using a similar strategy to Sec.5.7:

$$\eta_{\text{rad}} = \frac{\eta_{\text{det}} n_e \gamma_{\text{opt}}}{r_{\text{sub}}} \tag{7.9}$$

where r_{sub} is the steady state subensemble photon count, η_{det} is the photon detection efficiency, n_e is the number of molecules in the excited state and γ_{opt} is excited lifetime rate.

We estimate the current collection efficiency is $\eta_{\text{det}} \simeq 1\%$ from the product of the following estimates: objective collection efficiency (20%), transmission through optical components (40%), fiber coupling (25%), detector efficiency (80%), fraction of photons within the sideband (70%). Steady state subensemble photon count from the experiments is $r_{\text{sub}} \simeq 1$ Mcts/s. Finally the number of molecules in the excited state is given by:

$$n_e = n_{\text{probed}} f_e \tag{7.10}$$

where n_{probed} is the number of probed molecules within the spot size and f_e is the fraction of those within the excited state. We can estimate the number of probed molecules by knowing the total number of them within the laser spot size, and the subensemble size that is excited within:

$$n_{\text{probed}} = c_{\text{Cr}} \frac{V_{\text{confocal}}}{V_{\text{cell}}/Z} \frac{\Gamma_{\text{sub}}}{\Gamma_{\text{inhom}}} \tag{7.11}$$

where $c_{\text{Cr}} = 0.75\%$ is the concentration of Cr:Sn dilution ratio within the crystal, $V_{\text{confocal}} = 1.4\ \mu\text{m}^3$ is the laser spot volume, $V_{\text{cell}} = 1.12\ \text{nm}^3$ is the size of the crystal

unit cell, $Z = 2$ is the number of molecules per unit cell, and we had already found $\Gamma_{\text{sub}} = 2$ GHz and $\Gamma_{\text{inhom}} = 150$ GHz. Finally based on the steady state rate equations in Eq.7.1 with already known parameters, we estimate $f_e \simeq 1\%$. Putting all these numbers together, we approximate a quantum efficiency of $\sim 10\%$, maybe not so surprisingly similar to the estimate for SiC:Cr^{4+}calculated in Sec.5.7.

7.2 V^{3+} based molecules

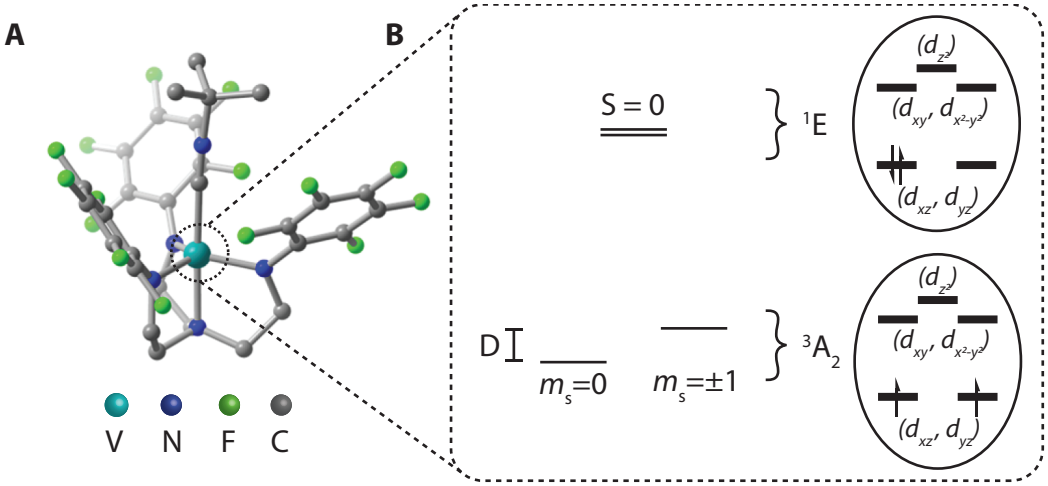

Figure 7.11: Physical and electronic structure of trigonal bipyramidal compound. (**A**) Molecular structure of the compound is determined by single-crystal X-ray diffraction. H atoms are omitted for clarity. Reprinted with permission from [2]. Copyright 2020 American Chemical Society. (**B**) Electronic level structure of the compound and qualitative d-orbital splitting diagram for the compound in ideal C_{3v} symmetry.

The electronic structure design principles for a transition metal based optically accessible spin qubit can be realized in many other ways. One such example is the trigonal bipyramidal compound, $(C_6F_5)_3$trenVCN^{t}Bu shown below. The ligand environment shown in Fig.7.11**A** creates the necessary d^2 configuration under strong tetrahedral ligand field where V^{3+} provides the two valance electrons. The familiar electronic structure that allows for optical access to ground state spins still form (Fig.7.11**B**), however, d_e ground state orbitals are comprised of d_{xz}, d_{yz} while the higher energy d_t orbital splits into $d_e = \{d_{xy}, d_{x^2-y^2}\}$ and

$d_a = d_{z^2}$.[4]

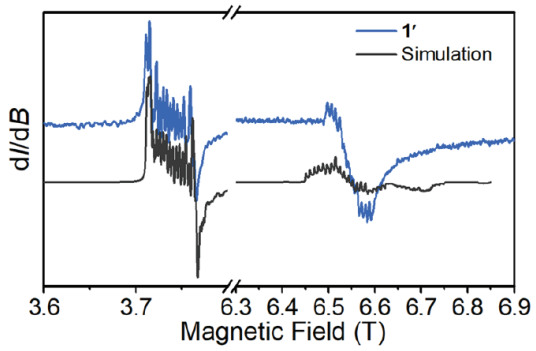

Figure 7.12: Electron spin resonance (ESR) of trigonal bipyramidal compound. 240 GHz cw-ESR spectrum of the dilute crystal powder at 5 K (blue). The asterisk denotes a small V^{4+} impurity. Simulations are in black. Reprinted with permission from [2]. Copyright 2020 American Chemical Society.

High frequency EPR experiments (240 GHz) at 5 K of diluted crystals in diamagnetic analogs confirm the expected S = 1 ground state of the display a $D = 108$ GHz and an $E = 600$ MHz with $g \sim 1.96$. The measurements also show a high hyperfine coupling to the ^{51}V $A = 250(5)$ MHz.

Finally the zero phonon line centered at 1237 nm split under high magnetic fields where individual ground state spin sublevels can be resolved because of the narrow optical emission and large D value, confirming the singlet excited state structure of this molecule, and the engineered spin-photon interface that is closer to the telecom band and could be used for optical control of the ground state spins.

7.3 Summary

In this chapter we demonstrated that transition metal based optically accessible spin qubits need not be within a solid state host. The same physics explored in Chapter 4 and techniques developed in Chapter 5 can be immediately applied to chemically synthesized qubit analogs

4. One can immedaitely see how these orbital energetics are shaped based on the qualitative description explained in Sec.3.1.1

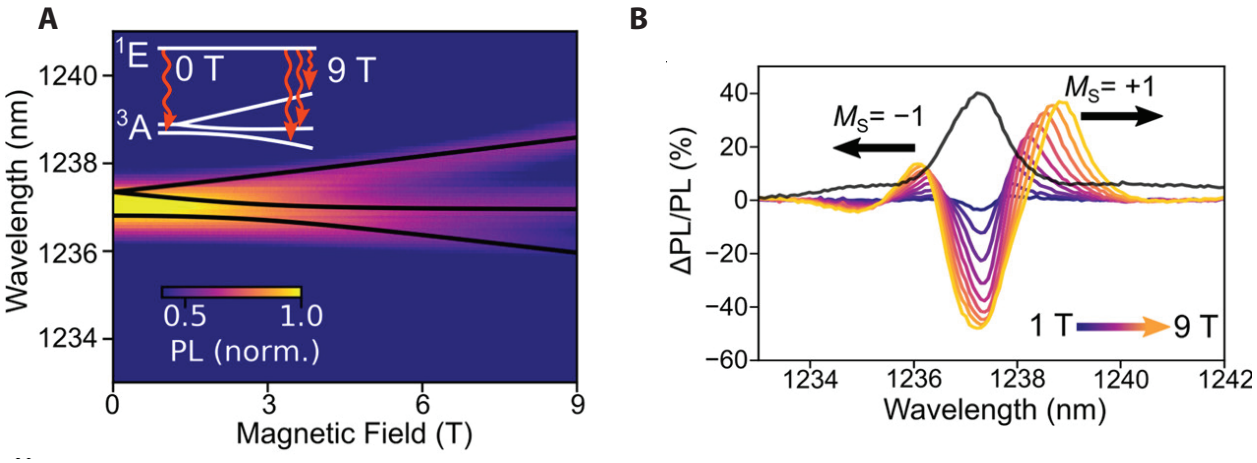

Figure 7.13: Resolving the ground state spin structure within the photoluminescence of the vanadium compound.(**A**) Variable-field PL spectra with simulated Zeeman splitting (black) and (**B**) differential PL collected on a single dilute crystal of the compound with the 0 T spectrum in black. The schematic in white illustrates variable field splitting of the ZPL, which originates from splitting of the m_s sublevels. Reprinted with permission from [2]. Copyright 2020 American Chemical Society.

where we demonstrate optical initialization, microwave coherent control, and optical readout of the ground-state spin in an ensemble of molecular qubits. Chemical synthesis provides a lot of benefits. Relative to solid state based spin qubits, molecular qubit preparation is cheap and scalable. As shown in this chapter, slight modifications of the molecule provide variable magnetic and electronic structures. Similar spin and electronic structures can also be engineered with different transition metal atoms and ligands spanning an optical spectrum from $\sim 1000 - 1240$ nm and a microwave spectrum from $\sim 0.5 - 110$ GHz, including the E values. It is likely possible increase initialization and readout fidelities by enhancing the spin selectivity of the optical excitation, for example by targeting compounds with large zero-field splittings such as the vanadium complex, or narrower subensemble optical linewidths. By lowering the crystal symmetry through chemical design, substantial E terms can be introduced as shown for compound **2** and **3**, which can enhance spin coherence in these compounds through noise-insensitive (i.e., clock-like) transitions[109]. Furthermore, multimetallic systems could be synthesized with interacting metal sites that exhibit distinct optical-spin interfaces, enabling both individual qubit addressability and multiqubit oper-

ations. Targeted nuclear spin placement around these metal centers could further provide long-lived quantum memories [110]. Alternatively, ligand functionalization and extension of these results to biocompatible metal ions [111] may enable sensing of targeted analytes. Furthermore, self-assembly could facilitate integration with photonic or electronic devices [112]. Finally, the highly tunable nature of molecules offers promise for rationally designed properties tailored to a specific purpose, e.g., telecom emission for long-distance quantum networks, or strong spin-phonon interactions for hybrid quantum systems. These results highlight pathways to design and create quantum technologies from the bottom-up.

Chapter 8

Outlook

In Chapter 1, we motivated the need for quantum technologies, and benefits and shortcomings of various platforms. Chapter 2, built the mathematical foundations for spin-qubit control and the electronic orbitals that contain the spins. Chapter 3 discussed the physics of orbitals to construct electronic structures that support a ground state spin qubit as well as an optical-spin interface to initialize and measure the qubit. The remaining chapters experimentally demonstrated these discussed principles using various transition metals and hosts. In this chapter we are going to do a quick recap of all of the results, their importance and how we can resolve some of the outstanding issues.

8.1 Comparison of the discussed platforms

Below is a master table (Table 8.1) summarizing some important parameters from the experimental demonstrations.

The summarized results are categorized under various qualities we need for optically-addressable spin qubits. So far, the experiments discussed in this thesis demonstrate a few important milestones for transition metal based qubits. Namely, we have measured a single transition metal ion based emitter, showed long coherence times with high initialization and readout fidelities and created such qubits both in commercially available mature semicon-

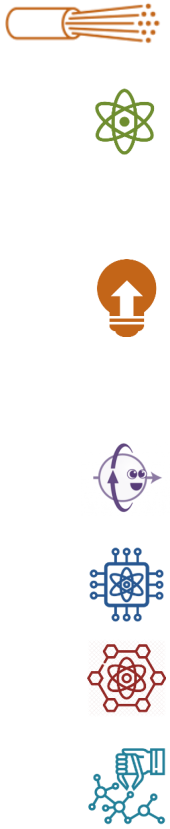

		$SiC:V^{4+}$	$SiC:Cr^{4+}$	$GaN:Cr^{4+}$	Cr^{4+} Molecules	V^{3+} Molecules
Fiber compatible	ZPL Emission	Telecom O-Band (1278-1387 nm)	Near Telecom (1040-1070 nm)	Near Telecom (1070 nm)	Near Telecom (1009 - 1025 nm)	Near O-band (1235 nm)
Single Emitter	Quantum Efficiency	>2%	>10%	-	>10%	-
	Excited state lifetime	~100 ns	155 µs	110 µs	3-7 µs	11 µs
	Single detected	Yes	Not yet	Not yet	Not yet	Not yet
Spin photon interface	DW	25-50%	>75%	>73%	30%	-
	Inhomogeneous Γ	2 GHz	5 GHz	8 GHz	150 GHz	-
	Homogeneous Γ	750 MHz (14 states)	30 MHz	800 MHz	2 GHz*	-
	Polarization + readout fidelity	-	~80%	>4%	14% (3%)	-
Coherence times	T_1	0.17-1.2 µs (3.3 K)	1.6 s (15 K)	>30 ms (19 K)	220 µs (4 K)	-
	T_2	-	> 80 µs (ensemble)	> 1 ns	640 ns (4 K)	427 ns (5 K, 8.5 T)
	Nuclear spin registers	Yes	Likely (^{53}Cr is I =3/2)	Likely	Likely	Likely
Device Integration	Stable near surface	Yes	likely	-	-	-
	Device integrable	likely	likely	-	-	-
Large architectures	Chemically Tunable	-	-	-	Yes	Yes
	Scalable	Likely	Likely	-	Yes ++	Yes ++
Size		Wafer	Wafer	Wafer	1 nm	1 nm

Table 8.1: Summary of results for the transition metal ion based optically accessible spin qubits. Green to red color scale indicate the impressiveness of the measured parameter.

ducting substrates and through chemical synthesis. Furthermore, the synthesized platform shows both an immense flexibility for creating qubits with different optical and magnetic interfaces while preserving the physics that allow their control and scalability as identical qubits can be mass produced. In order to build useful technologies out of transition metal ions there are a few properties that we would need. Below is a description of them, how current platforms hold up and some potential solutions.

8.2 Good to haves

Besides the **must have**s for an optically accessible spin qubit discussed in Sec.3.3.2, there are also some very important properties that are good to have for a useful system [113]. Most of these properties can be either introduced by engineering electronic structure through selecting a host crystal and/or ligand design, or through engineering devices and instruments (e.g. photonic cavities and dilution refrigerators), although some properties are much more difficult to solve than others.

- **Long** T_1: T_1 time is the ultimate limit to the memory time of a qubit and represents the time it takes for the system to thermalize. We already discussed many mechanisms responsible for spin-lattice relaxation and therefore strategically selected the d^2 configuration as a spin qubit candidate system, exemplified by Cr in SiC where T_1 time exceeding a second at 15 K. Sometimes closely spaced ground state can be unavoidable, especially if some other properties of the system are desirable such as bright telecom emission (Chapter 5). Some engineering solutions can help with certain T_1 decay mechanisms. The most obvious strategy is reducing the temperature of the system to freeze out the phonons which simply requires more expensive cryogenic instruments. Depending on the process for the T_1 decay, one can also use phononic crystals to reduce the interaction between the phonons and the spin [114]. Finally, if degenerate ground states are unavoidable, the further the energy separation between the ground states,

the higher the T_1 time will be for a given temperature [115]. One can potentially try modifying the ligand environment of a transition metal ion in the d^1 configuration by reducing the symmetry, for example through strain [116], to induce a splitting in the d_e orbital set to increase the T_1 time.

- **Long** T_2: T_2 time is a purely quantum mechanical scale with no classical analog and is generally referred as a spin dephasing time for the following reason: T_2 represents the error accumulation time for the phase between the two logical states: $|0\rangle + e^{i\phi}|1\rangle \rightarrow |0\rangle + e^{i(\phi+\varepsilon)}|1\rangle$. For example, we have seen how the phase can be extracted using interference in Sec.2.2.4, and any error in the phase can cause sensing and computation errors. The longer the T_2, the higher sensitivity a sensor can have, more qubit operations can be squeezed in within qubit lifetime for more complex calculations, and longer the quantum memory is, allowing for a larger light-cone, therefore a quantum network size for photon based entanglement scheme. T_2 is measured by using a refocusing π pulse that eliminates slow evolving and static fluctuations and therefore is limited by fast noise processes, most commonly caused by the spin bath. It is possible to increase the dephasing time with dynamical decoupling, where equally spaced π pulses deliberately flip flop the qubit phase, so the accumulated error cancels out for faster noise, increasing the T_2 time. We have already seen 2-orders of magnitude increase from T_2^* to T_2 for 4H-SiC:Cr^{4+} in Sec.5.4 by simply adding a single rephasing pulse. The two biggest magnetic noise contributors are either other paramagnetic species that belong to the same ensemble or different species, or nuclear spin bath of the environment. Technically, the upper limit for a T_2 is T_1, however, the errors of the π-pulses in a dynamical decoupling sequence can add up, limiting the noise cancelation capability of dynamical decoupling.

  As T_2 decay mechanism for spin qubits is bath induced, spin dephasing mitigation strategies to increase the T_2 time is universal across spin qubits, including the ones made out of transition metal ions. It is important to select a good host matrix with

minimal nuclear and unwanted paramagnetic spins to increase the T_2 time. We have already seen the effects of the host on spin coherence between 4H-SiC:Cr and GaN:Cr. Although both systems exhibit the same electronic structure, therefore optically accessible spin-1 ground states, the spin coherence in SiC is two two orders of magnitude larger than in GaN where nuclear spins of silicon and carbon isotopes are sparse while there are no stable spin-0 isotopes for nitrogen or gallium. Specifically, group-II,IV, VI and VIII[1] elements are mostly nuclear spin free making hosts made out of them ideal (Si, SiC, diamond etc.) for spin qubits [117]. Especially, they can be isotopically purified to further reduce the ambient spin noise to increase the T_2 time [118–121]. Finally, the spin system itself can be engineered to be insensitive to ambient magnetic noise by finding zero first order Zeeman (ZEFOZ) transitions either induced by hyperfine interaction with a strongly coupled nuclear spin at a specific magnetic field [118, 122], or by having an E term [39, 123], generally induced by reduced symmetry. The former strategy can be employed by selecting the transition metal ion with a nuclear spin, such as ^{51}V that is nuclear spin-7/2 and the latter strategy can be employed by reducing ligand symmetry [1]. Finally, although an abundant nuclear spin bath can limit coherence times, a sparse amount can be beneficial to be used as extra registers [120]. Furthermore, for molecular spin qubits, chemical design can allow for placing nuclear spins deliberately within close proximity to the spin qubits to increase the computational space without handicapping the electronic spin coherence [110].

- **Cycling Optical Transition**: We have already discussed the key component of an optical-spin interface in Sec.3.3.2. The Λ-like electronic structure coupled with narrow emission due to d^2 orbital configuration, enabled us to have spin addressability by selective pumping. However, when addressing a single spin for precise quantum initialization and readout measurements, we need to keep a few things in mind. The system can have some readout errors that limit readout fidelity and confidence of the correct

1. These elements are not very reactive and therefore are rarely found within materials.

spin measurement. Firstly, the probability of emitting a photon only in *bright* state is not 100% accurate. We have already run into this error in Sec.5.5 where the *dark* state wasn't completely dark which limited the readout fidelity. Secondly, some of the photons are lost that are emitted from the system due to collection inefficiencies[124]. How can we be confident that if we don't detect a photon, it is truly a *dark* state and not a lost photon from a *bright* state, or if we detect a photon, it is not a detector dark count? If the probability of decay from the excited state to the *bright* spin ground state is high, one can keep probing the system and with each extra detection event, one can be more confident that they are indeed measuring the spin state correctly. However, with each probing event, the spin state can flip, erasing the information of the initial qubit measurement state. The probability of having the *bright* state decay back to the *bright* state is called a cycling transition and is the key to measuring spins within a single shot [125] - which is a key requirement for many of the quantum technologies we discussed in Chapter 1 [126, 127].

Along with other spin and optical properties, the branching ratio of non rare earth defects within a solid state medium is mostly predetermined by the electronic structure that arises from the interactions with the host lattice. For rare earth defects $f - f$ transitions, the transition rates are governed by f-orbital dynamics, and the overlap integral between the ground state and the excited sublevels, where the f-orbitals are shielded from the outside influence. For either platform, one cannot deviate much from the branching ratios given by the system by altering orbitals. One, however, can engineer the probability of photon emission and absorption using a cavity, and modify the branching ratio and oscillator strengths. This recently allowed for single shot spin detection of rare earth ions [48]. A similar strategy may be needed for transition metal ions in the solid state. For example, the branching ratio for the d^2 configuration seems to be equal decay probability to any of the ground states which is exactly the opposite of a cycling transition! The same level structure forms a nice Λ-like system that allows

for high fidelity initialization and readout of most of the systems discussed in this thesis. This being said, under high magnetic fields, the excited state degenerate orbitals split and display non-equal branching ratios likely arising from spin-orbit effects as can be seen in Fig.4.1 [71]. Furthermore, the branching ratio for Cr_A (quasi-cubic site) is different from Cr_C (quasi-hexagonal site), whose only difference is the local symmetry. Since molecule based transition metal qubits have unlimited tunability capacity of their immediate ligand environment, aided by computational methods, it may be possible to engineer a cycling transitions through ligand design.

- **Fast optical emission**: The brighter the emitter, the more photons per second can be collected out of the system, shortening the optical initialization and readout times. If the defect emission is dim, then it becomes very challenging to detect a single emitter, a key pre-requisite for many of the quantum technologies. V^{4+} in SiC has the d^1 configuration and therefore has a short excited state lifetime of order 100 nanoseconds[2], which allowed for imaging a single emitter discuss in Sec.6.4. In contrast, Cr^{4+} in SiC has the d^2 configuration, and relies on the spin flip transition, and because they are forbidden, the excited state is long lived of order 100 microseconds, making detection of a single emitter without optical enhancement difficult. However, the slow decay rate can be increased through Purcell enhancement. Such cavities are already available for SiC, an example host used in this thesis [128]. We have also seen that molecular platforms offer symmetry flexibility. For example by reducing the symmetry of the local environment from $T_d \rightarrow S_4$, the spin flip transition can be made dipole allowed discussed in Sec.7.1.3. Although this cannot overcome the spin-forbidden nature of the transition, the dipole allowed nature likely played a role in increased optical lifetime of the molecular Cr^{4+} ion.

- **High quantum efficiency**: Every photon that comes out of the system is impor-

2. This rate may be due to non-radiative decay from the excited state as well.

tant, but sometimes population from the excited state relaxes to the ground state non-radiatively, generally releasing the energy in the form of phonons. If this non-radiative rate is high, then one will need to probe the system many more times to extract signal out of it to determine the ground state spin state, and furthermore, the cyclical transition can be broken under this non-radiative decay, increasing readout errors. Therefore it is important for an optical defect to relax radiatively more than non-radiatively, where the ratio of the radiative decay rate to the total decay rate is called quantum efficiency. The non radiative decay is complex to understand, and requires extensive theoretical considerations. It is also difficult to experimentally verify the quantum efficiency [129]. Ideally one needs to collect all of the photons coming from the defect and compare it the expected number of photons given the excited state lifetime. Since there are many inefficiencies between optical components, photon-emission profile, and detectors, it is difficult to obtain an accurate measurement. A conservative comparing of expected number of photons to measured ones allowed us to place quantum efficiency of Cr^{4+} based qubits over 10% (Sec.5.7, Sec.7.1.7) and SiC:V^{4+} >2% (Sec.6.3.2). Vibronic coupling of the ${}^1E \leftrightarrow {}^3A_2$ transition within strong tetrahedral d^2 configuration is especially low because the optical transition is contained within the non-bonding orbitals of d_e, likely contributing to the high observed quantum efficiencies. The quantum efficiency can also be enhanced by increasing the radiative decay probability through optical cavities [128].

- **High Debye-Waller factor**: As we have seen in the PL data, besides the direct transition from the excited state to the ground state (ZPL), sometimes a phonon and a photon are emitted at the same time, causing a red shifted sideband emission. The ratio of the ZPL emission to total emission is called the Debye-Waller factor and we have already discussed its importance in Sec.4.2.1. To quickly remind the reader, since the defect emission is entangled with the spin state, $|\uparrow, \text{bright}\rangle + |\downarrow, \text{dark}\rangle$, it is possible to entangle two remote spins by interfering their emission and erasing the information

where the photon came from. The only way one can erase the information where the photons came from is if the two photons are identical, and therefore from the ZPL [75, 130, 131]. The remote spin entanglement rate is proportional to the square of Debye-Waller factor as both spin qubits need to emit from the ZPL at the same time for successful entanglement. Some of the vacancy based defect systems such as the NV center in diamond and divacancy in SiC have a Debye-Waller factor of $< 10\%$ [79, 132]. In contrast d^1 configuration (V^{4+}, Mo^{5+}) in SiC has a Debye-Waller factor $25 - 50\%$ (Sec.6.3.2) and the d^2 configuration in SiC and GaN has a Debye-Waller factor of $> 73\%$ (Sec.4.2.1) arising from the optical transition weakly coupling with the phonons as the transition is contained within the d_e set. All of these numbers can be further improved, again, with photonic cavities where the probability of optical emission from a wavelength band, such as the ZPL, can be increased [128, 133].

- **Life time limited linewidths**: An ideal quantum emitter has optical linewidths that are excited state lifetime transform limited. However, most of the semiconducting material systems are filled with stray electrons and holes which create their own local electric field that can Stark shift the optical emission much faster than detectable bandwidth resulting in widened optical linewidths [38] which, for example, can limit photon based entanglement rates [134]. Recent work demonstrated that one can remove these charges with electric fields in SiC that allows for reaching lifetime limited linewidths of divacancy defect in SiC. Currently V^{4+} and Cr^{4+} within SiC are 3-4 magnitudes away from the the lifetime limited emission, and a similar electronic device strategy can be employed to narrow the optical linewidths. For molecular work, possible origins of hole linewidths above the transform limit may include optical dephasing from electron-phonon coupling and spectral diffusion from environmental electronic fluctuations in the crystal due to for example, structural reconfigurations or time-dependent variations in local photoexcitation density [135]. Depending on the reason, different strategies need to be employed to reduce the hole linewidths of molecular qubits.

- **Telecom emission**: As discussed in Chapter 1, telecom emission is incredibly important to integrate a future quantum technology into the existing fiber optic network to leverage the non-local properties of quantum technologies. For most of the defect centers, the ZPL emission energy is predetermined and has very limited tuning capabilities. Erbium in 3+ is extremely popular as a rare-earth platform precisely because the lowest energy f-f transition lies in the middle of the telecom E-band, the optimal transmission regime. V^{4+} also emits in the telecom but in O-band, is hosted in SiC a mature semiconducting host, has a fast lifetime that allows detection of a single emitter without any photonic enhancements and has an embedded electronic and a nuclear spin that can be used as a qubit. V^{3+} in SiC has a d^2 configuration and emits around the 2 μm regime [136]. Even though this is outside of the existing telecom range, 2 μm is the optimal transmission point for ZBLAN fiberoptic cables. A 2 μm photon within a theoretically perfect ZBLAN can travel for 300 km before the probability of losing it is 50%, an order of magnitude longer distance than an O-band photon in a standard fiberoptic cable [137]. V^{3+} would have the d^2 configuration, with potentially long spin T_1 times, and Λ like optical structure. Therefore the techniques explored in this thesis for spin control, initialization and readout could be readily applied to that platform. The ZPL emission wavelength of transition metal based qubits can also be tuned through ligand design, so far within a range of 200 nm by either changing the immediate ligand environment or the transition metal ion itself. This flexibility demonstrates the great potential for wavelength tunability of molecular transition metal qubits and it may be possible to design them with O or E band spin-photon interface.

- **Reliable creation**: For a feasible technology, devices must be created in a reliable fashion. This is the Achilles heel of defect based quantum platforms. Some defect platforms are purely composed of intrinsic defects (e.g. vacancy, anti-site, polytype inclusion etc.) which can be created by damaging the host (e.g. irradiation [38], implantation[84, 138]) followed by annealing. Localizing such defects and creating

them with good efficiencies is still an open research question [139]. If the defect center needs an extrinsic atom (e.g. Nitrogen in NV centers, transition metal), then they are easier to localize with techniques such as nano-implantation [86, 87] and delta doping [140]. In this spirit, we studied implantation characteristics of Cr ions in SiC discussed in Sec.5.1 and find that they have creation efficiencies $> 10\%$ and use this knowledge to prepare both Cr and V samples in SiC that we study in Chapter 5 and Chapter 6. During implantation, however, each local site is slightly different due to local strain, charge traps, other defects and even natural isotopic variation of atoms that are part of the lattice. Having atomistic control over molecular systems is much easier compared to defects in host crystals, as each chemically synthesized molecule is the same (up to statistical isotope distribution), and every electron is accounted for. Molecular qubits also are extremely portable since they are a self contained unit within a $\sim$1 nm size that can be moved around and integrated into electronic devices similarly to other organic molecular compounds that are widely used in the electronics industry (e.g. organic LED) [141]. The cheap and reliable creation of molecular qubits sets them up to be a scalable solution to optically accessible spin qubits.

- **Ease of device integration**: Most of the solutions we discussed above rely on opto-electronic devices. When defects are near surfaces [142, 143], or within highly strained environments due to fabrication, the electronic structure can change, and the surface charge fluctuations can broaden the optical linewidths [128]. To build reliably produced multi qubit structures one needs to be able to place defects with lattice site precision within a device. Since transition metal ions are substitutional defects, and can be created through implantation it may be possible to well localize them in a host crystal using a nono-implanter [86, 87] as discussed earlier. V^{4+} does not blink, spectrally diffuse or shift within the data point collection time, although only being a 100 nm from a surface as discussed in Sec.6.4. Similarly, the d^2 electronic structures optical paths are insensitive to strain and therefore may survive within the harsh, highly fabri-

cated hosts. Both of these qubits could potentially be integrated within optoelectronic devices. That being said, although a nano-implantation can give nanometer resolution of qubit placement, this is still a stochastic method and is still not sufficient for exact lattice placement which can be a challenge for creating large ordered, identical arrays within devices. Under this consideration, molecular qubits can be a better candidate for device integration. It may be possible to functionalize molecular qubits to attach to electrodes for Stark control that are fabricated [144] in a precise relationship to an optical cavity for ideal coupling [112]. Furthermore, molecules can be synthesized in 1-,2- or 3- dimensional structures [145, 146] to create exactly ordered arrays, where each molecular spin is individually addressable through their own unique spin-photon interface and individually controllable through zero field splitting parameters.

8.3 Concluding remarks

To recap, in this thesis we explored transition metal ion *d*-orbitals as electron hosts to build optically addressable spin qubits. Careful thinking about the electronic structure that supports a ground state spin qubit and an optical path that initializes and measures it led us to explore specific symmetries and charge states. Unlike other solid state platforms, the electronic structure of transition metal ions and therefore the qubit properties highly depend on the immediate local environment, making them both portable between similar hosts, such as GaN and SiC and tunable through ligand design. This flexibility can enable introducing spin qubits within novel semiconductors as well as engineering electronic structures with various spin selection rules, for example, a cycling transition. Transition metal based qubits can impact all three pillars of quantum technologies. Individually addressable, chemically synthesized arrays of molecular qubits can be dipolarly coupled to explore large information processing devices. Telecom emission of vanadium can be used for quantum communication, while potentially high spin-orbit effects of transition metals can be integrated within opto-

electro-mechanical devices for transducing quantum information across various quantum degrees of freedom to wire together different platforms to realize a quantum modem. The nanometer size of molecular spin qubits, combined with mass production capabilities and the potential of chemical functionalization sets them up as promising quantum sensors that can be set and measured remotely using light. All of these potentials highlight the strengths of transition metal ions as optically accessible spin qubits for use in quantum computation, communication and sensing. The understandings and results demonstrated in this thesis set transition metal ions as an emerging, highly flexible and very promising quantum bit platform.

Appendix A

Mathematics

A.1 Definitions

A.1.1 Pauli Matrices

The three Pauli matrices are defined as:

$$\sigma_x = \begin{pmatrix} 0 & 1 \\ 1 & 0 \end{pmatrix} \qquad \sigma_y = \begin{pmatrix} 0 & -i \\ i & 0 \end{pmatrix} \qquad \sigma_z = \begin{pmatrix} 1 & 0 \\ 0 & -1 \end{pmatrix} \tag{A.1}$$

Along with the $\mathcal{I}$ matrix, they create a basis for the 2×2 complex matrix space.

A.1.2 Spin Matrices

S is the spin number of a system is a positive integer multiples of $1/2$ (e.g. $1/2, 1, 3/2, ...$). The total dimensions of a spin-S system is $2S + 1$ and each basis state can be represented with the quantization m. Therefore a good label for ket object in the spin S vector space is $|S, m\rangle$ where $m = -S, ..., S$. Sometimes simply $|m\rangle$ is used for short hand notation too. The general spin matrices are constructed the following way:

$$\begin{aligned}
\langle m'|S_x|m\rangle &= (\delta_{m',m+1} + \delta_{m'+1,m})\frac{1}{2}\sqrt{S(S+1) - m'm} \\
\langle m'|S_y|m\rangle &= (\delta_{m',m+1} - \delta_{m'+1,m})\frac{1}{2i}\sqrt{S(S+1) - m'm} \\
\langle m'|S_z|m\rangle &= \delta_{m',m}m
\end{aligned} \tag{A.2}$$

For a spin-1/2 system we see that $S_i = \sigma_i/2$ where $i \in \{x, y, z\}$ and σ is a Pauli matrix defined Eq. A.1.

A.1.3 Spherical transformations

Let (x, y, z) be a point in Cartesian coordinates and (r, θ, ϕ) be the same point in spherical coordinates. One transforms from one coordinate system to another the following way:

$$x = r\cos\phi\sin\theta \tag{A.3}$$

$$y = r\sin\phi\sin\theta \tag{A.4}$$

$$z = r\cos\theta \tag{A.5}$$

$$r = \sqrt{x^2 + y^2 + z^2} \tag{A.6}$$

$$\theta = \arccos\frac{\sqrt{x^2 + y^2}}{z} \tag{A.7}$$

$$\phi = \arctan\frac{y}{x} \tag{A.8}$$

The surface and volume integral elements are:

$$\mathrm{d}\Omega = \sin\theta\mathrm{d}\theta\mathrm{d}\phi \tag{A.9}$$

$$\mathrm{d}\tau = r^2\mathrm{d}\Omega\mathrm{d}r = r^2\sin\theta\mathrm{d}\theta\mathrm{d}\phi\mathrm{d}r \tag{A.10}$$

Differential elements are:

$$\nabla = \frac{\partial}{\partial r}\hat{r} + \frac{1}{r}\frac{\partial}{\partial\theta}\hat{\theta} + \frac{1}{r\sin\theta}\frac{\partial}{\partial\phi}\hat{\phi} \tag{A.11}$$

$$\nabla^2 = \frac{1}{r^2}\frac{\partial}{\partial r}\left(r^2\frac{\partial}{\partial r}\right) + \frac{1}{r^2\sin\theta}\frac{\partial}{\partial\theta}\left(\sin\theta\frac{\partial}{\partial\theta}\right) + \frac{1}{r^2\sin^2\theta}\frac{\partial}{\partial\phi} \tag{A.12}$$

A.2 Proofs

Exponential Pauli Matrices

Claim: $e^{ia(\hat{n}\cdot\vec{\sigma})} = \mathcal{I}\cos a + i(\hat{n}\cdot\vec{\sigma})\sin a$ where $\hat{n}$ is a 3-dimensional vector with a unit length, a is a scalar, and $\vec{\sigma} = (\sigma_x, \sigma_y, \sigma_z)^T$, a column vector whose elements are Pauli matrices defined at Eq. A.1.

Proof: First, we observe that $\sigma_i^2 = \mathcal{I}$, where $i \in \{x, y, z\}$. Then $(\hat{n}\cdot\vec{\sigma})^2 = (\sum_i n_i\sigma_i)^2 = \sum_i (n_i\sigma_i)^2 = \sum_i n_i^2\mathcal{I} = \mathcal{I}$. Therefore $(\hat{n}\cdot\vec{\sigma})^{2k} = \mathcal{I}$ and $(\hat{n}\cdot\vec{\sigma})^{2k+1} = (\hat{n}\cdot\vec{\sigma})$ where $k \in \mathbb{N}$. Finally we can Taylor expand the exponential where $p = 2k$ and $q = 2k+1$:

$$\begin{aligned} e^{ia(\hat{n}\cdot\vec{\sigma})} &= \sum_{k=0}^{\infty} \frac{i^k[a(\hat{n}\cdot\vec{\sigma})]^k}{k!} \\ &= \sum_{p=0}^{\infty} \frac{(i)^{2p}a^{2p}(\hat{n}\cdot\vec{\sigma})^{2p}}{(2p)!} + \sum_{q=0}^{\infty} \frac{(i)^{2q+1}a^{2q+1}(\hat{n}\cdot\vec{\sigma})^{2q+1}}{(2p+1)!} \\ &= \mathcal{I}\sum_{p=0}^{\infty} \frac{(-1)^p a^{2p}}{(2p)!} + i(\hat{n}\cdot\vec{\sigma})\sum_{q=0}^{\infty} \frac{(-1)^q a^{2q+1}}{(2p+1)!} \\ &= I\cos a + i(\hat{n}\cdot\vec{\sigma})\sin a \end{aligned} \tag{A.13}$$

Simultaneous Diagonalization

Claim: Suppose A, B are two operators. They can both be simultaneously diagonalized (share eigenvectors) if and only if they commute.

Proof: We need to prove this claim in both directions. First assume that they share their eigenvectors and $|\psi\rangle$ is an eigenstate for both of them with eigenvalues a, b respectively. This means:

$$\begin{aligned} [A,B]\,|\psi\rangle &= (AB - BA)\,|\psi\rangle = AB\,|\psi\rangle - BA\,|\psi\rangle \\ &= Ab\,|\psi\rangle - Ba\,|\psi\rangle = bA\,|\psi\rangle - aB\,|\psi\rangle = (ba - ab)\,|\psi\rangle = 0 \end{aligned} \tag{A.14}$$

Similarly one can show that if two operators commute, then their eigenstates must be the same. For this proof, assume that the eigenvalues of A are non-degenerate (unique). So if $[A, B] = 0$, and $A|\psi\rangle = a|\psi\rangle$. Then we can look at:

$$\begin{aligned} BA|\psi\rangle &= aB|\psi\rangle = a|\phi\rangle \\ &= AB|\psi\rangle = A|\phi\rangle \end{aligned} \tag{A.15}$$

where $|\phi\rangle = B|\psi\rangle$ and in the second line we used the commutation. This means $A|\phi\rangle = a|\phi\rangle$ which is another eigenstate of A with the same eigenvalue, contradicting our non-degeneracy assumption, unless $B|\psi\rangle = b|\psi\rangle$. If there are degeneracies in the space spanned by the eigenvectors, the subspace can be rearranged to be in a block diagonal form, and a similar proof follows but this time we talk about the degenerate subspace as opposed to a single eigenvector.

Appendix B

D Orbitals

B.1 Y_l^m Functions

Here is a list of the relevant $Y_n^m(\theta, \phi)$ functions:

$$Y_0^0(\theta,\phi) = \frac{1}{2}\sqrt{\frac{1}{\pi}} \tag{B.1}$$

$$Y_2^0(\theta,\phi) = \frac{1}{4}\sqrt{\frac{5}{\pi}}\left(3\cos^2\theta - 1\right) \tag{B.2}$$

$$Y_2^{\pm 1}(\theta,\phi) = \frac{\mp 1}{2}\sqrt{\frac{15}{2\pi}}\sin\theta\cos\theta e^{\pm i\phi} \tag{B.3}$$

$$Y_2^{\pm 2}(\theta,\phi) = \frac{1}{2}\sqrt{\frac{15}{2\pi}}\sin^2\theta e^{\pm 2i\phi} \tag{B.4}$$

$$Y_4^0(\theta,\phi) = \frac{3}{16\sqrt{\pi}}\left(3 - 30\cos^2\theta + 35\cos^4\theta\right) \tag{B.5}$$

$$Y_4^{\pm 1}(\theta,\phi) = \frac{\mp 3}{9}\sqrt{\frac{5}{\pi}}\sin\theta\cos\theta\left(7\cos^2\theta - 3\right)e^{\pm i\phi} \tag{B.6}$$

$$Y_4^{\pm 2}(\theta,\phi) = \frac{3}{8}\sqrt{\frac{5}{2\pi}}\sin^2\theta\left(7\cos^2\theta - 1\right)e^{\pm 2i\phi} \tag{B.7}$$

$$Y_4^{\pm 3}(\theta,\phi) = \frac{\mp 3}{8}\sqrt{\frac{35}{\pi}}\sin^3\theta\cos\theta e^{\pm 3i\phi} \tag{B.8}$$

$$Y_4^{\pm 4}(\theta,\phi) = \frac{3}{16}\sqrt{\frac{35}{2\pi}}\sin^4\theta e^{\pm 4i\phi} \tag{B.9}$$

B.2 Real d-orbitals

$$d_{z^2} = Y_2^0 = \frac{3}{4}\sqrt{\frac{5}{\pi}}\left(\frac{z^2 - r^2/3}{r^2}\right) \tag{B.10}$$

$$d_{yz} = \frac{1}{i\sqrt{2}}(Y_2^1 + Y_2^{-1}) = \sqrt{\frac{15}{4\pi}}\frac{\mathrm{sgn}(x)yz}{r^2} \tag{B.11}$$

$$d_{xz} = \frac{1}{\sqrt{2}}(Y_2^1 - Y_2^{-1}) = \sqrt{\frac{15}{4\pi}}\frac{|x|z}{r^2} \tag{B.12}$$

$$d_{xy} = \frac{1}{i\sqrt{2}}(Y_2^2 - Y_2^{-2}) = \sqrt{\frac{15}{4\pi}}\frac{xy}{r^2} \tag{B.13}$$

$$d_{x^2-y^2} = \frac{1}{\sqrt{2}}(Y_2^2 + Y_2^{-2}) = \sqrt{\frac{15}{16\pi}}\frac{x^2 - y^2}{r^2} \tag{B.14}$$

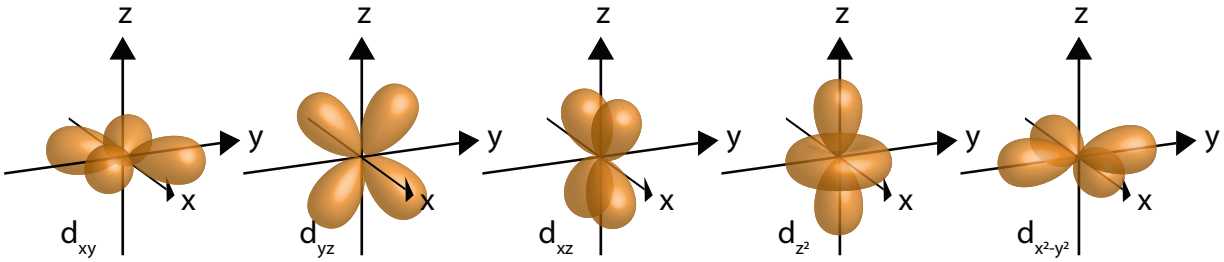

Figure B.1: The geometric shape of real d-orbitals.

Appendix C

Symmetry Elements

C.1 Notation

Below is a summary of notation used within group theory discussions [68].

C.1.1 Schoenflies Symmetry Notation

- E: Identity element. Note: do not confuse this with the Mulliken symbol for the doubly degenerate orbitals in Sec.C.1.2.
- C_n: Rotation through $2\pi/n$. For example C_2 is a 180° rotation while C_3 is a 120° rotation. For example 4H-SiC has C_3 symmetry, where the crystal remain unchanged if rotated by 120° by the c-axis.
- σ: Reflection in a plane
- σ_h: Reflection in a 'horizontal' plane which is perpendicular to the highest rotational symmetry axis $\hat{C}$.
- σ_v: Reflection in a 'vertical' plane which contains the highest rotational symmetry axis $\hat{C}$. For example there are 3 such planes in 4H-SiC, these planes are made out of the c-axis and a vector in one of the non c-axis bond directions.

- σ_d: Reflection in a 'diagonal' plane that contains the highest rotational symmetry axis $\hat{C}$ and bisects the angle between the two fold axes perpendicular to $\hat{C}$.

- i: Inversion i.e. $i(x, y, z) \rightarrow (-x, -y, -z)$. The point group is reflected across the central point. Note: For example 4H-SiC or more symmetric configurations such as T_d discussed in this thesis lack inversion symmetry.

- S_n: improper rotation that is first a rotation by $2\pi/n$ followed by a reflection in a horizontal plane: $S_n = \sigma_h C_n$. For example T_d point group contains S_4 symmetry: first a 90° rotation followed by a reflection across the x, y plane.

- iC_n: as the label suggests this is a compound rotation-inversion which consists of a rotation by $2\pi/n$ followed by an inversion.

Generally point groups are denoted by the symmetry elements they contain. C_n are cyclic groups, C_{nv} contain both C_n symmetry and σ_v symmetry while C_{nh} have C_n and σ_h. S_n groups have mostly compound operations. D_n are dihedral groups and have non-equivalent symmetry axes in perpendicular planes and when there is also additional mirror planes, then we get D_{nh} groups. There are five qubic groups T, O, T_d, T_h, O_h where there is not a principal axis but instead four threefold axes.

C.1.2 Mulliken Symbols

Following symbols are used to describe orbitals and their transformations within a given geometry.

- A: Non-degenerate state that is symmetric with respect to the rotation about the principal axis C_n.

- B: Non-degenerate state that is anti-symmetric with respect to the rotation about the principal axis C_n.

- E: doubly degenerate (derived from the German word for degenerate: *Entartet*)
- T: Triply degenerate.
- $\__1$: Symmetric under σ_h, i.e. symmetric with respect to a horizontal mirror plane perpendicular to the principal axis C_n.
- $\__2$: Anti-symmetric under σ_h, i.e. anti-symmetric with respect to a horizontal mirror plane perpendicular to the principal axis C_n.
- $\__g$: Symmetric under i, i.e. symmetric with respect to inversion through the center of the atom (derived from the German word for even: *Gerade*)
- $\__u$: Anti-symmetric under i, i.e. anti-symmetric with respect to inversion through the center of the atom (derived from the German word for odd: *Ungerade*)
- _': Symmetric under σ_v, i.e. symmetric with respect to the vertical mirror plane containing the principal rotation axis.
- _": Anti-symmetric under σ_v, i.e. anti-symmetric with respect to the vertical mirror plane containing the principal rotation axis.

If a property does not exist, the label is omitted. For example, T_d lacks inversion symmetry and therefore the Mulliken symbol representations of orbitals do not contain $\__{g,u}$ subscripts.

C.2 Dipole Transition Tables

Below are some of examples of transition tables that allow for dipolar transition between the triplet ground state and the singlet first excited state that would be useful for designing molecular spins qubits. For example Table 3.1 shows us that as T_d deforms into S_4, the ground state of ${}^3A_2 \rightarrow {}^3B$ and the excited state ${}^1E \rightarrow (A + B)$ and the dipole transition of $T_2 \rightarrow (B + E)$ which allows us to create the dipole transition table below:

$\otimes (B + E) \otimes$	A	B	E
A	(B+E)	A+E	2A+2B+E
B	A+E	(B+E)	2A+2B+E
E	2A+2B+E	2A+2B+E	2A+2B+4E

Table C.1: Dipole transition products for the S_4 symmetry. Green cells contain the totally symmetric representation A and therefore allow a dipole transition while red cells do not.

As discussed in Sec.7.1.3, although the transition between the first excited state E and the ground state of A_2 was dipolarly forbidden, under the reduced symmetry of S_4, the new ground state B has a dipolar transition to one of the first singlet excited state with the character A.

$\otimes (A_1 + E) \otimes$	A_1	A_2	E
A_1	A_1+E	A_2+E	A_1+A_2+$2E$
A_2	A_2+E	A_1+E	A_1+A_2+$2E$
E	A_1+A_2+$2E$	A_1+A_2+$2E$	$2A_1$+$2A_2$+$4E$

Table C.2: Dipole transition products for the C_{3v} symmetry. Green cells contain the totally symmetric representation A and therefore allow a dipole transition while red cells do not.

$\otimes (A_1 + B_1 + B_2) \otimes$	A_1	A_2	B_1	B_2
A_1	A_1+B_1+B_2	A_2+B_1+B_2	A_1+A_2+B_1	A_1+A_2+B_2
A_2	A_2+B_1+B_2	A_1+B_1+B_2	A_1+A_2+B_2	A_1+A_2+B_1
B_1	A_1+A_2+B_1	A_1+A_2+B_2	A_1+B_1+B_2	A_2+B_1+B_2
B_2	A_1+A_2+B_2	A_1+A_2+B_1	A_2+B_1+B_2	A_1+B_1+B_2

Table C.3: Dipole transition products for the C_{2v} symmetry. Green cells contain the totally symmetric representation A and therefore allow a dipole transition while red cells do not.

The tables for D_2 and D_{2d} do not allow dipole transitions between the first singlet excited state and the spin triplet ground state. All of the orbital transitions for C_3, C_2 and C_s symmetries are dipole allowed.

Appendix D

Experimental Details

D.1 Confocal Microscopy

An example illustration of a confocal microscopy setup is shown below.

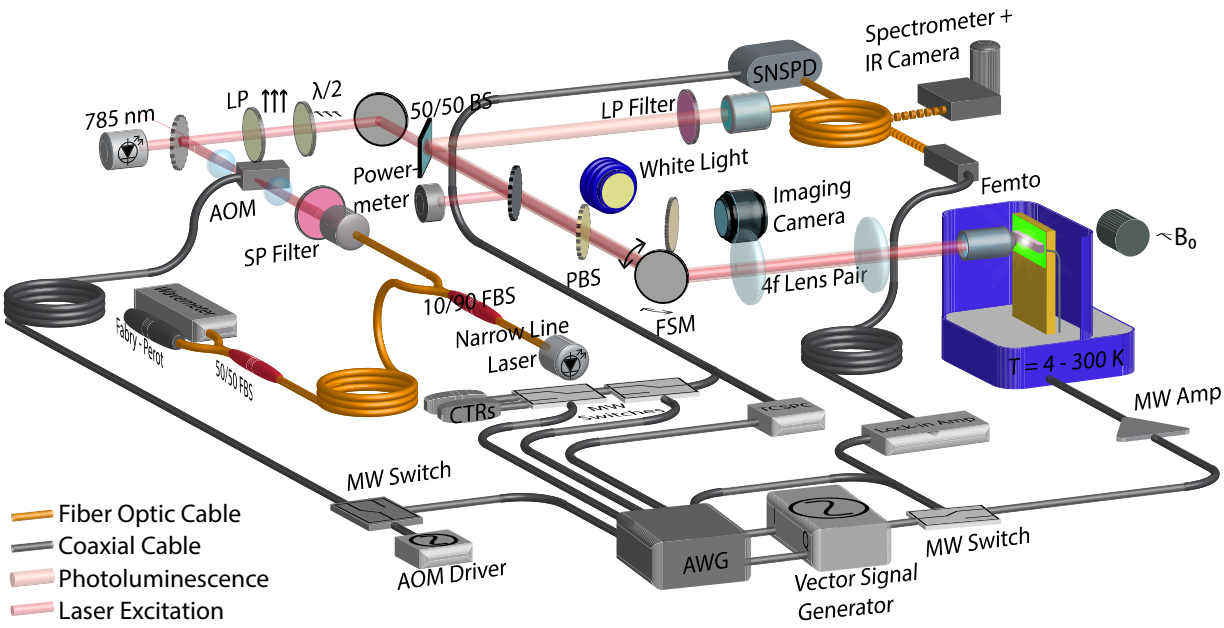

Figure D.1: An example confocal microscopy setup.

D.1.1 Optical Excitation

The experiments in this thesis both use a resonant and an off resonant laser. The off resonant excitation for the d^2 systems use a red laser with a wavelength ranging from 650nm to 730nm. 4H-SiC:V^{4+} experiments require a UV excitation (365 nm) achieved by a small diode for both above bandgap excitation and charge stabilisation. The resonant excitation laser is picked to address the zero-phonon lines for hole burning experiments. The laser is carefully characterized when needed with the following tools: a Fabry-Perrot cavity allows detecting mode hop events, a wavemeter carefully calibrates the wavelength and a powermeter monitors the laser power stability. The narrow line excitation laser can be modified two ways: an acousto-optical modulator can turn the laser on and off with 20-100 nanosecond raise/fall time, and an electro-optic modulator can add sidebands at microwave driving frequencies up to 12 GHz. Various excitation laser colors are combined with dichroic beam splitters. The excitation polarization can be modified with optical waveplates. The excitation can be separated from the collection either by a dichroic mirror or a beam splitter with appropriate short and long pass filters in each path. The excitation path then can go through a fast scanning mirror followed by a $4f$ lens pair for precise sample excitation. The laser then can get focused onto the sample either by a high NA lens or an objective. Depending on the setup, the focusing optic can be inside the cryostat in a heated housing, or outside with a window correction collar.

D.1.2 Optical Collection

The resultant photoluminescence (excitation) traverses the same path back until the beam splitter or the dichroic mirror. A new path cleans the collected signal with additional filters and sends the collected light to one of the few different photo detectors. For example, a spectrometer combined with an array of liquid nitrogen cooled InGaAs detector can measured the spectral configuration of the signal. When the signal is strong, and the experiments can be done quickly, a single pixel femtowatt detector can be used in conjunction with a DAQ or

a lock-in amplifier to detect the optical signal. When the signal is weak (<3 million counts per second), a superconducting nanowire single-photon detector (SNSPD) will register the photon counting events. The detection events are converted to TTL pulses with a pulse converter and a DAQ counter channel registers these events. The counts can be binned by microwave switches where the output is connected to different counter channels.

D.1.3 Optical Imaging

To image the sample a pellicle beam splitter that prevents ghosting is used. The beam splitter is mounted on a flip mount to remove it out of the optical path when the data is collected. The imaging camera is a standard visible CCD with lens focused to infinity. The imaging path is combined with a white light source via a second pellicle beam splitter. The white light source is also collimated to infinity which illuminates the sample when imaging.

D.1.4 Microwave Excitation

A microwave source generates the necessary signal. The microwave source can either be a vector one where I and Q control is done with an on-device bias or an external IQ modulator. The control electronics do not always reliably output 0V bias so it is a good practice to further attenuate microwaves with a switch. The output is fed into a microwave amplifier and sent to the cryostat. The sample is situated by a microwave antenna. In plane microwave field driving is achieved with a coplanar waveguide that is impedance matched to 50Ω at 1 GHz. One should be careful and avoid nickel flashing for gold plated PCBs as the residual nickel can cause significant magnetic field inhomogeneity. For the SiC:V^{4+} experiments, a second PCB on top of the sample with a coplanar loop design generates a c-axis oriented driving field while a window in the middle of the loop still allows optical access. The top mounted antenna also allowed gluing the sample directly to the cold finger, allowing for better thermal contact to reduce the sample temperature as low as possible needed for the longer T_1 times for coherent spin measurements.

D.1.5 Magnetic Field Application

Most of the experiments in this thesis required a c-axis magnetic field. A permanent magnet on a linear stage is centered at the optical path. The stage can adjust the magnetic field magnitude. A gaussmeter can be either placed where the sample is or a known distance away from it, say D, to calibrate the field at the sample. For the latter case, the magnetic field at the gaussmeter is fit with the following function:

$$B_{\text{gaussmeter}}(x) = \frac{A}{(B+x)^3} + C \tag{D.1}$$

where x is the linear stage location, and A, B, C are free fit parameters related to magnitude of the field, distance from the magnet and constant field correction. Once these parameters are extracted, the magnetic field at the sample can be calculated by:

$$B_{\text{sample}}(x) = \frac{A}{(B+D+x)^3} + C \tag{D.2}$$

This approach allows for calibrating the field at the sample with ± 1 Gauss accuracy. For in plane magnetic fields the sample is flipped sideways as shown in Fig.D.1.

D.1.6 Time synchronization

All of the microwave and optical switches, IQ modulators and photon counter electronics need to be time synchronized. For experiments that are not logic intensive a digital delay generator is sufficient for time resolved measurements. When there are many channels that need to be controlled an arbitrary waveform generator created TTL pulses with at least 1 ns resolution. Excited state lifetime is generally measured by looking at photon arrival time binning using either photon counting card, or directly looking at photon arrival times with a DAQ.

D.2 High Field Measurements

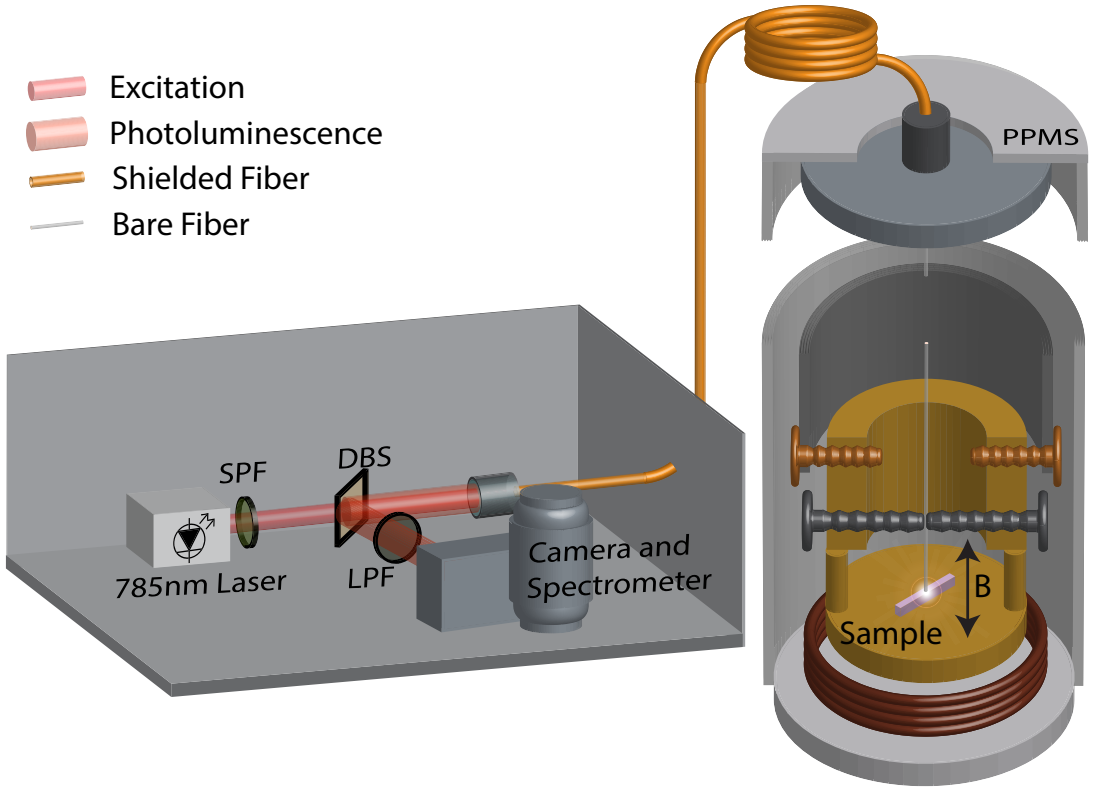

Figure D.2: Illustration of the custom built optical PPMS probe.

High-field measurements up to B = 9T were performed in a cryostat with an integrated superconducting magnet (Quantum Design Physical Property Measurement System, PPMS. The sample was cooled to a temperature of 10 K through helium exchange gas. To provide optical access to the sample, we use an optical fiber (Thorlabs, FP400ERT) mounted in a custom-built probe. The sample end of the probe mounts to the base of the PPMS through a sample-mount puck. The (unconnectorized) end of the optical fiber at the sample is mounted directly on the sample to provide excitation and PL collection, and is clamped in place. A custom-made vacuum compatible fiber feedthrough connects this fiber to excitation and collection optics with similar elements discussed in Sec.D.1.

References

[1] SL Bayliss, DW Laorenza, PJ Mintun, BD Kovos, Danna E Freedman, and DD Awschalom. Optically addressable molecular spins for quantum information processing. *Science*, 370(6522):1309–1312, 2020.

[2] Majed S Fataftah, Sam L Bayliss, Daniel W Laorenza, Xiaoling Wang, Brian T Phelan, C Blake Wilson, Peter J Mintun, Berk D Kovos, Michael R Wasielewski, Songi Han, et al. Trigonal bipyramidal V^{3+} complex as an optically addressable molecular qubit candidate. *J. Am. Chem. Soc.*, 142(48):20400–20408, 2020.

[3] Gary Wolfowicz, Christopher P Anderson, Berk Diler, Oleg G Poluektov, F Joseph Heremans, and David D Awschalom. Vanadium spin qubits as telecom quantum emitters in silicon carbide. *Sci. Adv.*, 6(18):eaaz1192, 2020.

[4] Berk Diler, Samuel J Whiteley, Christopher P Anderson, Gary Wolfowicz, Marie E Wesson, Edward S Bielejec, F Joseph Heremans, and David D Awschalom. Coherent control and high-fidelity readout of chromium ions in commercial silicon carbide. *npj Quantum Inf.*, 6(1):1–6, 2020.

[5] William F Koehl, Berk Diler, Samuel J Whiteley, Alexandre Bourassa, N Tien Son, Erik Janzén, and David D Awschalom. Resonant optical spectroscopy and coherent control of Cr^{4+} spin ensembles in SiC and GaN. *Phys. Rev. B*, 95(3):035207, 2017.

[6] Yaniv Erlich and Dina Zielinski. DNA fountain enables a robust and efficient storage architecture. *Science*, 355(6328):950–954, 2017.

[7] John Preskill. Quantum computing in the NISQ era and beyond. *Quantum*, 2:79, 2018.

[8] Gideon Lichfield. Google CEO Sundar Pichai on achieving quantum supremacy, 2020.

[9] Charles H Bennett and Gilles Brassard. Quantum cryptography: Public key distribution and coin tossing. In *Proceedings of the International Conference on Computers, Systems and Signal Processing*, pages 175–179, 1984.

[10] Charles H. Bennett, Gilles Brassard, Claude Crépeau, Richard Jozsa, Asher Peres, and William K. Wootters. Teleporting an unknown quantum state via dual classical and Einstein-Podolsky-Rosen channels. *Phys. Rev. Lett.*, 70:1895–1899, 1993.

[11] Christian L Degen, F Reinhard, and Paola Cappellaro. Quantum sensing. *Rev. Mod. Phys.*, 89(3):035002, 2017.

[12] Yi Xia, Wei Li, Quntao Zhuang, and Zheshen Zhang. Quantum-enhanced data classification with a variational entangled sensor network. *Phys. Rev. X*, 11:021047, 2021.

[13] Engineering National Academies of Sciences and Medicine. *Quantum Computing: Progress and Prospects*. The National Academies Press, Washington, DC, 2019.

[14] David EJ Waddington, Mathieu Sarracanie, Huiliang Zhang, Najat Salameh, David R Glenn, Ewa Rej, Torsten Gaebel, Thomas Boele, Ronald L Walsworth, David J Reilly, et al. Nanodiamond-enhanced MRI via in situ hyperpolarization. *Nat. Commun.*, 8(1):1–8, 2017.

[15] Aleksei Yur'evich Kitaev. Quantum computations: algorithms and error correction. *Uspekhi Mat. Nauk*, 52(6):53–112, 1997.

[16] Colin P Williams. Quantum gates. In *Explorations in Quantum Computing*, pages 51–122. Springer, 2011.

[17] PJ Howard. Telecommunication cables. In *Telecommunications Engineer's Reference Book*, pages 15–1. Elsevier, 1993.

[18] Fulvio Flamini, Nicolo Spagnolo, and Fabio Sciarrino. Photonic quantum information processing: a review. *Rep. Prog. Phys.*, 82(1):016001, 2018.

[19] Jeremy L O'brien, Akira Furusawa, and Jelena Vu**c**ković. Photonic quantum technologies. *Nat. Photonics*, 3(12):687–695, 2009.

[20] Jianjun Yu and Junwen Zhang. Recent progress on high-speed optical transmission. *Digit. Commun. Netw.*, 2(2):65–76, 2016.

[21] S Takeda and A Furusawa. Toward large-scale fault-tolerant universal photonic quantum computing. *APL Photonics*, 4(6):060902, 2019.

[22] Colin D Bruzewicz, John Chiaverini, Robert McConnell, and Jeremy M Sage. Trapped-ion quantum computing: Progress and challenges. *Appl. Phys. Rev.*, 6(2):021314, 2019.

[23] Joseph M Zadrozny, Jens Niklas, Oleg G Poluektov, and Danna E Freedman. Millisecond coherence time in a tunable molecular electronic spin qubit. *ACS Cent. Sci.*, 1(9):488–492, 2015.

[24] Jonathan A. Jones. Quantum computing with NMR. *Prog. Nucl. Magn. Reson. Spectrosc.*, 59(2):91–120, 2011.

[25] Victor V. Albert, Jacob P. Covey, and John Preskill. Robust encoding of a qubit in a molecule. *Phys. Rev. X*, 10:031050, 2020.

[26] Daqing Wang, Hrishikesh Kelkar, Diego Martin-Cano, Dominik Rattenbacher, Alexey Shkarin, Tobias Utikal, Stephan Götzinger, and Vahid Sandoghdar. Turning a molecule into a coherent two-level quantum system. *Nat. Phys.*, 15(5):483–489, 2019.

[27] Lieven MK Vandersypen, Matthias Steffen, Gregory Breyta, Costantino S Yannoni, Mark H Sherwood, and Isaac L Chuang. Experimental realization of Shor's quantum factoring algorithm using nuclear magnetic resonance. *Nature*, 414(6866):883–887, 2001.

[28] Vishal Ranjan, Sebastian Probst, Bartolo Albanese, Thomas Schenkel, Denis Vion, Daniel Esteve, JJL Morton, and Patrice Bertet. Electron spin resonance spectroscopy with femtoliter detection volume. *Appl. Phys. Lett.*, 116(18):184002, 2020.

[29] Andrea Morello, Jarryd J Pla, Patrice Bertet, and David N Jamieson. Donor spins in silicon for quantum technologies. *Adv. Quantum Technol.*, 3(11):2000005, 2020.

[30] Victoria A Norman, Sridhar Majety, Zhipan Wang, William H Casey, Nicholas Curro, and Marina Radulaski. Novel color center platforms enabling fundamental scientific discovery. *InfoMat*, 2020.

[31] Victoria A Norman, Sridhar Majety, Zhipan Wang, William H Casey, Nicholas Curro, and Marina Radulaski. Novel color center platforms enabling fundamental scientific discovery. *InfoMat*, 2020.

[32] Marcus W Doherty, Neil B Manson, Paul Delaney, Fedor Jelezko, Jörg Wrachtrup, and Lloyd CL Hollenberg. The nitrogen-vacancy colour centre in diamond. *Phys. Rep.*, 528(1):1–45, 2013.

[33] Joe C Campbell. Recent advances in avalanche photodiodes. *J. Light. Technol.*, 34(2):278–285, 2016.

[34] Itamar Holzman and Yachin Ivry. Superconducting nanowires for single-photon detection: progress, challenges, and opportunities. *Adv. Quantum Technol.*, 2(3-4):1800058, 2019.

[35] H. Y. Chen, S. A. Bhave, and G. D. Fuchs. Acoustically driving the single-quantum spin transition of diamond nitrogen-vacancy centers. *Phys. Rev. Appl.*, 13:054068, 2020.

[36] Daniil M. Lukin, Melissa A. Guidry, and Jelena Vu**c**ković. Integrated quantum photonics with silicon carbide: Challenges and prospects. *PRX Quantum*, 1:020102, 2020.

[37] Samuel J Whiteley, Gary Wolfowicz, Christopher P Anderson, Alexandre Bourassa, He Ma, Meng Ye, Gerwin Koolstra, Kevin J Satzinger, Martin V Holt, F Joseph Heremans, et al. Spin–phonon interactions in silicon carbide addressed by Gaussian acoustics. *Nat. Phys.*, 15(5):490–495, 2019.

[38] Christopher P Anderson, Alexandre Bourassa, Kevin C Miao, Gary Wolfowicz, Peter J Mintun, Alexander L Crook, Hiroshi Abe, Jawad Ul Hassan, Nguyen T Son, Takeshi Ohshima, et al. Electrical and optical control of single spins integrated in scalable semiconductor devices. *Science*, 366(6470):1225–1230, 2019.

[39] Kevin C Miao, Joseph P Blanton, Christopher P Anderson, Alexandre Bourassa, Alexander L Crook, Gary Wolfowicz, Hiroshi Abe, Takeshi Ohshima, and David D Awschalom. Universal coherence protection in a solid-state spin qubit. *Science*, 369(6510):1493–1497, 2020.

[40] Noel H Wan, Tsung-Ju Lu, Kevin C Chen, Michael P Walsh, Matthew E Trusheim, Lorenzo De Santis, Eric A Bersin, Isaac B Harris, Sara L Mouradian, Ian R Christen, et al. Large-scale integration of artificial atoms in hybrid photonic circuits. *Nature*, 583(7815):226–231, 2020.

[41] Eric Bersin, Michael Walsh, Sara L Mouradian, Matthew E Trusheim, Tim Schröder, and Dirk Englund. Individual control and readout of qubits in a sub-diffraction volume. *npj Quantum Inf.*, 5(1):1–6, 2019.

[42] Huiliang Zhang, Keigo Arai, Chinmay Belthangady, J-C Jaskula, and Ronald L Walsworth. Selective addressing of solid-state spins at the nanoscale via magnetic resonance frequency encoding. *npj Quantum Inf.*, 3(1):1–8, 2017.

[43] PV Klimov, AL Falk, BB Buckley, and DD Awschalom. Electrically driven spin resonance in silicon carbide color centers. *Phys. Rev. Lett.*, 112(8):087601, 2014.

[44] CE Bradley, J Randall, MH Abobeih, RC Berrevoets, MJ Degen, MA Bakker, M Markham, DJ Twitchen, and TH Taminiau. A ten-qubit solid-state spin register with quantum memory up to one minute. *Phys. Rev. X*, 9(3):031045, 2019.

[45] Philippe Goldner, Alban Ferrier, and Olivier Guillot-Noël. Rare earth-doped crystals for quantum information processing. In *Handbook on the Physics and Chemistry of Rare Earths*, volume 46, pages 1–78. Elsevier, 2015.

[46] Tian Zhong and Philippe Goldner. Emerging rare-earth doped material platforms for quantum nanophotonics. *Nanophotonics*, 8(11):2003–2015, 2019.

[47] Tian Zhong, Jonathan M. Kindem, John G. Bartholomew, Jake Rochman, Ioana Craiciu, Varun Verma, Sae Woo Nam, Francesco Marsili, Matthew D. Shaw, Andrew D. Beyer, and Andrei Faraon. Optically addressing single rare-earth ions in a nanophotonic cavity. *Phys. Rev. Lett.*, 121:183603, 2018.

[48] Mouktik Raha, Songtao Chen, Christopher M Phenicie, Salim Ourari, Alan M Dibos, and Jeff D Thompson. Optical quantum nondemolition measurement of a single rare earth ion qubit. *Nat. Commun.*, 11(1):1–6, 2020.

[49] Ioana Craiciu, Mi Lei, Jake Rochman, Jonathan M. Kindem, John G. Bartholomew, Evan Miyazono, Tian Zhong, Neil Sinclair, and Andrei Faraon. Nanophotonic quantum storage at telecommunication wavelength. *Phys. Rev. Appl.*, 12:024062, 2019.

[50] AJ Kenyon. Erbium in silicon. *Semicond. Sci. Technol.*, 20(12):R65, 2005.

[51] Mark A Hughes, Naitik A Panjwani, Matias Urdampilleta, Kevin P Homewood, Ben Murdin, and J David Carey. Spin echo from erbium implanted silicon. *Appl. Phys. Lett.*, 118(19):194001, 2021.

[52] Adam Kinos, David Hunger, Roman Kolesov, Klaus Mølmer, Hugues de Riedmatten, Philippe Goldner, Alexandre Tallaire, Loic Morvan, Perrine Berger, Sacha Welinski,

et al. Roadmap for rare-earth quantum computing. *arXiv preprint arXiv:2103.15743*, 2021.

[53] Morten Kjaergaard, Mollie E Schwartz, Jochen Braumüller, Philip Krantz, Joel I-J Wang, Simon Gustavsson, and William D Oliver. Superconducting qubits: Current state of play. *Annu. Rev. Condens. Matter Phys.*, 11:369–395, 2020.

[54] Anasua Chatterjee, Paul Stevenson, Silvano De Franceschi, Andrea Morello, Nathalie P de Leon, and Ferdinand Kuemmeth. Semiconductor qubits in practice. *Nat. Rev. Phys.*, pages 1–21, 2021.

[55] Frank Arute, Kunal Arya, Ryan Babbush, Dave Bacon, Joseph C Bardin, Rami Barends, Rupak Biswas, Sergio Boixo, Fernando GSL Brandao, David A Buell, et al. Quantum supremacy using a programmable superconducting processor. *Nature*, 574(7779):505–510, 2019.

[56] Anatole Abragam and Brebis Bleaney. *Electron paramagnetic resonance of transition ions*. OUP Oxford, 2012.

[57] Brian N Figgis and Michael A Hitchman. *Ligand field theory and its applications*, volume 158. Wiley-Vch New York, 2000.

[58] Cheng-Wei Lee, Meenakshi Singh, Adele Tamboli, and Vladan Stevanović. Transition metal impurities in silicon: Computational search for a semiconductor qubit. *arXiv preprint arXiv:2105.05927*, 2021.

[59] Ramamurti Shankar. *Principles of quantum mechanics*. Springer Science & Business Media, 2012.

[60] Jun John Sakurai and Eugene D Commins. *Modern quantum mechanics, revised edition*. American Association of Physics Teachers, 1995.

[61] Tim Maudlin. *Philosophy of physics: Quantum theory*, volume 33. Princeton University Press, 2019.

[62] Ugo Fano and Giulio Racah. Irreducible tensorial sets. *Irreducible tensorial sets*, 1959.

[63] Tom Bosma, Gerrit JJ Lof, Carmem M Gilardoni, Olger V Zwier, Freddie Hendriks, Björn Magnusson, Alexandre Ellison, Andreas Gällström, Ivan G Ivanov, NT Son, et al. Identification and tunable optical coherent control of transition-metal spins in silicon carbide. *npj Quantum Inf.*, 4(1):1–7, 2018.

[64] R Heitz, P Thurian, I Loa, L Eckey, A Hoffmann, I Broser, K Pressel, BK Meyer, and EN Mokhov. Identification of the 1.19-eV luminescence in hexagonal GaN. *Phys. Rev. B*, 52(23):16508, 1995.

[65] Hartmut Yersin and Walter J Finkenzeller. Triplet emitters for organic light-emitting diodes: basic properties. *Highly Effic. OLEDs with Phosphorescent Mater.*, pages 1–97, 2008.

[66] Myrtille OJY Hunault, Yoshihisa Harada, Jun Miyawaki, Jian Wang, Andries Meijerink, Frank MF De Groot, and Matti M Van Schooneveld. Direct observation of cr^{3+} $3d$ states in ruby: Toward experimental mechanistic evidence of metal chemistry. *J. Phys. Chem. A*, 122(18):4399–4413, 2018.

[67] Vikas K. Sewani, Rainer J. Stöhr, Roman Kolesov, Hyma H. Vallabhapurapu, Tobias Simmet, Andrea Morello, and Arne Laucht. Spin thermometry and spin relaxation of optically detected cr^{3+} ions in ruby al_2o_3. *Phys. Rev. B*, 102:104114, 2020.

[68] Mildred S Dresselhaus, Gene Dresselhaus, and Ado Jorio. *Group theory: application to the physics of condensed matter*. Springer Science & Business Media, 2007.

[69] Petr Siyushev, Mathias H. Metsch, Aroosa Ijaz, Jan M. Binder, Mihir K. Bhaskar, Denis D. Sukachev, Alp Sipahigil, Ruffin E. Evans, Christian T. Nguyen, Mikhail D.

Lukin, Philip R. Hemmer, Yuri N. Palyanov, Igor N. Kupriyanov, Yuri M. Borzdov, Lachlan J. Rogers, and Fedor Jelezko. Optical and microwave control of germanium-vacancy center spins in diamond. *Phys. Rev. B*, 96:081201, 2017.

[70] Carlo Bradac, Weibo Gao, Jacopo Forneris, Matthew E Trusheim, and Igor Aharonovich. Quantum nanophotonics with group IV defects in diamond. *Nat. Commun.*, 10(1):1–13, 2019.

[71] NT Son, A Ellison, Björn Magnusson, MF MacMillan, WM Chen, Bo Monemar, and Erik Janzén. Photoluminescence and Zeeman effect in chromium-doped 4H and 6H SiC. *J. Appl. Phys.*, 86(8):4348–4353, 1999.

[72] PG Baranov, VA Khramtsov, and EN Mokhov. Chromium in silicon carbide: electron paramagnetic resonance studies. *Semicond. Sci. Technol.*, 9(7):1340, 1994.

[73] J Baur, K Maier, M Kunzer, U Kaufmann, J Schneider, H Amano, I Akasaki, T Detchprohm, and K Hiramatsu. Infrared luminescence of residual iron deep level acceptors in gallium nitride (GaN) epitaxial layers. *Appl. Phys. Lett.*, 64(7):857–859, 1994.

[74] J Baur, U Kaufmann, M Kunzer, J Schneider, H Amano, I Akasaki, T Detchprohm, and K Hiramatsu. Photoluminescence of residual transition metal impurities in GaN. *Appl. Phys. Lett.*, 67(8):1140–1142, 1995.

[75] Hannes Bernien, Bas Hensen, Wolfgang Pfaff, Gerwin Koolstra, Machiel S Blok, Lucio Robledo, TH Taminiau, Matthew Markham, Daniel J Twitchen, Lilian Childress, et al. Heralded entanglement between solid-state qubits separated by three metres. *Nature*, 497(7447):86–90, 2013.

[76] William Esco Moerner and Gary C Bjorklund. *Persistent spectral hole-burning: science and applications*, volume 1. Springer, 1988.

[77] WB Gao, Atac Imamoglu, H Bernien, and R Hanson. Coherent manipulation, measurement and entanglement of individual solid-state spins using optical fields. *Nat. Photonics*, 9(6):363–373, 2015.

[78] Roland Nagy, Matthias Niethammer, Matthias Widmann, Yu-Chen Chen, Péter Udvarhelyi, Cristian Bonato, Jawad Ul Hassan, Robin Karhu, Ivan G Ivanov, Nguyen Tien Son, et al. High-fidelity spin and optical control of single silicon-vacancy centres in silicon carbide. *Nat. Commun.*, 10(1):1–8, 2019.

[79] David J Christle, Paul V Klimov, F Charles, Krisztián Szász, Viktor Ivády, Valdas Jokubavicius, Jawad Ul Hassan, Mikael Syväjärvi, William F Koehl, Takeshi Ohshima, et al. Isolated spin qubits in SiC with a high-fidelity infrared spin-to-photon interface. *Phys. Rev. X*, 7(2):021046, 2017.

[80] Manuel Cardona and Mike LW Thewalt. Isotope effects on the optical spectra of semiconductors. *Rev. Mod. Phys.*, 77(4):1173, 2005.

[81] G. F. Imbusch, W. M. Yen, A. L. Schawlow, G. E. Devlin, and J. P. Remeika. Isotope shift in the R lines of chromium in ruby and MgO. *Phys. Rev.*, 136:A481–A486, 1964.

[82] Theodore G Castner Jr. Raman spin-lattice relaxation of shallow donors in silicon. *Phys. Rev.*, 130(1):58, 1963.

[83] William F Koehl, Bob B Buckley, F Joseph Heremans, Greg Calusine, and David D Awschalom. Room temperature coherent control of defect spin qubits in silicon carbide. *Nature*, 479(7371):84–87, 2011.

[84] Abram L Falk, Bob B Buckley, Greg Calusine, William F Koehl, Viatcheslav V Dobrovitski, Alberto Politi, Christian A Zorman, Philip X-L Feng, and David D Awschalom. Polytype control of spin qubits in silicon carbide. *Nat. Commun.*, 4(1):1–7, 2013.

[85] Shunchong Wang, Minjie Zhan, Gang Wang, Hongwen Xuan, Wei Zhang, Chunjun Liu, Chunhua Xu, Yu Liu, Zhiyi Wei, and Xiaolong Chen. 4H-SiC: a new nonlinear material for midinfrared lasers. *Laser Photonics Rev.*, 7(5):831–838, 2013.

[86] David N Jamieson, William IL Lawrie, Simon G Robson, Alexander M Jakob, Brett C Johnson, and Jeffrey C McCallum. Deterministic doping. *Mater. Sci. Semicond. Process.*, 62:23–30, 2017.

[87] JL Pacheco, M Singh, DL Perry, JR Wendt, G Ten Eyck, RP Manginell, T Pluym, DR Luhman, MP Lilly, MS Carroll, et al. Ion implantation for deterministic single atom devices. *Rev. Sci. Instrum.*, 88(12):123301, 2017.

[88] Lukas Spindlberger, András Csóré, Gergö Thiering, S Putz, Robin Karhu, J Ul Hassan, NT Son, T Fromherz, A Gali, and M Trupke. Optical properties of vanadium in 4H silicon carbide for quantum technology. *Phys. Rev. Appl.*, 12(1):014015, 2019.

[89] B Kaufmann, A Dörnen, and FS Ham. Crystal-field model of vanadium in 6H silicon carbide. *Phys. Rev. B*, 55(19):13009, 1997.

[90] J Baur, M Kunzer, and J Schneider. Transition metals in SiC polytypes, as studied by magnetic resonance techniques. *Phys. Status Solidi A*, 162(1):153–172, 1997.

[91] M Kunzer, HD Müller, and U Kaufmann. Magnetic circular dichroism and site-selective optically detected magnetic resonance of the deep amphoteric vanadium impurity in 6H-SiC. *Phys. Rev. B*, 48(15):10846, 1993.

[92] Manuel Cardona and Mike LW Thewalt. Isotope effects on the optical spectra of semiconductors. *Rev. Mod. Phys.*, 77(4):1173, 2005.

[93] MLW Thewalt, M Steger, A Yang, N Stavrias, M Cardona, H Riemann, NV Abrosimov, MF Churbanov, AV Gusev, AD Bulanov, et al. Can highly enriched ^{28}Si reveal new things about old defects? *Physica B Condens. Matter*, 401:587–592, 2007.

[94] VM Acosta, A Jarmola, E Bauch, and D Budker. Optical properties of the nitrogen-vacancy singlet levels in diamond. *Phys. Rev. B*, 82(20):201202, 2010.

[95] David D Awschalom, Ronald Hanson, Jörg Wrachtrup, and Brian B Zhou. Quantum technologies with optically interfaced solid-state spins. *Nat. Photonics*, 12(9):516–527, 2018.

[96] Janik Wolters, Nikola Sadzak, Andreas W Schell, Tim Schröder, and Oliver Benson. Measurement of the ultrafast spectral diffusion of the optical transition of nitrogen vacancy centers in nano-size diamond using correlation interferometry. *Phys. Rev. Lett.*, 110(2):027401, 2013.

[97] Alexander Lohrmann, BC Johnson, JC McCallum, and Stefania Castelletto. A review on single photon sources in silicon carbide. *Rep. Prog. Phys.*, 80(3):034502, 2017.

[98] Maximilian Ruf, Mark IJspeert, Suzanne Van Dam, Nick De Jong, Hans Van Den Berg, Guus Evers, and Ronald Hanson. Optically coherent nitrogen-vacancy centers in micrometer-thin etched diamond membranes. *Nano Lett.*, 19(6):3987–3992, 2019.

[99] K Maier, J Schneider, W Wilkening, S Leibenzeder, and R Stein. Electron spin resonance studies of transition metal deep level impurities in SiC. *Mater. Sci. Eng., B*, 11(1-4):27–30, 1992.

[100] Russell S Drago. *Physical methods for chemists*. Surfside Scientific Publishers, 1992.

[101] Kay D Jahnke, Alp Sipahigil, Jan M Binder, Marcus W Doherty, Mathias Metsch, Lachlan J Rogers, Neil B Manson, Mikhail D Lukin, and Fedor Jelezko. Electron–phonon processes of the silicon-vacancy centre in diamond. *New J. Phys.*, 17(4):043011, 2015.

[102] Milos Rancić, Morgan P Hedges, Rose L Ahlefeldt, and Matthew J Sellars. Coherence

time of over a second in a telecom-compatible quantum memory storage material. *Nat. Phys.*, 14(1):50–54, 2018.

[103] Alejandro Gaita-Ariño, Fernando Luis, Stephen Hill, and Eugenio Coronado. Molecular spins for quantum computation. *Nat. Chem.*, 11(4):301–309, 2019.

[104] Jesús Ferrando-Soria, Eufemio Moreno Pineda, Alessandro Chiesa, Antonio Fernandez, Samantha A Magee, Stefano Carretta, Paolo Santini, Inigo J Vitorica-Yrezabal, Floriana Tuna, Grigore A Timco, et al. A modular design of molecular qubits to implement universal quantum gates. *Nat. Commun.*, 7(1):1–10, 2016.

[105] Stefan U Koschmieder, Brian S McGilligan, Gregory McDermott, John Arnold, Geoffrey Wilkinson, Bilquis Hussain-Bates, and Michael B Hursthouse. Aryl and aryne complexes of chromium, molybdenum, and tungsten. X-Ray crystal structures of [Cr (2-MeC_6H_4)(μ-2-MeC_6H_4)(PMe_3)]$_2$, Mo(η^2-2-MeC_6H_3)(2-MeC_6H_4)$_2$(PMe_2Ph)$_2$, and W(η^2-2,5-$Me_2C_6H_2$)(2,5-$Me_2C_6H_3$)$_2$-(PMe_3)$_2$. *J. Chem. Soc., Dalton Trans*, (11):3427–3433, 1990.

[106] Joseph M Zadrozny, Jens Niklas, Oleg G Poluektov, and Danna E Freedman. Millisecond coherence time in a tunable molecular electronic spin qubit. *ACS Cent. Sci.*, 1(9):488–492, 2015.

[107] Arzhang Ardavan, Olivier Rival, John JL Morton, Stephen J Blundell, Alexei M Tyryshkin, Grigore A Timco, and Richard EP Winpenny. Will spin-relaxation times in molecular magnets permit quantum information processing? *Phys. Rev. Lett.*, 98(5):057201, 2007.

[108] Arzhang Ardavan, Alice M Bowen, Antonio Fernandez, Alistair J Fielding, Danielle Kaminski, Fabrizio Moro, Christopher A Muryn, Matthew D Wise, Albert Ruggi, Eric JL McInnes, et al. Engineering coherent interactions in molecular nanomagnet dimers. *npj Quantum Inf.*, 1(1):1–7, 2015.

[109] Muhandis Shiddiq, Dorsa Komijani, Yan Duan, Alejandro Gaita-Ariño, Eugenio Coronado, and Stephen Hill. Enhancing coherence in molecular spin qubits via atomic clock transitions. *Nature*, 531(7594):348–351, 2016.

[110] MV Gurudev Dutt, L Childress, L Jiang, E Togan, J Maze, F Jelezko, AS Zibrov, PR Hemmer, and MD Lukin. Quantum register based on individual electronic and nuclear spin qubits in diamond. *Science*, 316(5829):1312–1316, 2007.

[111] Michael K Wojnar, Daniel W Laorenza, Richard D Schaller, and Danna E Freedman. Nickel (II) metal complexes as optically addressable qubit candidates. *J. Am. Chem. Soc.*, 142(35):14826–14830, 2020.

[112] Rohit Chikkaraddy, Bart De Nijs, Felix Benz, Steven J Barrow, Oren A Scherman, Edina Rosta, Angela Demetriadou, Peter Fox, Ortwin Hess, and Jeremy J Baumberg. Single-molecule strong coupling at room temperature in plasmonic nanocavities. *Nature*, 535(7610):127–130, 2016.

[113] Gary Wolfowicz, F Joseph Heremans, Christopher P Anderson, Shun Kanai, Hosung Seo, Adam Gali, Giulia Galli, and David D Awschalom. Quantum guidelines for solid-state spin defects. *Nat. Rev. Mater.*, pages 1–20, 2021.

[114] Xiao-Xiao Li, Bo Li, and Peng-Bo Li. Simulation of topological phases with color center arrays in phononic crystals. *Phys. Rev. Res.*, 2(1):013121, 2020.

[115] R Orbach. Spin-lattice relaxation in rare-earth salts. *Proc. R. Soc. London. Ser. A. Math. Phys. Sci.*, 264(1319):458–484, 1961.

[116] Srujan Meesala, Young-Ik Sohn, Benjamin Pingault, Linbo Shao, Haig A. Atikian, Jeffrey Holzgrafe, Mustafa Gündoğan, Camille Stavrakas, Alp Sipahigil, Cleaven Chia, Ruffin Evans, Michael J. Burek, Mian Zhang, Lue Wu, Jose L. Pacheco, John Abraham, Edward Bielejec, Mikhail D. Lukin, Mete Atatüre, and Marko Lon**c**ar. Strain engineering of the silicon-vacancy center in diamond. *Phys. Rev. B*, 97:205444, 2018.

[117] Michael J Graham, Joseph M Zadrozny, Majed S Fataftah, and Danna E Freedman. Forging solid-state qubit design principles in a molecular furnace. *Chem. Mater.*, 29(5):1885–1897, 2017.

[118] Gary Wolfowicz, Alexei M Tyryshkin, Richard E George, Helge Riemann, Nikolai V Abrosimov, Peter Becker, Hans-Joachim Pohl, Mike LW Thewalt, Stephen A Lyon, and John JL Morton. Atomic clock transitions in silicon-based spin qubits. *Nat. Nanotechnol.*, 8(8):561–564, 2013.

[119] Wayne M Witzel, Malcolm S Carroll, Andrea Morello, Łukasz Cywiński, and S Das Sarma. Electron spin decoherence in isotope-enriched silicon. *Phys. Rev. Lett.*, 105(18):187602, 2010.

[120] Alexandre Bourassa, Christopher P Anderson, Kevin C Miao, Mykyta Onizhuk, He Ma, Alexander L Crook, Hiroshi Abe, Jawad Ul-Hassan, Takeshi Ohshima, Nguyen T Son, et al. Entanglement and control of single nuclear spins in isotopically engineered silicon carbide. *Nat. Mater.*, 19(12):1319–1325, 2020.

[121] Gopalakrishnan Balasubramanian, Philipp Neumann, Daniel Twitchen, Matthew Markham, Roman Kolesov, Norikazu Mizuochi, Junichi Isoya, Jocelyn Achard, Johannes Beck, Julia Tissler, et al. Ultralong spin coherence time in isotopically engineered diamond. *Nat. Mater.*, 8(5):383–387, 2009.

[122] DL McAuslan, JG Bartholomew, MJ Sellars, and Jevon Joseph Longdell. Reducing decoherence in optical and spin transitions in rare-earth-metal-ion–doped materials. *Phys. Rev. A*, 85(3):032339, 2012.

[123] Mykyta Onizhuk, Kevin C. Miao, Joseph P. Blanton, He Ma, Christopher P. Anderson, Alexandre Bourassa, David D. Awschalom, and Giulia Galli. Probing the coherence of solid-state qubits at avoided crossings. *PRX Quantum*, 2:010311, 2021.

[124] P Siyushev, F Kaiser, V Jacques, I Gerhardt, S Bischof, H Fedder, J Dodson, M Markham, D Twitchen, F Jelezko, et al. Monolithic diamond optics for single photon detection. *Appl. Phys. Lett.*, 97(24):241902, 2010.

[125] David D Awschalom, Ronald Hanson, Jörg Wrachtrup, and Brian B Zhou. Quantum technologies with optically interfaced solid-state spins. *Nat. Photonics*, 12(9):516–527, 2018.

[126] Emre Togan, Yiwen Chu, Alexei S Trifonov, Liang Jiang, Jeronimo Maze, Lilian Childress, MV Gurudev Dutt, Anders Søndberg Sørensen, Phillip R Hemmer, Alexander S Zibrov, et al. Quantum entanglement between an optical photon and a solid-state spin qubit. *Nature*, 466(7307):730–734, 2010.

[127] Songtao Chen, Mouktik Raha, Christopher M Phenicie, Salim Ourari, and Jeff D Thompson. Parallel single-shot measurement and coherent control of solid-state spins below the diffraction limit. *Science*, 370(6516):592–595, 2020.

[128] Alexander L Crook, Christopher P Anderson, Kevin C Miao, Alexandre Bourassa, Hope Lee, Sam L Bayliss, David O Bracher, Xingyu Zhang, Hiroshi Abe, Takeshi Ohshima, et al. Purcell enhancement of a single silicon carbide color center with coherent spin control. *Nano Lett.*, 20(5):3427–3434, 2020.

[129] Ilya P Radko, Mads Boll, Niels M Israelsen, Nicole Raatz, Jan Meijer, Fedor Jelezko, Ulrik L Andersen, and Alexander Huck. Determining the internal quantum efficiency of shallow-implanted nitrogen-vacancy defects in bulk diamond. *Opt. Express*, 24(24):27715–27725, 2016.

[130] Bas Hensen, Norbert Kalb, MS Blok, AE Dréau, Andreas Reiserer, RFL Vermeulen, RN Schouten, M Markham, DJ Twitchen, Kenneth Goodenough, et al. Loophole-free bell test using electron spins in diamond: second experiment and additional analysis. *Sci. Rep.*, 6(1):1–11, 2016.

[131] Matteo Pompili, Sophie LN Hermans, Simon Baier, Hans KC Beukers, Peter C Humphreys, Raymond N Schouten, Raymond FL Vermeulen, Marijn J Tiggelman, Laura dos Santos Martins, Bas Dirkse, et al. Realization of a multinode quantum network of remote solid-state qubits. *Science*, 372(6539):259–264, 2021.

[132] I Aharonovich, S Castelletto, DA Simpson, CH Su, AD Greentree, and S Prawer. Diamond-based single-photon emitters. *Rep. Prog. Phys.*, 74(7):076501, 2011.

[133] Birgit Judith Maria Hausmann, Brendan John Shields, Qimin Quan, Yiwen Chu, Nathalie Pulmones de Leon, R Evans, Michael John Burek, Alexander S Zibrov, M Markham, DJ Twitchen, et al. Coupling of NV centers to photonic crystal nanobeams in diamond. *Nano Lett.*, 13(12):5791–5796, 2013.

[134] Benjamin Kambs and Christoph Becher. Limitations on the indistinguishability of photons from remote solid state sources. *New J. Phys.*, 20(11):115003, 2018.

[135] Hans Riesen. Hole-burning spectroscopy of coordination compounds. *Coord. Chem. Rev.*, 250(13-14):1737–1754, 2006.

[136] M Kunzer, U Kaufmann, K Maier, and J Schneider. Magnetic circular dichroism and electron spin resonance of the A-acceptor state of vanadium, V^{3+}, in 6H-SiC. *Mater. Sci. Eng. B*, 29(1-3):118–121, 1995.

[137] Ioana Cozmuta, Solenn Cozic, Marcel Poulain, Samuel Poulain, and Jose RL Martini. Breaking the silica ceiling: ZBLAN-based opportunities for photonics applications. In *Optical Components and Materials XVII*, volume 11276, page 112760R. International Society for Optics and Photonics, 2020.

[138] Junfeng Wang, Xiaoming Zhang, Yu Zhou, Ke Li, Ziyu Wang, Phani Peddibhotla, Fucai Liu, Sven Bauerdick, Axel Rudzinski, Zheng Liu, et al. Scalable fabrication of single silicon vacancy defect arrays in silicon carbide using focused ion beam. *ACS Photonics*, 4(5):1054–1059, 2017.

[139] Elizabeth MY Lee, Alvin Yu, Juan J de Pablo, and Giulia Galli. Stability and molecular pathways to the formation of spin defects in silicon carbide. *arXiv preprint arXiv:2109.06420*, 2021.

[140] Kenichi Ohno, F Joseph Heremans, Lee C Bassett, Bryan A Myers, David M Toyli, Ania C Bleszynski Jayich, Christopher J Palmstrøm, and David D Awschalom. Engineering shallow spins in diamond with nitrogen delta-doping. *Appl. Phys. Lett.*, 101(8):082413, 2012.

[141] Mats Fahlman, Simone Fabiano, Viktor Gueskine, Daniel Simon, Magnus Berggren, and Xavier Crispin. Interfaces in organic electronics. *Nat. Rev. Mater.*, 4(10):627–650, 2019.

[142] Wenlong Zhang, Jian Zhang, Junfeng Wang, Fupan Feng, Shengran Lin, Liren Lou, Wei Zhu, and Guanzhong Wang. Depth-dependent decoherence caused by surface and external spins for NV centers in diamond. *Phys. Rev. B*, 96:235443, 2017.

[143] Sorawis Sangtawesin, Bo L. Dwyer, Srikanth Srinivasan, James J. Allred, Lila V. H. Rodgers, Kristiaan De Greve, Alastair Stacey, Nikolai Dontschuk, Kane M. O'Donnell, Di Hu, D. Andrew Evans, Cherno Jaye, Daniel A. Fischer, Matthew L. Markham, Daniel J. Twitchen, Hongkun Park, Mikhail D. Lukin, and Nathalie P. de Leon. Origins of diamond surface noise probed by correlating single-spin measurements with surface spectroscopy. *Phys. Rev. X*, 9:031052, 2019.

[144] Romain Vincent, Svetlana Klyatskaya, Mario Ruben, Wolfgang Wernsdorfer, and Franck Balestro. Electronic read-out of a single nuclear spin using a molecular spin transistor. *Nature*, 488(7411):357–360, 2012.

[145] Tsutomu Yamabayashi, Matteo Atzori, Lorenzo Tesi, Goulven Cosquer, Fabio Santanni, Marie-Emmanuelle Boulon, Elena Morra, Stefano Benci, Renato Torre, Mario

Chiesa, et al. Scaling up electronic spin qubits into a three-dimensional metal–organic framework. *J. Am. Chem. Soc.*, 140(38):12090–12101, 2018.

[146] Ainhoa Urtizberea, Eva Natividad, Pablo J Alonso, Miguel A Andrés, Ignacio Gascón, Michel Goldmann, and Olivier Roubeau. A porphyrin spin qubit and its 2D framework nanosheets. *Adv. Funct. Mater.*, 28(31):1801695, 2018.